The Effect of Reactive Elements on the Growth of Al_2O_3 Scales

by

Bruce Andrew Pint

S.B. Massachusetts Institute of Technology
(1988)

Submitted to the Department of Materials Science and Engineering in Partial Fulfillment of the Requirements for the Degree of

DOCTOR OF PHILOSOPHY IN CERAMICS

at the

MASSACHUSETTS INSTITUTE OF TECHNOLOGY

MAY 1992

Signature of Author _____
Department of Materials Science and Engineering
May 1, 1992

Certified by _____
Linn W. Hobbs
Professor of Materials Science
Thesis Supervisor

Accepted by _____
Linn W. Hobbs
Professor of Materials Science
Chairman, Departmental Committee
on Graduate Students

To

my family and friends

for all of their love and support

and especially my parents,

i love you

The Effect of Reactive Elements on the Growth of Al_2O_3 Scales

by

Bruce A. Pint

Submitted to the Department of Materials Science and Engineering on May 1, 1992 in partial fulfillment of the requirements for the degree of Doctor of Philosophy in Ceramics

Abstract

The growth of Al_2O_3 scales on FeCrAl and ß-NiAl was studied between 1000°C and 1500°C. By segregating to the oxide grain boundaries and the metal oxide interface, reactive element additions such as Y and Zr are found to improve the oxidation behavior of these materials. Without the addition of a reactive element, α-Al_2O_3 is found to grow by the combined diffusion of Al and O. When doped with a reactive element, the cation boundary diffusion through the α-Al_2O_3 scale is suppressed, thus reducing the oxidation rate. At temperatures of 1000°C and less, where metastable θ-Al_2O_3 is formed, oxide growth is predominantly by outward diffusion of Al.

Reactive element additions are also observed to improve oxide adhesion during cyclic oxidation tests. At the metal-oxide interface, the reactive element eliminates the detrimental role of indigenous sulfur ostensibly by prohibiting its segregation to this interface. Reactive element segregation on the oxide grain boundaries slows the grain growth in the scale, most probably by a solute drag effect.

An oxide dispersion in the alloy is found to produce a consistent, long-lasting improvement in the oxidation behavior. Ion implantation of Y is found to be an inappropriate technique for the study of the reactive element effect at the temperatures used in this study. At lower temperatures, the Y implant stabilizes the first-forming, faster-growing metastable θ-phase. At higher temperatures, the Y implant, which is concentrated at the substrate surface, is insufficient to produce a long-term change in the oxidation behavior. Alloy additions of Zr to NiAl were beneficial at lower temperatures, but scales on doped alloys nevertheless became less protective than undoped scales at 1400°C.

Thesis Supervisor: Linn W. Hobbs
Title: Professor of Ceramics and Materials Science

Table of Contents

List of Figures

List of Tables

Acknowledgments

The author is first of all fiscally indebted to a number of organizations. DOE for the first year and a half of my time as a graduate student, the NSF for the initial work on this study and the Timken Co. for emergency funds in 1990. The final 14 months of the project were funded by EPRI (with a special thanks to Jon Stringer).

Over the past 8 years at MIT there have been a host of individuals who have helped me in my studies and in learning about myself and the world around me. First of all my thanks to Marcia Conroy my freshman advisor who made me feel like more than a number and got me a job at the MIT Museum. Many glasses of wine and long lunches after I worked there, my thanks goes to Warren, Barbara, Michael, Joan, Don and Sandy and my second set of sisters, Sally, Phoebe and Kathy for their support and concern for things beyond science.

With 8 years of learning from the MSE department, there are also a fair number of people to thank there. Thanks to Profs. Witt, Roylance, Wuensch, Tuller, Spjut, Cima and Sadoway for making learning a little more interesting.

This monster study also had the support of a very large cast. First of all, I would like to thank Prof. Linn Hobbs for agreeing to take me and my project on after my first advisor, Prof. Greg Yurek, left MIT. I would also like to thank my other committee members, Profs. John Vander Sande and Yet-Ming Chiang for numerous useful comments and suggestions. For the alloys, thanks goes to Dr. Joe Doychak and Dr. Jim Smialek at NASA Lewis, Dr. William Lipscomb at Inco, Dr. Bo Jonsson at Kanthal and Ralph Mason and Dr. Wei Gao at MIT. I would also like to thank the future Dr. Mason for numerous discussions about oxide dispersions and mechanical alloying. Also a special thanks goes to Dr. Joe Doychak for his helpful suggestions especially regarding the catalyst literature on Al_2O_3 phase transformations. Only a small thanks goes to Drs. Bornstein and Smeggil at UTRC for supplying some material.

For their help and expertise with ion implantation and the implanter at MIT, much thanks goes to Mr. Richard Perilli and Dr. Amitabh Jain. Also, Mr. Pirelli was a great help on the design and debugging of the vacuum furnace not to mention the loan of the mechanical pump.

A number of people have helped me with the analytical work in the thesis, Joe Adario on GAXRD, Libby Shaw AES and XPS, Len Sudenfield on SEM, John Martin on SIMS, and Dr. Tony Garratt-Reed,

with whom it has been a pleasure to work for the past 6 years on the STEM. All of these individuals added there insights and expertise to this work, and saved me many hours by teaching me their craft. Thanks also to Fred Wilson, Pat Kearney and John Centorino for their advice and a few laughs

A very special thanks also goes to Mr. Guenter Arndt without whose help and advice (and nuts and bolts) neither of the furnaces would have ever worked. He has kept a smile on my face with his spirit and understated advice. Inspiration comes in many forms but my admiration goes to this man who has kept the wheels of research turning at this Institute for many years with very little credit and not enough respect from those who should know better.

I would also like to thank Prof. Greg Yurek for my start in high temperature oxidation. Things always have a way of working out in the end. Also thanks to a few of the people in the lab when I started, Mike Maloney, Yong-Kil Kim, Kaz Przybylski and Cathy Cotell who helped me get started. Ms. Cotell deserves a special thanks for her advice and for arranging to get samples ion implanted at NRL. Thanks to other members of the group including Wei Gao, Chuxin Zhou, Julia Duncan and Linn's former secretary, Liz Van Kirk; also to UROPers, David Yao, Christy Choi, Kelly Wills and Karl Cheng.

Thanks also to Dr. Rosendo Fuquen and Dr. Dennis Hetzner at the Timken Co. for advice and encouragement about graduate school.

There are also a few friends to thank including my former roommates, Jordan Dentz and Mark Buonanno. My officemates Mike Warwick, Alex Otto and Ms. Duncan. Some old friends who keep in touch Eric Katz, Ryoichi Shiono, Ken Yu, and Paohua Kuo and a few even older friends Bridget, Chris, Vita, Ray and Jeff. (There is no place like home.) Also to a few who taught me some other lessons, Heidi, M.A. and the HAG. Last but not least thanks to Jack Smith for numerous long and fruitful discussions. Success will never be measured in dollars and cannot be achieved if one's honor is lost along the way.

A final thanks goes to the DJs at WBCN. The hours of rock n' roll are uncountable, and The Boston Globe, whose ink has indelibly stained my fingertips and my life. Finally a spiritual thanks to Frs. O'Donnell and Cambell and the other Paulist priests who every week helped to keep me in perspective. After all, this is only a piece of paper and, in the "big picture", we are all more important.

1.0 Introduction

Small additions of certain "reactive" elements (REs) have a large beneficial effect on the oxidation behavior of alloys. This improvement, known as the reactive element effect (REE), has been used in the manufacture of high-temperature, oxidation resistant alloys since its discovery 55 years ago [Pfeil, 1937]. From an engineering perspective, the primary effect is a marked enhancement in the spallation resistance of protective oxide scales, such as Cr_2O_3 and Al_2O_3, grown on these alloys. Also, reductions in the oxidation rate by as much as 100 times have been documented for the case of alloys that form Cr_2O_3 scales. These effects and others have been studied extensively since their discovery. However, the basic reasons for the beneficial effects of reactive elements have not been fully determined.

In recent years, the study of corrosion processes has changed dramatically. With the recent advent of a number of superior analytical tools, the study of oxidation mechanisms has taken a quantum leap forward. The scanning transmission electron microscope (STEM) combines the high resolution of electron microscopy with the analytical capabilities of energy dispersive X-ray analysis (EDXA). Also, secondary ion mass spectrometry (SIMS) can identify tracer elements (such as ^{18}O) to identify diffusion mechanisms without some of the uncertainties of inert marker experiments.

Using these techniques, a new understanding has emerged of the effect of reactive elements on the oxide growth mechanisms,

microstructures and growth rates. The primary observation has been that foreign ions, such as Y^{3+}, segregate to oxide grain boundaries in Cr_2O_3 and Al_2O_3 scales [Przybylski, et al., 1987; Cotell, et al., 1987; Yurek, et al., 1987a]. The segregants are present as individual ions and not in separate phases.

Another recent finding about the REE that seems clear is that a combined effect of the RE and sulfur exists. According to the results of Smeggil et al. [1985] and Smialek [1987a], one role of REs in enhancing the spallation resistance of oxide scales is the "gettering" of sulfur, an impurity in all commercial alloys. According to this model, sulfur not tied up by reaction with a RE can segregate to the alloy/scale interface. This segregation lowers the interfacial free energies of the metal and oxide and promotes decohesion of the scale from the alloy by lowering the energy required for spallation.

For chromia-formers, segregation of the RE to the oxide grain boundaries has been demonstrated and the REE fully outlined as follows:

(1) a change in the rate-limiting step of oxidation, from predominantly chromium transport outwards to oxygen diffusion inward, which reduces the parabolic oxidation rate;

(2) an improvement in scale adhesion;

(3) a change in oxide microstructure including a reduction in oxide grain size;

(4) improved selective oxidation of Cr, thus requiring less Cr in the alloy to form a continuous Cr_2O_3 scale.

All these effects have been observed for the oxidation of alloys that form Cr_2O_3 scales, while only the second effect has been clearly observed for alloys that form Al_2O_3 scales. These effects have been attributed to the segregation of the RE ions, e.g. Y^{3+}, to grain boundaries in Cr_2O_3 scales [Przybylski and Yurek, 1989].

These effects have, in fact, been studied extensively for chromia forming alloys. However, as maximum-use temperatures increase (>1200°C), chromia is no longer protective, due to its volatility. At higher temperatures, alumina gives better protection due to its relatively low volatility, its slow grow kinetics, and its chemical inertness. The same type of fundamental understanding established for chromia scale growth is now required for alumina scales. Applications for high temperature intermetallics such as nickel aluminide (T_m = 1638°C), are being developed, and the oxidation behavior of such materials needs to be studied more closely in order to maximize their potential.

While various alloy systems form Al_2O_3 scales, the concentration here is on the formation of compact, dense scales at very high temperatures (>1300°C). This excludes systems such as TiAl where, because of the thermodynamic stability of TiO_2, a mixed TiO_2-Al_2O_3 scale is formed. It also excludes a variety of lower melting point intermetallics such as FeAl, Ni_3Al, and $NiAl_3$.

This study focuses on the oxidation mechanisms of alloys that form Al_2O_3 scales (primarily FeCrAl and ß-NiAl), and the effects of yttrium and zirconium on the oxidation mechanisms and the resistance to scale spallation, in order to optimize oxidation resistance at elevated temperatures.

The goals of this study are relatively simple:

(1) to characterize the oxidation behavior of undoped alloys, especially the oxidation mechanism and the oxide microstructure;

(2) to determine the effect of RE additions on the oxidation behavior; and

(3) to examine the effect of temperature on these phenomena over the range 1000° to 1500°C.

2.0 Literature Review

As in many other scientific fields, the literature on high temperature oxidation has grown by orders of magnitude in the past 20 years. The following is an attempt to peruse the large mass of printed matter to identify the most salient issues.

2.1 Oxidation Behavior of Alumina-forming Alloys

By way of introduction to the subtleties of this rather small, but vigorous field, a few basic facts of high temperature (>600°C) oxidation are outlined. High temperature oxidation involves very basic thermodynamics and kinetics. The aim of corrosion protection is not to prevent the reaction of metal and oxidant (in this study exclusively oxygen) but to use the reaction product to inhibit further oxidation. In order to achieve this goal, the oxide must be dense and stable, preferably slow-growing, and adherent to the metal. For engineering purposes, these characteristics are usually achieved by combining some base element such as Fe, Ni, or Co with one or more elements, such as Cr, Al or Si, which form protective oxides. Figure 2.1 shows an Ellingham diagram of the free energies of formation of various oxides. In general, oxides with lower free energies also have slower growth rates. For illustration, the case of Ni-Al alloys will be discussed. The lines for NiO and Al_2O_3 are emphasized in Figure 2.1. Because Al_2O_3 has a lower formation free energy than NiO, it is thermodynamically more stable. Thus, in equilibrium, Al will oxidize preferentially to Ni. In the absence of equilibrium, the

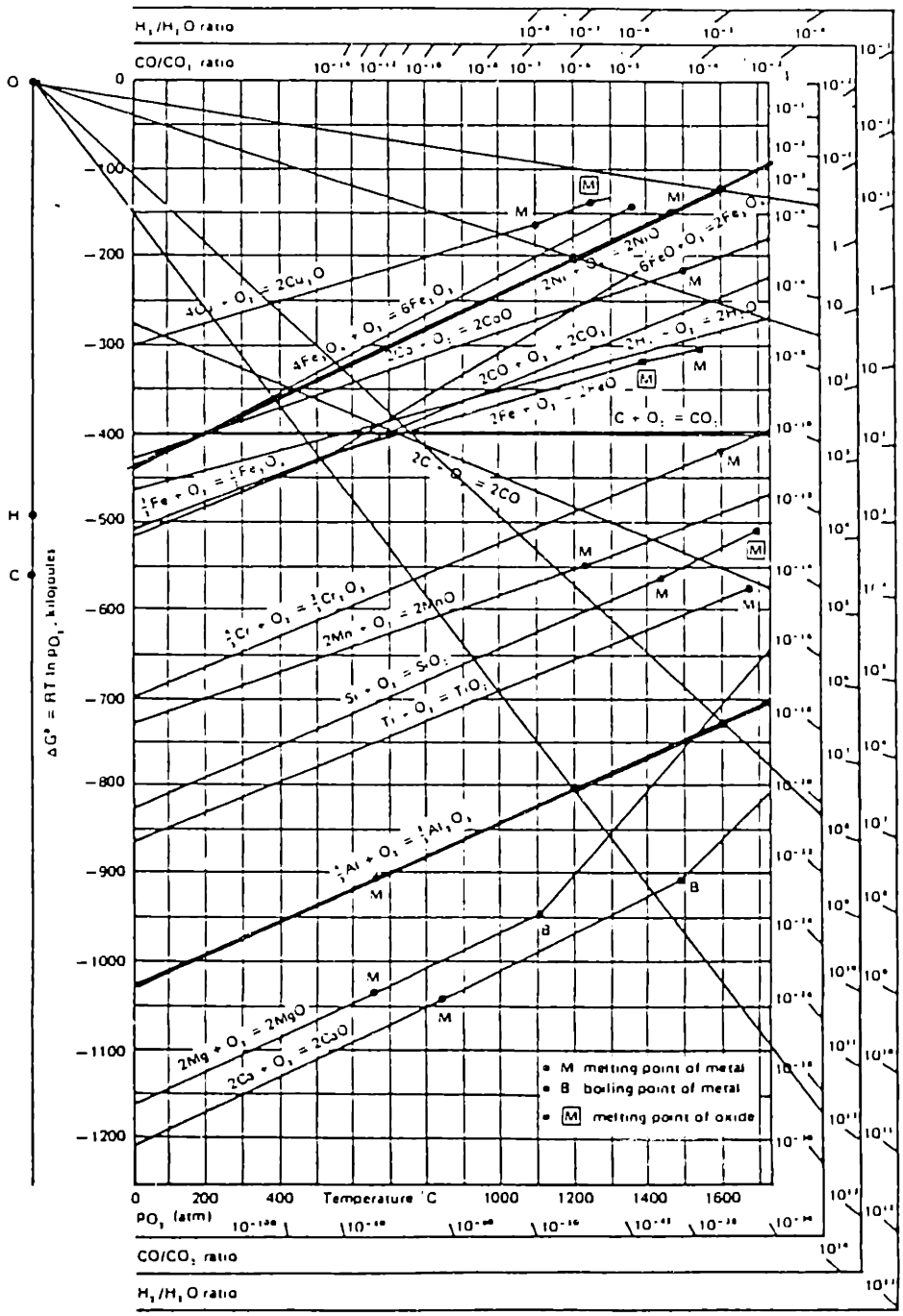

Figure 2.1 Ellingham diagram showing the free energy of formation of various oxides versus temperature [Gaskell, 1981, p.287].

kinetics of the oxidation reaction require a minimum Al content in order to achieve preferential or selective oxidation of Al.

The basic stages of the oxidation reaction are shown schematically in Figure 2.2. Assuming there is sufficient Al, a protective steady-state Al_2O_3 scale will form. Prior to the steady-state stage is a transient stage, when less noble oxides, such as NiO or $NiAl_2O_4$ may form. Typically, this initial layer is undercut by Al_2O_3 to begin steady-state oxidation. Al_2O_3 grows three orders of magnitude more slowly than NiO, so the change to steady-state also usually implies a substantial reduction in the oxidation rate [Fueki and Wagner, 1965]. When the substrate becomes depleted in Al, Ni-rich oxides form rapidly, leading to breakaway oxidation. At this point, protective oxidation is no longer possible, and the reaction proceeds more rapidly to eventual full consumption of the metal.

There are, of course, variations on this simple model. For instance, breakdown may occur in the steady-state period followed by the formation of a healing Al_2O_3 scale. Repeated breakdown-healing cycles may even characterize the steady-state period. The breakaway period implies that the reaction is out of control and no healing will occur. Thus, to produce an oxidation resistant alloy, the goal is to minimize the transient stage and maximize the length of the steady-state oxidation period.

From a kinetic standpoint, the hallmark of protective, steady-state oxidation is a parabolic rate law. In this case, the rate is limited by diffusion through the oxidation product which, as it becomes thicker, slows the reaction rate. One begins with Fick's second law,

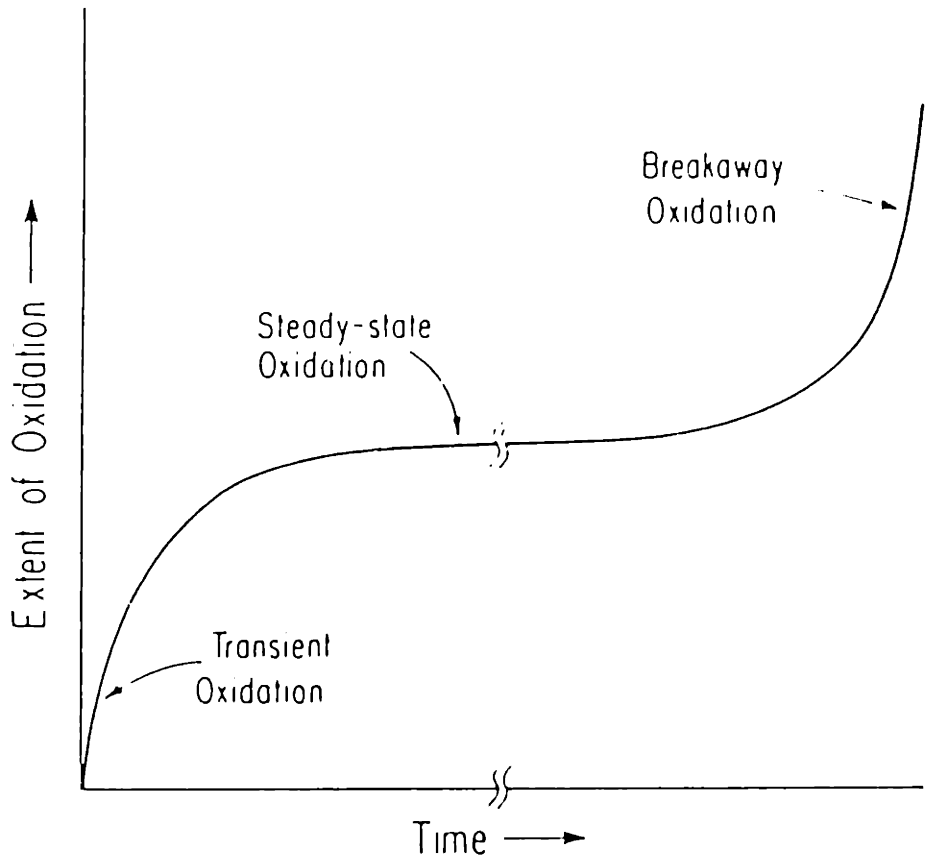

Figure 2.2 Schematic model of protective oxidation showing the extent of oxidation (e.g. weight gain, scale thickness, metal consumed) versus time [Yurek, 1987].

$$\frac{\partial c}{\partial t} = \frac{\partial}{\partial x}\left(D \frac{\partial c}{\partial x}\right), \qquad (2.1)$$

where c = concentration, x = the diffusion distance, D = the diffusion coefficient, and t = time. The concentration of reactants across the scale is assumed constant, as is the diffusion coefficient D. Representing by Δx the instantaneous scale thickness and with all of the constants subsumed in one constant k, Equation 2.1 reduces to:

$$d(\Delta x)/dt = k/\Delta x \qquad (2.2)$$

which, when integrated, results in the parabolic rate law:

$$(\Delta x)^2 = 2k_p t + C \qquad (2.3)$$

where C is the integration constant, physically representing a simple correction for the scale thickness formed during the non-parabolic transient stage.

The above is a first-order introduction into the basic thermodynamics and kinetics of oxidation. The complexities are outlined in the rest of the chapter.

2.1.1 Ni-Al Alloys

The Ni-Al phase diagram is shown in Figure 2.3. The interest here is on high temperature alloys that will also grow a continuous Al_2O_3 scale. Therefore, the right hand side of the phase diagram is emphasized for high temperature alloys. The next step is to

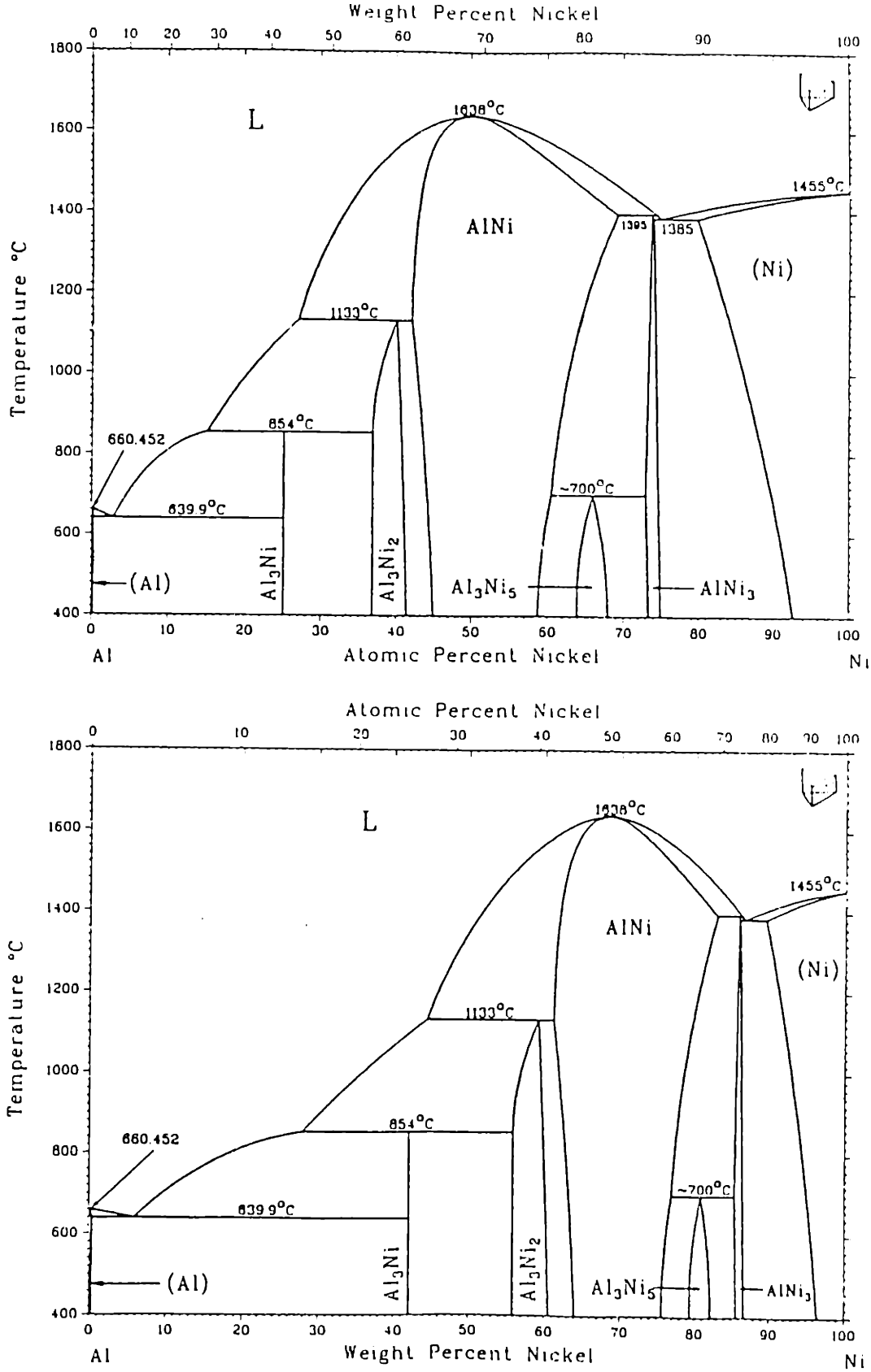

Figure 2.3 The Ni-Al phase diagram [Binary Alloy Phase Diagrams, p.142].

determine the amount of Al necessary to form a protective Al_2O_3 scale.

One of the earliest reported studies of the oxidation of Ni-Al alloys was carried out by Pettit [1967]. Working with Al compositions between 3 and 25wt%, he established a minimum aluminum content for the formation of a protective Al_2O_3 scale for temperatures between 900° and 1300°C in 0.1atm O_2 and in a CO-CO_2 gas mixture with a CO/CO_2 ratio of 2.0, Figure 2.4. Using both thermodynamic fundamentals and experimental evidence, Pettit identified three separate mechanisms: Region I, primarily NiO formation; Region II, initially Al_2O_3 but giving way to NiO when the alloy becomes Al depleted; Region III, external Al_2O_3 layer. Pettit calculated that the aluminum concentration at the alloy surface must be less than 1ppm in order for NiO or $NiAl_2O_4$ to be thermodynamically stable oxides. Therefore, if the diffusion flux of aluminum in the alloy, J_{alloy}, is greater than the rate of consumption of Al to form oxide, J_{oxide} (independent of oxidation mechanism), Al_2O_3 will form a permanent protective scale. This is because the near-surface Al consumed by scale growth is replaced, i.e. no depletion occurs.

Based on the relationship between Al content and temperature (Figure 2.4), Pettit concluded that Al_2O_3 grows by oxygen diffusion inward and that NiO forms when oxygen is able to diffuse through the scale faster than aluminum can diffuse in the alloy. Also, due to the temperature-composition dependence for the formation of a continuous Al_2O_3 scale, he concluded that the diffusion of aluminum

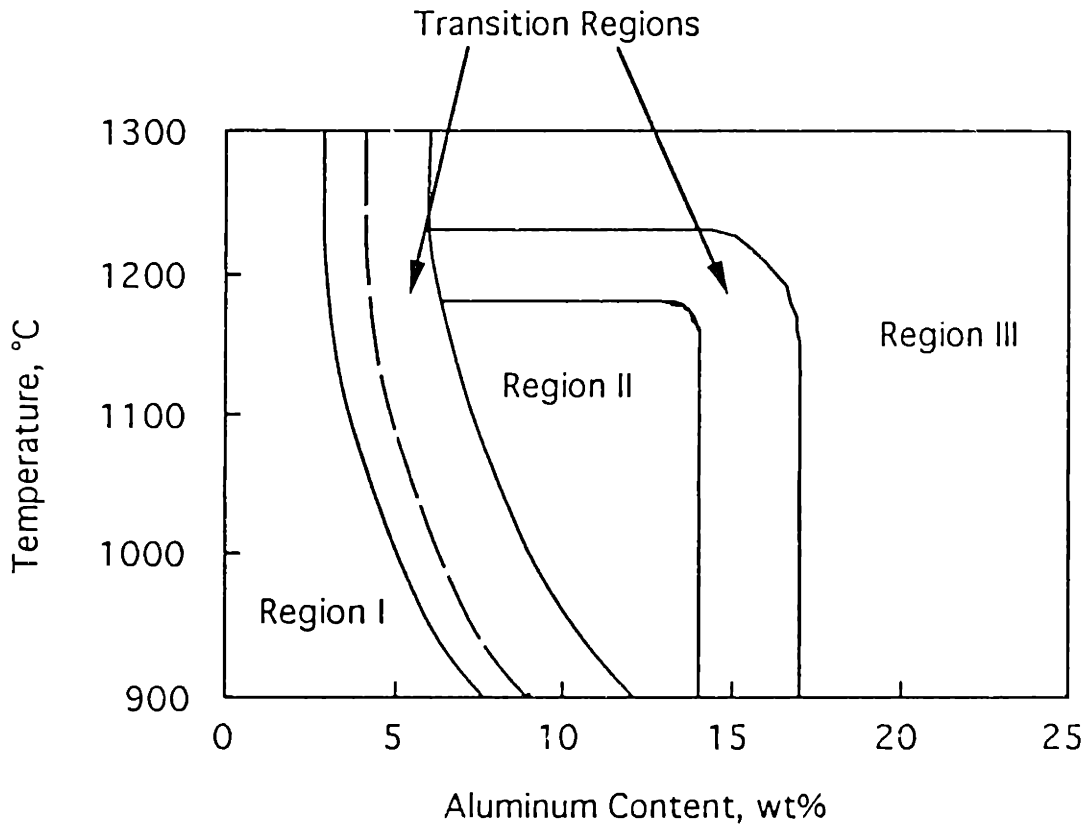

Figure 2.4 Dependence of the oxidation products for Ni-Al alloys on temperature and alloy composition. Region I: primarily NiO, Region II: initially Al_2O_3, but eventually NiO, Region III: primarily Al_2O_3. The dashed curve indicates the transition from internal to external oxidation for specimens oxidized in CO-CO_2 mixtures where Al_2O_3 is the only stable oxide [Pettit, 1967].

in nickel is more temperature dependent than the diffusion of oxygen in Al_2O_3.

More recent studies have looked at other issues regarding NiAl oxidation. Jedlinski et al. [1987] studied the difference between polycrystalline and single-crystal stoichiometric ß-NiAl. They reported that the oxidation of single-crystal ß-NiAl showed slower growth of α-Al_2O_3 than both unimplanted or Y-implanted polycrystalline ß-NiAl. The absence of grain boundaries in the alloy favored the formation of a coarse-grained scale, which grew more slowly. No mention was made of the adherence of Al_2O_3 on single-crystal ß-NiAl.

Doychak et al. [1988] studied Ni-rich Ni-Al intermetallics. The conclusion was that the rate increased slightly with lower Al content over the range 26-50at%Al. The motivation for studying the lower Al content alloys is the improvement in ductility relative to stoichiometric ß-NiAl [Russell and Edington, 1972]. However, in cyclic tests even with Zr-doping, alloys with less than 40at% Al were found to spall readily at 1200°C. This also corresponds to a composition outside the ß-NiAl phase field and includes some γ'-Ni_3Al which has a much lower melting point.

Some work also has been conducted on $NiAl_3$, which was found to form more adherent Al_2O_3 scales than ß-NiAl [Young and de Wit, 1983]. However, the usefulness of this material is limited by its relatively low melting temperature, ≈900°C.

Several studies have found that at temperatures below 1000°C, metastable Al_2O_3 phases such as γ, δ, and θ are formed [Doychak, et al., 1985; Smialek and Gibala, 1983]. This literature is

not reviewed further because the lowest temperature in this study is 1000°C. However, the transient formation of metastable oxides and especially the $\theta-\alpha$ phase transformation at 1000°C is discussed further in Section 2.1.3.

2.1.2 FeCrAl Alloys

There are a number of studies which give essentially only kinetic data for FeCrAl [e.g., Hagel, 1965a] A few important characterization results will be noted about the general oxidation behavior. More data about FeCrAl oxidation is included in later sections.

Golightly et al. [1975] noted that the undoped Al_2O_3 scale on FeCrAl was severely buckled. This study also noted that Y-doped Al_2O_3 was not buckled. The reason for this difference in microstructure was ascribed to a change in the oxidation mechanism. The undoped buckled scale being caused by simultaneous Al and O transport and new oxide being formed in the center of the scale.

Another standard study of FeCrAl alloys looked at the effect of the addition of Al on the oxidation rate [Lambertin and Beranger, 1990]. According to this study, the formation of a continuous Al_2O_3 scale required 4wt%Al. Higher Al contents reduced the transient period but did not change the oxidation rate significantly.

More recent work by Bennett et al. [1991] examined the oxidation of doped and undoped FeCrAl from 1200°C to 1400°C. This study concluded that higher Al contents were required as the

temperature was increased. An unusual feature that was observed after oxidation was the formation of voids in the interior of the alloy. This occurred on both doped and undoped alloys and apparently did not effect oxide adherence. It was proposed that residual gas in the alloy from processing coalesced to form these voids.

2.1.3 Transient Oxidation Behavior

The transient period is most typically characterized by the formation of less noble oxides (FeO and Cr_2O_3 in the case of FeCrAl). In the case of Al_2O_3, the transient period can also be complicated by the formation of the metastable θ-Al_2O_3 instead of the stable α-Al_2O_3. For instance, Doychak, et al. [1988] investigated the transient oxidation of a ß/γ' Ni-Al alloy using TEM parallel sections. After 0.05hr at 1100°C, $NiAl_2O_4$ was formed over the γ'-Ni_3Al phase while θ-Al_2O_3 was formed over the ß-NiAl phase. At longer times, the θ-Al_2O_3 transforms to α and the the Ni-rich oxide was undercut to form a continuous α-Al_2O_3 scale.

Hagel [1965a] was one of the first studies to report the formation of θ-Al_2O_3 scales on various alumina-formers below 1000°C. Rybicki and Smialek [1989] more clearly outlined the effect of the phase transformation of Al_2O_3 on Zr-doped ß-NiAl. In this work, they detail the formation of θ-Al_2O_3 at temperatures below 1000°C and the transformation to α-Al_2O_3. At 1000°C, the rate of growth of θ is approximately two orders of magnitude faster than the growth of α. This was attributed to a change in the oxidation mechanism between the two phases.

The scale phase and the phase transformation also has a large effect on the oxide morphology. θ-Al_2O_3 forms a blade like morphology while the transformation, especially near 1000°C, produces surface ridges on the α scale and cracks within the scale. The cracks are attributed to the >10% volume reduction during transformation to α-Al_2O_3. This type of microstructure was also observed by Doychak, et al. [1985].

At higher temperatures (>1200°C), the transient period is reduced due to faster diffusion of Al in the alloy and thus a faster formation of a continuous Al_2O_3 scale. Also at higher temperatures, the formation of θ-Al_2O_3 is limited to very short times or does not form at all.

2.2 Attempts to Explain the Reactive Element Effect

In 1937, the use of certain elements to improve alloy oxidation behavior was patented in the U.K. by Pfeil [1937]. Since that time, countless observations have been made of this so-called "reactive element effect" (REE). The phenomenon has also been misnamed the "rare earth effect," but two of the primary elements, Y and Zr, are not rare earths. The REE literature has been reviewed numerous times, with the compilation by Whittle and Stringer [1980] being cited most often. More recently it was reviewed by Moon [1988] and Jedlinski [1990]. The following is a brief synopsis of the effects followed by the most popular theories to explain the role of REs.

In both chromia- and alumina-forming systems, the reactive element effect is most basically characterized from an engineering

or macroscopic view by a reduction in the rate of oxidation and an improvement in oxide adherence. The change in oxidation rate for chromia-formers is 1-2 orders of magnitude, while the reduction for alumina-formers is less. A reduction of 2-4 times is often reported, but some authors have reported no change in the rate [Bennett, et al., 1990]. On the other hand, the greater effect in alumina-formers appears to be the improvement in oxide adherence. Without some type of modification, spallation of Al_2O_3 scales from most alloys is severe. Undoped Cr_2O_3 scales are usually somewhat adherent. Both oxides are observed to be more adherent when doped with a RE.

The macroscopic change in the oxidation rate also implies an atomistic change in the rate-limiting step for the oxidation reaction. In chromia-formers, the addition of an RE changes the predominant oxidation mechanism from primarily outward Cr transport without a dopant to predominantly inward O diffusion with a RE [Cotell, et al., 1990a]. For alumina-formers the effect is not so well documented (see Section 2.4).

A RE addition is also reported to improve the selective oxidation of chromia-formers, i.e less Cr is required in the alloy to achieve a continuous Cr film. This effect has not been directly observed in alumina-formers. The addition of a RE furthermore results in a change in the oxide microstructure and especially a reduction in the oxide scale grain size.

All of these experimental observations, taken together, show an improvement in the oxidation behavior of RE-doped alloys.

However, the exact mechanisms by which a RE addition changes the oxidation behavior have not been conclusively identified.

While experiments have abounded, coherent explanations for the role of these elements have been few, and a robust theory explaining all of the effects has not been put forth. Like grammar rules, whenever a theory is laid out, there always seems to be some exception. The following is an attempt to cover all the bases. However, the amount of coverage given to each theory does not necessarily reflect the number of papers advocating a particular theory. Some of the theories, for instance the peg theory and the void theory, either have been shown to be obsolete or are relatively simple concepts that do not require much explanation.

2.2.1 The Segregation Theory

Listed first by no accident is a theory which attempts to explain all of the observed REE based on one observation -- the segregation of the RE to the oxide-metal interface and the oxide grain boundaries. While the theory is far from proven conclusive, it does take all of the major effects into account. It is also attractive because of its simplicity and inclusiveness in explaining all of the RE effects. Grain boundary segregation is reviewed more extensively in Section 2.7.

While other researchers have hypothesized previously and since observed this segregation, the segregation theory was first outlined by Przybylski and Yurek [1989] for chromia-formers. The major observation, by Cotell et al., [1987], was that the growth

mechanism for Y-implanted Cr (2 x $10^{16}/cm^2$) was changed to primarily oxygen transport inward. The grain boundary flux of outward-diffusing Cr was limited by the segregation of Y to the oxide grain boundaries. Due to this change in mechanism and a solute-drag effect, the segregant also had a profound effect on the oxide microstructure. Without a dopant, new oxide formed at the gas interface, leading to large columnar grains (axis normal to the metal interface) near the gas interface at 900°C. With a dopant, the much thinner scale had a finer grain size and more equiaxed grains. Columnar grains were observed in this case near the metal interface, exactly the opposite of the undoped case.

According to this theory, the RE addition reduces scale spallation due to a number of factors. The change in oxidation mechanism and oxidation rate reduces the scale thickness thus reducing growth stresses. Przybylski and Yurek [1989] also concluded that while impurities (like S) in the alloy were deleterious to the oxide adhesion, removing them without a RE addition would not improve long-term adherence. Eventually the faster-growing undoped scale would generate sufficient stress to cause failure. Thus S removal could not be substituted for a RE addition in the long run.

A broad-based attempt to apply this theory to alumina-formers has not appeared in the literature.

2.2.2 Interface Theories

In order to save space, several theories related to the metal-oxide interface will be discussed together in this section.

(1) The Graded Seal. This is the simple idea that a RE-rich layer forms between the substrate and the oxide. According to this hypothesis, the rate-limiting step is modified because of slower diffusion through this layer and adhesion is improved because this layer acts as a strengthening intermediary phase. This theory persisted because early analytical techniques such as EPMA did not have sufficient resolution to detect a thin layer [Wood and Boustead, 1968]. When more advanced analytical techniques (such as XTEM) began to be employed, the interface between the oxide and the substrate could be analyzed. These studies found that such a layer did not exist [e.g. Ramanarayanan, et al., 1984; Katz, et al., 1987].

(2) Oxide Pegs. This idea was based on observations of internal oxidation of the RE when the RE was added by alloying (see Sec. 2.3.1). The selective internal oxidation of the RE near the surface would often form oxide protrusions into the substrate which were attached to the external scale. These oxide "fingers" were proposed to grab onto the alloy, thus improving scale adherence [Felten, 1961; Allam, et al., 1978; Pendse and Stringer, 1985; etc.]

Over the past 20 years, as RE additions have moved beyond simple alloying, this theory has become less prominent. Addition of the RE by ion implantation and oxide dispersions improves the oxide adherence without the formation of pegs. Thus, while pegs may play a role, they are not necessary to improve adherence.

(3) Interface Bonding. According to this hypothesis, the undoped metal-oxide bond is normally weak. By adding a RE to the alloy, the bond is strengthened. Obviously, this theory is somewhat unspecific regarding exact mechanisms. After the detrimental role of indigenous sulfur was demonstrated [e.g., Smeggil, 1985], S was identified as the reason for the weak undoped interface. The role of sulfur is discussed more thoroughly in Sections 2.2.5 and 2.5.

(4) Void Theory. This theory is another hypothesis arising from observations of the alloy-oxide interface. In this case, the undoped interface is observed to have voids at the interface, while the doped interface is adherent and no voids are observed. An idea attributed to Stringer [1966] is that the RE in the alloy acts as a vacancy sink. Thus, vacancies are captured by the RE rather than coalescing into voids at the alloy-oxide interface. Kumar, et al., [1974] proposed that an internally-oxidized RE in the alloy forms dislocation loops which annihilate these vacancies. (No attempt was made to look for these dislocations.) Accordingly, when the RE addition becomes saturated with vacancies, voids would form and cause failure.

Tsuzi [1980] observed, in FeCr with 0.87% Y, that no voids were present at the alloy-oxide interface, but voids were found centered on internally-oxidized Y_2O_3 particles in the alloy. These voids were observed in metallographic cross-sections and no consideration was made of possible polishing effects or the difference in thermal expansion between Y_2O_3 and FeCr. The void explanation has also been used in numerous other systems including the addition of Y to Ni_3Al [Kuenzly and Dougiass, 1974].

Experimental observations have not always been consistent with this hypothesis. A Y_2O_3-dispersed NiCr alloy oxidized at 900°C [Pint, et al., 1988] and 1000°C [Katz, et al., 1987] was investigated for possible void formation near YAl_xO_w particles in the alloy. Before and after oxidation, TEM parallel sections of the alloy near the oxide interface were examined. No voids were found at these interfaces in either case. However, at both temperatures, the oxide adherence was excellent.

One of the weaknesses of the void theory is that it deals mainly with the issue of improved adherence. It does not address the other RE effects such as the observed changes in the oxidation mechanism or the oxide microstructure.

2.2.3 Scale Plasticity

This hypothesis is experimentally based, mainly on the observation of a reduction in the oxide grain size with the addition of a RE. It is proposed that this reduction in grain size improves the mechanical properties of the scale (e.g. plasticity), thus improving the oxide adherence [Antill and Peakall, 1968; Francis and Jutson, 1968; Ramanarayanan, et al., 1983]. This idea is fully consistent with the segregation theory in that the segregation of the RE to the oxide grain boundaries slows the grain growth, producing a finer grained scale. A reduction in grain size would alter the mechanical properties of the scale, with a likely improvement in ease of creep deformation and thus a greater ability to relieve growth stresses.

However, there is no evidence to show conclusively that a finer oxide scale is more adherent than a larger grained scale.

2.2.4 Elimination of Growth Stresses

This theory is also based on one observation -- the change in the rate-limiting step of oxidation. In both chromia and alumina scales, cation transport is reduced with the addition of a RE [Mrowec, et al., 1987]. Mrowec, et al. concluded that the entire REE (especially slower growth and improved adherence) is due to a change in the oxidation mechanism and not due to any interfacial phenomena, such as sulfur segregation or oxide pegging. Golightly et al. [1976] had earlier proposed a similar explanation for alumina-formers. When cation transport is eliminated, metal vacancies responsible for the outward diffusion are no longer generated, thus eliminating voids at the metal-oxide interface and improving oxide adhesion. Oxide microstructures are also modified by the change in the scale growth mechanism.

Also involved in this type of argument is the calculation of stresses in a growing oxide film [e.g. Cathcart, 1976]. The contention here is that, for chromia-formers, comparing doped and undoped scales is inappropriate, because the faster oxidation rate in the undoped case will cause higher stresses, always leading to agreater failure rate. With a reduction by 1-2 orders of magnitude in the scale growth rate for RE-doped substrates, it is more logical to compare scales of equal thickness. However, this type of argument does not hold for the case of alumina-formers where

reductions in the oxidation rate are generally less than an order of magnitude. In this case, the doped and undoped scales of equivalent thicknesses exhibit radically different behavior. Undoped alumina scales often spall completely, leaving only the bare metal [Przybylski, et al., 1987].

The major difference between this theory and the segregation theory is that this theory does not recognize the role of sulfur as important to adherence.

2.2.5 The Sulfur Effect

One of the more recent additions to the list of possible explanations is the sulfur effect. This hypothesis goes beyond the findings of Funkenbush, et al. [1985] and Smialek [1987a] about oxide adherence (see Section 2.5) to conclude that the presence of sulfur explains all REEs. First proposed by Lees in 1987 in an unreviewed journal article, this hypothesis remains largely unsubstantiated. Like other theories, this idea relies on one simple premise -- that sulfur causes all of the detrimental effects in high temperature oxidation. According to this theory, the RE combines with sulfur and prevents it from affecting the oxidation behavior.

In the absence of sulfur, however, a RE addition would be unnecessary -- adherence would be good, the oxide would naturally grow by the slower anion transport, and presumably the grain size would be reduced. Yet despite the fact that ultra low-sulfur alloys are available, none of these effects has been observed except for the improvement in oxide adherence. A recent paper by Fox, Lees, and

Lorimer [1991], studied the oxide formed on Cr-165ppmS (approximately ten times the S content found in a conventional alloy). Using EDXA on an FEG-STEM, S was detected to have segregated to high angle grain boundaries and the metal-oxide interface. This was claimed to be proof of the sulfur effect - S segregated to these interfaces promoted the outward diffusion of Cr and oxide spallation. No published work has shown any evidence that in a sulfur-free alloy, Cr_2O_3 or Al_2O_3 grow predominantly by inward oxygen diffusion. Furthermore, Smialek [1989] demonstrated that there was no change in the oxide microstructure when S was removed from NiCrAl. The only effect of S removal was to improve oxide adhesion.

While this hypothesis is plausible, there is simply no published experimental evidence to prove that S has any effect other than being detrimental to scale adherence.

2.3 Methods of Reactive Element Addition

Now that the benefits of a RE addition have been expounded, the more practical issue of actually adding the RE to a system becomes significant. While most of the first 30 years of RE research examined mainly RE alloy additions, the last two decades have emphasized other types of additions. A RE oxide dispersion is particularly attractive because of the dual purpose of the dispersion. A stable RE oxide (such as Y_2O_3) not only benefits the oxidation behavior but also improves the creep properties at high temperature. A second technique, first used in the electronics industry, is ion

implantation. This surface treatment essentially allows any element to be added to any solid substrate in the near-surface region. Both oxide dispersions and ion implantation provide a uniform source of the RE, eliminating problems associated with alloying.

2.3.1 Alloying Additions

While alloying of the reactive element would seem to be the simplest and easiest way of adding the element to the system, the success of RE alloy additions is sometimes limited because of their phase separation in the metal. Numerous studies have found a more beneficial effect of a RE when it is more evenly dispersed in the alloy. For example, a Hf addition produces better oxidation behavior than an equal addition of Y in CoCrAl [Allam, et al., 1978]. Hf is more soluble in CoCrAl, while Y is found to be concentrated in second-phase particles at the alloy grain boundaries. Yet, besides the formation of Y-rich intermetallics, there is no other evidence to suggest that Y is not as effective as Hf as a RE addition.

Kuenzly and Douglass [1974] found general detrimental effects for the addition of 0.5wt%Y to Ni_3Al at temperatures between 1100° and 1200°C. While Y prevented short-term spallation and eliminated void formation at the alloy-oxide interface, it did not affect the weight gain and it enhanced the formation of NiO. Kuenzly and Douglass found that Y in the Ni_3Al-0.5Y alloy is present as Ni-Y intermetallics, which upon oxidation form Y_2O_3 and eventually yttrium-aluminum garnet (YAG). After longer exposures, YAG

particles in the scale were believed to act as stress concentrators and to cause spallation during cooling. Similar results were found in the case of Y additions to NiCrAl alloys [Kumar, et al., 1974].

In cases where second phases are not formed in the alloy, more successful results are found. One significant example is the use of alloyed Zr in NiAl. This is the type of RE addition used in many of the studies done by the NASA group and Doychak [Barrett, 1988; Doychak, et al., 1985, 1989a, 1989b; Reddy, et al., 1982].

2.3.2 Ion Implantation

Surface implantation of a RE has been found to yield more uniform effects than alloying, for which RE-rich particles often form in the alloy. Microstructurally, this leads to a more uniform scale, where no oxide pegs or other anomalies are found. For instance, Sprague and Johnston [1983] found that voids formed beneath oxide films on both CoCrAl and CoCrAl + 0.5%Y but did not form when the alloy was implanted with Y. The conclusion was that because Y segregated in the alloy, the voids on CoCrAlY formed in areas without Y. The even-distribution of the implant eliminated these undoped regions.

Jedlinski and Mrowec [1987] studied the effect of implanted yttrium on the oxidation of Ni-Al (51.9 at%Al) between 1000 and 1300°C. Without Y implants, Al_2O_3 scales exhibited poor adherence. With doses of $2x10^{16}$ Y^+/cm^2 at 70keV, adherence was improved and weight gain was reduced.

Further work by Mrowec, Gil and Jedlinski [1987] showed that an ion-implanted yttrium dose of 2 x 10^{16} cm^{-2} at 70kV was required to improve Al_2O_3 adherence on ß-NiAl in 2hr cyclic tests at 1200°C in air, Figure 2.5. [Mrowec, et al., 1987] Similar work by Jedlinski and Mrowec [1987] used "perfect" to describe the adherence of the scales on Y-implanted NiAl. However, a similar dose of lanthanum (which exhibits all of the REE in chromia-formers) had no effect on adherence, but did slightly slow the growth of Al_2O_3 in isothermal tests.

Ion implantation of Y also has been used extensively to study the REE in chromia-formers [Przybylski and Yurek, 1989]. Collins et al. [1979] separately implanted 35 different elements into Cr substrates to determine which species exhibited the REE. No specific effect of ionic radius or valence was found. Cotell, et al. [1990b] demonstrated that an Y implantation level of 1 x $10^{15}/cm^2$ was insufficient to change the oxidation mechanism. A fluence of 2 x $10^{16}Y^+/cm^2$ was required to affect the oxidation behavior.

Extensive AEM work has also been done on Cr_2O_3 scales. One of the microstructural features unique to ion implantation in this case is the formation of coherent $YCrO_3$ perovskite-type particles within the Cr_2O_3 scale [Przybylski, et al., 1986]. Y was also found to segregate to the Cr_2O_3 grain boundaries. The formation of Y-rich precipitates was believed to be due to the high concentration of Y in the near surface region. Similar Y-rich grains were found by Bennett, et al. [1985] in Y implanted ($10^{17}/cm^2$) stainless steel after oxidation for 6500hr at 825°C. In this case, the particles were identified as Y_2O_3 by microdiffraction.

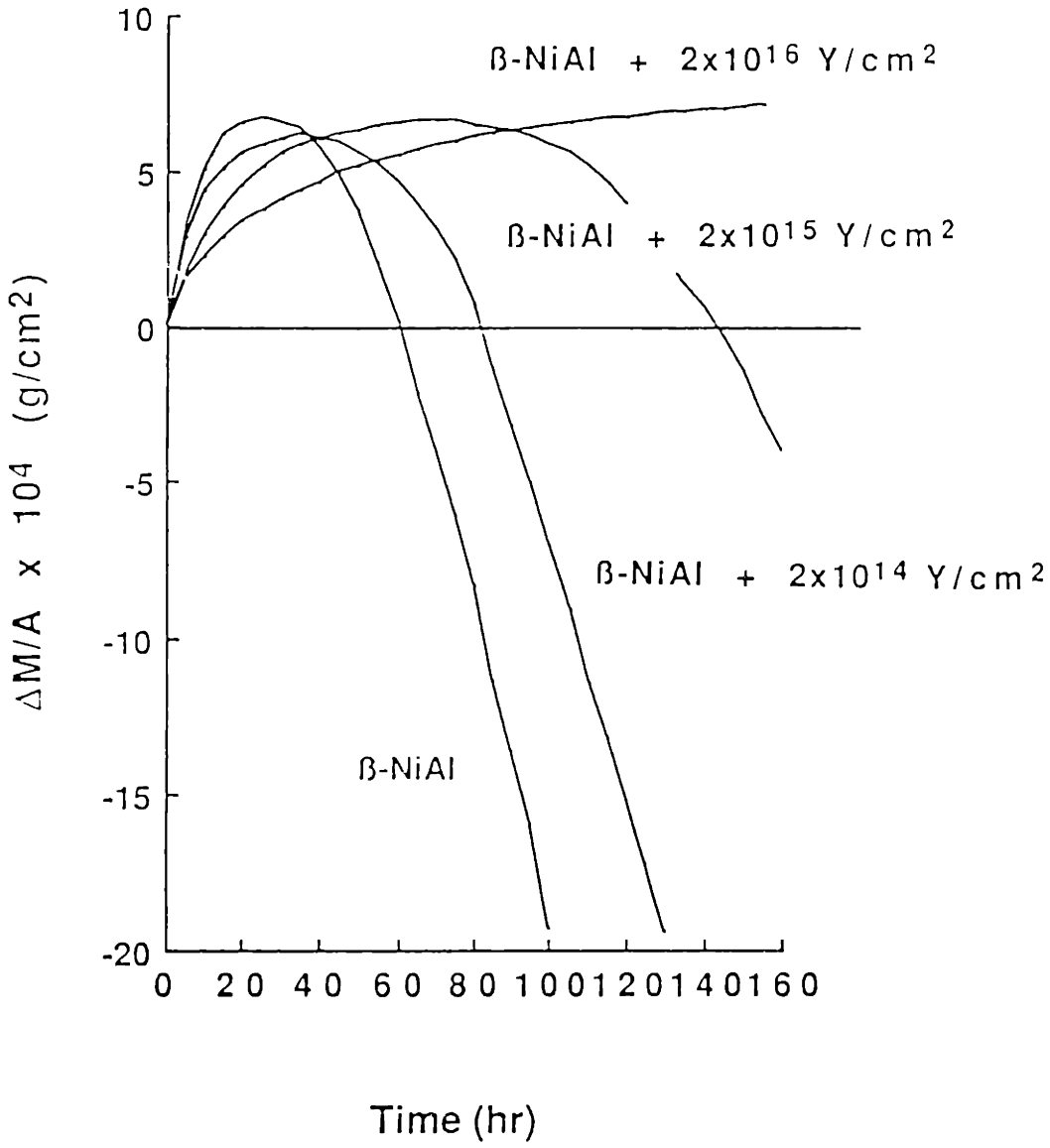

Figure 2.5 Weight change versus time for various implants of Y in ß-NiAl cyclicly oxidized (1hr cycles) in air at 1200°C [Mrowec, et al., 1987].

The limited nature of a surface implant has also been occasionally explored. Bennett, et al. [1980] found that a Y implant (3 x $10^{15}/cm^2$ at 300kV) in FeCrAl was only effective up to 500hr at 1100°C. Al implants up to $10^{17}/cm^2$ had no effect at longer times. However an alloy addition of 0.86% Y produced the REE for at least 3271hr. A similar limitation was also found by Antill, et al. [1976] with Y and Ce implants into stainless steels. In Y implanted (2 x $10^{16}/cm^2$) Cr, Cotell, et al. [1990a], also found that towards the end of a 20hr exposure at 1025°C there were signs the REE were diminishing.

There is no experimental evidence to suggest that the implantation process itself effects the oxidation behavior. For instance, Pivin et al. [1980] implanted both Y and Ar into Ni-Cr, Fe-Ni-Cr, and Fe-Ni-Cr-Al alloys. In each of the alloys, implanted Ar had no effect on the oxidation properties. Thus it is a chemical effect of the implanted species and not a result of the radiation damage caused by ion implantation.

2.3.3 Oxide Dispersions

A RE oxide dispersion in an alloy, generally provides the best method for introducing the RE uniformly throughout the material. It has the additional benefit for high-temperature structural materials that the oxide dispersion improves the creep resistance of the material by pinning dislocations (oxide dispersion strengthening, ODS). The drawback of the dispersion is in the fabrication. In order

to achieve a uniform dispersion, powder metallurgy techniques such as mechanical alloying are necessary [Benjamin, 1970].

There has been general agreement in the literature about the beneficial effects of a RE oxide dispersion. The most significant issue has been the case of a non-RE oxide dispersion (especially Al_2O_3) which reportedly improves the oxide adherence on both Al_2O_3 [Tien and Pettit 1972] and Cr_2O_3 [Wright, et al., 1975]. This result is both interesting and frustrating. If it is true, it requires a rethinking of some aspects of the REE. However, the observation is always missing characterization beyond simple isothermal kinetics and cyclic weight changes. No further investigation has been published regarding the other REEs; such as changes in oxide microstructure and growth mechanisms.

For instance, the Wright paper concludes that the Al_2O_3 dispersion reduces the oxidation rate. However, it is never clarified whether this is a reduction in the transient growth of a Ni-rich layer or in the steady-state growth of Cr_2O_3. Yurek, et al., [1987] found that a Y_2O_3 dispersion in Ni-20Cr decreased the thickness of the outer Ni-rich layer. The result also begs the question why all commercial ODS alloys contain a RE oxide dispersion. A dispersion of only Al_2O_3 must be cheaper than one including Y_2O_3 (Inco MA956) or ZrO_2 (Kanthal APM).

Another important issue regarding the role of an oxide dispersion is its effect on selective oxidation and the transient period. A rather intuitive argument by Stringer [1972] is that the oxide dispersion promotes the heterogeneous nucleation of a continuous oxide film. This allows a protective scale to form with

less Cr or Al in the alloy and undercuts less-noble oxides faster. Seltzer and Wilcox [1972] also subscribed to this idea, showing that the diffusivity of Cr in the alloy was dependent on the alloy grain size. However, the selective oxidation to form Cr_2O_3 was independent of the alloy grain size and modified by an oxide dispersion. Further work by Whittle, et al. [1977] showed that 1wt% additions of Zr, Hf and Ti did not affect the oxidation behavior of Co-10Cr and Co-15Cr. These alloys normally do not form continuous protective Cr_2O_3 layers. However, when these same alloy additions were internally oxidized (at low P_{O_2} so no Cr_2O_3 is formed), a continuous adherent scale forms under isothermal conditions. Yet all of these studies relied mainly on kinetic and some XRD work for their evidence.

Microstructural characterization does not support these macroscopic (kinetic) observations. Braski, et al. [1986], studying Ni-20Cr with and without Y_2O_3, revealed that in the early stages with a low (10^{-19} - 10^{-21}atm) oxygen potential there was no effect of the dispersion on nucleation. The most significant effect was on the oxide microstructure, not on nucleation. One possible difference in this case is that with a low P_{O_2}, where NiO is not formed, an effect of the oxide dispersion on the transient period would not be expected.

In summary, there appears little question that RE-oxide dispersions exhibit the REE. However, it is also possible that an oxide dispersion also adds some additional effects which modify selective oxidation, transient oxidation and oxide adherence. Insufficient microstructural characterization prevents conclusive

arguments to be made about these effects. There is also much more experimental evidence regarding oxide dispersions in chromia-formers than alumina-formers.

2.4 Conflicting Al_2O_3 Oxidation Mechanism Experiments

Virtually no argument arises in the case of chromia-formers about the oxidation mechanism. Both inert markers and ^{18}O tracers show that undoped Cr_2O_3 grows predominantly by the outward diffusion of Cr. When a RE addition is made, the rate-limiting step is changed to the inward diffusion of oxygen. For the case of Y-implanted Cr, this was demonstrated using both inert markers and an ^{18}O tracer by Cotell [1988].

Al_2O_3 appears to be a more complicated case with little agreement in the literature.

2.4.1 Inert Marker Experiments

The premise on which inert marker experiments are based is quite simple. If anion diffusion is the primary growth mechanism, then the markers should remain at the original metal surface and oxide grow beneath them. In the case of growth by cation diffusion, the oxide should grow over the markers, and they should be found beneath the oxide at the metal-oxide interface. In the case of mixed mode growth, the markers should be found within the scale.

Pettit's initial work on Ni-Al alloys concluded that Al_2O_3 scales grew by the inward diffusion of oxygen. However, because of

the thin non-adherent scale on these alloys, no marker or other experiments were conducted to confirm this hypothesis. Marker experiments on more adherent Al_2O_3 scales, such as those formed on Fe-25Cr-4Al-Y alloys at temperatures between 1100° and 1300°C, have been performed by Wukusick and Collins [1964]. They concluded that Al_2O_3 scales grow by inward diffusion of oxygen. This result has been confirmed a number of times for alloys forming Al_2O_3 scales [Hindam and Smeltzer, 1980a; Huang, et al., 1985]. Hindam and Smeltzer [1980b] noted in a second paper that ridges on both metal-oxide and oxide-gas interfaces on Ni-32.2Al indicated growth by counter-current diffusion of Al and O despite markers being detected on the scale surface.

Young and de Wit [1984] cast further doubt on the validity of marker-type experiments. Using NRA, Young and De Wit [1985] found that Al_2O_3 on NiAl (50at%Al) grew primarily by Al transport outward at 900°C in 1.0atm O_2. Some ^{18}O was found to penetrate up to the alloy-oxide interface, but this was proposed to occur by limited short-circuit oxygen diffusion. Surprisingly, Pt and Pd markers in the same experiment were found at the oxide-gas interface, indicating growth by oxygen diffusion inward. At 1150°C, similar results were found. Oxygen diffusion inward had gained in magnitude compared to 900°C, but NRA showed Al diffusion outward was still the dominant mechanism. Marker experiments again showed the opposite result.

Young, Bishop and de Wit [1986] implanted Pt into pregrown Al_2O_3 on NiAl. After further oxidation at 900°C, the Pt was detected by RBS near the center of the scale, indicating that new

oxide had grown over it, which coincides with the ^{18}O tracer results. However, the exact position of the Pt appeared to move slightly during oxidation, leading to the conclusion that this type of inert marker was not completely reliable either.

After the findings of Young and de Wit, Mrowec, et al. [1987] also compared marker and tracer experiments. Au markers and ^{18}O tracer experiments for undoped NiAl both indicated a mixed growth mode after 24hr at 1075°C. This is noteworthy because no other study has found inert markers within an Al_2O_3 scale However, for Y-implanted NiAl, the two techniques did not agree. In this case, ^{18}O/SIMS showed Al diffusion was predominant in scales, but Au markers found at the gas surface were deemed inconclusive. Thus, the emphasis in the literature has switched to almost exclusively ^{18}O tracer experiments for determining the growth mechanism of Al_2O_3.

2.4.2 ^{18}O Tracer Experiments

The results of numerous ^{18}O tracer experiments have been reviewed by Jedlinski and Borchardt recently [1991]. One useful diagram from this paper which draws from the theoretical work of Basu and Halloran [1986] is shown in Figure 2.6. After comparing the results of numerous studies, Jedlinski and Borchardt concluded that no simple model can describe the formation of Al_2O_3 and that the effect of Y "was found to be quite complex". They also emphasized the potential role of pores and cracks for explaining the variety of results.

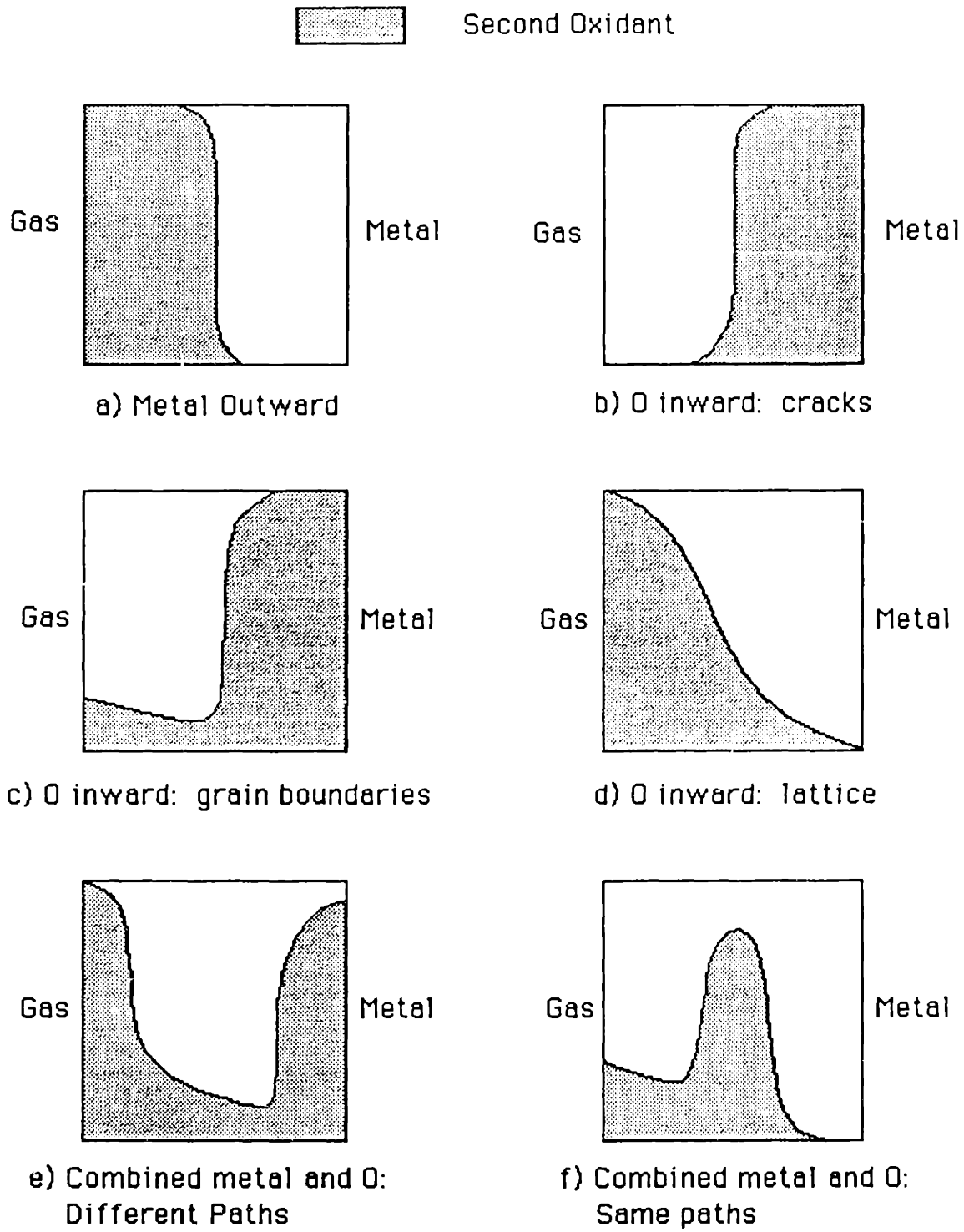

Figure 2.6 Theoretical sputter depth profiles for ^{18}O tracer diffusion experiments given different growth mechanisms. The shaded area refers to the location of the second oxidant (either ^{16}O or ^{18}O).

The one point that does not get emphasized enough in the review is the role of the Al_2O_3 phase (either θ or α) on the growth mechanism. Also, the various effects of RE additions is not adequately dissected. Instead they are lumped together, making the role of the RE difficult to interpret. A few studies appear to clarify the "complex" role of RE additions.

Young and de Wit [1986] found using an ^{18}O tracer that the alloying of NiAl with Y caused a change in oxidation mechanism. As part of the same research group, van Manen, et al. [1987] determined that, while small additions of yttrium (0.07wt%) caused a decrease in oxygen transport at 1000°C, larger amounts (0.5wt%) caused the opposite effect. They concluded that the effect of the larger yttrium concentration is to retard the transformation of Al_2O_3 from the initially-formed, metastable θ-Al_2O_3 phase to the stable α-Al_2O_3 phase. They speculated that the α phase favors oxygen transport, while the θ phase favors aluminum transport, thereby explaining the difference between the high- and low-yttrium cases. However, in most cases, they failed to isolate the single phase and concluded that the RE addition affects the phase transformation, not the growth mechanism.

More conclusive experiments have been conducted on NiCrAl and FeCrAl, both with and without an RE addition. In these cases, unlike NiAl, primarily α-Al_2O_3 is found at the temperatures investigated. Reddy et al. [1982] found by ^{18}O tracer experiments that Al_2O_3 scales on NiCrAl+Zr grow primarily by oxygen diffusion inward. This was proposed to be due to the effect of the addition of Zr. NiCrAl without Zr grew by a combination of Al and O transport.

The same result was also found for undoped FeCrAl and Y_2O_3 dispersed FeCrAl (MA956) alloys. Quadakkers, et al. [1989] concluded that the primary role of the RE addition was to suppress cation diffusion in both Cr_2O_3 and Al_2O_3.

Thus while there appears to be confusion about the effect of an RE addition on NiAl, there does not appear to be any confusion for MCrAl alloys. NiAl appears to be a more complicated situation. However, as outlined by van Manen, et al. [1987], the complication that many studies do not consider is the potential role of the Al_2O_3 phase transformation that occurs near 1000°C.

2.5 Scale Adhesion and the Role of Sulfur

One of the most important issues from an engineering standpoint is oxide adherence. Even if the oxide grows slowly, if it spalls readily upon cooling (or at temperature), then the lifetime of the substrate is limited. Eventually the Al (or Cr, Si) content will be depleted to the point where less noble oxides will be formed. If the oxide remains adherent, less depletion occurs and the parabolic nature of the reaction will slow the degradation at long times.

Over the past ten years, a number of oxide adherence studies were undertaken, with many concentrating on alumina-formers. The other RE effects were ignored in order to concentrate on explaining the reasons for oxide spallation. Indigenous sulfur in the alloy was found to be a major factor. The general conclusion was that without a RE, sulfur-free alloys had better adherence. With a RE, sulfur was found to be neutralized in some manner.

2.5.1 The Detrimental Role of Sulfur

The first work to discuss the detrimental role of sulfur on oxide adherence was Ikeda, et al. [1983], working on stainless steels. By heating the metal in vacuum, sulfur was observed to segregate to the surface by AES. This study concluded that La additions improved the adherence by gettering sulfur. Also, BN and TiC surface layers lowered the S surface segregation in vacuum, and subsequently improved the oxidation adherence.

Funkenbush, et al. [1985] and Smialek [1987a], working independently, demonstrated more conclusively the role of sulfur. Smeggil, et al. [1986] demonstrated that while adding Y to NiCrAl improved oxide adherence, adding Y_2S_3 decreased adherence (ten times worse than undoped NiCrAl), and adding Y_2S_3 and Y produced good adherence again. Y_2S_3 additions were proposed to form YS, thus liberating S which caused scale exfoliation. When additional Y was added with Y_2S_3, all of the S could then be tied up as YS. Smeggil et al. [1985] also ion implanted S (to a peak concentration of 7wt%) into NiCrAlY and found that the oxide adherence was reduced in this case. It was also predicted that if sulfur were eliminated from the alloy, good scale adherence could be attained without a RE addition.

In a simpler approach, Smialek [1987a] removed the metal surface of NiCrAl (by polishing) after each oxidation cycle. After several cycles of this, oxide adherence was improved. This treatment was observed to lower the bulk alloy S concentration. S segregating to the metal surface during oxidation was presumably

removed during polishing, leaving a low S content alloy with improved oxide adherence.

Lees [1987] produced a similar improvement by hydrogen annealing pure Cr to reduce the S content in the alloy. Smeggil and Peterson [1988] used AES and XPS to look at S surface segregation during vacuum heating (600°C) of NiCrAl. Using XPS, S was found to be present as both S^{-2} and S^{x}. The AES work confirmed the findings of Ikeda, et al. [1983].

A lone dissenting vote has been cast by Briant and Luthra [1985]. While they did detect S segregation using AES, a NiCrAl alloy prepared with a very low S content did not exhibit improved oxide adhesion in cyclic testing.

One frustrating issue again is that, for the most part, adherence improvements were mainly characterized by cyclic weight change data. Smialek [1989] looked at the scale morphology and concluded that the scale on a S-free, undoped NiCrAl had a different morphology from that formed on NiCrAlY. The oxide grain size was larger in the undoped case. Also, no oxide pegs or voids were observed in the undoped case. No other characterization has been reported concerning the structure or growth mechanism of adherent scales on sulfur-free alloys.

2.5.2 Reactive Element-Sulfur Interactions

Both studies by Smialek [1987b] and Smeggil, et al. [1986] stated that the control of S was a "first order" REE. Smialek even determined a relationship for the amount of Zr required to

counteract a given quantity of S. However, in many of these studies there has been little mention of exactly how an addition (RE or other) interacts with indigenous S.

Three different theories have been proposed for the interaction of a reactive element and sulfur. The first is that the RE such as Y reacts with the indigenous S to form a stable sulfide, thus preventing the sulfur from degrading oxide adhesion [Smeggil, 1986]. The second premise is that yttrium segregated to the alloy-oxide interface lowers the driving force for sulfur segregation to this interface, thus eliminating its detrimental role [Pint, et al., 1991]. The third is that RE oxide dispersions or internally oxidized RE particles provide a free surface for S segregation, diverting it from the metal-oxide interface [Lees, 1987]. This last idea is discussed in the next section.

All of these ideas remain largely unproven. Smeggil, et al. [1986] was unable to find any indication of the reduction of Y_2S_3 to YS. Sigler [1989] studied FeCrAl alloys with a wide range of alloy additions, including Y, Ce, Ti, Zr, Hf, Nb, V, Ta, and Mo. He concluded that additions which formed more stable sulfides than Al_2S_3 were beneficial. This excluded Nb, V, Ta and Mo. However, for the elements that improved oxide adherence, no effort was made to detect their sulfides in the alloy.

A RE effect tied to the segregation driving force is also largely circumstantial. When good adherence is found, the RE and not S is found at the metal-oxide interface. When adherence is poor (with no RE addition), S is found to segregate.

One piece of evidence regarding the role of Y was provided by Briant and Luthra [1988]. Samples of pure metal (Fe, Ni, Cr, Al, and Y) were doped with 100ppm S and heated in vacuum. Heavy surface segregation of S was detected on each of the blocks except Y, which remained clean. While this observation does not preclude the formation of YS, it does question why none of the other metals were able to form internal stable sulfides under the same conditions as Y. This experiment points to a potential link between the RE and interfaces in general.

2.5.3 Sulfur-Interface Interactions

S is considered to be a surface-active element, segregating to boundaries in both metals [e.g., Chaung, et al., 1979; Briant and Taub, 1988] and oxides [Kim, et al., 1986; Fox, et al., 1991]. This idea has been used to explain the effect of oxide dispersions. Oxide particles in the alloy provide interfaces for indigenous S segregation. This diversion lowers the amount of segregation at the metal-oxide interface, thus improving oxide adherence. The idea has been used to explain the reported improvement of oxide adherence with the addition of any stable oxide (RE or non-RE such as Al_2O_3 or TiO_2). Thus, the chemical composition of the dispersion is unimportant, only the alloy-particle interface which it provides.

Two studies at M.I.T. looked for experimental evidence to test this idea. Katz, et al. [1987] found that in Y_2O_3-dispersed FeCrAl (Inco MA956) with 110ppm S, there was no S detected (FEG-STEM/EDXA, <2nm probe) before or after oxidation at alloy-particle

interfaces. A theoretical calculation showed that if all of the S (110ppm) in the alloy segregated, there would be an entire monolayer of S surrounding each particle. This level of segregation would be easily detected by STEM/EDXA. Also no YS_x particles were detected although it is possible that these were preferentially removed during TEM sample preparation.

A second study by Pint, et al. [1989] looked at an Y_2O_3-dispersed Ni-20%Cr alloy (Inco MA754) oxidized at 900°C in H_2-H_2O-H_2S environments. This alloy contained 10ppm S. When H_2S was added to the gas mixture, S was detected at particle-metal interfaces near the scale. However, S segregation was not found when H_2S was absent from the gas mixture. Thus, while several studies have detected indigenous S segregation to oxide and alloy grain boundaries, free surfaces and the metal-oxide interface, it is still only a hypothesis that it segregates to other interfaces.

2.5.4 Adhesion Testing

While cyclic testing remains the most widely used technique for gauging oxide adhesion, there are other techniques as well. Acoustic emissions have been monitored in order to detect signs of cracking, both isothermally and during cooldown [Huang, et al., 1985]. Using micro-indentation, Tortorelli and Kaiser [1991] have attempted to quantify the mechanical properties of scales, including their adhesion. Sigler [1989] deformed the oxidation coupons after oxidation with a punch to analyze oxide adherence. These techniques

remain somewhat controversial and difficult to interpret. In general, cylic testing is favored because of its simplicity.

2.6 Al_2O_3 Microstructural Features

There are certain morphologies and microstructures which are typical of a particular oxide, such as porous or dense scales, columnar or equiaxed grains, even oxide blades and whiskers. The review here concentrates on structures typical of Al_2O_3 scales, especially those above 1000°C. There is also a section on substrate morphologies beneath growing Al_2O_3 scales. One point of confusion is the convoluted nature of some Al_2O_3 surface morphologies. Surface roughness or convolutions can be caused by variations in the scale thickness, or by a uniform thickness scale that is not flat. Furthermore the convoluted scale may be adjacent to a flat substrate interface or an equally convoluted substrate. Each of these cases is defined in this section to clarify these descriptions as used in this study.

2.6.1 Convoluted Al_2O_3 -- "Buckling"

One of the common structures for undoped α-Al_2O_3 scales formed on FeCrAl alloys is the case where a scale of uniform thickness is convoluted but the underlying alloy remains relatively flat. For the purposes of this study, scale exhibiting this type of convolution will be referred to as "buckled". This type of structure is shown schematically in Figure 2.7a. The scale in this case has

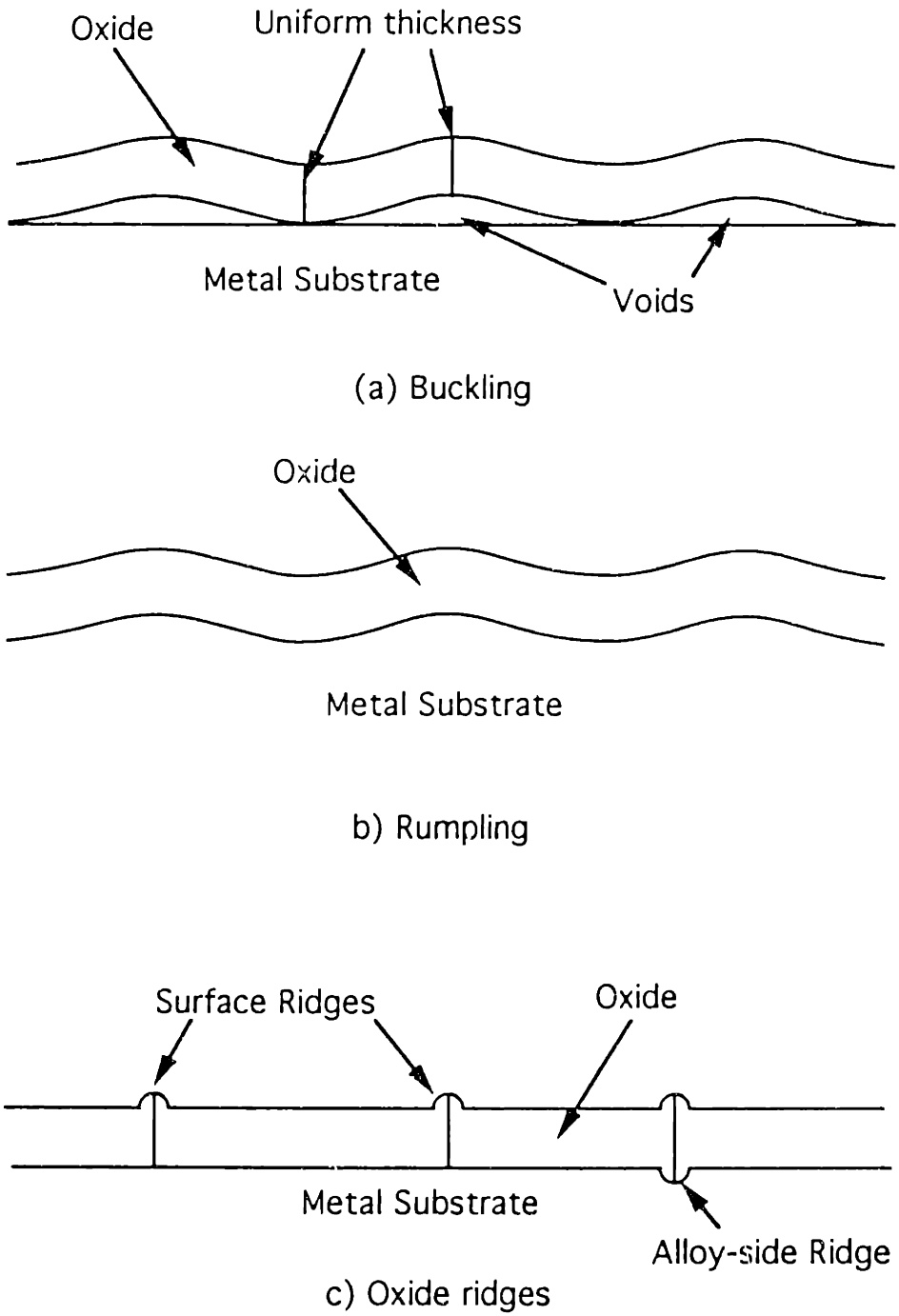

Figure 2.7 Schematic of various Al_2O_3 oxide morphologies.

buckled, leaving voids between the alloy and the oxide. In view of the reduced contact between the metal and oxide in this case, poor adhesion is the inevitable consequence.

Smialek, et al. [1988] noted the buckling of Al_2O_3 scales grown on FeAl at 1100°C. As mentioned previously, this morphology was also noted by Golightly, et al. [1976] in Al_2O_3 formed at 1200°C on FeCrAl without a RE addition. This structure was attributed to lateral growth of the scale due to mixed mode oxidation, i.e. both Al and O diffusing simultaneously. Poor oxide adherence was also observed. In the case of a Y alloy addition, no buckling was observed [Golightly, et al., 1976]. The doped scale was uniform in thickness and relatively flat, as was the alloy-oxide interface. The only exceptions noted when Y was present were oxide protrusions (pegs) into the alloy in the vicinity of FeY_x particles in the alloy. The elimination of scale buckling was attributed to Y blocking the diffusion of Al through the lattice. Thus the doped scale was proposed to grow only by O diffusion and was not buckled.

No other studies have produced a different theory for these convolutions [e.g., Mrowec, et al., 1987]. One speculation is that these scales also buckle because of decohesion promoted by the segregation of S to the metal-oxide interface. Unfortunately no studies have been reported on S-free FeCrAl which could be examined for scale buckling

Tien and Pettit [1972] noted that the buckling was affected by polishing scratches after oxidation of FeCrAl at 1200°C. In this study, the samples were polished to 600grit and buckle ridges tended to follow the larger surface scratches. This study also noted

that, while buckling was observed, there were also areas where the substrate reflected the convolution of the scale. For this study, these two cases are defined separately.

2.6.2 Convoluted Al_2O_3 -- "Rumpling"

A second type of convolution is characterized by the alloy conforming to the oxide convolutions, making for a more complete oxide-metal interface. This will be referred to as "rumpling" to distinguish it from buckling. This structure is shown schematically in Figure 2.7b. From the surface, rumpling and buckling look the same. However, in the case of rumpling, fewer voids are formed and the scale is in better contact with the substrate. Thus, scale adhesion is not necessarily reduced when rumpling is observed.

Bennett, et al. [1991] observed this behavior at 1200°C and 1400°C with undoped FeCrAl. The extent to which convolutions of the alloy followed those of the oxide increased with temperature over this range. This study included higher temperatures than the study by Golightly, et al. [1976] at 1200°C. Thus the rumpling is likely a product of higher oxidation temperatures. With a melting temperature of ≈1470°C, the FeCrAl substrate may be mechanically deformed more easily as the melting point is approached. Thus the stiffer Al_2O_3 scale may be able to deform the underlying substrate as the temperature is increased.

Neither sort of rumpling or buckling is as clearly observed on NiAl at lower temperatures [Doychak, et al., 1989b].

2.6.3 Oxide Ridge Structure

The work on NiAl oxidation also identified another important microstructural feature of alumina scales: the ridge structure of α-Al_2O_3. In this case, oxide ridges on the gas surface of the scale are formed which correspond to oxide grain boundaries, Figure 2.7c. These surface features are not to be confused with rumpling or buckling of the scale for which the entire scale thickness is affected. For the ridges, there is a localized increase in scale thickness. Ridges are observed at the gas interface of the oxide and, less frequently, at the alloy interface [Hindam and Smeltzer, 1980b].

Doychak et al. [1988] proposed that the ridge morphology found after long times at 1000°C was a remnant of the phase transformation of θ-Al_2O_3 to α. The ridge spacing was also inversely related to the oxidation temperature. However, at higher temperatures (>1200°C), metastable Al_2O_3 phases are not observed to form. Therefore, it is difficult to relate the finer ridge structure observed at high temperatures to the coarser ridges found at lower temperatures.

2.6.4 Oxide Blades and Whiskers

Another class of surface morphologies typical of alumina-formers is surface blades and whiskers. Numerous studies have noted that Al_2O_3 scales grown below 1000°C have a blade-type structure. A number of the earlier studies did not characterize the phase of the Al_2O_3 scale [e.g. Young, et al., 1986; Pint, et al., 1989].

However, more recent studies have conclusively identified this morphology using GAXRD [Rybicki and Smialek, 1989] and SAD [Doychak, et al., 1989a] as belonging to the θ-Al_2O_3 phase.

Whiskers have also been observed to form on the surface of undoped α-Al_2O_3 scales from 1000°C to 1200°C [e.g. Przybylski and Mrowec, 1984; Mrowec, et al., 1987; Jedlinski and Mrowec, 1987]. Voss, et al. [1982] observed elongated voids near the center of α-Fe_2O_3 whiskers and attributed their growth to rapid outward surface diffusion along these defects.

In any case, it is difficult to imagine an oxide protrusion being formed by an inward growth mechanism. This would mean that new oxide would be formed at the bottom of the structure rather than at the tip. Thus, both whiskers and blades are indicators of an outward growth mechanism.

2.6.5 Epitaxial Growth Relations

Doychak, et al. [1989a] studied the oxidation of electro-polished, Zr-doped NiAl at 800°C and 1100°C. Single crystals of various orientations were oxidized and then thinned for parallel TEM sections in order to look for epitaxial growth relations. At 800°C, the scale was identified using selected area diffraction (SAD) as initially $NiAl_2O_4$ and δ-Al_2O_3 which were found to grow epitaxially. In the later stages of oxidation (up to 100hr), the scale was identified as θ-Al_2O_3. At 1100°C, the scale up to 1hr was composed of mainly θ-Al_2O_3 which transformed to α-Al_2O_3 at longer times. The transient scale in each case was found to grow epitaxially.

The motivation for this work was to look for a potential slow growth direction of the oxide and possibly formation of a monocrystalline scale, as was observed for Cr_2O_3 on Cr [LaBranche, 1985]. In the latter case, the overall scale growth rate was reduced because grain boundaries were not present in the scale to provide fast diffusion pathways. In the case of ß-NiAl, certain orientations were found to oxidize at a slower rate than others but not significantly slower, and a monocrystalline scale was not formed [Doychak, et al. 1989a]. The rate in this case was determined by the scale thickness. This change in rate with orientation was also noted in polycrystalline samples where the scale morphology was different, depending on the orientation of the substrate grains [Doychak, et al. 1989a].

Some additional work by Jedlinski and Mrowec [1987] on single crystal ß-NiAl indicated that the scale growth rate on unimplanted single-crystal NiAl was slower than on Y-implanted polycrystalline NiAl at 1000°C and that Y-implanted single crystal NiAl exhibited the slowest scale growth of the three substrates over several hundred hours. No mention of the oxide phase or orientation was made in the study, however.

In general, little work has been done with single crystal, alumina-forming substrates or on preferred growth directions for Al_2O_3.

2.6.6 Substrate Morphologies (Beneath Al_2O_3)

As a final point, the substrate at the alloy-oxide interface also has been observed to have a particular morphology. There are two major morphologies observed after oxidation: oxide grain imprints into the alloy and regions with an extremely smooth surface [Tien and Pettit, 1972; Giggins, et al., 1974; Golightly, et al., 1976; Smialek, 1978; Hindam and Smeltzer, 1980b].

Oxide grain imprints in the alloy are attributed to at least a partial inward growth mechanism. This morphology is also an indicator of good contact between the alloy and the oxide at temperature and is seen in both doped and undoped substrates.

Typically, in the case of undoped substrates, certain regions are also observed to be unusually smooth. It has been proposed that these areas lose contact with the scale at temperature. Once a gap develops, grain imprints are lost and the scale continues to grow by the evaporation of Al which is sufficient to sustain the scale growth rate [Hindam and Smeltzer, 1980b]. The evaporation leaves a smooth and in some cases terraced substrate morphology [Tien and Pettit, 1972].

These smooth-surfaced areas have also been observed to be faceted [Smialek, 1978]. For a polycrystalline Ni-42at%Al substrate, the evaporation left faceted voids which appeared to vary in orientation with that of the substrate. Howes [1969] also noted faceted voids in FeCr. Whatever the morphology of these voids, the loss of contact between the metal and oxide is an indicator of the poor adherence of undoped Al_2O_3.

2.7 Oxide Grain Boundary Segregation

There are a large number of experimental observations regarding the segregation of foreign ions to oxide grain boundaries, detected by a variety of techniques. Rather than reviewing this entire literature, a few pertinent features are covered in this section.

2.7.1 Experimental Observations

A number of analytical techniques has been used to detect the segregation of foreign ions to oxide grain boundaries. These include autoradiography, spark-source mass spectroscopy, AES, XPS, EDXA in SEM and STEM, extended x-ray absorption fine structure (EXAFS) and atom probe measurements [Cook and Schrott, 1988; Garratt-Reed, 1987].

The earliest detection of Y segregation to 0.05at%Y_2O_3-Al_2O_3 grain boundaries was in a study by Nanni, et al. [1976] using AES. In this case, the Y addition had been observed to reduce the Al_2O_3 sintering rate, and the extent of segregation was estimated at more than 0.2 monolayer. Bender, et al. [1980] observed Y segregation on 0.05wt%Y_2O_3-Al_2O_3 grain boundaries and Cr on NiO boundaries using STEM/EDXA with a probe size of <30nm. This study also showed that more primitive techniques, such as microhardness tests, were not good indicators of segregation in oxides. EXAFS was employed by Loudjani, et al. [1985] to study the chemical state of the Y segregation in α-Al_2O_3 doped with 1at%Y_2O_3. However, most of the

doped Y was found to have precipitated as $Y_3Al_5O_{12}$ (YAG), and segregation of ions was not detected.

Segregation of foreign ions in oxide scales was first detected by Ramanarayanan, et al. [1984]. Using XTEM of scales grown on a commercial Y_2O_3-dispersed FeCrAl alloy (MA956), Y was found to segregate to the oxide grain boundaries. No mention was made of segregation to the metal-oxide interface. Y and Ti boundary segregation was detected in the scale on MA956 after oxidation at 1000°C [Przybylski, et al., 1987]. In a related study at MIT, metal-oxide segregation was detected by Katz, et al. [1987] after oxidation of MA956 for 100hr at 1000°C.

Various studies at MIT using FEG-STEM, have also found the segregation of Y, Ti and S to Cr_2O_3 and Al_2O_3 scale grain boundaries [Kim, et al., 1986; Yurek, et al., 1987a & 1987b; Cotell, 1988]. Other research groups have also identified ion segregation in scales, such as Y segregation to $NiCr_2O_4$ grain boundaries [Bennett, et al., 1988] and Ce to Cr_2O_3 grain boundaries [Bennett, et al., 1992].

2.7.2 Reasons for Segregation

A number of arguments can be made regarding the possible reasons for segregation. The most important point is that there are a variety of driving forces for segregation. Two of the most often-cited reasons for segregation of foreign ions to oxide grain boundaries are charge and ion size.

A study of TiO_2 co-doped with Nb and Al demonstrated that segregation was dependent on the concentration of the dopants and

the annealing temperature [Ikeda, et al., 1991]. With Ti, Al and Nb being nearly equal in ion size, this is a case where the charge of the segregant and the space charge at the boundary are the most important factors. Mitamura, et al. [1979] also attributed the segregation of Fe to MgO boundaries as due to a space charge effect. Fe and Mg are approximately the same size. Samples quenched from a higher temperature had less segregation which was consistent with space charge predictions.

Using AEM, Bender, et al. [1980] studied three cases where there was no detectable segregation; Ni-doped MgO, Ni-doped Al_2O_3 and Al-doped NiO. MgO and NiO are isovalent and of the same size; thus, no segregation is expected. However, Al and Ni are not isovalent but are close in size. This may indicate that either ionic size is more important in this system or that the level of segregation is too low to be detectable by AEM.

There are also instances of isovalent ion segregation where, due to lack of a charge effect, the ion size is concluded to be the cause of segregation. The driving force for this type of segregation is the relief of lattice strain. It is also an explanation for aliovalent ion segregation when the ion is significantly larger than the matrix ion. One example is the segregation of Ca to Al_2O_3 boundaries [Cook and Schrott, 1988; Chiang, et al., 1981]. Li and Kingery [1984] studied the grain boundary segregation of a number of different ions in Al_2O_3. They concluded that the solute misfit strain energy was responsible for the segregation of both Y and Zr.

Chiang, et al. [1981] studied the concurrent segregation of Sc, Ca, and Si to MgO boundaries using AES. The larger Ca and Si ions

were concluded to segregate by a strain relief mechanism; however, the similarly-sized Sc did not fit this case and also had a more widely spread distribution on the boundary. It was therefore concluded that Sc segregated by a space charge effect.

Thus, there appear to be cases where space charge is more important and others where lattice misfit determines whether or not segregation will occur. In the previously cited cases for Y segregation in Al_2O_3, a space charge theory would not seem to apply to the isovalent Y. However, El-Aiat and Kroger [1982] studied the conductivity of Y-doped Al_2O_3 and proposed that Y acted like a donor because of its size misfit in the lattice. Cawley and Halloran [1986] strongly disagreed with this interpretation and demonstrated that the solubility of Y in Al_2O_3 was too low to account for the results of El-Aiat and Kroger. Cawley and Halloran concluded that tramp impurities were more likely to dope Al_2O_3. Thus, for the larger Y and Zr ions, size misfit seems to be a more appropriate argument.

2.8 Pertinent Data

A few additional facts are included in this section regarding the reported thermodynamic, crystallographic and diffusion data for Al_2O_3 and other compounds encountered in this study.

2.8.1 Thermodynamic Data

A few remarks about equilibrium phases treated in this study are in order. The Ni-Al phase diagram has already been presented,

Figure 2.3. Also, the Al-O phase diagram is not particularly useful, since α-Al_2O_3 is the only stable phase. The melting temperature of α-Al_2O_3 is approximately 2050°C. The melting point of Y_2O_3 is 2440°C [Warshaw and Roy, 1959], while that of ZrO_2 is 2995±20°C [Noguchi and Kozuka, 1966].

Investigations of the Y_2O_3-Al_2O_3 system have identified two stable compounds, at molar ratios of 3:5 and 2:1, and a metastable 1:1 compound, $YAlO_3$ [Warshaw and Roy, 1959]. XRD detected almost no solubility in the system for any of the phases. The two stable phases are the garnet-structure, $Y_3Al_5O_{12}$ (YAG), and a distorted cubic structure $Y_4Al_2O_9$. While the $YAlO_3$ phase is often observed, after an extended anneal at 1400°C this compound was found to transform into the two other phases.

2.8.2 Crystallographic Data

α-Al_2O_3 belongs to the R3c space group with a rhombohedrally-centered hexagonal lattice with a = 4.763Å and c = 13.003Å. Each cation is coordinated to 6 oxygens in a distorted octahedron, 2/3 of cation sites are full, and each oxygen has 4 cation nearest neighbors.

γ, δ, and θ-Al_2O_3 are variations of a spinel-type cubic anion sublattice with γ considered to be the most spinel-like, δ a tetragonal structure and θ a more distorted, monoclinic structure. θ has the space group C2/m (similar to β-Ga_2O_3) with lattice dimensions of a=11.813Å, b=2.906, c=5.625 and β=104.6°.

NiAl has the simple cubic CsCl structure with a stoichiometric lattice constant of 2.89Å.

2.8.3 Diffusion Data

Several studies have been conducted to determine diffusion coefficients in Al_2O_3. The most widely studied and disputed has been the lattice diffusion of oxygen in single-crystal α-Al_2O_3. A summary of these data is shown in Figure 2.8 which is from Cawley, et al. [1986]. Reddy and Cooper [1982] analyzed the samples of Reed and Wuensch [1980] using a proton activation technique, (NRA). There was good agreement between their analysis and Reed's SIMS data; however, the samples prepared by Reddy had a higher diffusivity than those of Reed and Wuensch. Reddy's samples were prepared by a gaseous exchange of ^{18}O, while Reed's were prepared by fully oxidizing a vapor-deposited Al film in ^{18}O. Reddy concluded that the diffusivity of oxygen was by a vacancy mechanism and observed a reduction in D_O with the addition of Ti. Reed concluded that the diffusion was extrinsically controlled by the presence of Si impurities.

Cawley, et al. [1986] found the diffusion coefficient to be independent of impurities and partial pressure of oxygen in the range 1 - 10^{-15}atm. They found two models to be consistent with the data; one for impurity point defect clusters, and the other for Schottky clusters of 3 oxygen vacancies and 2 aluminum vacancies. They further concluded that SIMS is the superior analytical tool for studying diffusion because of the high (≈10Å) depth resolution.

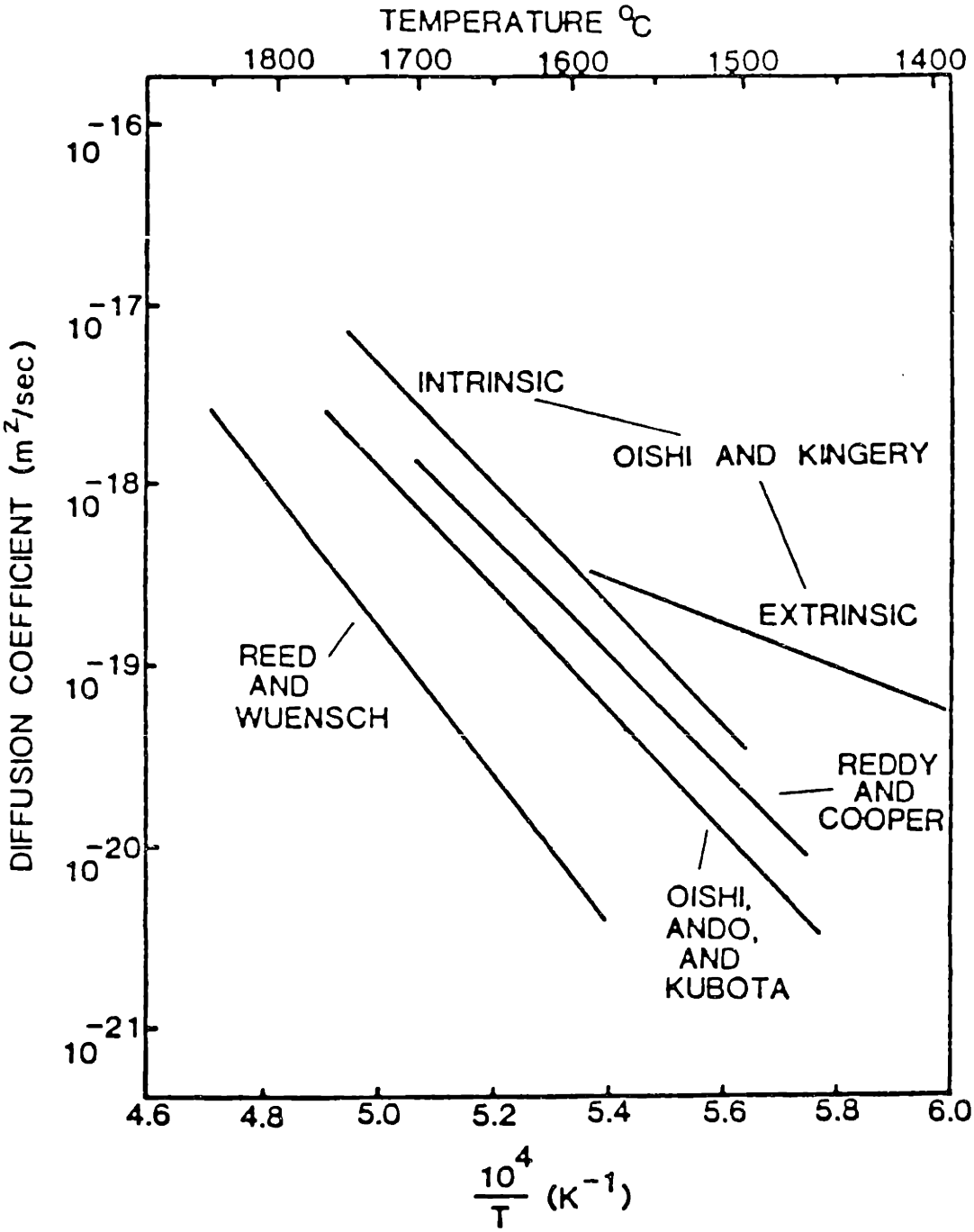

Figure 2.8 Diffusion data from the literature for Al and O in single- and poly-crystalline Al_2O_3 [Cawley, et al., 1986].

Far fewer data have been reported for O boundary diffusion and Al diffusion. Oishi and Kingery [1960] studied the diffusion of O in polycrystalline α-Al_2O_3 from 1200° to 1800°C. Paladino and Kingery [1962] studied the diffusion of Al using radioactive ^{26}Al. While studying only polycrystalline (average grain sizes of 130 and 200μm) α-Al_2O_3, Paladino and Kingery concluded that Al diffuses by the same mechanism in both single- and poly-crystalline alumina from 1670° to 1905°C. Smialek [1979] pointed out how limited this conclusion was with respect to oxidation at temperatures like 1000°C where scales have submicron grain sizes. He concluded that, at lower temperatures, boundary diffusion of Al should be considered as a viable diffusion path.

One point should be emphasized about the Al_2O_3 grown during oxidation: it cannot be considered even nominally pure. In contact with the substrate, the oxide is doped by the other elements in the substrate, both base metals, like Fe, Co, Ni and Cr, and REs Using RBS, Young and de Wit [1983] found 0.5at% Ni in the Al_2O_3 scale grown on NiAl and $NiAl_3$ from 700°C-900°C. These impurities likely dominate the defect structure of the oxide. This makes comparisons with published Al_2O_3 diffusion data difficult.

2.9 Summary

Several important points emerge from review of the literature on the oxidation of nickel- and iron- base, alumina-forming alloys:

(1) There is not complete agreement regarding the mechanism of alumina scale growth on alloys; the $\theta - \alpha$ phase transformation has not been clarified in many papers

(2) The effect of a RE addition on alumina films, especially on the scale growth mechanism, is not well defined; and

(3) Little work has been done at higher temperatures, e.g. between 1200° and 1500°C.

Thus, there is need for more work in this area to establish a better understanding of these phenomena and to expand the knowledge to higher temperatures where applications are moving.

A review of the various theories about the REE reveals a decided paucity of appropriate microstructural characterization. Several prior hypotheses have been discarded once proper characterization was done, while others remain in doubt because of the lack of characterization. Clearly, many hypotheses have been proposed, based on various theories and models, without sufficient accompanying experimental observations. Thus, the emphasis in this study is on observations using a variety of analytical techniques, and on determining a REE theory for alumina-formers consistent with these observations.

3.0 Experimental Procedure

This section describes the variety of materials, environments and characterization techniques that were employed in this study. While some materials were studied more thoroughly and some techniques used more frequently (and with greater success), all are described in equal detail herein.

3.1 The Alloys

Since the thrust of this work was the characterization of the oxidation products, all of the alloys and intermetallic compounds used in this study were procured from others. Conventionally-cast Fe-20Cr-10Al and Ni-20Cr-10Al alloys were made by Dr. Wei Gao at MIT. Commercial FeCrAl alloys were obtained from Dr. William Lipscomb at Inco (in 1985) and Mr. Bo Jonsson at Kanthal (in 1990). The first set of NiAl samples (with Al contents of 23, 30 and 36wt%) were obtained from Norman Bornstein at the United Technologies Research Center. Additional NiAl samples (31.5wt%Al only) were obtained from Dr. Joseph Doychak at NASA Lewis Research Center. A final material, Ni_3Al with a Y_2O_3 dispersion, was obtained from Dr. Ralph Mason at MIT.

Two commercial oxide dispersion strengthened (ODS) FeCrAl alloys were studied along with an undoped FeCrAl alloy. Their compositions, determined by inductively coupled plasma spectroscopy (ICPS), are given in Table 3.1. Inco alloy MA956 is a commercial Fe-20Cr-4.5Al-0.35Ti alloy containing an oxide

Table 3.1 Chemical composition of the FeCrAl alloys.

FeCrAl Alloys	Inco MA956	Kanthal APM	Conventional FeCrAl
Dispersion	Y_2O_3-Al_2O_3	ZrO_2-Al_2O_3	None
Fe	75.38wt%	73.31wt%	70.97wt%
Cr	19.22	20.42	19.27
Al (Al, Al_2O_3)	4.32	5.54	9.71
Y (Y_2O_3)	0.50	< 0.01	
Zr (ZrO_2)		0.10	
Ti	0.36	0.03	
Si		0.23	
Mn		0.08	
C	0.01	0.03	0.02
O	0.20	0.0526	
S	0.011	0.001	0.002

Table 3.2 Chemical composition of the Ni-Al alloys.

NiAl Alloys	Ni-31.5Al	Ni-31Al + Zr	Ni-23Al	Ni-30Al	Ni-36Al	Ni_3Al +Y_2O_3
Ni	68.30wt%	67.88wt%	Balance	Balance	Balance	Balance
Al	31.68	31.30	23.5wt%	29.75w%	36.0wt%	11.9wt%
Fe	< 0.01	0.03				
Cr	< 0.01	< 0.01				
Si	< 0.01	0.02				
Cu	N/A	0.54				
Zr	N/A	0.23				1.06 (Y)
C	0.02	0.02				
S	0.002	0.002				

dispersion of Y_2O_3-Al_2O_3 particles. Initial studies were made at MIT by Przybylski [1987] at 1000°C. This was the first RE-doped alumina-former that was analyzed by AEM to detect the segregation of Y and Ti [Ramanarayanan, et al., 1984]. Also, another commercial ODS alloy, Kanthal's APM (Fe-20Cr-5Al-0.3Si + ZrO_2-Al_2O_3 dispersion) was studied. Apart from the addition of 0.23wt% Si rather than 0.36wt% Ti (as in MA956) the largest difference between the two alloys is the oxide dispersions. The alloy grain size was also significantly smaller in APM, of order 10μm, rather than the ≈1mm grains in MA956. As a base material, a vacuum induction-melted Fe-20Cr-10Al alloy was also studied, in order to study the oxidation behavior without a RE. A similarly cast Ni-20Cr-10Al alloy was also briefly considered. Both of these materials were vacuum annealed prior to oxidation at 1100°C for 24hr.

Ni-Al samples were studied with a variety of Al contents and several different additions, Table 3.2. Only the two stoichiometric NiAl compositions, with and without Zr, were analyzed by ICPS to determine the exact compositions. Most of the characterization work centers on these two materials. Only the Al content specified by the supplier is indicated for the other materials. The Al contents include four different compositions from the ß-NiAl phase field and Ni_3Al.

While most of the work in the study concentrated on adding the reactive element to NiAl by ion implantation, two other cases were studied. Ni_3Al had an oxide dispersion of Y_2O_3 and one NiAl ingot from NASA had a 0.23%Zr alloy addition, which is the same composition that is used in many of the NASA experiments. The

Y_2O_3-dispersed Ni_3Al was prepared by a powder metallurgical process. A prealloyed ingot of Ni-12.1wt%Al-0.02%B was ultrasonically gas atomized to form a powder which was then wet attrited and powders between 38 and 180μm were then ball milled with 2vol% Y_2O_3 to form composite powders. These powders were then canned, hot degassed, and extruded at 1175°C to form a 12.7mm diameter bar [Mason, 1992].

The grain size of the NiAl materials varied somewhat depending on where in the ingot the coupon was cut, but for the most part a grain size of 0.5-3.0mm was observed.

3.1.1 Specimen Preparation

All alloy coupons were ground with SiC paper through 600grit (≈40μm), then polished through 0.3μm alumina powder, to achieve a mirror-like finish. Immediately prior to oxidation the sample was ultrasonically cleaned in acetone followed by high purity methanol. Samples were weighed prior to and after oxidation on a Mettler AE163 balance.

3.1.2 Surface Area Calculations

Specimen surface areas prior to oxidation were measured before the final cleaning and calculated in two ways. Measurements were taken using a Mitutoyo digital micrometer. For samples with sharp corners (i.e. nearly quadrilateral), the thickness and the length of each edge were measured and the area calculated geometrically.

Similarly for nearly-circular specimens, the diameter was measured in two locations, and from this dimension and the thickness a geometrical area was calculated. For oval or oddly-shaped specimens (broken or otherwise misshapen), the thickness was measured and the shape was traced on 1mm spaced graph paper from which a surface area could be deduced. Comparisons indicated less than a 5% difference between the two techniques.

3.2 Ion Implantation

In view of the problems associated with the formation of Ni-Y intermetallics with alloy additions of Y, this option for introducing the RE was not considered. Likewise, the processing problems associated with producing Y_2O_3-dispersed NiAl precluded this choice. Thus, because of its availability at M.I.T., ion implantation was chosen as the method of RE addition. Based on previous work, one level of doping (fluence = $2x10^{16}$ cm^{-2}) was used for each of the specimens.

3.2.1 Implantation at MIT

ß-NiAl was ion implanted with $2x10^{16}$ Y^+/cm^2 at 70kV. A Y^+ current of several µA was achieved by using a heated YCl_3 source and Ar as the carrier gas. Two sets of Ni-Al samples were implanted using this technique.

Prior to implantation the samples were ultrasonically cleaned in acetone followed by methanol. Samples were mounted for

implantation using silver paint which could be removed after implantation without leaving a residue.

Implantation of La was also attempted. $LaCl_3$ was used as a source material with an Ar carrier gas. However, because of low La^+ currents and problems with the implanter, this work was discontinued.

3.2.2 Implantation at NRL

In order to confirm the effect of Y implantation, another group of NiAl samples, prepared in the same way as described above, were implanted with Y ($2 \times 10^{16} cm^{-2}$ at 70kV) at the Naval Research Laboratory (NRL) in Washington D.C.. Higher currents are achieved in the NRL implanter by reacting Y metal powder and a Cl_2 carrier gas. As part of an additional study of the implantation process, Cr and Al were also implanted at NRL to the same level ($2 \times 10^{16} cm^{-2}$ at 70kV) into NiAl. Special thanks goes to Dr. Catherine M. Cotell for arranging to have this work done.

3.2.3 Pre-oxidation Characterization

Several samples were characterized before and after Y implantation to look at the effect of the implantation and to estimate the peak depth of the implant. The Y implant was modeled using a TRIM - 88 simulation. The peak implant concentration of 4.2at% occurred at a depth of 22.9nm.

Several surface analytical techniques (GAXRD, RBS, XPS, and SIMS) were used to characterize the substrate after implantation. Given the shallow implant depth, none of these techniques was able to quantify the peak depth, although RBS, SIMS and XPS indicated the same order of magnitude as the simulation.

GAXRD was used to look at the effect of the implant on the crystal structure. In the near surface region, there was little effect on the lattice spacing and no indication of amorphization. There was a larger peak shift from changing the Al content in ß-NiAl than from implanting Y. In one case there was a single weak peak which matched the YAl intermetallic. However, there was no other evidence to confirm this observation.

RBS was done at NRL and again through the MIT-Harvard Joint Surface Analytical Facility. The NRL work showed that a Ni- and O-rich layer was formed at the surface. This layer could be a passivation layer formed at room temperature or an indication that Al is selectively sputtered during implantation. RBS at Harvard showed that there was virtually no difference between the MIT and NRL implants with regard to implant quantity or depth profile.

XPS analysis of the NiAl produced an opposite result to RBS. XPS indicated that Ni was depleted from the surface and mainly Al and O were found at the surface. An XPS sputter profile indicated an Al-O layer of ≈100Å thickness. Sputtering by SIMS showed a surface enriched in O but did not indicate any significant difference in the Ni-Al ratio. Thus, while it is clear that the implantation process formed a thin surface oxide layer, the composition of the layer could not be verified. While selective oxidation at high temperature

favors the formation of Al_2O_3, passivation or sputtering of the lighter Al atom favors NiO formation.

3.3 Isothermal Oxidation Experiments

Oxidation weight gain was measured continuously using a Cahn 1000 microbalance. At lower temperatures, a 1mg scale was used to record data with an accuracy of approximately 0.01mg. At temperatures above 1200°C, a 10mg scale was used, reducing the accuracy to 0.05mg. These are total weight gain accuracies. With areas of 2-5cm^2, the associated errors are acceptably reduced when converted to mg/cm^2.

Coupons ≈1.5cm x 1.5cm x 0.1cm were polished to a 0.3μm alumina finish before oxidation. Isothermal oxidation experiments were performed at 1000°, 1200°, 1400° and 1500°C in 1.0 atm of dry, flowing O_2. Specimens were cold-inserted into a hot vertical furnace for periods from 0.1 to 100hr. Cyclic tests are discussed in Section 3.4.

3.3.1 Furnace/Balance Apparatus

The oxidation rig is shown in Figure 3.1. The clam-shell type furnace was heated by six vertical $MoSi_2$ elements. The insulation was Kaowool fiber board for the top and bottom and flexible ZrO_2 blanket material on the walls (both rated to 1650°C). The temperature was kept near constant by a Eurotherm controller (Model #990) using a B-type thermocouple and Eurotherm thyristor

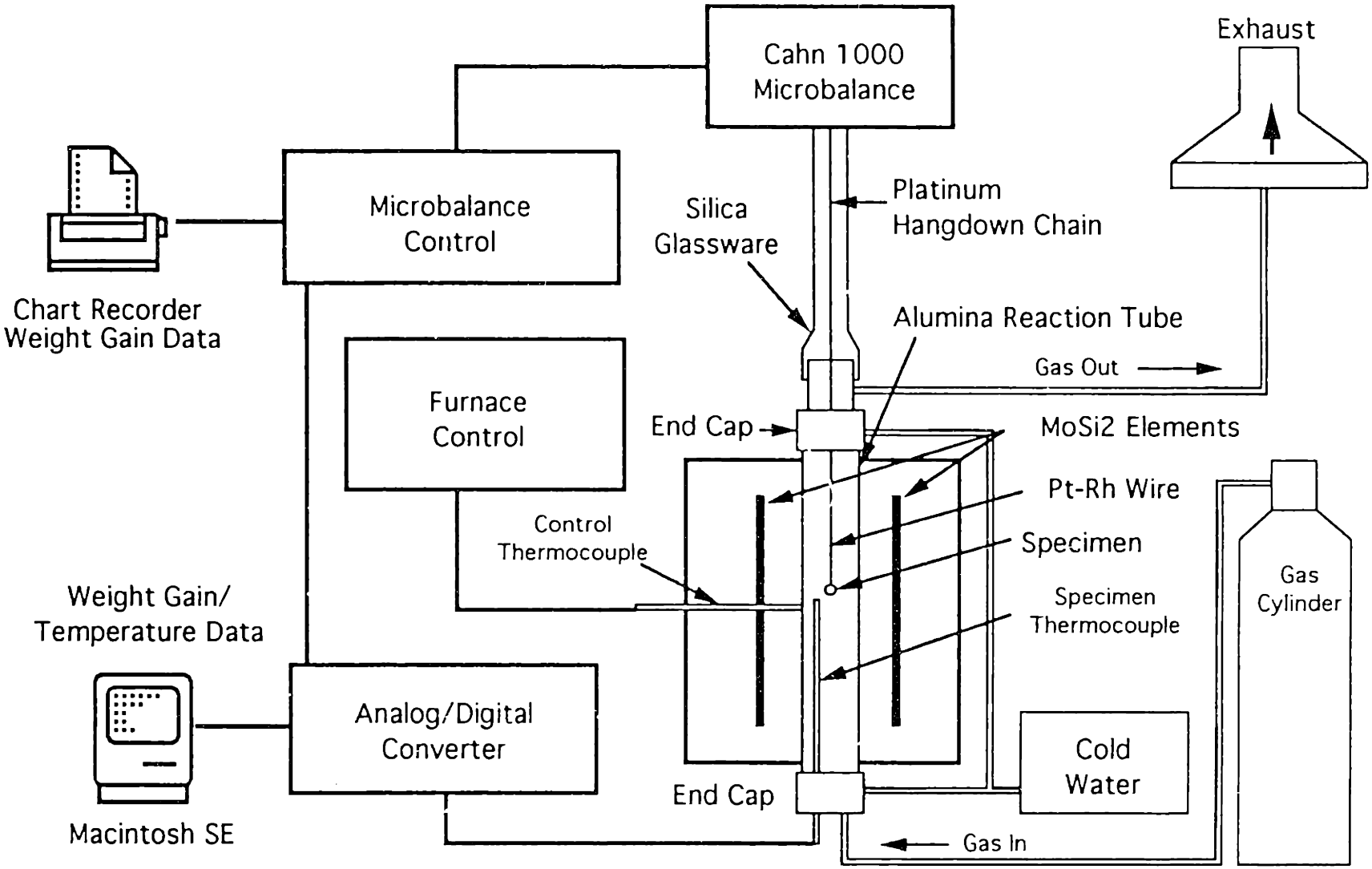

Figure 3.1 Schematic diagram of the oxidation apparatus.

(Model #932/40A). At 1000°C, the temperature fluctuated by ±4°C, but this fluctuation decreased as the temperature was increased. At 1500°C, the fluctuation was only ±2°C. In order to achieve sufficient power, a transformer was used to lower the line voltage from 240 to 120V, thus increasing the current. While the furnace elements could potentially go higher, 1500°C was the highest temperature that the furnace could maintain on a steady basis, sufficient for isothermal experiments.

The reaction tube was alumina (3.2cm ID) with water-cooled stainless steel endcaps. The lower cap contained inlets for gas and for a thermocouple sheath. The hot-zone temperature was monitored by a Type S thermocouple. The upper cap was connected to silica glassware which connected to the microbalance. A gas outlet is situated immediately above the upper endcap. The glassware directly above the furnace was cooled by two small electric fans. The balance is approximately 0.9m above the endcap to keep it at room temperature and to allow the specimen to be raised from the furnace.

The sample is attached to a multi-component hangdown chain. The upper half is a Pt chain, while the lowest part which goes into the hot zone is a Pt-33wt%Rh wire. In the middle of the chain (outside of the furnace), is a piece of iron which can be manipulated using a magnet outside the glassware. The magnet is used to gently raise and lower the specimen so as not to shake the balance.

Except for one experiment in flowing air, all of the experiments were conducted in 1atm of dry, flowing, O_2. The minimum gas purity was 99.8%. The gas was dried over $CaSO_4$

(Drierite) and flowed from the bottom end cap to the top of the furnace, where it was exhausted through Tygon tubing to an exhaust hood. Flow into the furnace was controlled by bubbling the O_2 through a column of dibutyl phthalate. The column exerted a back pressure on the gas, diverting it through a capillary. The pressure difference across the capillary was measured using a simple manometer consisting of two small vertical columns of dibutyl phthalate. The difference in height between the two columns was fixed for all of the experiments to achieve a flow rate in the reaction tube of approximately 58cm/min (≈ 28.3 l/hr, 1 cu.ft./hr, 470cm^3/min, or 1cm/s).

3.3.2 Standard Thermocouple

The furnace temperature was monitored constantly by a Type S thermocouple in the reaction tube. In order to check the accuracy of this thermocouple, a standard Type S thermocouple was used to check the accuracy each time the furnace temperature was changed. This thermocouple was manufactured by Leeds & Northrup Co., St. Petersburg, FL, serial number BS-8828. It was calibrated by the former National Bureau of Standards in May 1988 (Test No. 240845).

3.3.3 Pt-Rh Evaporation

Above 1200°C, the evaporation of the Pt-Rh hangdown wire began to become significant, the linear evaporation (expressed as weight loss), approaching the long term oxidation weight gain. The

weight loss was standardized by using a 2.0cm long, 0.41mm diameter, Pt-10wt%Rh wire to attach the sample to the Pt-33wt%Rh hangdown wire. In order to calculate the weight loss, a sintered Al_2O_3 coupon was placed in the furnace for 50hr exposures at each reaction temperature. A linear rate of weight loss was determined at each temperature, Table 3.3. The rate was found to be independent of the P_{O_2} content of the gas stream and most dependent on the gas flow rate. Therefore the flow rate was kept constant for all of the experiments (≈1cm/s).

The evaporation of the hangdown wire also lead to the formation of an inadvertant marker during oxidation. Rh particles (approximately 50nm in diameter) were found in the scale of many samples when thinned for AEM both near the gas interface and near the center of the scale. These particles were not visible by any other characterization techniques because of their small size.

3.4 Cyclic Oxidation Experiments

Since the largest stresses between the metal and oxide are generated during cooldown, cyclic experiments were performed in order to test the oxide adherence. Samples were exposed to the reaction temperature for a fixed cycle time and then allowed to cool to room temperature before reinsertion. In order to maintain consistency, these experiments were performed in the same apparatus as the isothermal experiments. A cold-insertion technique again was used, and the samples were rapidly (in 2s) removed from the hot zone to cooldown. An initial test at 1500°C

Table 3.3 Linear evaporation rates for the Pt-Rh hangdown wire at each of the reaction temperatures.

Reaction Temperature	Evaporation Rate (mg/hr)
1000°C	0.00075
1200°C	0.0185
1400°C	0.1025
1500°C	0.2295

Table 3.4 Comparison of the weight gain during 1 cycle at each reaction temperature.

Temperature (°C)	Cycle Time (hr)	Rate Constant (g^2/cm^4s)	Weight Gain (after 1 cycle) (mg/cm^2)	Oxide Thickness (μm)
1200°C	2.0	$\approx 6 \times 10^{-12}$	0.208	1.13
1400°C	1.0	$\approx 5 \times 10^{-11}$	0.424	2.31
1500°C	0.2	$\approx 2 \times 10^{-10}$	0.379	2.07

charging. Initial testing showed C coating resulted in too much charging. Charging problems with Au and Pd were nevertheless still encountered in several cases, especially with non-adherent scales and very rough scales.

The two SEM's used in this study were an AMR Model 1000 and a Cambridge Model S-250. The Cambridge instrument was equipped with a Si-Li drifted x-ray detector with a Be window and a Kevex energy dispersive X-ray analyzer.

Only a few cross-sections were examined, primarily pieces of non-adherent scales mounted to image only the oxide. A few attempts to make metallographic cross-sections did not yield much information. Occasionally, a TEM cross-section was examined in the SEM to get an idea of the scale thickness near the thin area and away from it.

3.6 Glancing Angle X-ray Diffraction (GAXRD)

The thin oxide scales produced in this project required thin film x-ray diffraction techniques in order to determine their phase composition. Rigaku models 200 (12kW) and 300 (18kW), coupled to a Rigaku x-ray diffractometer equipped with a glancing angle attachment, were used in this study. After some preliminary experiments, a fixed glancing angle of 0.5° was selected in order to get diffraction information from primarily the surface region. This involves simply fixing the incident angle and varying the detector through 2θ values of 20° to 137° (the widest range possible).

Experiments were carried out using a rotating Cu Kα anode at 50kV and 150mA, using an incident slit of 0.2mm wide. No receiving slit was used. The samples were rotated (at ≈100rpm) during analysis in order to average out orientation effects. In most cases, the samples were scanned at a rate of 10°(2θ)/min, using a step size of 0.05. Table 3.5 lists the principle JCPDS cards referenced in this study.

Table 3.5 Primary JCPDS cards used in this study.

Compound Phase	JCPDS Card	Compound Phase	JCPDS Card
θ-Al_2O_3	35,121	NiO	22,1189
θ-Al_2O_3	23,1009	Cr_2O_3	6,504
α-Al_2O_3	10,173	Y_2O_3	25,1200
β-NiAl	20,19	$Y_3Al_5O_{12}$	33,40
Ni_3Al	9,97	ZrO_2	17,923
$NiAl_2O_4$	10,339		

3.7 TEM/STEM Sample Preparation

The majority of TEM/STEM samples were prepared after oxidation to study the scale microstructure and microchemistry. A few alloy specimens were thinned, both prior to oxidation and after oxidation to study the alloy microstructure, and especially for those materials with an oxide dispersion to study its distribution.

Samples of the oxide scales were prepared both parallel and perpendicular (transverse) to the alloy-oxide interface [Hobbs and

Mitchell, 1983]. To make a parallel sample, the coupon was cored with a 3mm ultrasonic drill to a depth of ≈300μm. The sample was then ground from the opposite side to produce a disk. The resulting disk was next jet electropolished in a 10% perchloric acid - methanol solution at -40°C to remove the metal; the scale side was coated with a clear resin to protect it during electropolishing. This procedure typically produced a sample with a hole through the metal substrate, revealing the scale. Because the polishing is stopped by a light sensor and the resin and Al_2O_3 scale are translucent, the electropolishing did not always produce a hole in the scale. To produce an electron-transparent sample (and sometimes a hole), the scale then must be ion thinned.

Ion thinning was effected using a Gatan 600 duomill with an Ar beam at 6kV and ≈0.5mA per gun. While the exact depth of the thin area in the sample cannot be determined, an approximate depth can be estimated. For examining the scale near the gas interface, the sample was milled exclusively from the alloy side. Milling was done from the scale side of the disk in order to examine the oxide near the alloy. And finally by milling from both sides, the thin area is close to the center of the scale.

The technique to produce transverse sections is a hybrid form of the method first described by Tinker and Labun [1982] and later modified by King [1984] and then by Cotell [1988]. Strips of oxidized coupon are epoxied between halves of a Ta rod then epoxied inside a 3mm OD stainless steel tube, Figure 3.2. This "sandwich" is then sliced, mechanically thinned and polished, dimpled and ion thinned. A Cu or Ni slotted grid is often glued to the sample before ion

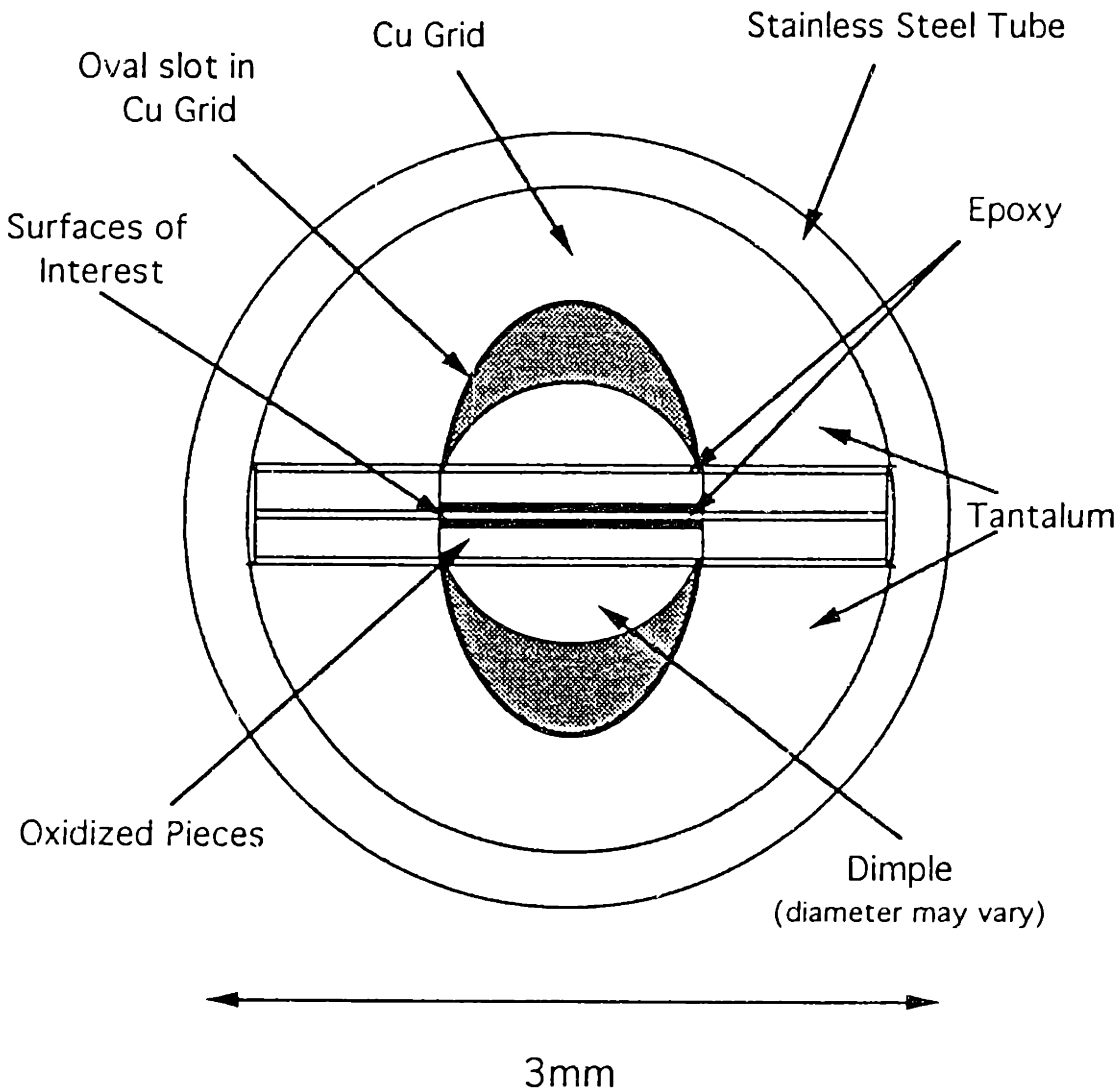

Figure 3.2 Schematic diagram of a TEM transverse section.

thinning in order to protect the epoxy from milling away from the edges of the disk.

3.7.1 Contamination Problems

One problem encountered during sample preparation is contamination. Especially during the ion milling process, several sources of contamination are encountered. For example, Ar peaks are often detected during EDXA analysis from the milling. A more critical problem is Mo deposited from the sample holder. The S Kα and Mo Lα characteristic x-ray energies are very close together; thus when Mo is present S detection is hampered. One solution to this problem is the use of a Ta holder. The ion milling process also presents a problem of self-contamination. Depending on the substrate, Ni or Fe and Cr can be spread across the sample during milling, especially when making a parallel section. This contamination prevents quantification of the amount of these elements detected in the scale, although it usually does not affect segregation comparisons.

3.8 AEM Analysis

The primary instrument used in this study was a field-emission gun scanning transmission electron microscope (FEG-STEM) equipped with energy dispersive x-ray analysis (EDXA) and electron energy-loss spectroscopy (EELS). The STEM work was done with a Vacuum Generator Microscopes Ltd. (East Grinstead, UK) model HB5

instrument with a <2nm electron probe using a windowless Si-Li x-ray detector (solid angle of 0.077Sr). The small probe size is critical for detecting grain boundary segregation. The electron energy was 100kV for all experiments and the EELS was used in a few situations to determine the elements present in individual particles. Some conventional TEM work was done using a JEOL Co. (Tokyo, Japan), model 200-CX instrument.

3.8.1 EDXA Data

One of the most difficult parts of analyzing grain boundary segregation is trying to quantify x-ray spectra after analysis. Comparing spectra originating from and away from the grain boundary can confirm the presence or absence of a particular element based on its characteristic x-ray peaks. However, to quantify this observation is not straightforward. The excitation volume from which the x-rays are detected is dependent on the probe diameter, the sample thickness and the beam spreading. Once this volume is determined, the issue is then to determine what fraction of the this volume is grain boundary and which belong to the grain interior.

While these parameters are well worth studying, it was not the focus of this work. The most pertinent issue here is qualitative not quantitative. The question is whether REs segregate to Al_2O_3 grain boundaries. To simplify the issue of quantification, a simple method was chosen. The probe size and the grain boundary width were assumed to be constant and the beam spreading ignored

[Furdanowicz, et al., 1991] Thus, the ratio of grain boundary volume to grain volume is constant, independent of sample thickness. Weight percentages were calculated from the EDXA spectra using the Cliff and Lorimer [1975] method of thin film analysis. Weight percentages were ignored when the net count was less than twice the squareroot of the gross count. The ratio of the cation weight percentages were compared on and away from the boundary, e.g. Zr wt% / Al wt%.

3.9 $^{18}O/^{16}O$ Sequential Oxidation Experiments

In order to avoid the problems associated with inert marker experiments (Sec. 2.4.1), sequential oxidation experiments were used in order to study the oxidation mechanism of Al_2O_3. The basic premise is relatively simple. The sample is oxidized first in an environment rich in one oxygen isotope, followed by oxidation in a second environment rich in a second isotope. The resultant oxide can then be examined by a variety of techniques, e.g. SIMS or NRA, in order to determine the distribution of the isotopes in the scale. SIMS was chosen in this case because of the availability of the instrument at MIT.

In practice, however, a number of limitations make the actual experiment more difficult. First of all, in the case of alumina-formers without a RE addition, the second oxidation period must occur immediately after the first without cooling the sample, in order to avoid oxide spallation. Thus both environments must be achievable in the same furnace. Also, due to "crater" effects

associated with sputtering through a very thick scale, the total scale thickness was kept to a maximum of 1μm. This was a significant restriction at higher temperatures, even with the relatively slow-growing Al_2O_3 scales. Crater effects will be discussed further in Section 3.10.

3.9.1 Gas Exchange Vacuum Furnace

A small-volume vacuum furnace was used for the sequential oxidation experiments. Using SiC heating elements, this furnace was built especially for these experiments, Figure 3.3. By placing the SiC elements perpend-icular to the reaction tube, the endcaps did not require water cooling. Using a vacuum feedthrough rod, the samples could be moved from the furnace hot zone to near room temperature at the ends while still in vacuum The furnace was primarily designed to be able to perform the isotope exchange at 1500°C when the total oxidation time was 160s (40s/120s). Thus the atmosphere had to be changed within approximately 10s in order to perform the experiment. This short time prohibited the use of an extensive vacuum system or an ^{18}O storage system.

Because the experiments were a maximum of 1hr in duration, an extensive control system was not used. Instead a simple variac was used to control the furnace temperature. The hot zone was measured (≈2.5cm) and calibrated using the standard thermocouple described in Section 3.3.2. The temperature was monitored during the experiment using a Type-S thermocouple. The furnace hot zone was somewhat small, but with the specimen size (≈0.5cm x 0.5cm x

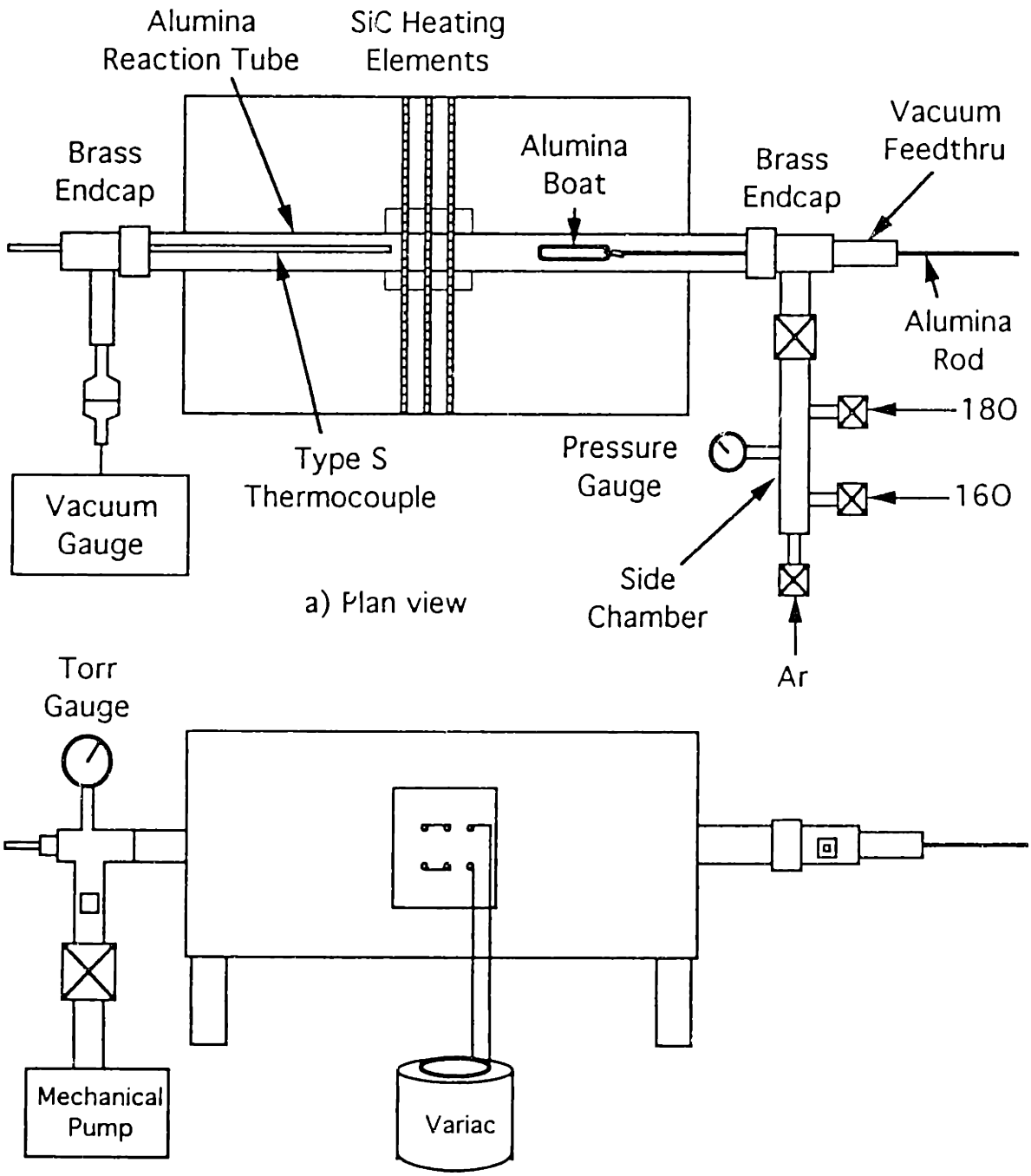

Figure 3.3 Schematic diagram of the vacuum isotope exchange furnace.

0.1cm) being much smaller than the other experiments it was sufficient. The sample size was kept small to fit in the SIMS holder.

To start the experiments, the samples were placed in an alumina boat, with a Pt cage surrounding the samples. The cage prevented the samples from falling out of the boat while also allowing faster heating by not having the sample in contact with the slow-heating alumina boat. With the sample in the cold end of the reaction tube, the chamber was evacuated with a simple mechanical pump. The vacuum was measured with a thermocouple vacuum gauge. The initial gas was first introduced into a side chamber to get a fixed volume while the reaction tube was evacuated to <100mTorr. The pump was then isolated. The first oxidant was next introduced into the reaction tube, and the sample moved into the hot zone. The two gases used were research grade oxygen, which typically is ≈99.8% ^{16}O, and oxygen enriched to >95% ^{18}O. The isotope order was varied depending on the experiment.

After the first oxidation, the reaction tube and the side chamber were evacuated. At lower temperatures, the system was evacuated for 1min, at 1500°C for 5s. The side chamber was then isolated and filled with the second isotope gas. A pressure of 10psi in this chamber corresponded to approximately 50Torr in the reaction tube. When the chamber had pumped to a minimum of 200mTorr, the pump was then isolated and the second oxidant introduced to the reaction tube. At the end of the second oxidation period, the sample was then moved out of the hot zone to cool. The system was finally evacuated and flushed with Ar three times while the samples cooled.

3.10 SIMS Sputter Depth Profiles

A Vacuum Generator Microscopes Ltd., model IX705 secondary ion mass spectrometer (SIMS) was used to make sputter depth profiles of the sequentially-grown oxide. This type of analysis, often referred to as dynamic SIMS, is surface specific and can easily distinguish between ^{16}O and ^{18}O. After numerous attempts, the best results were obtained with a Cs source with a negative extraction potential. The sample was coated with Au to limit charging. The species detected in the FeCrAl and NiAl samples are listed in Table 3.6. The ones that were profiled in most cases were ^{16}O, ^{18}O, $^{27}Al^{16}O$, $^{27}Al^{18}O$ and either ^{56}Fe or ^{58}Ni, depending on the substrate. These species produced the strongest and most consistent signals.

Table 3.6 Possible species detectable by SIMS.

Species	Atomic Wt.	Species	Atomic Wt.
^{16}O	16	$Al^{18}O_2$	63
^{18}O	18	$Al_2{}^{16}O$	70
Al	27	$Al_2{}^{18}O$	72
$Al^{16}O$	43	$Fe^{16}O$	72
$Al^{18}O$	45	Al216O2	86
Fe	56	$Al_2{}^{18}O^{16}O$	88
Ni	58	Y	89
$Al^{16}O_2$	59	$Al_2{}^{18}O_2$	90
$Al^{16}O^{18}O$	61	Zr	90

In order to achieve a well-structured crater in a reasonable amount of time, a beam current of 3nA and a sample area of ≈20μm x 40μm (500X setting) was used. The idea of sputter depth profiles is that material is removed at a uniform linear rate from the bottom of the crater. When a deep crater is created, there are potential problems. Crater effects include problems associated with rounding of the crater walls especially when the crater gets deep. This may produce an uneven sputtering rate, slowing as the crater gets deeper. Also, rather than the signal coming exclusively from the bottom of the crater, some ions may be sputtered from the crater walls. To limit this problem, a high resolution 5% gate was used. This selected ions only from the central 5% of the crater to analyze. This also helped avoid detector saturation.

Typical total sputter times were 1.5 to 3hr. However, because the crater sides and bottom were so rough, no clear estimation could be made of the sputter rate. The rough crater also made identification of the metal-oxide interface difficult to determine. Detection of negative ions emphasized the O isotopes and limited detection of positive metal ions (Fe, Cr, Al, or Ni). Thus, termination of the profile was made when the O signals fell to a sufficiently small value. In a few instances, the sputtering was stopped due to problems with the Cs source or sample charging problems.

3.10.1 SIMS Data Presentation

Interpreting the raw data generated by the depth profiles was not straightforward. While in some instances a clear differentiation could be made between, for example, an ^{18}O layer and a ^{16}O layer, this was not always the case. Several samples showed only subtle changes in the profile.

After trying several techniques, the one which worked the best was to compare the isotope fractions profiled through the scale. This technique is also preferred because of its simplicity. The species representing ^{16}O (^{16}O and $Al^{16}O$) were combined, as were those representing ^{18}O (^{18}O and $Al^{18}O$). The sum of the signals from all four of these were the total of all O isotopes detected. This produced fractions reflecting the total ^{16}O and ^{18}O detected. The procedure allows a normalization of the signals, eliminating signal enhancement near the Au coated surface and signal decay at long sputter times. This type of plot is somewhat confusing because it does not identify the metal-oxide interface. However, since there was no clear marker of the surface, precise identification was not possible. Thus the end of the profile can be regarded as approximately the metal-scale interface.

4.0 FeCrAl Alloys

The first study of the reactive element effect used commercial FeCrAl alloys with a reactive element oxide dispersion -- Y_2O_3 in MA956 (Fe-20Cr-5Al and ZrO_2 in APM (Fe-20Cr-5Al). This was compared to a conventionally cast Fe-20Cr-10Al alloy.

This part of the study builds on the initial work done at MIT [Przybylski, 1987] studying the segregation phenomena in scales formed at 1000°C on MA956.

4.1 Results at 1000°C

Besides the REE, at 1000°C one of the most important issues was the phase transformation in Al_2O_3 from the metastable θ to the stable α phase and the transient stage formation of less-noble oxides.

4.1.1 Kinetic Results

The isothermal kinetic data at 1000°C are shown in Figure 4.1.1. As would be expected for the REE, the commercial FeCrAl's have a lower oxidation rate than the undoped FeCrAl. However, the most interesting aspect of the oxidation at this temperature is a repeatable minor breakdown of the scale on the undoped FeCrAl at ≈15hr and at 90hr. A parabolic rate law is obeyed except during the breakdown events in the undoped FeCrAl. Comparing only the early oxidation period, the reduction in rate constant is between a factor of 2 and 4 with a RE addition. However after the breakdown, the

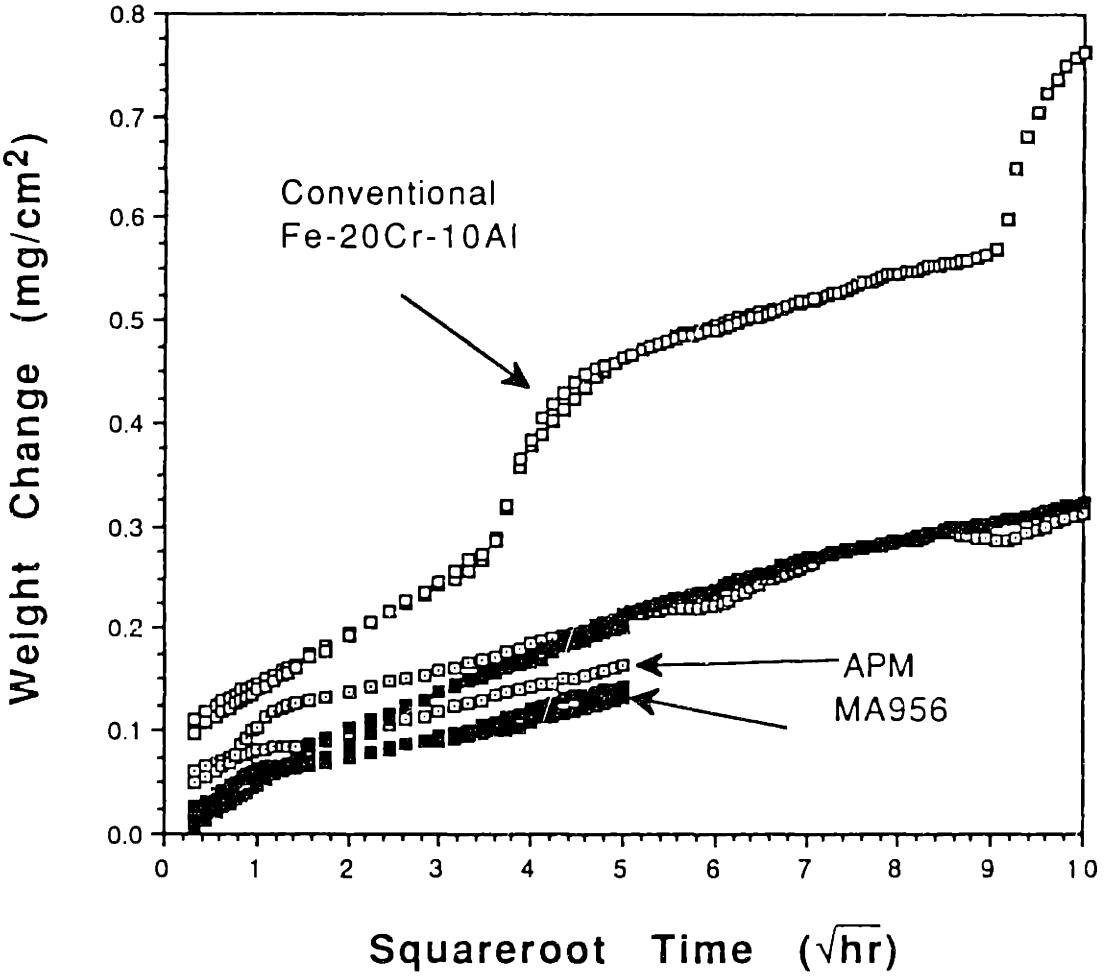

Figure 4.1.1 Parabolic plot of weight gain versus squareroot of time for FeCrAl alloys at 1000°C in 1atm O_2.

second parabolic region of the undoped FeCrAl has a lower rate more comparable to the RE case.

No cyclic experiments were performed at 1000°C. Also, short term experiments (12min and 1hr) did not produce reliable, repeatable results due to problems in stabilizing the balance in a very short time (to establish a starting weight) and in resolving the very small weight gains.

4.1.2 SEM Results

The oxide morphology was very different with and without a RE addition at 1000°C. Unless otherwise specified, the images found here and throughout the thesis are SEM secondary electron images. Figure 4.1.2 shows the partially spalled scales on FeCrAl after 1hr. Based on the kinetic information, this spallation occurred during cooldown. In contrast, Figure 4.1.3 shows the scale on APM after 100hr; a relatively-uniform, adherent scale is observed throughout. Figure 4.1.4a is a higher magnification of the FeCrAl scale after 1hr. The scale is "buckled" throughout, see Figure 2.7a. After 100hr, Figure 4.1.4b, the buckling is still observed but at a scale almost twice as large. Also, an occasional whisker occurs on the surface after 100hr. These were not observed after 1hr, but become more prominent at 1200°C. Figure 4.1.5 again compares the scales on FeCrAl after 1hr and 100hr. While after 1hr the surface appears to be covered by a sub-micron ridge-type structure, after 100hr the ridges appear to have coarsened and now look more like pores than ridges. In areas where the oxide has spalled off, the underlying alloy

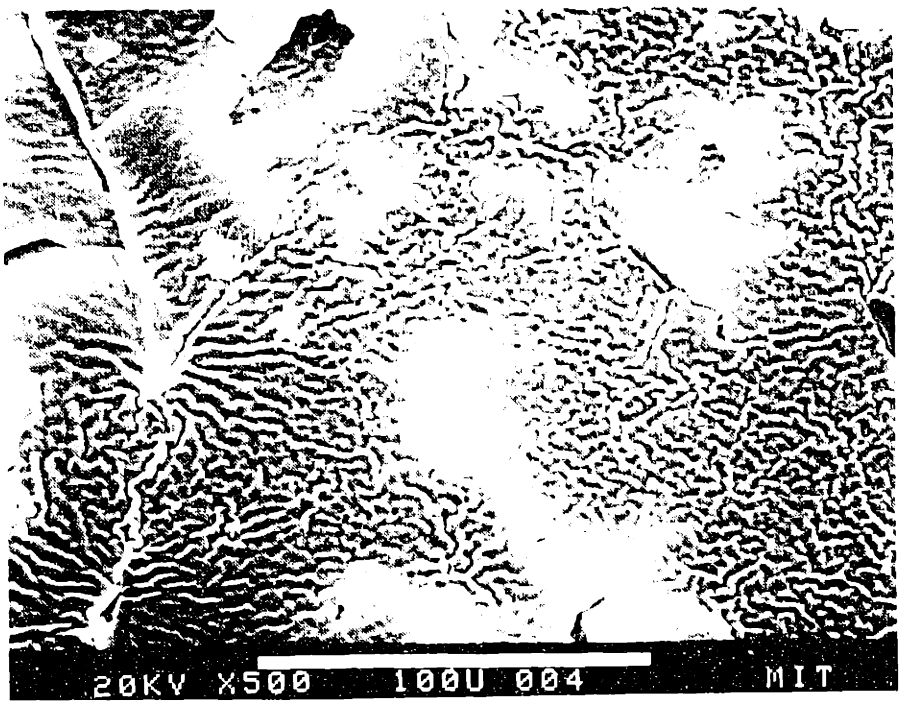

Figure 4.1.2 SEM secondary electron image of the undoped FeCrAl after oxidation for 1hr at 1000°C, showing the convoluted, spalled scale.

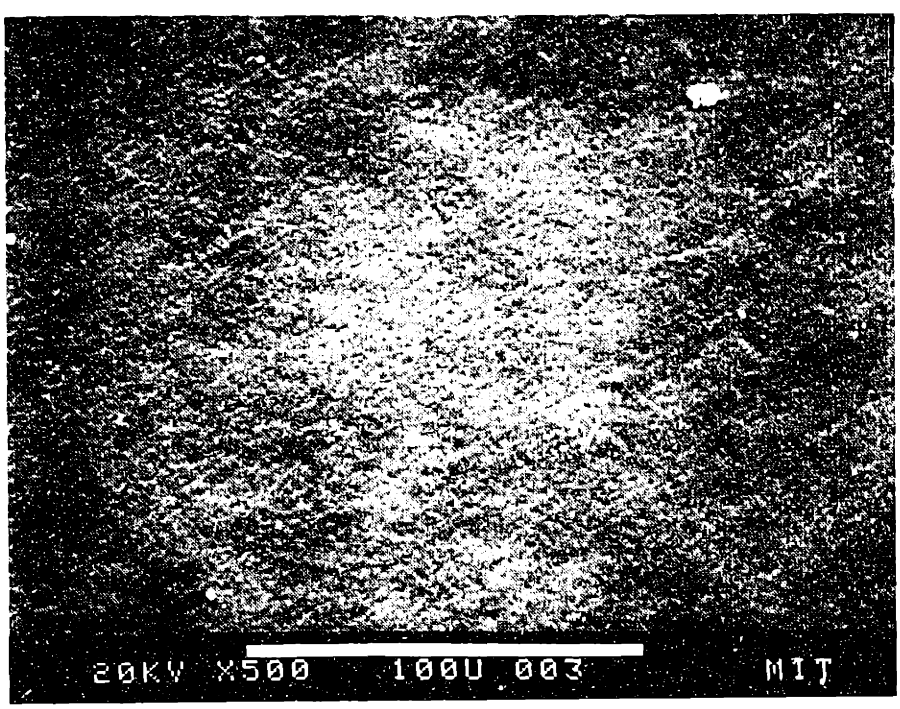

Figure 4.1.3 SEM secondary electron image of APM after oxidation for 100hr at 1000°C. No oxide convolution or spallation is observed.

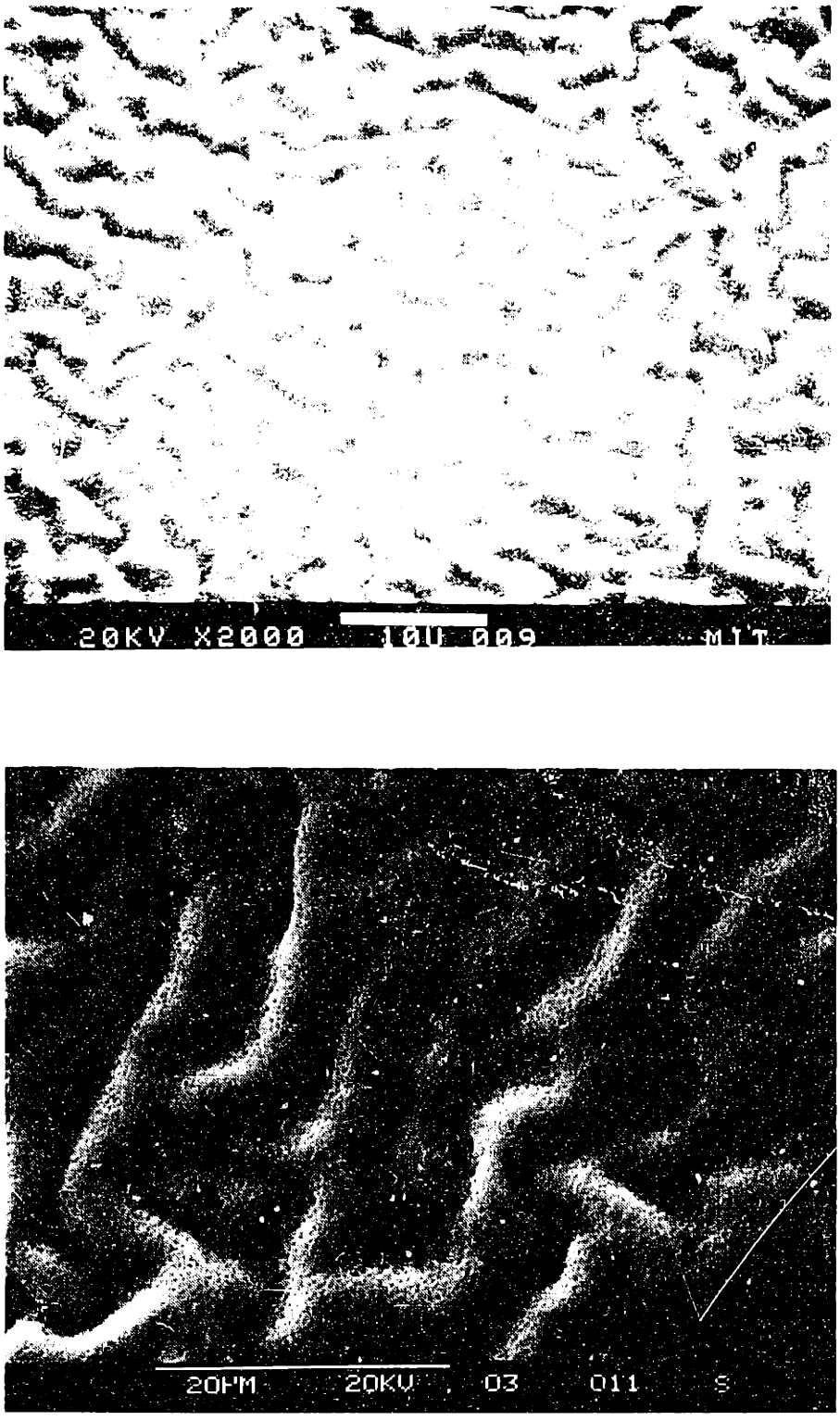

Figure 4.1.4 SEM secondary electron images of the undoped FeCrAl after oxidation at 1000°C for (a) 1hr and (b) 100hr.

Figure 4.1.5. SEM secondary electron images of the undoped FeCrAl after oxidation at 1000°C for (a) 1hr and (b) 100hr.

reflects the buckling of the scale and the alloy-oxide contact, Figure 4.1.6. On the same scale as the buckling, the alloy is observed to have areas of oxide grain imprinting (the bottom of the buckle) and smooth areas where the alloy presumably lost contact with the oxide (the top of the buckle). Based on the smooth alloy morphology, Al transport would most likely have occurred by vapor or surface diffusion across this gap. Although only a small fraction of adherent oxide is examined here, there is no clear explanation from the morphology to explain the kinetic breakdown events shown in Figure 4.1.1. In general, the severe spallation of the undoped scale during cooldown disguises any failure that may have occurred isothermally.

The scales formed on the ODS alloy were much more uniform than those on FeCrAl. Most likely due to the oxide dispersion, the most prominent feature on the surface of MA956 after 1hr and 100hr are large oxide grains intermixed in a matrix of smaller grains, Figure 4.1.7. While occasionally these particles are found by EDXA to be rich in Y or Ti, they have no special chemical composition. The oxide grain growth is evident between 1 and 100hr. However, while the largest grains on the surface of MA956 after 100hr are comparable to those formed on FeCrAl (using the grain imprints in Figure 4.1.6b), the average oxide grain size on MA956 is much finer than that measured on the undoped FeCrAl.

APM also has a very flat surface, but some important distinctions are noted. One major difference on APM after 1hr, as compared to MA956, were occasional areas with blade-like oxide grains, Figure 4.1.8a. These are indicative of θ-Al_2O_3. After 100hr, these regions are no longer observed but this surface is also unique,

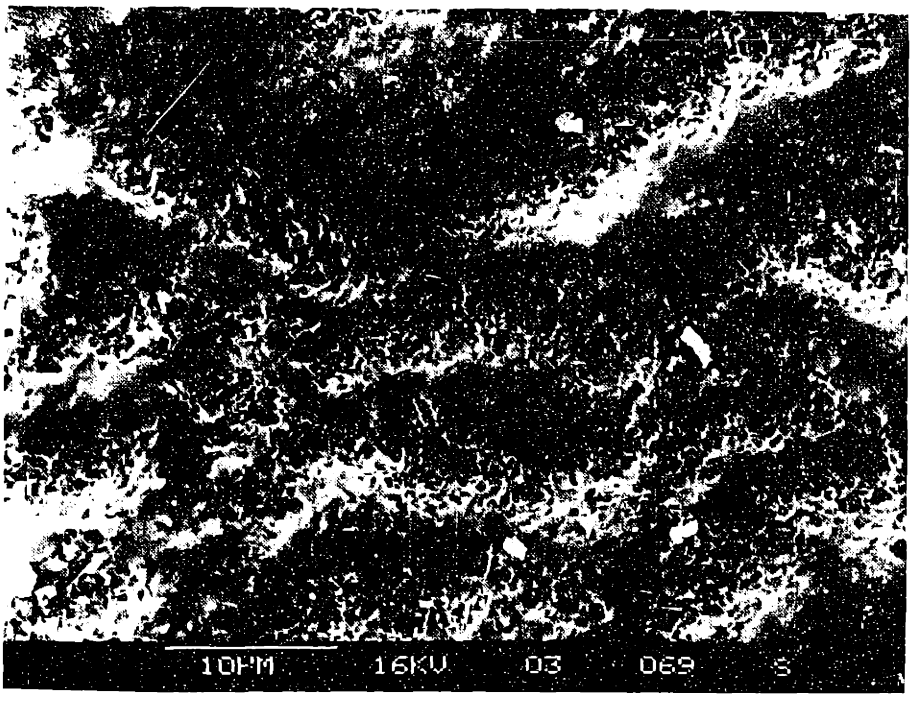

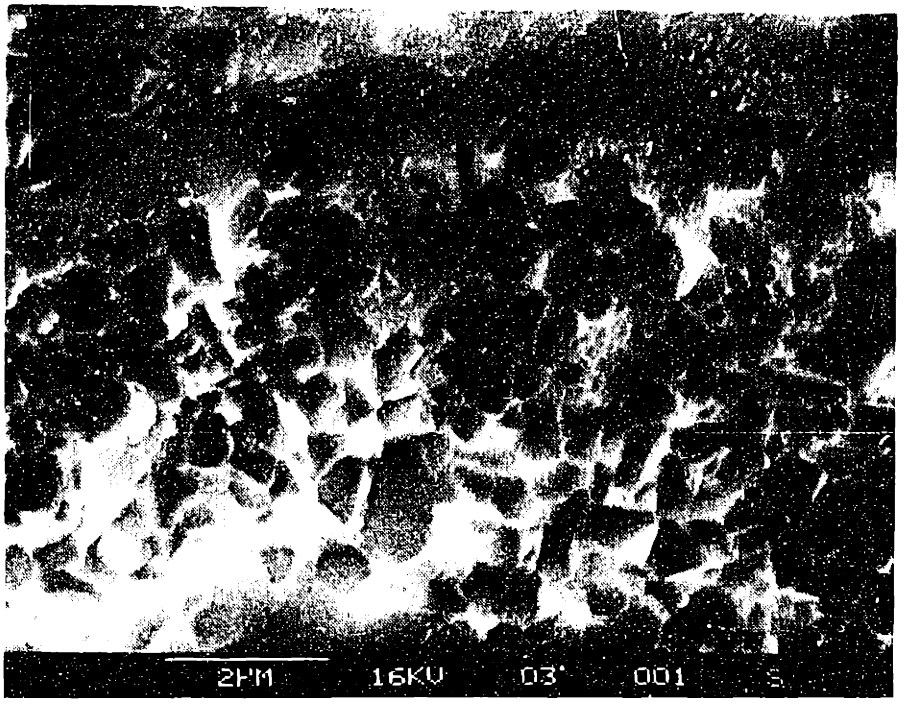

Figure 4.1.6 SEM secondary electron images of an undoped FeCrAl alloy substrate beneath the oxide grown for 100hr at 1000°C. The oxide spalled away during cooldown. Note in (b) the oxide grain imprints in the alloy.

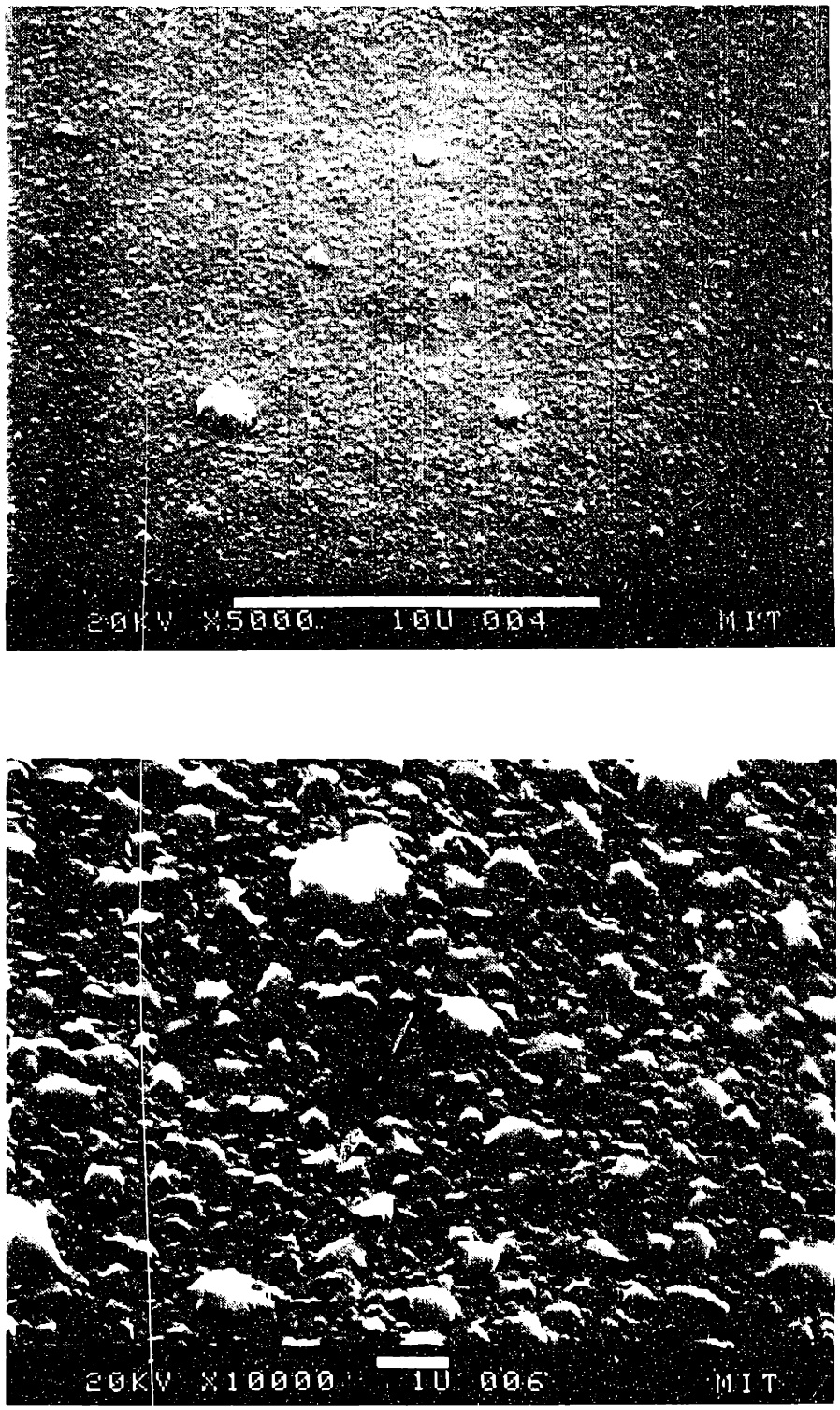

Figure 4.1.7 SEM secondary electron images of MA956 after oxidation at 1000°C for (a) 1hr and (b) 100hr.

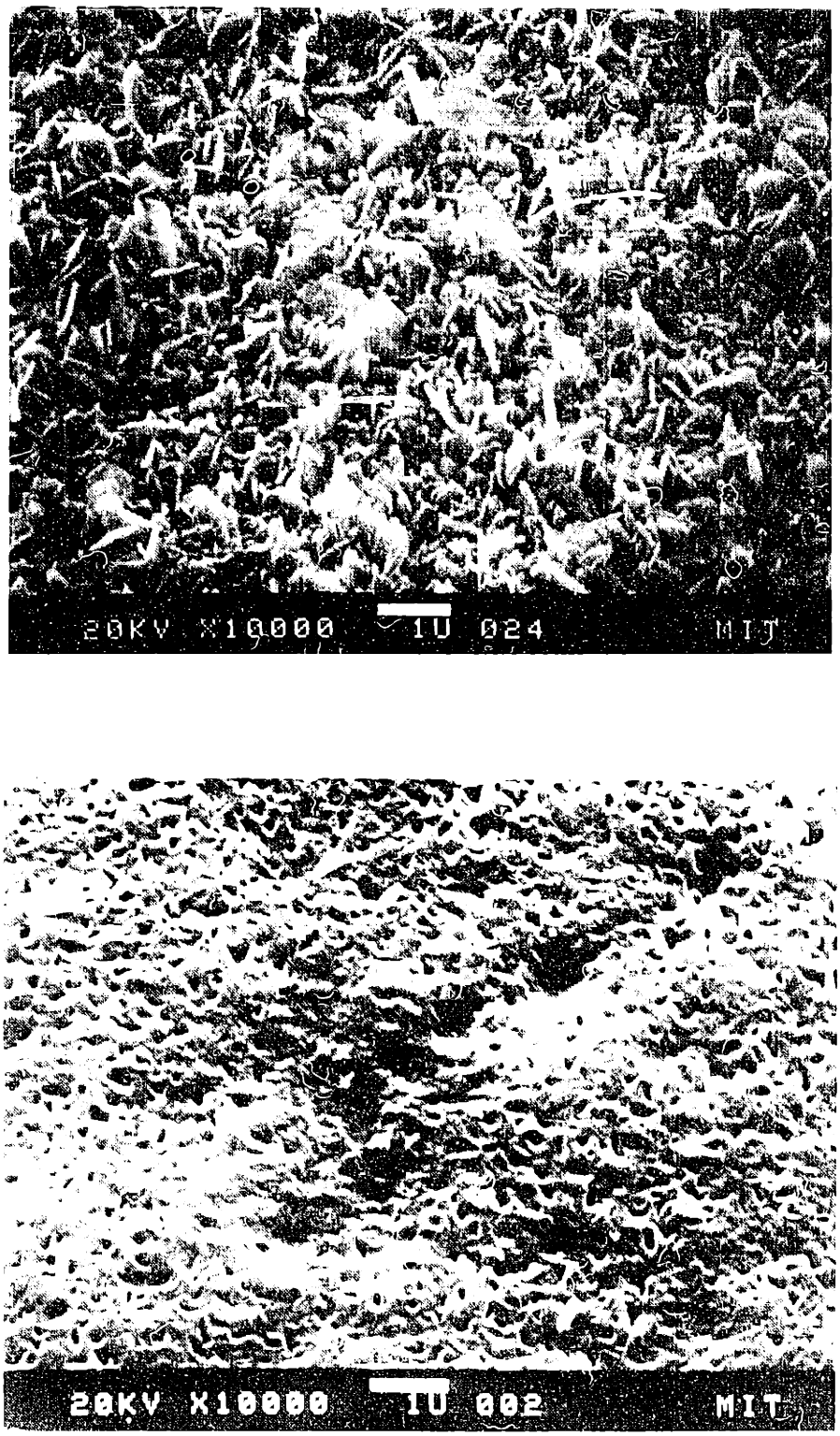

Figure 4.1.8 SEM secondary electron images of APM after oxidation at 1000°C for (a) 1hr and (b) 100hr.

Figure 4.1.8b. The pores on the surface of APM after 100hr are reminiscent of those found on the undoped FeCrAl; however, the scale on APM is flat like that observed on MA956. One interesting anomaly found on the surface of APM after 100hr is shown in Figure 4.1.9. There are only a few of these small "nests" on the entire surface but the morphology is striking. The center is a particle with a high Zr content (by EDXA). The surrounding oxide is again indicative of the metastable θ-Al_2O_3 but in this case it has been retained after 100hr at 1000°C while the majority of the scale had transformed to α-Al_2O_3 in less than 1hr.

In order to study the early stages of oxidation at 1000°C, samples of APM and MA956 were oxidized for only 12min. However, at these very short times, the blade-like morphology has not developed sufficiently to distinguish clearly between the α and θ morphologies.

4.1.3 Glancing Angle X-ray Diffraction Results

The SEM observations of APM and MA956 after oxidation at 1000°C for 1hr suggested the possibility of a different oxide phases forming on each alloy. GAXRD indicated, however, that after 1hr and 25hr exposures, both APM and MA956 formed only α-Al_2O_3. No diffraction peaks were detected for the metastable θ-Al_2O_3.

Kinetic weight gain experiments and SEM morphologies could not determine which oxide phase was formed during short exposures, and GAXRD is also hampered by the small volume of oxide formed at short times. After a 12min exposure both APM and MA956 were

Figure 4.1.9 SEM secondary electron images of APM after oxidation at 1000°C for 100hr. The central particle was identified by EDXA as Zr-rich. The surrounding blade-like oxide structure is indicative of metastable θ-Al_2O_3.

found to form predominantly α-Al_2O_3, Figure 4.1.10. This does not rule out a difference in the θ to α phase transformation on the two alloys. However, other reasons could explain the different oxide morphologies on the doped FeCrAl alloys. For instance, formation of less-noble oxides during the transient stage may result in a slightly different morphology.

In order to study the growth mechanism of θ-Al_2O_3, oxide grown on MA956 and APM at 950°C for 1hr was examined. While the thin oxide made quantification difficult, the primary θ-Al_2O_3 peak observed for these samples was larger than that for α-Al_2O_3, Figure 4.1.11.

4.1.4 Tracer Results

The sequential isotope oxidation experiments performed were actually carried out at 950±10°C in order to form the metastable θ-Al_2O_3 phase. Since θ-Al_2O_3 was not observed to form on MA956 even after only a 12min exposure at 1000°C, the temperature was reduced in the hope of forming the metastable phase. Oxidation was carried out for 15min in ^{18}O and for 45min in ^{16}O. Excessive spalling on the undoped FeCrAl prevented analysis of the scale on that alloy.

As confirmed by GAXRD, the θ-Al_2O_3 phase was sputtered through by SIMS. Figure 4.1.12 shows the sputter depth profiles for both MA956 and APM. In both cases, the second oxidant was detected most strongly near the gas surface, indicating that the scale grew mainly by the outward diffusion of Al. This confirms the work of

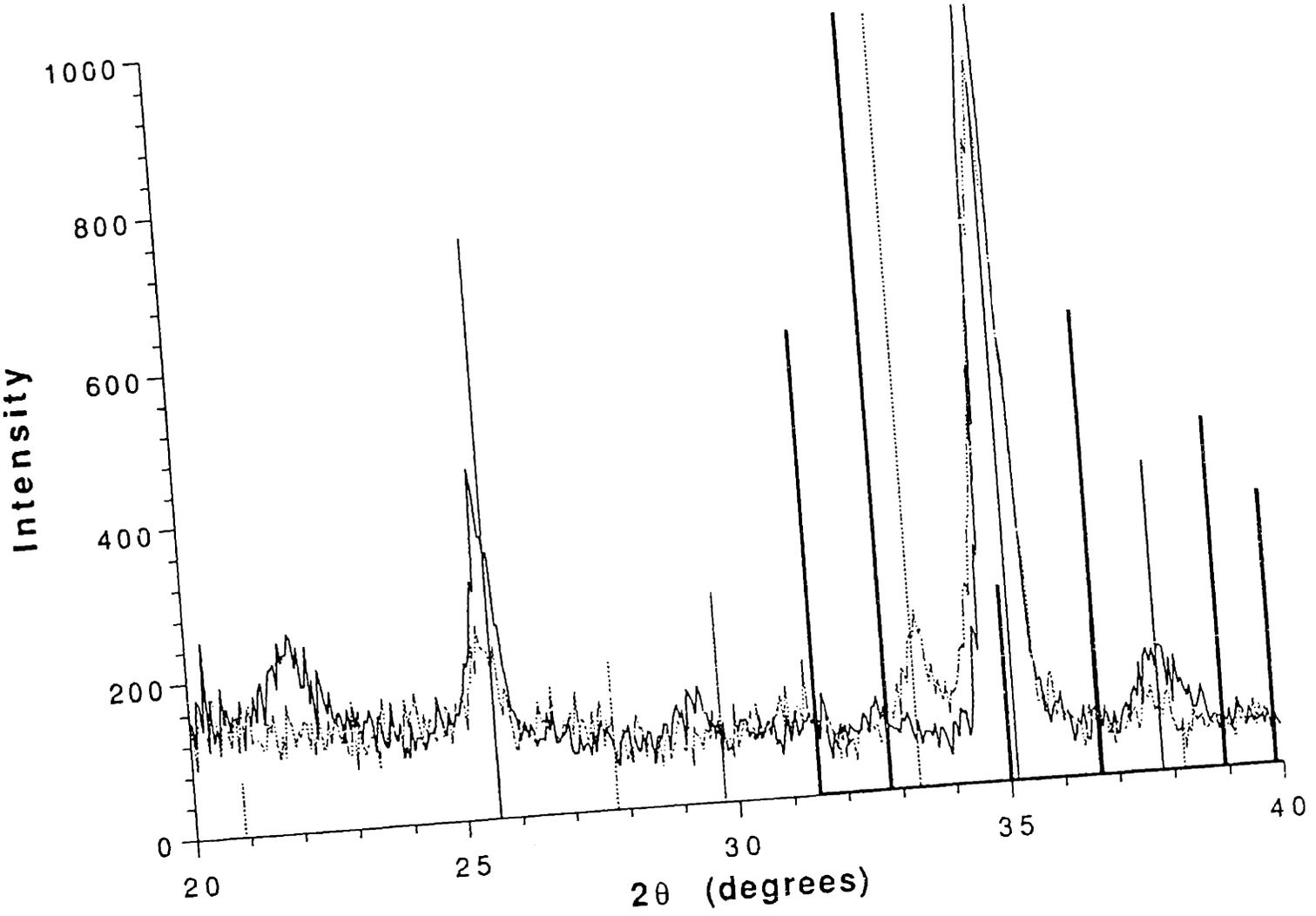

Figure 4.1.10 GAXRD profile of scales formed on MA956 (solid) and APM (dashed) after oxidation for 12min at 1000°C in 1atm O_2. The thin solid lines denote α-Al_2O_3 and the wider lines θ-Al_2O_3. No significant θ-Al_2O_3 peaks are detected in either scale. A peak in the MA956 scale profile (33.5°) matches $Y_3Al_5O_{12}$ (YAG) which is marked by the broken lines.

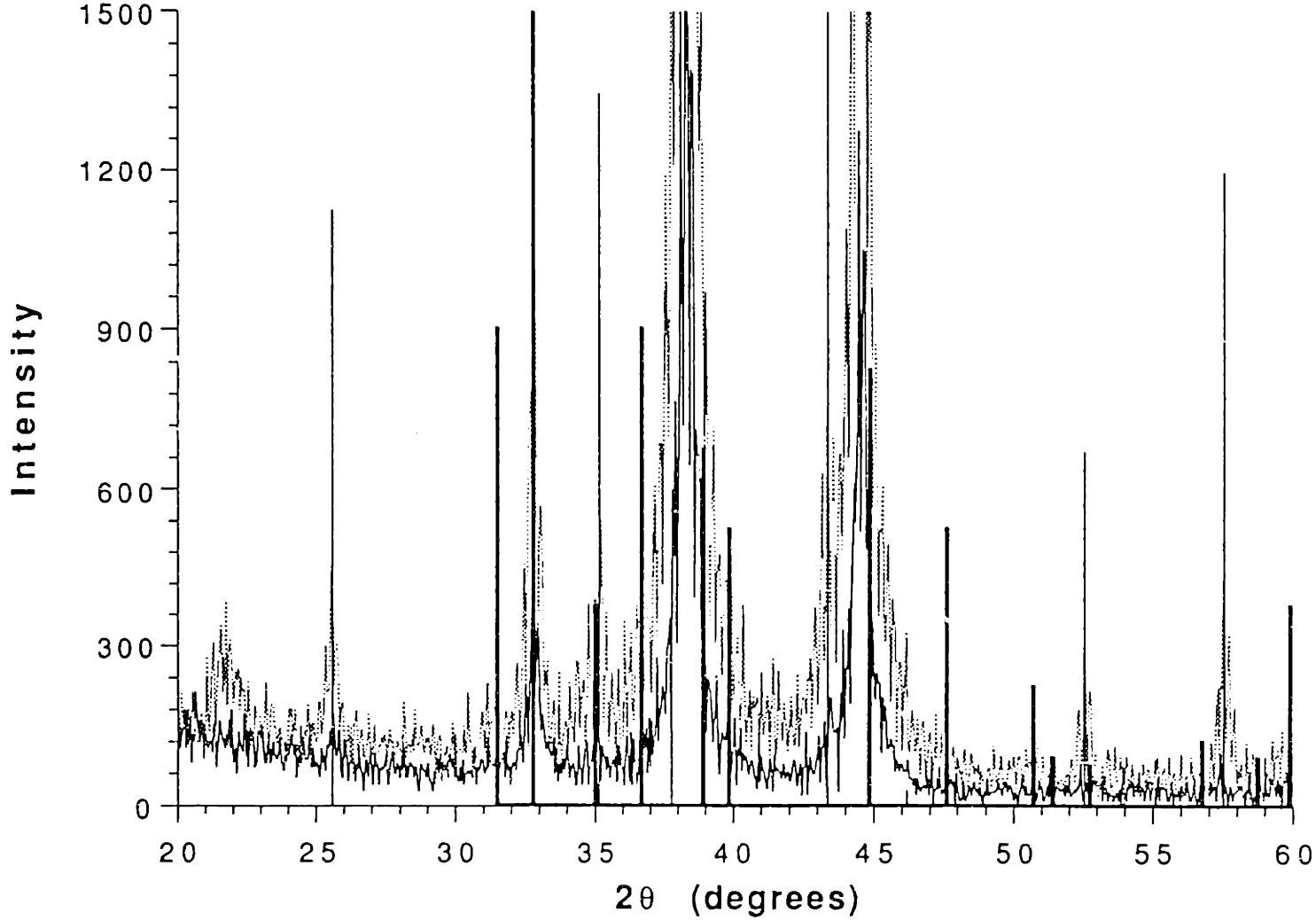

Figure 4.1.11 GAXRD profile of scales formed on MA956 (solid) and APM (dashed) after oxidation for 1hr at 950°C in 1atm O_2. The thin solid lines denote α-Al_2O_3 and the wider lines θ-Al_2O_3. In both scales, the θ peaks are larger than the α peaks.

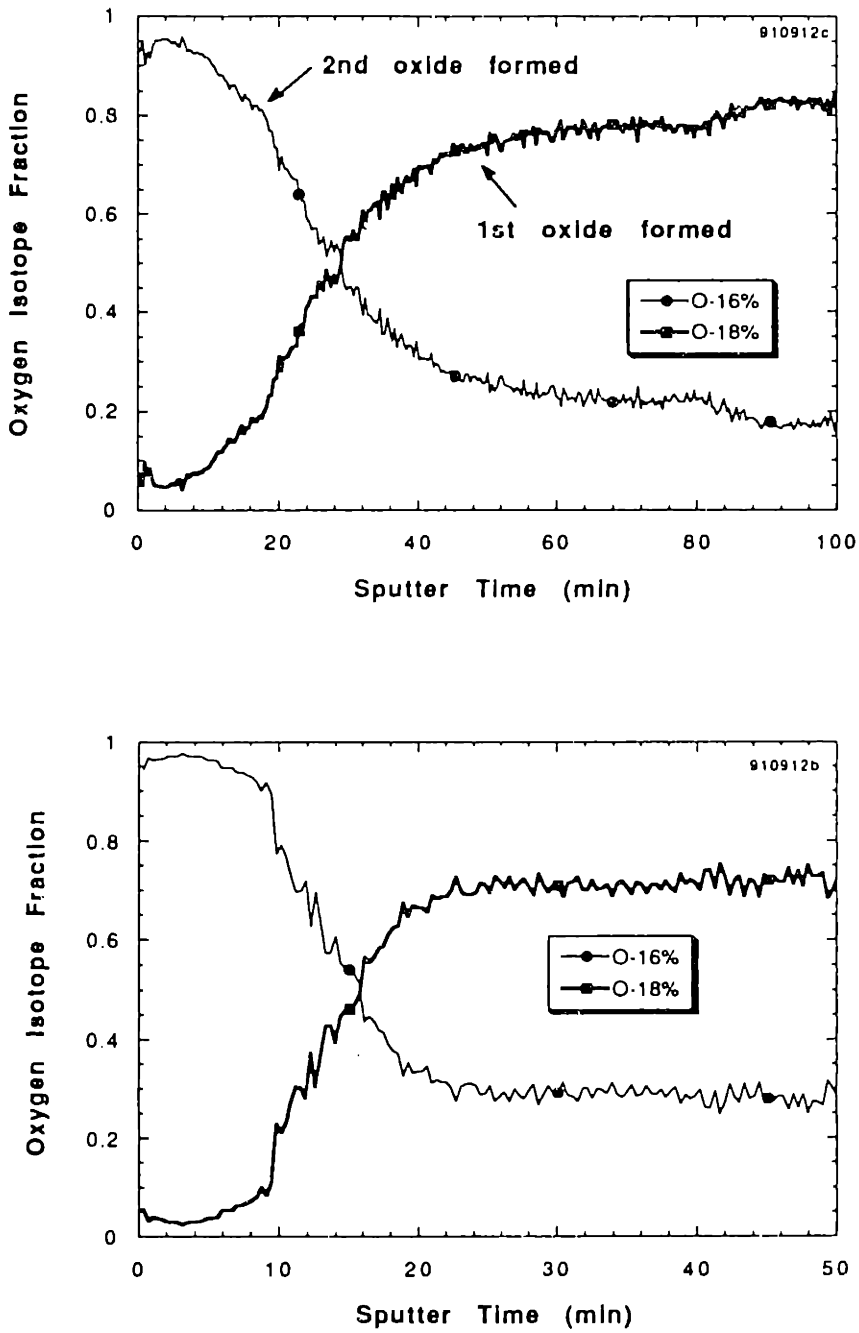

Figure 4.1.12 SIMS sputter depth profiles of the primarily θ-Al_2O_3 scale formed after oxidation for 15min in ^{18}O and 45min in ^{16}O at 950°C on (a) MA956 and (b) APM. The second oxidant ^{16}O is found primarily near the surface indicating that the scale grows primarily by the outward diffusion of Al.

van Manen, et al. [1987] that also observed θ-Al_2O_3 growing by outward transport using NRA.

4.1.5 AEM Results

As mentioned in the introduction to this chapter, previous work on MA956 had detected the segregation of Y to the oxide grain boundaries [Przybylski, et al., 1987] and to the alloy-oxide interface [Katz, et al., 1987]. A few additional observations were made of the scale on undoped FeCrAl and on APM in order to confirm the analogous segregation of Zr to the oxide grain boundaries.

Due to the excessive spallation on undoped FeCrAl, only small pieces of oxide were left after a 100hr oxidation. These pieces were placed on a Cu grid and ion thinned from both sides to look at the center of the oxide scale. Figure 4.1.13 shows the numerous voids observed in the scale. The voids are observed both on grain boundaries and within grains and they are not evenly dispersed. Some areas contain no voids while others contain a large volume fraction. In thick areas of the sample, the voids were never seen to extend through the entire sample thickness. This indicates that no single void provides a long range pathway for material transport. However, networks of voids may exist. No elements were found to segregate to the oxide grain boundaries in this sample and no Rh particles were observed.

The α-Al_2O_3 scale formed on APM after 100hr was examined in parallel sections near both alloy and gas interfaces. In these sections, only a few voids were observed on the entire sample.

Figure 4.1.13 STEM bright field image of the scale on undoped FeCrAl after oxidation at 1000°C for 100hr. Parallel section near the center of the scale. Numerous voids are apparent.

Figure 4.1.14 STEM bright field image of the scale near the gas interface on APM after oxidation at 1000°C for 100hr. The arrows mark Rh particles on the grain boundaries. Few voids are observed.

Figure 4.1.14 shows the oxide near the gas interface. The small dark spots in this bright field image are Rh particles from the evaporation of the hangdown wire. These particles are not observed near the alloy interface. Both locations had essentially equiaxed grains, but the grain size was noticeably different. The average grain size was 180nm near the gas interface and 360nm near the alloy, Table 4.1. While the coarser grains near the alloy may suggest that these grains were grown first and coarsened, it could also reflect preferred orientation in an inward direction such as in solidification.

In both areas, Zr was found to segregate preferentially to the oxide grain boundaries. The segregation level was relatively low except on boundaries near a ZrO_2 particle where the Zr/Al ratio was much higher. There was a higher average Zr/Al ratio (0.017) near the alloy interface than the gas interface (0.006), but comparing these values is difficult. Variations in sample thickness can cause changes in this ratio. The average Zr/Al value at 1000°C is given in Table 4.2. This table also includes the Y/Al and Ti/Al ratios for MA956 at 1000°C from Przybylski's work. Two differences are noted: since the alloy contains little Ti relative to MA956 (0.03 vs. 0.36wt%), no Ti segregation is detected; and, with a smaller amount of Zr (0.1%) compared to Y (0.5%) and a coarser oxide distribution in the alloy, there are fewer RE-rich oxide particles in the oxide but only slightly less segregation. Equivalent amounts of segregation are consistent with the oxidation kinetics which show no difference in the oxidation rates of the two materials.

Table 4.1 Al_2O_3 scale average grain size after oxidation of FeCrAl alloys for various times. The technique used to measure the grains is listed along with the approximate location within the scale.
* from Przybylski, et al. [1987].

Temperature/ Location	APM (μm/time)	MA956 (μm/time)	FeCrAl (μm/time)
1000°C near alloy	0.36/100h TEM	0.5/100h TEM*	
center			
gas	0.18/100h TEM	0.20/100h SEM	0.35/100h SEM
1200°C near alloy			1.2/50h SEM
center			0.9/50h TEM
gas	0.6/100h TEM	0.24/50h SEM	0.6/50h SEM
1400°C near alloy			
center	1.1/1h SEM		
gas		1.1/1h SEM	3.0/1hr SEM

Table 4.2 Apparent EDXA weight percentage ratios on Al_2O_3 grain boundaries in scales grown on APM and MA956. †Data for MA956 at 1000°C from Przybylski, et al. [1987].

Temperature	APM: Zr/Al	MA956: Y/Al	MA956: Ti/Al	MA956: Y/Ti
1000°C	0.012	0.014†	0.037†	2.643
1200°C	0.130	0.049	0.071	1.431
1400°C	- -	0.017	0.003	0.184

Analysis of a parallel section of APM oxidized for 0.2hr revealed the formation of a mixed phase oxide scale, mainly Cr-rich but with nodules of Al_2O_3. No grain boundaries were adequate for observation. Again, this transient oxidation behavior is probably indicative of the coarser RE oxide distribution - in areas with less Zr, transient oxides predominate.

A transverse section was also made of the scale on APM after oxidation for 0.2hr. In some areas the scale was ≈200nm thick but the gas interface was always smooth, with no signs of oxide blades or pores. Based on the SEM surface morphologies, this suggests that the outermost scale was milled away. From EDXA, the scale was rich in Al but also contained significant quantities of Cr and Fe. Unfortunately, the thickness across the sample was not uniform - thinner near the gas interface and thicker near the alloy. Thus there was no way to quantify the composition of the oxide. The significant (up to 70wt%) Cr and Fe content in the scale may indicate that the initial scale morphology on APM is more effected by the formation of transient (Fe- and Cr-rich) oxides than by the θ-α-Al_2O_3 phase transformation. The same may be true for the undoped FeCrAl which had a similar morphology as APM.

The metal-oxide interface was also examined in two locations where it was sufficiently thin. The Zr content was higher on the interface than on either side. However, in this case because of the low Al content in both the alloy and the oxide, a realistic Zr/Al ratio could not be calculated which would be comparable to the values in Table 4.2.

4.2 Results at 1200°C

The improvement in oxide adherence is probably the most significant effect of the RE addition at 1200°C. Thus, cyclic experiments were conducted in order to study this effect. At 1200°C, the stable α-Al_2O_3 phase is the dominant oxidation product; thus the role of the phase transformation is diminished, and little GAXRD analysis was necessary.

4.2.1 Isothermal Oxidation Results

Isothermal kinetic results are shown in a parabolic plot, Figure 4.2.1. Both with and without a reactive element, a general parabolic behavior is observed. As at 1000°C, there was excellent repeatability for the undoped FeCrAl; however, no breakdown events were observed at this temperature. Depending on the curve used, there is a 2-4 times reduction in the parabolic rate constant with the addition of a RE.

After the isothermal exposure, the scale on the undoped FeCrAl spalled almost completely. No spallation was noted on the alloys with a RE addition. Further testing was done to better assess the adherence.

4.2.2 Cyclic Oxidation Adherence Results

Compared to the change in the oxidation rate, the improvement in adherence by the addition of the RE is the more pronounced REE at 1200°C. A plot of the weight change versus number of cycles is

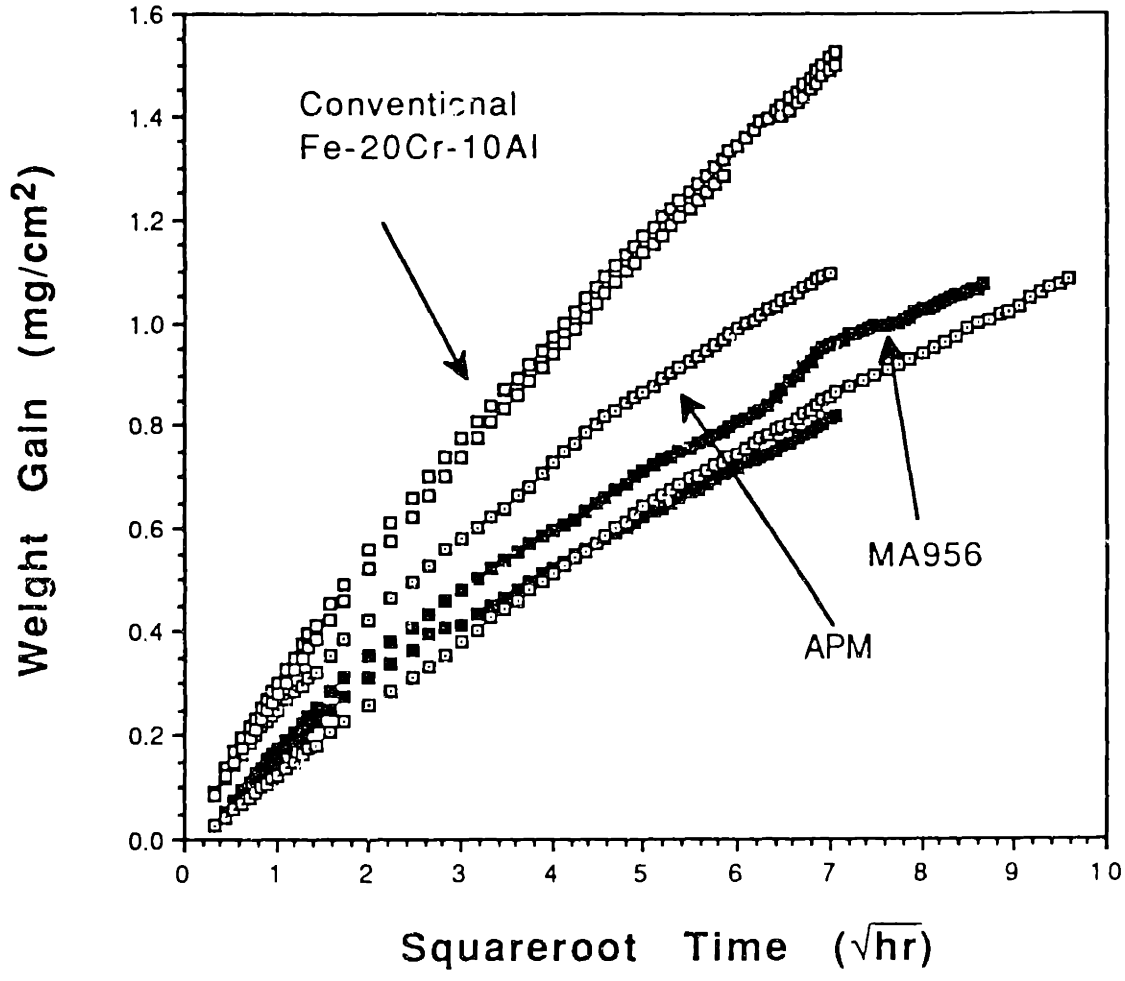

Figure 4.2.1 Parabolic plot of weight gain versus squareroot of time for FeCrAl alloys at 1200°C in 1atm O_2.

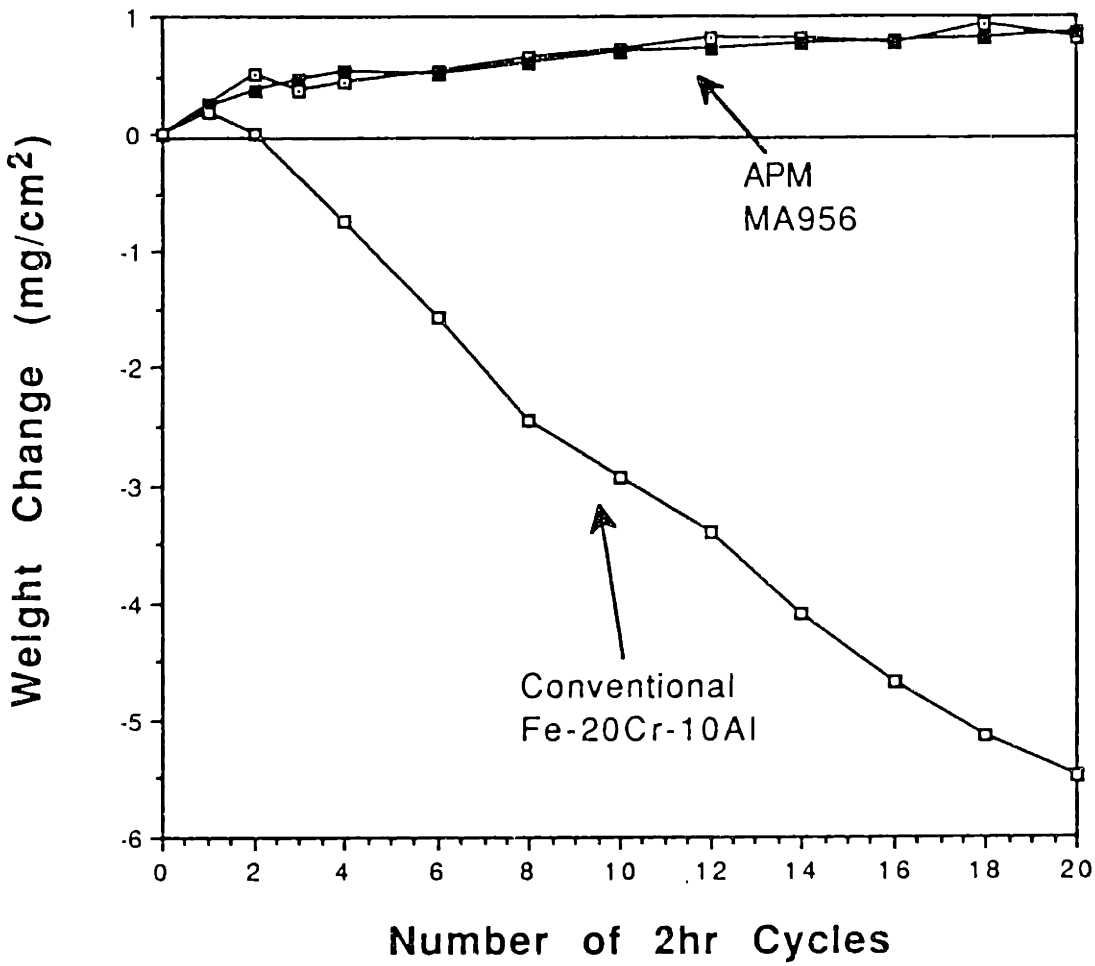

Figure 4.2.2 Isothermal weight gains plotted with the weight change over 20 2-hr cycles at 1200°C in 1atm O_2. Both alloys with a RE addition show nearly perfect oxide adherence.

shown in Figure 4.2.2. Both APM and MA956 show nearly perfect adherence, while the undoped FeCrAl exhibits massive scale exfoliation. Based on the isothermal measurements, the thickness of the oxide on the doped and undoped material is not significantly different. Thus, an argument based on increased stresses from a thicker scale would not seem to apply in this case.

4.2.3 SEM Results

Since all of the scale spalled off the undoped FeCrAl at 1200°C, it was not possible to examine the scale on the alloy. Instead a piece of oxide was mounted perpendicular to the beam and tilted to examine the gas and alloy interfaces and the cross-section. Figure 4.2.3 shows the cross-sections of the scale on undoped FeCrAl after oxidation for (a) 2hr and (b) 50hr. As at 1000°C, the scales here are also buckled. The more striking feature at 1200°C is the high density of whiskers on the surface, especially after 50hr, Figure 4.2.4a. The alloy side of the oxide was relatively smooth and featureless, Figure 4.2.4b.

The oxide on the commercial FeCrAl alloys was much more adherent and had fewer features. One significant difference between the two RE-doped alloys was the effect of the alloy on the oxide morphology. On APM after a 2hr exposure, remnants of the alloy grain structure could be seen clearly, as well as after 100hr, Figure 4.2.5. At higher magnification these features appeared to be simply thicker oxide growing on particular grains, Figure 4.2.6a. The overall morphology was reminiscent of the structure at 1000°C with

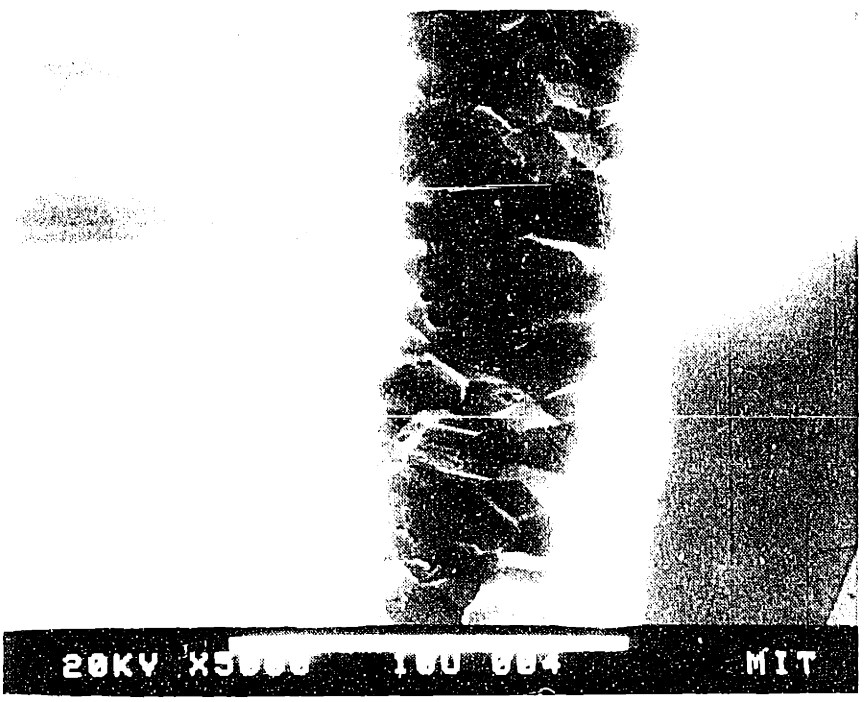

Figure 4.2.3 SEM secondary electron images of undoped FeCrAl after oxidation at 1200°C for (a) 2hr and (b) 50hr.

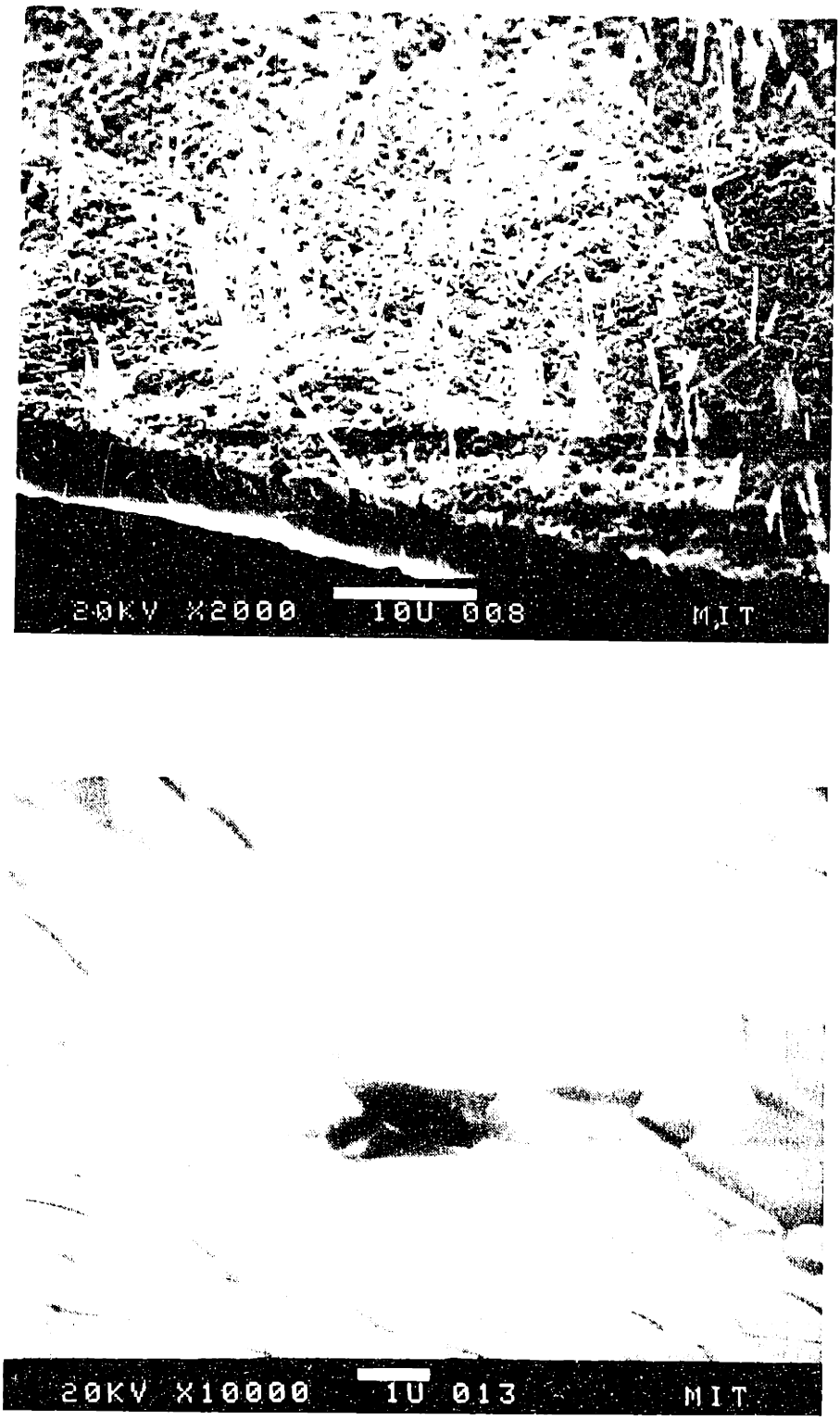

Figure 4.2.4 SEM secondary electron images of undoped FeCrAl after oxidation at 1200°C for 50hr. Morphologies of the (a) gas interface and (b) alloy interface.

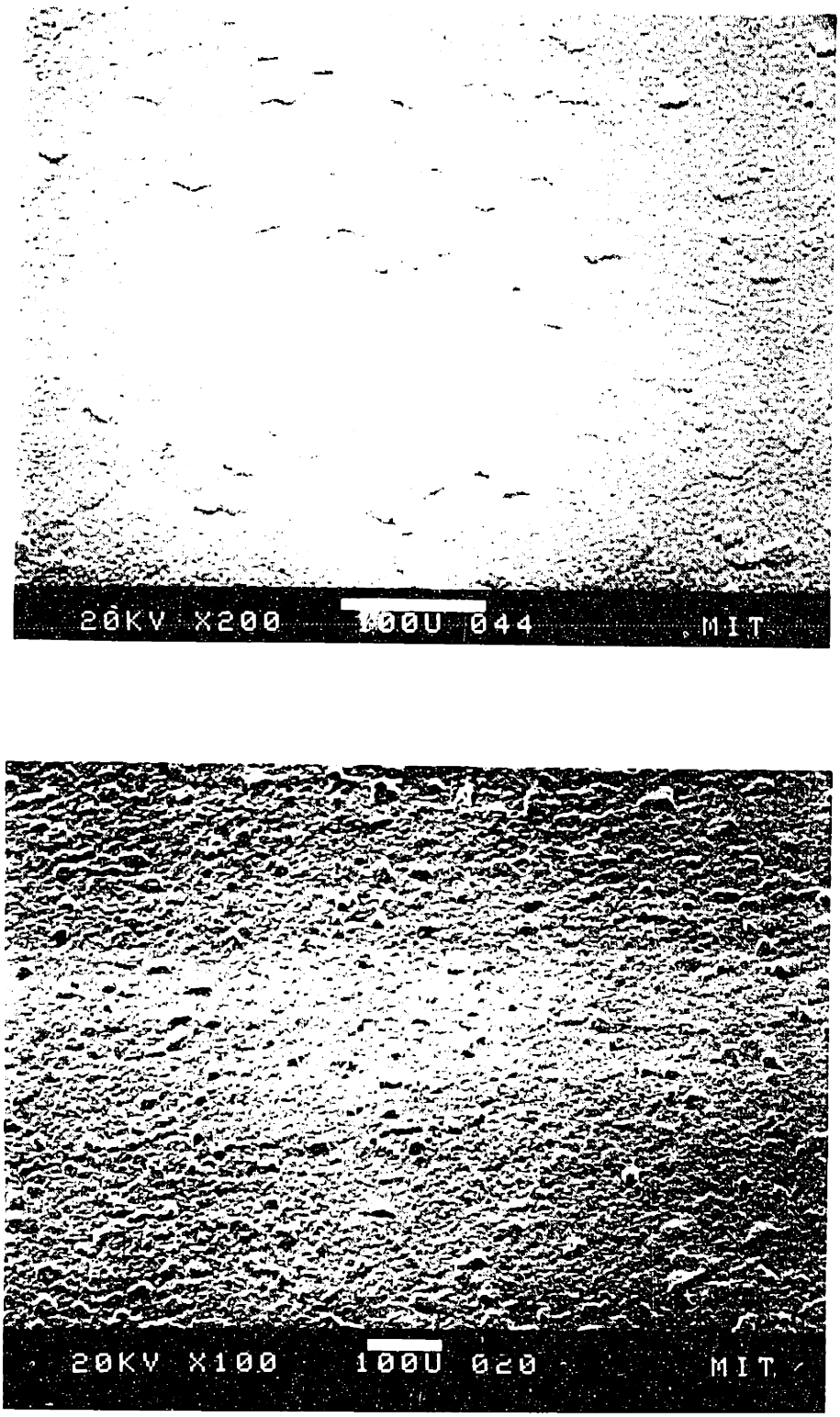

Figure 4.2.5 SEM secondary electron images of APM after oxidation at 1200°C for (a) 2hr and (b) 100hr. The features at each time correspond to the alloy grain size.

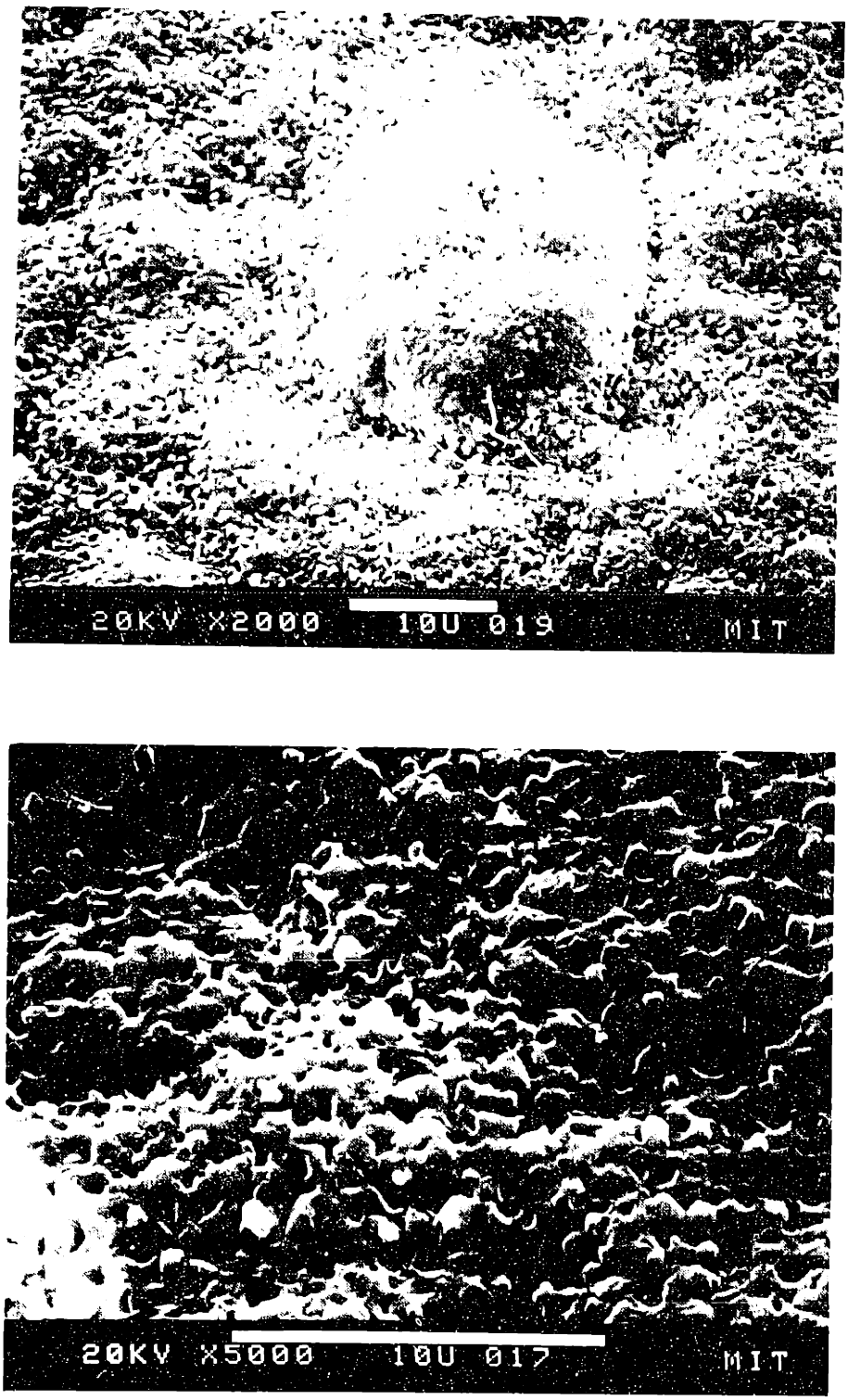

Figure 4.2.6 SEM secondary electron images of APM after oxidation at 1200°C for 100hr.

a coarser pore/grain size. At the edge of the sample is the only area where spallation occurs, revealing the oxide cross-section, Figure 4.2.7. Compared to the undoped FeCrAl cross-section in Figure 4.2.3b, the scale on APM appears to be more columnar in nature.

The columnar structure is also observed on MA956. However, the surface morphology on MA956 is very different. The scale on MA956 is uniformly flat and not visibly affected by the alloy microstructure, except for the sprinkling of larger grains, Figure 4.2.8. These may be remnants of the initial heterogeneous nucleation caused by the oxide dispersion in the alloy. At higher magnification, grain growth is again observed between 2hr and 50hr exposures, Figure 4.2.9.

A study was also made of the scale on MA956 after cyclic testing. The only oxide spallation observed was at the sample edges. However, at higher magnification the oxide was observed to be cracked throughout, Figure 4.2.10. While this may be the precursor to long term breakdown, it did not cause any significant failure after 20, 2hr cycles. Scale cracking on APM appeared to be concentrated on those areas of thicker oxide growth, as observed in isothermal exposures, Figure 4.2.6a.

4.2.4 Tracer Results

Sequential isotope oxidation experiments were performed on each of the three FeCrAl materials at 1200°C. The more adherent oxides on MA956 and APM were more easily examined than the spalled oxide on undoped FeCrAl. Figure 4.2.11a shows the depth

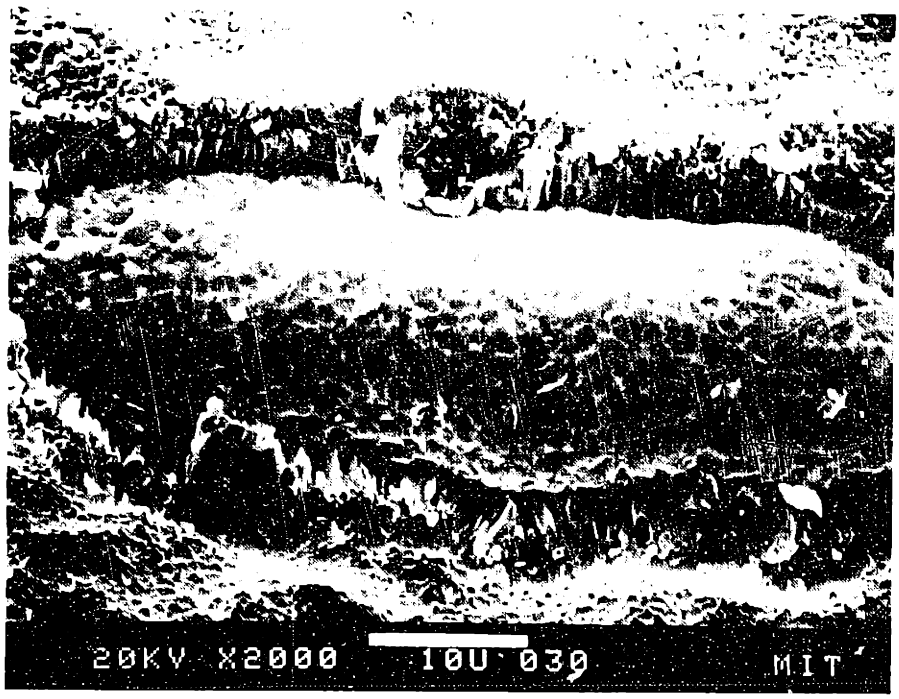

Figure 4.2.7 SEM secondary electron images of APM after oxidation at 1200°C for 100hr. The oxide has spalled away at the edge of the sample revealing the columnar structure of the oxide

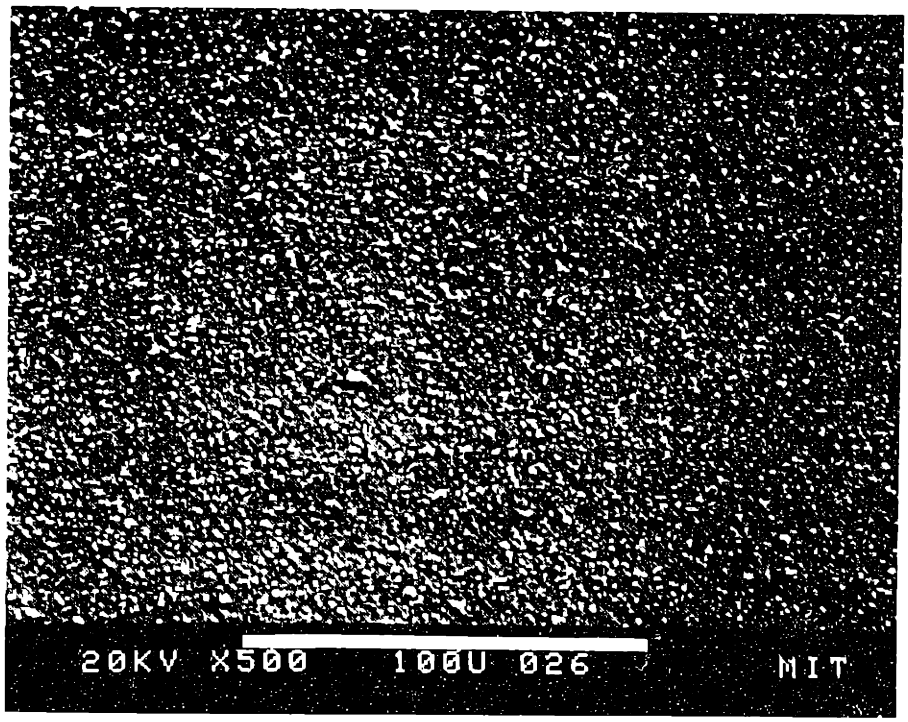

Figure 4.2.8 SEM secondary electron images of MA956 after oxidation at 1200°C for 50hr.

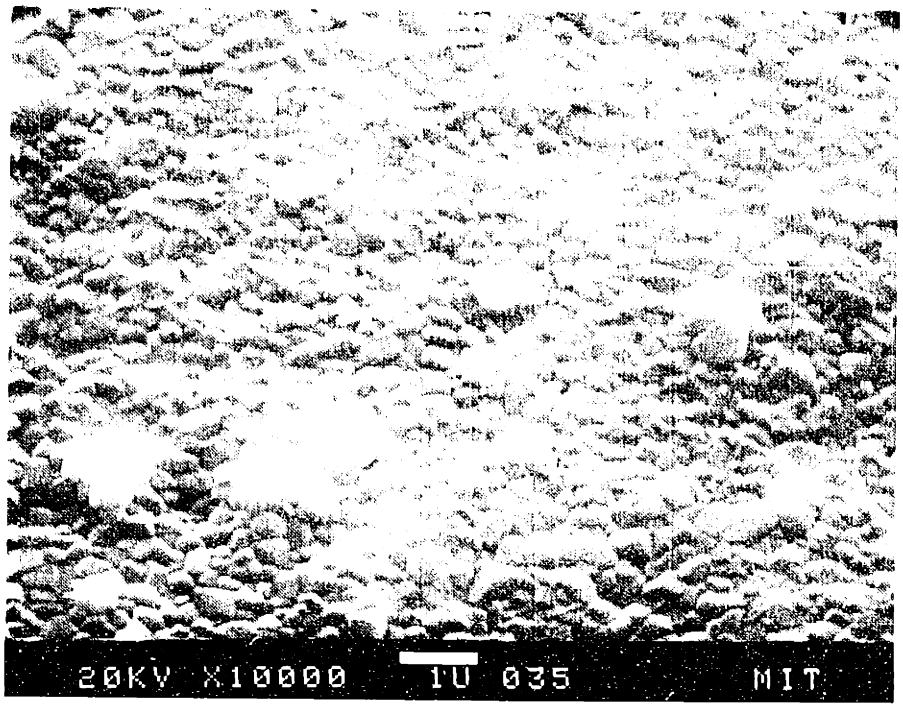

Figure 4.2.9 SEM secondary electron images of MA956 after oxidation at 1200°C for (a) 2hr and (b) 50hr.

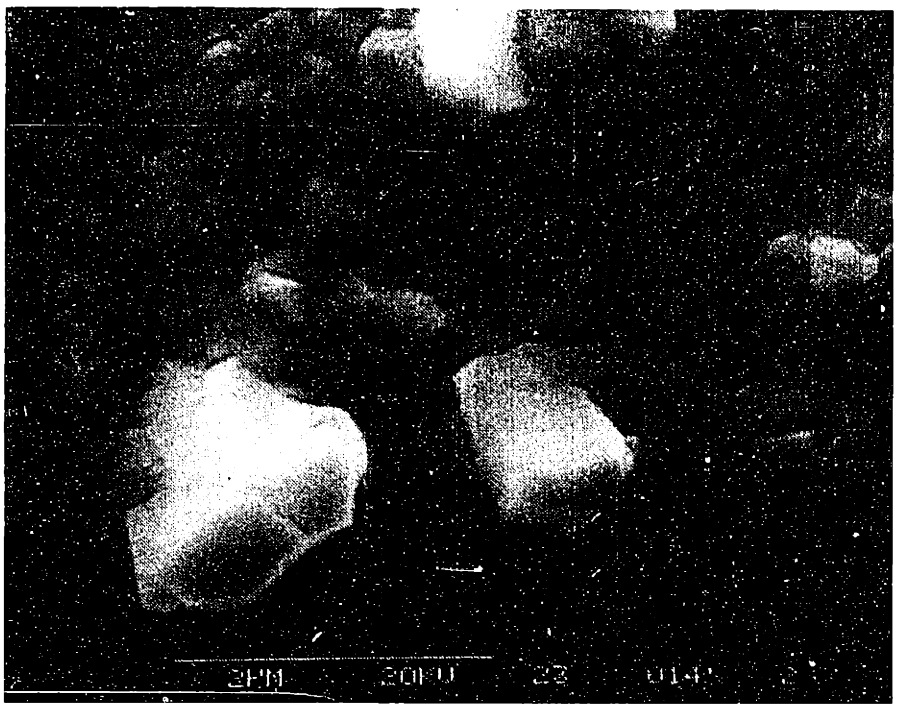

Figure 4.2.10 SEM secondary electron images of MA956 after oxidation at 1200°C for 20, 2hr cycles.

profile of the oxide formed on MA956 after 15min in ^{16}O and 5min in ^{18}O. Two areas of ^{18}O enrichment are noted - first a very sharp peak at the surface and a second weaker but wider area near the alloy interface. Although it could be anomalous, the first peak could imply a small amount of lattice diffusion of the second oxidant. The second peak, which represents the most heavily concentrated area of ^{18}O in the scale, is the hallmark of a predominant inward oxidation mechanism. The location of the peak also indicates oxygen diffusion via short-circuit pathways (see Figure 2.6). This ^{18}O peak compromises less than 50% of the total oxygen signal at that depth, probably due to the short exposure time and crater effects after an extended sputtering time. A similar profile was found for APM.

The scale formed on the undoped FeCrAl was again difficult to analyze because of the nearly complete spallation. In a few cases, sputtering the scale appeared to cause the scale to flake off of the substrate. One complete sputter profile appeared to indicate that the first oxidant ^{18}O was located at the center of the scale while new oxide (^{16}O) formed both at the gas and alloy interfaces, Figure 4.2.11b. This profile could not be repeated, but it correponds well to the profiles found for the scale on undoped NiAl (see Section 5.2.5). Further attempts to characterize this scale included placing large pieces of spalled oxide $\approx 20mm^2$ in area on a stub. However, no sensible data could be acquired.

Thus, unlike the θ-Al_2O_3 phase described in Section 4.1.4, the doped α-Al_2O_3 scale formed on MA956 at 1200°C forms by short-circuit oxygen diffusion. Also, the undoped α-Al_2O_3 appears to grow

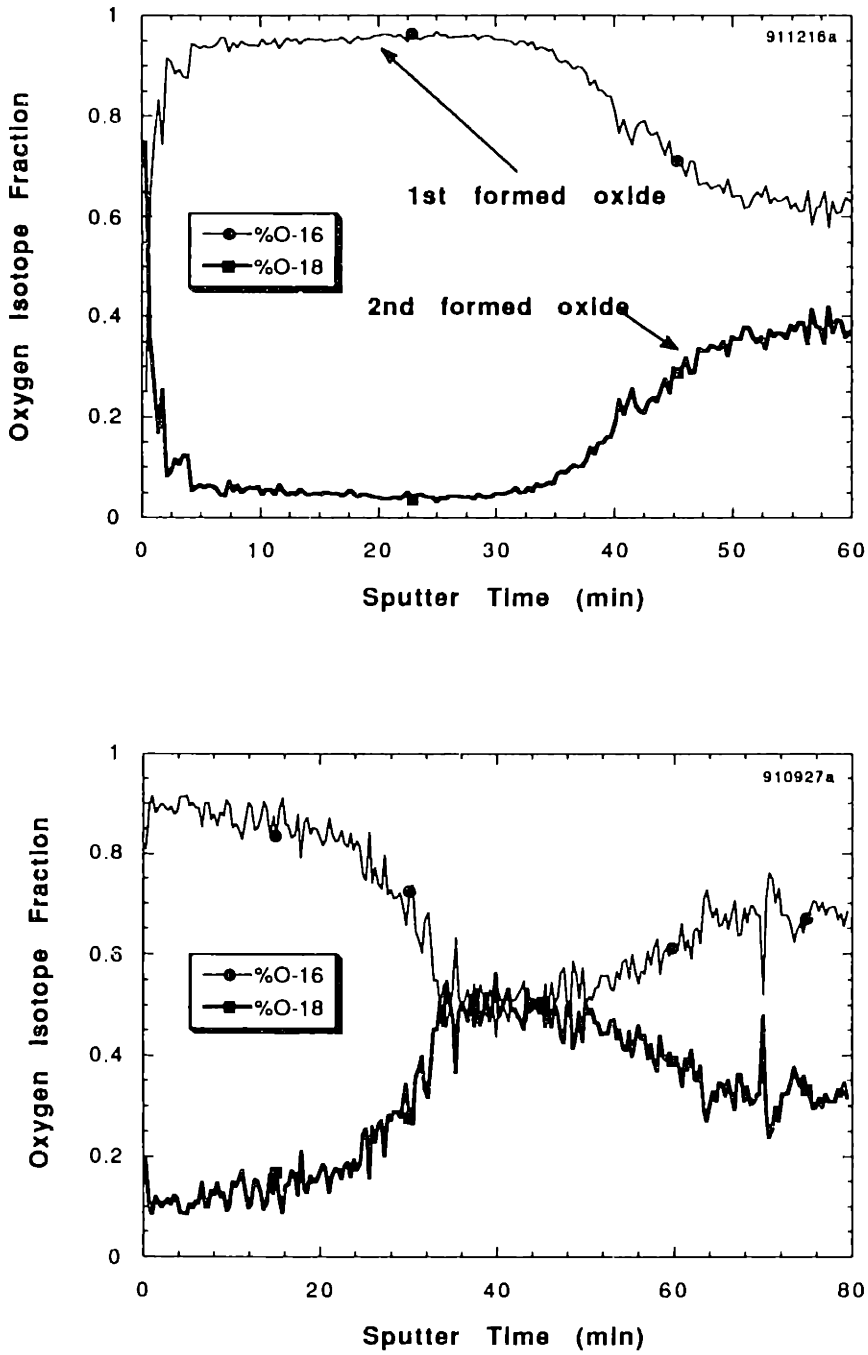

Figure 4.2.11 SIMS sputter depth profiles of the primarily α-Al_2O_3 scale formed after oxidation at 1200°C on (a) MA956 oxidized for 15min ^{16}O and 5min ^{18}O and (b) FeCrAl oxidized for 10min ^{18}O and 30min ^{16}O.

by a different mechanism with both Al and O diffusing simultaneously.

4.2.5 AEM Results

Again, due to the massive spallation, study of the oxide formed on undoped FeCrAl proved difficult. The only possibility for TEM study was to ion thin a piece of the spalled oxide. Figure 4.2.12 shows a thin area near the center of the oxide formed after 50hr. Many of the larger grains contain a void in their centers.

The first test of the segregation theory for this study was made on a short exposure of MA956 for 25hr in air at 1200°C. The EDXA x-ray map from the STEM is shown in Figure 4.2.13. Both Y and Ti are observed to segregate strongly to the oxide grain boundaries, Table 4.2. A more controlled exposure for APM was then used to achieve the same result after 100hr in O_2, Figure 4.2.14. The only boundary where the segregation is not clear is the boundary in the lower left corner which is not parallel to the beam, thus making analysis difficult. The segregation of Ti is not detected in scales grown on APM because of the low Ti content in the alloy.

A transverse section of APM was made to check if Zr would also segregate to the alloy-oxide interface. Figure 4.2.15 is a schematic showing the apparent EDXA weight percentage ratios across the interface in two separate locations. In this case, Ti is found to segregate as in MA956. A questionable S peak (possibly Mo contamination, see section 3.7.1) was apparent in several spectra,

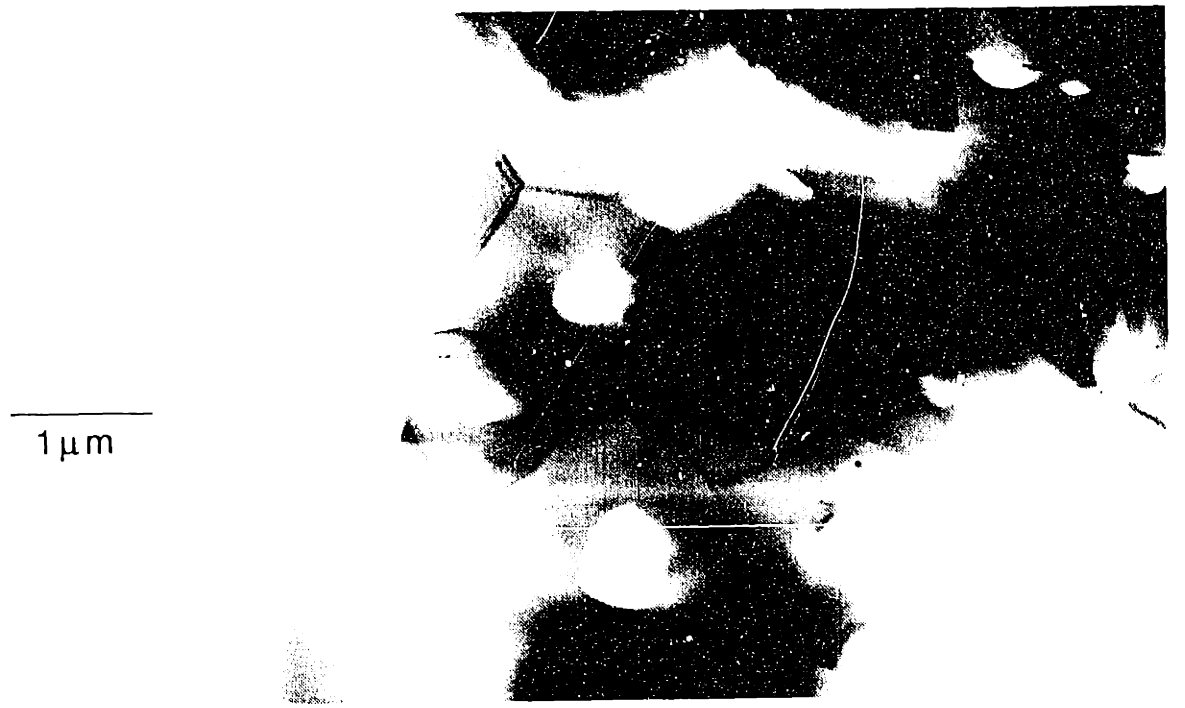

Figure 4.2.12 STEM bright field image of the oxide formed on undoped FeCrAl after oxidation for 50hr at 1200°C. A large void is found in the center of many grains.

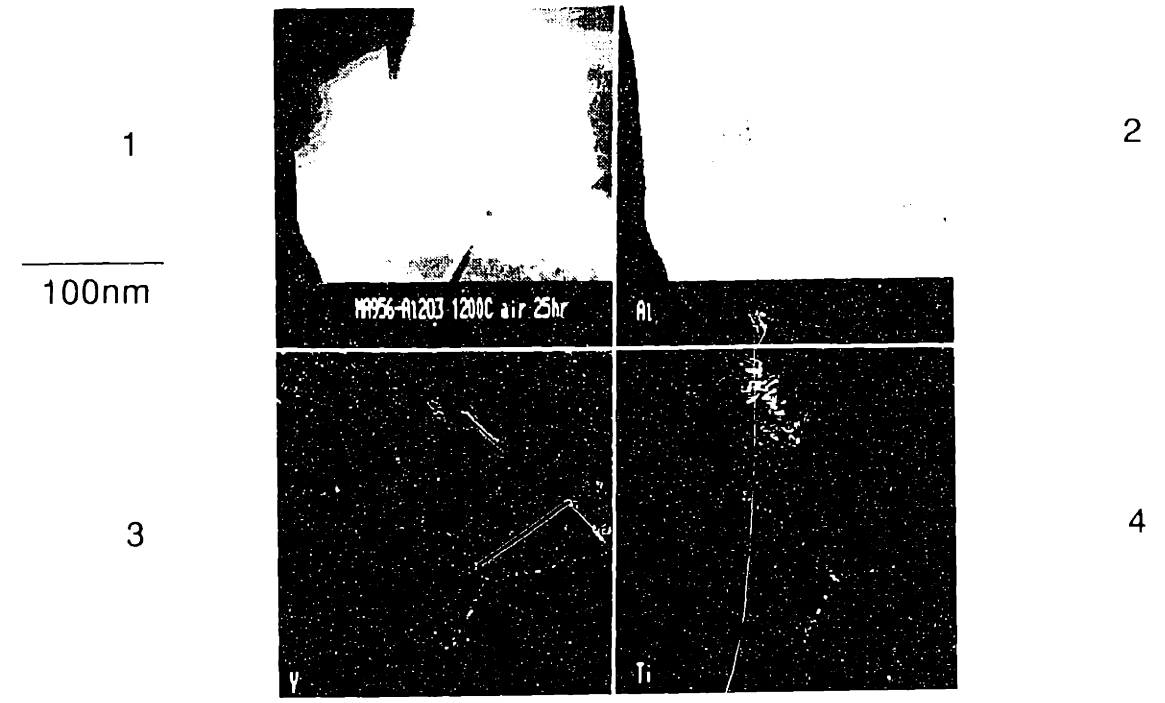

Figure 4.2.13 STEM high resolution X-ray map of Al_2O_3 formed on MA956 near the oxide-gas interface after 25hr at 1200°C; 1) the binary image, and X-ray maps of 2) Al, 3) Y, and 4) Ti.

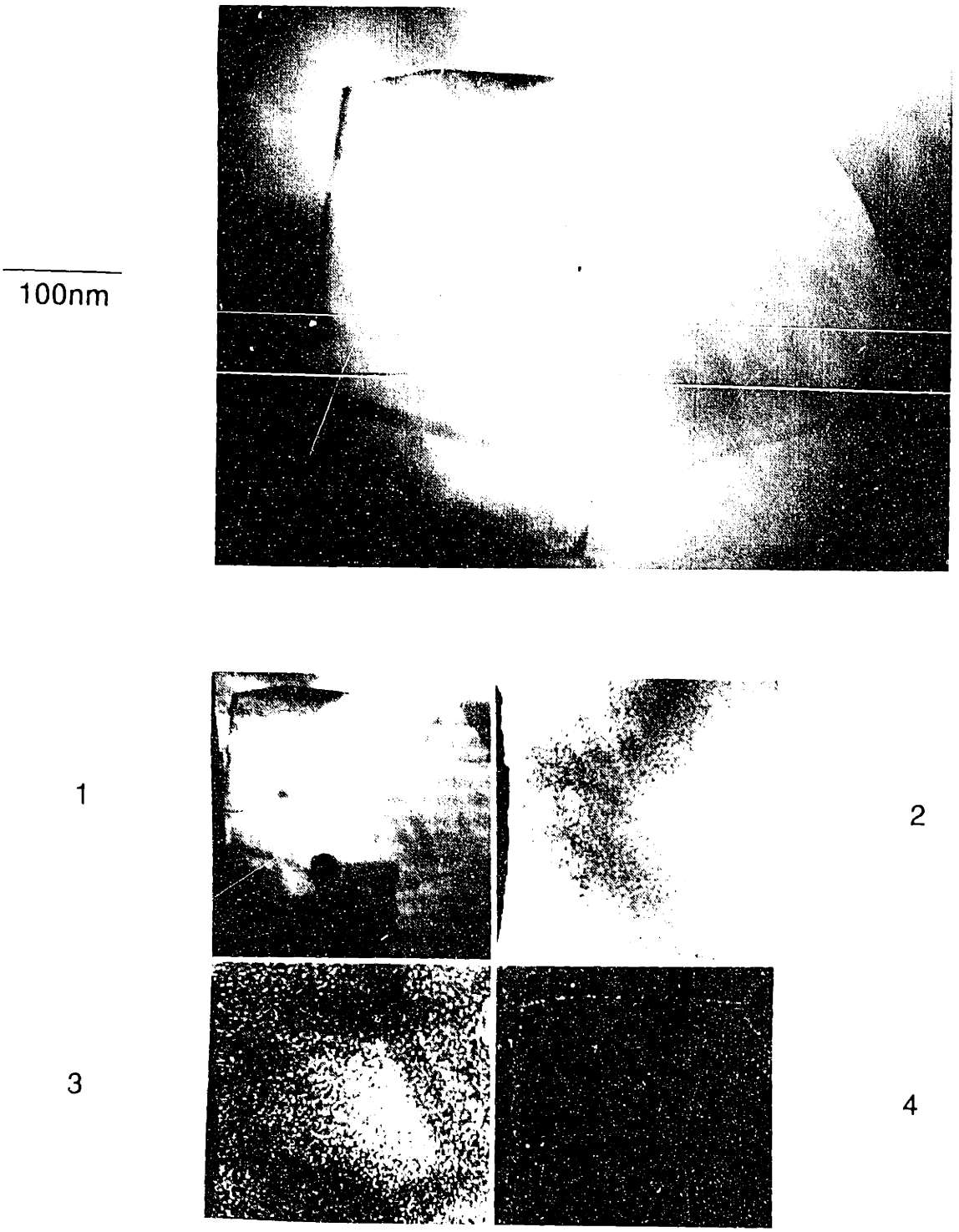

Figure 4.2.14 STEM (a) bright field image and (b) high resolution X-ray map of Al_2O_3 formed on APM near the oxide-gas interface after 100hr at 1200°C; 1) the binary image; X-ray maps of 2) Al, 3) Cr, and 4) Zr.

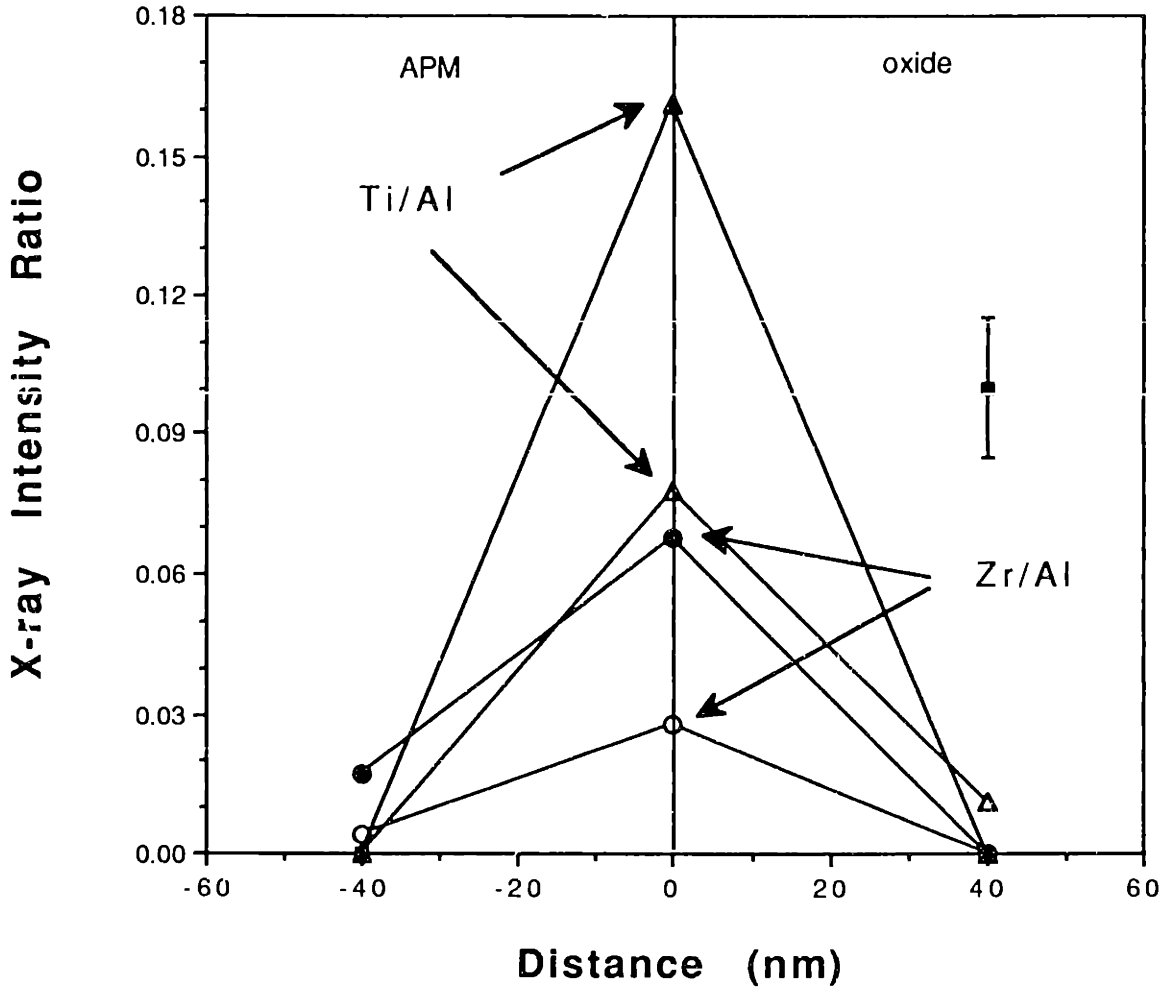

Figure 4.2.15 Plot of the apparent EDXA weight percentage ratios for Ti and Zr across the alloy-oxide interface after oxidation for 100hr at 1200°C. Ti is found to segregate more strongly than Zr. The filled and open symbols represent two separate analysis points.

but it appeared to be stronger in the alloy and thus not to have segregated to the interface in the same way as Ti and Zr.

4.3 Results at 1400°C

A broader range of experiments was performed at 1400°C after the discovery of TiN_x particles near the oxide-gas interface in the scale on MA956. These particles are believed to cause cracking within the oxide, but not catastrophic spallation [Pint, et al., 1992]. No sequential isotope oxidation experiments were done at 1400°C.

4.3.1 Isothermal Oxidation Results

The kinetic data are plotted in Figure 4.3.1. Just as for the data at lower temperatures, a parabolic rate law is followed. However, unlike at lower temperatures, the scale on MA956 appeared to spall after isothermal oxidation for 25 and 75hr at 1400°C. Based on the kinetic data, this spallation occurred during cooldown. After oxidation for only 1hr, MA956 showed no signs of spallation. APM was oxidized for 25 and 50hr and, while it oxidized at a similar rate, it showed no signs of spallation. The undoped FeCrAl exhibited various behaviors. The sample with the higher weight gain was much thinner than the other. Most likely, it became depleted in Al and began to form less noble oxides, increasing the weight gain. The other sample appeared to form a more uniform scale. In comparison with the doped alloys, this sample had a slightly higher weight gain, but less than a factor of 2 difference on average. The undoped FeCrAl appeared to spall after the isothermal oxidation more

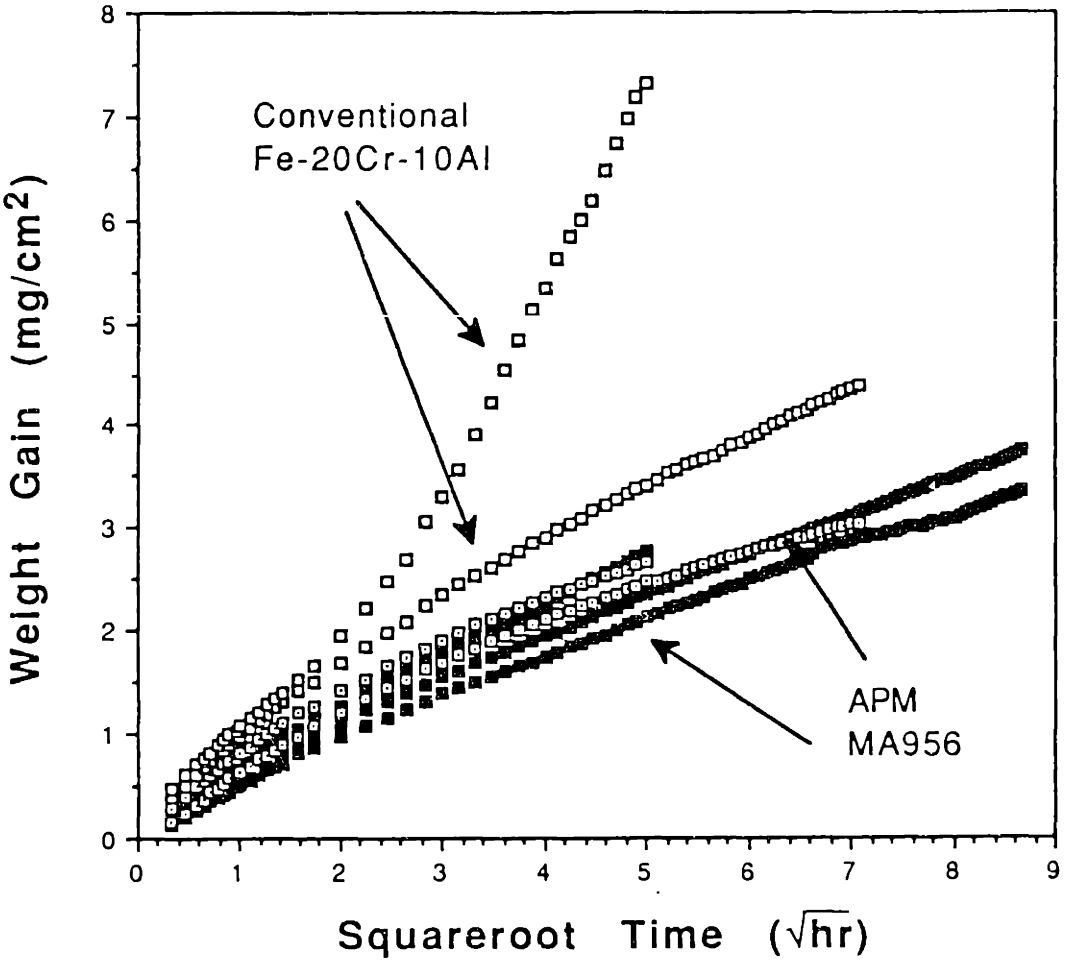

Figure 4.3.1 Parabolic plot of weight gain versus squareroot of time for FeCrAl alloys at 1400°C in 1atm O_2.

severely than MA956. Surprisingly though, the spallation at 1400°C was not as severe as at 1200°C. Only localized spallation occurred, rather than the entire scale breaking off, as at 1200°C.

In order to study the possible sources of nitrogen in the scale (for the formation of TiN_x), MA956 was subsequently oxidized in a carefully-flushed O_2 atmosphere and again in flowing air. No appreciable difference was noted in the oxidation rate in air compared to that in O_2. The same quantity and type of spalling was observed on both alloys.

4.3.2 Cyclic Oxidation Adherence Results

Each alloy was oxidized for twenty, 1hr cycles in dry, flowing O_2, Figure 4.3.2. As noted in the isothermal results, the spallation of Al_2O_3 on the undoped FeCrAl material was not as severe as at 1200°C. Despite the faster oxidation rate, the weight loss at 1400°C was less and the first few cycles showed relatively good adherence followed by a more serious breakdown.

The doped FeCrAl materials both exhibited relatively good adherence at 1400°C. The spalling on MA956 observed after 25hr was not observed after the first few cycles. By the 6th cycle, the level of spallation was similar. However, more serious breakdown was not observed. APM which did not appear to spall in isothermal tests, exhibited a different behavior. After 10 cycles, large microcracks were observed on the surface. These cracks became more pronounced during the next 10 cycles but no major breakdown was observed.

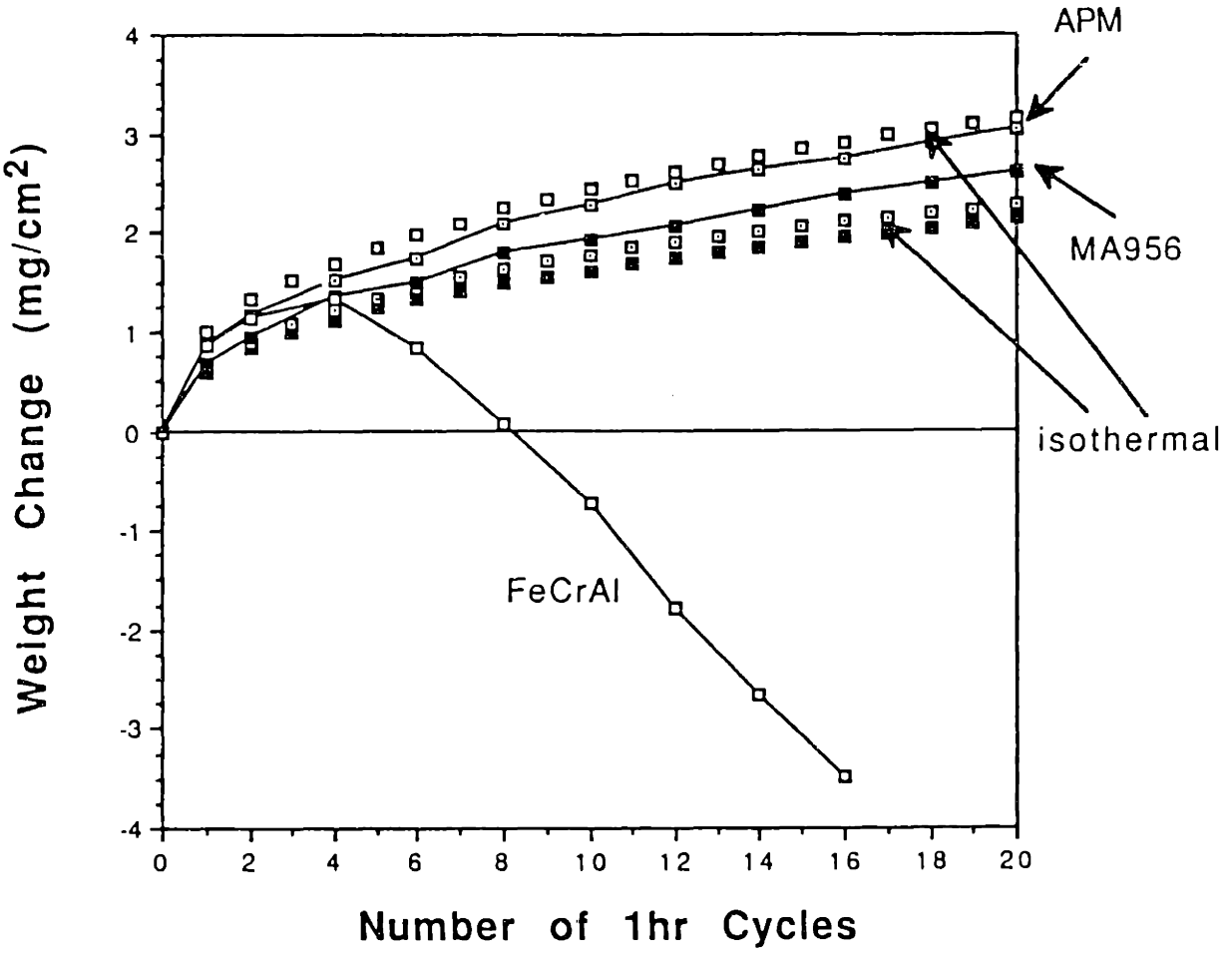

Figure 4.3.2 Isothermal weight gains plotted with the weight change over 20 1-hr cycles at 1400°C in 1atm O_2. Both alloys with a RE addition show good oxide adherence.

4.3.3 SEM Results

The SEM studies at this temperature were mainly geared for studying the spallation morphologies. Figure 4.3.3b is a typical view of the scale morphology on MA956 after oxidation for 25hr at 1400°C. The scale surface appears much rougher than at lower temperatures (e.g. Figure 4.2.9), but the same type of grain growth occurs near the surface, Figure 4.3.3a. Spallation occurs on less than 10% of the surface and is only found in small isolated areas 20-200μm across, Figure 4.3.4. This spallation occurs *within* the oxide, not to the bare metal. One of the spall regions contained a Ti-rich particle (identified by EDXA) while others contained Fe- and Cr-rich particles, Figure 4.3.4b. These particles could be remnants of the initial transient stage or new growth after spallation. At higher magnification, spallation appears to have proceeded intragranularly, Figure 4.3.5. The grains appear to be cleaved fairly uniformly and voids are observed both within grains and on grain boundaries. Identical spallation occurs from samples oxidized in O_2 (Figure 4.3.4) and in air (Figure 4.3.5). Higher magnification of the unspalled scale on MA956 revealed faceted Y-rich grains on the surface, Figure 4.3.6. At lower temperatures these grains were not as clearly evident.

Attempts to make a transverse section of the scale on MA956 after oxidation for 25hr were unsuccessful. However, analysis of the unthinned TEM sample in the SEM revealed a great deal. Figure 4.3.7 shows a typical section of the scale. Two important features are noted. First of all, while the gas interface appeared flat, the

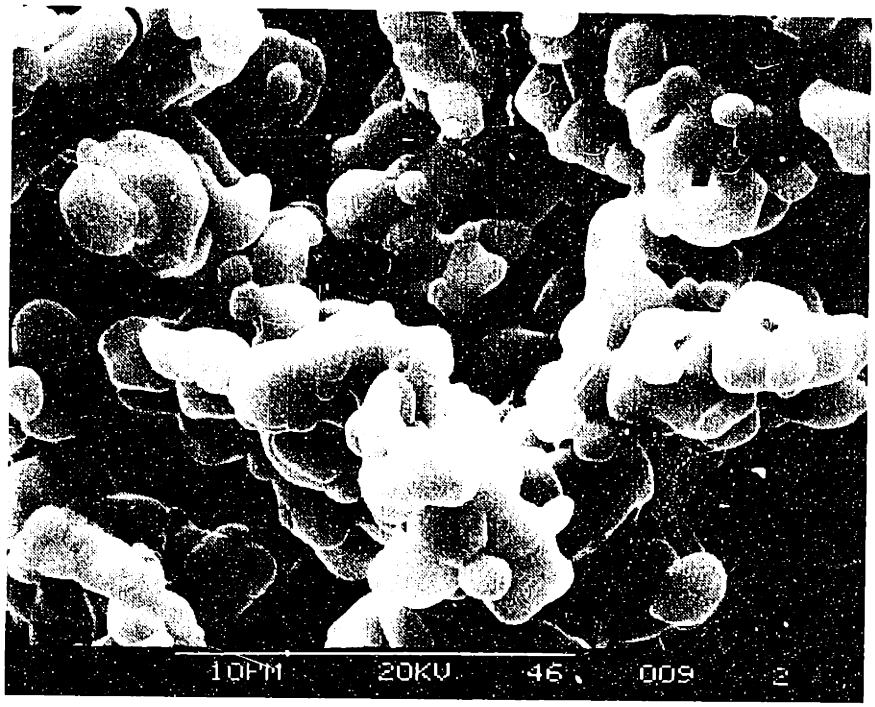

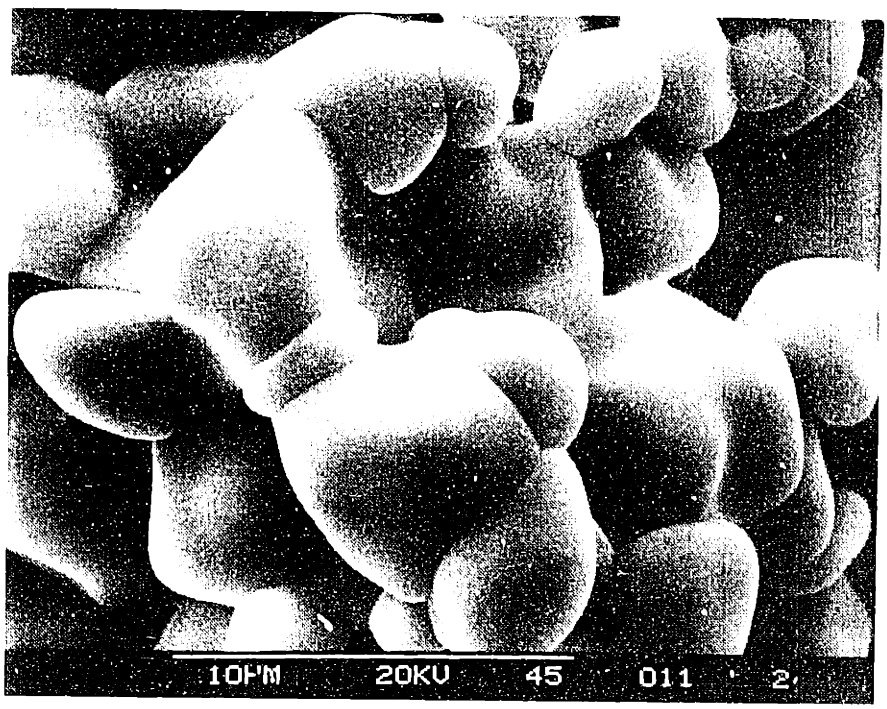

Figure 4.3.3 SEM secondary electron images of MA956 after oxidation at 1400°C for (a) 1hr and (b) 25hr.

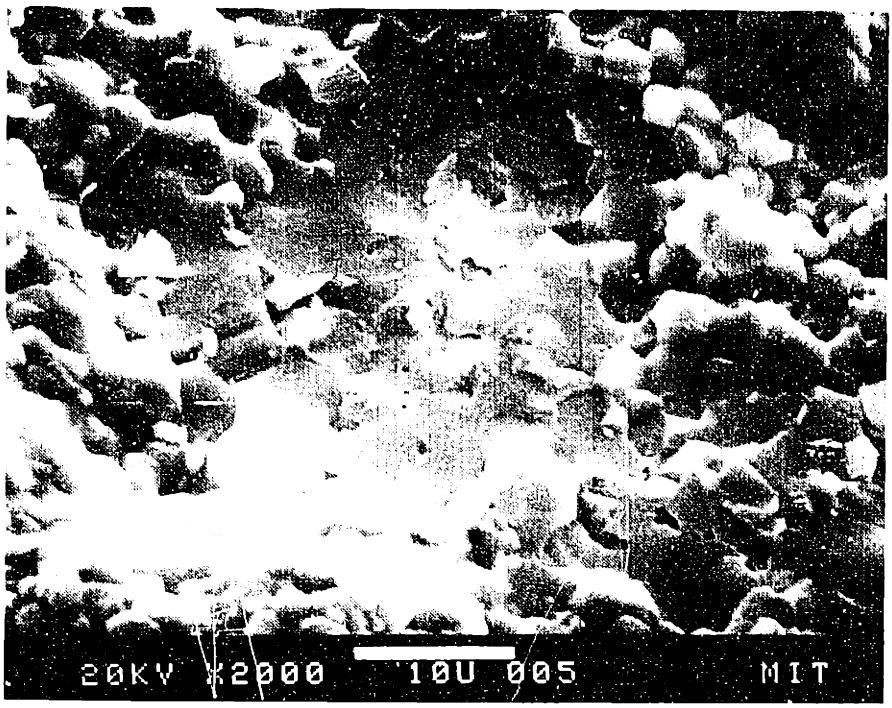

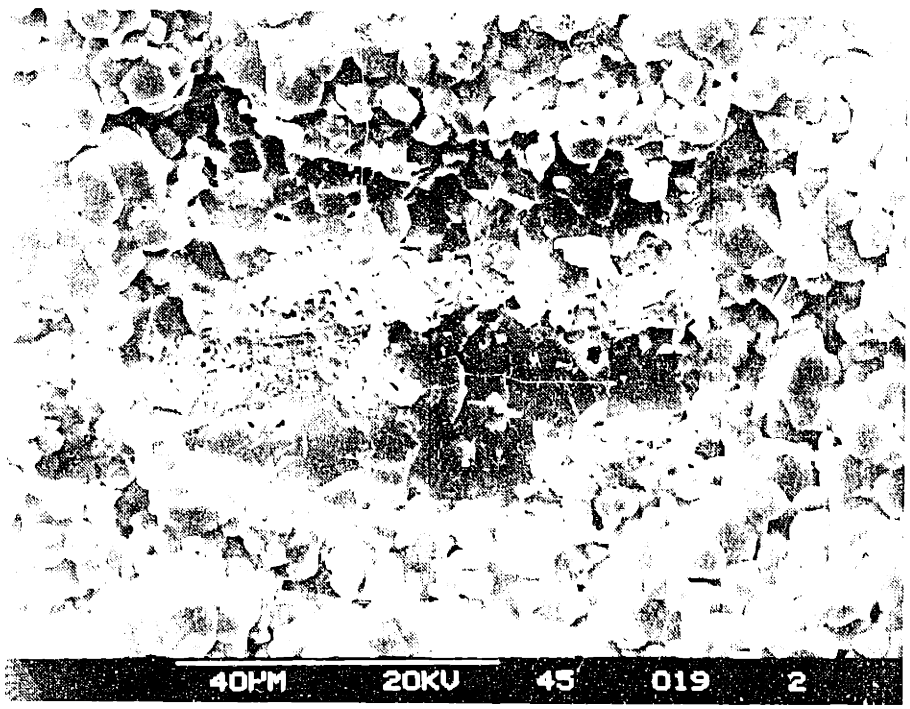

Figure 4.3.4 SEM secondary electron images of oxide spall regions on MA956 after oxidation at 1400°C for 25hr. Spallation is within the oxide, not to the bare metal. The central region in (b) is rich in Fe and Cr.

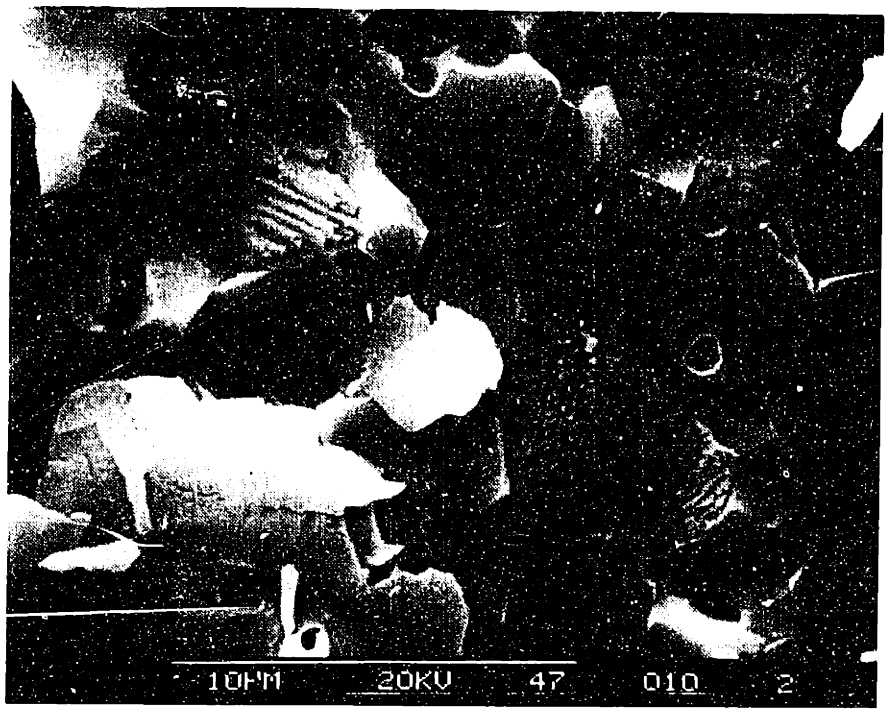

Figure 4.3.5 SEM secondary electron image of MA956 after oxidation at 1400°C for 25hr in air High magnification of the center of a spalled region showing the intragranular fracture.

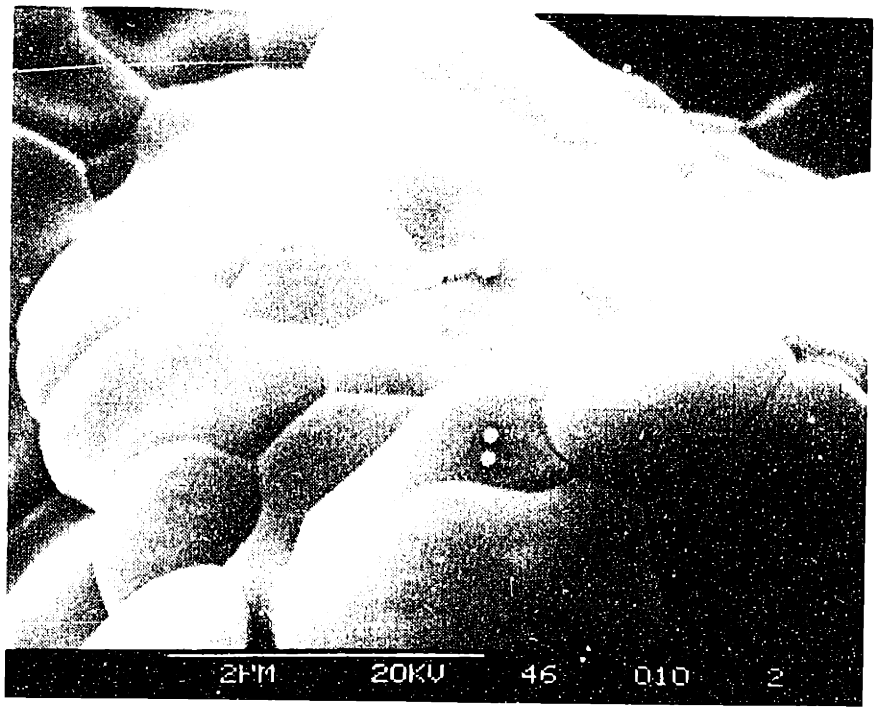

Figure 4.3.6 SEM secondary electron image of MA956 after oxidation at 1400°C for 1hr. The faceted grains are identified by EDXA as rich in Y. The small round spots are contamination from the electron probe.

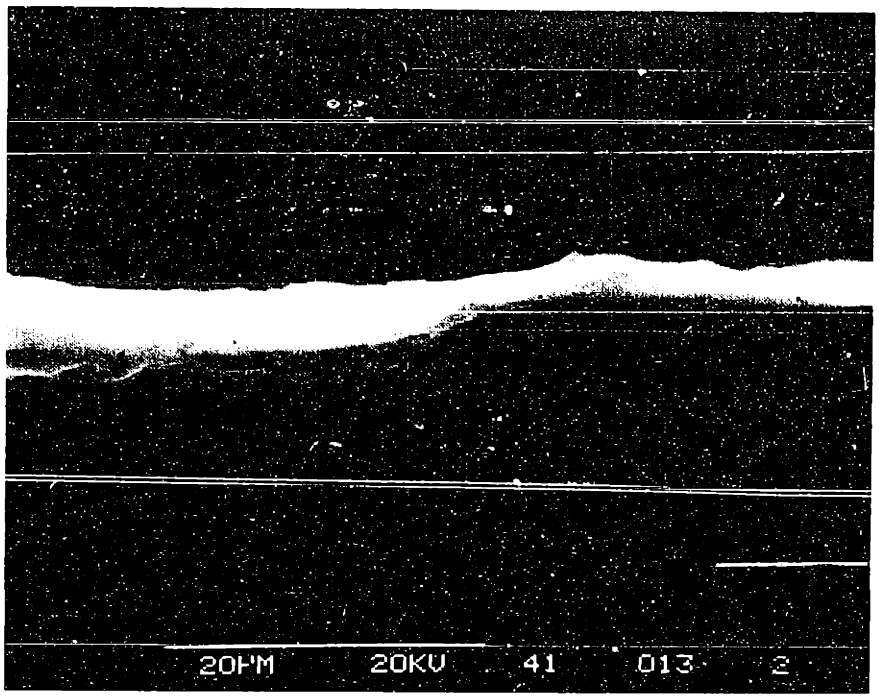

Figure 4.3.7 SEM secondary electron image of scale cross-section on MA956 after oxidation for 25hr at 1400°C in 1atm of O_2. The scale appears to be "rumpled" with the alloy following the convolutions of the scale. Voids can be seen at the alloy-oxide interface.

metal interface appears to be rumpled (see Figure 2.7b). This rumpling was observed across the entire cross-section and was periodic. Secondly, small voids are observed throughout the scale while larger voids are found at the metal-oxide interface. However, these voids do not appear to cover a large fraction of the interface nor do they correspond at all to the periodic rumpling.

As at lower temperatures, the scale on undoped FeCrAl has a different oxide morphology from MA956. After 1hr, a fine ridge-like structure is evident, Figure 4.3.8a; however, after 50hr this structure appears to have coarsened and lost its ridge-like nature, Figure 4.3.8b. Otherwise the structure is relatively flat with almost no whiskers. This is significant departure from the scales observed after 1000° (Figure 4.1.4) and 1200°C (Figure 4.2.3).

The scale on APM exhibited no significant isothermal spallation, and the scale appeared relatively smooth. The only significant feature was the small particles appearing on the scale surface, Figure 4.3.9. These particles were observed after 1hr and 25hr exposures. Many but not all of these particles were found to be rich in Zr using EDXA. After a cyclic exposure of 20 cycles, large macrocracking of the sample occurred which could not be related to the alloy grain structure, Figure 4.3.10. This type of cracking was not observed on cyclicly-oxidized MA956, which spalled in the same manner as the isothermal exposures. Neither alloy exhibited breakaway oxidation, but based on the macrocracking, APM appeared to be heading towards a more critical breakdown.

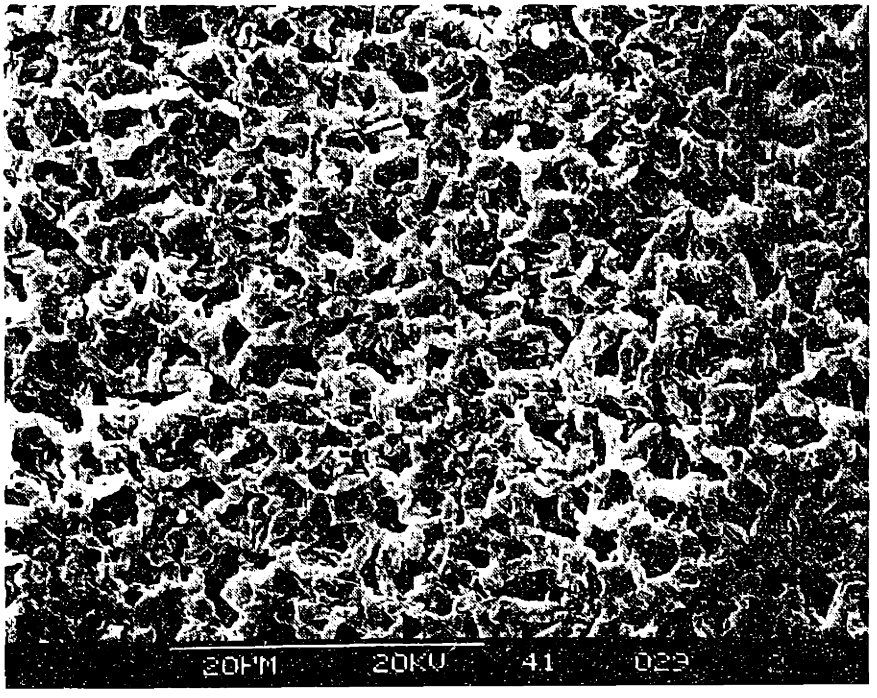

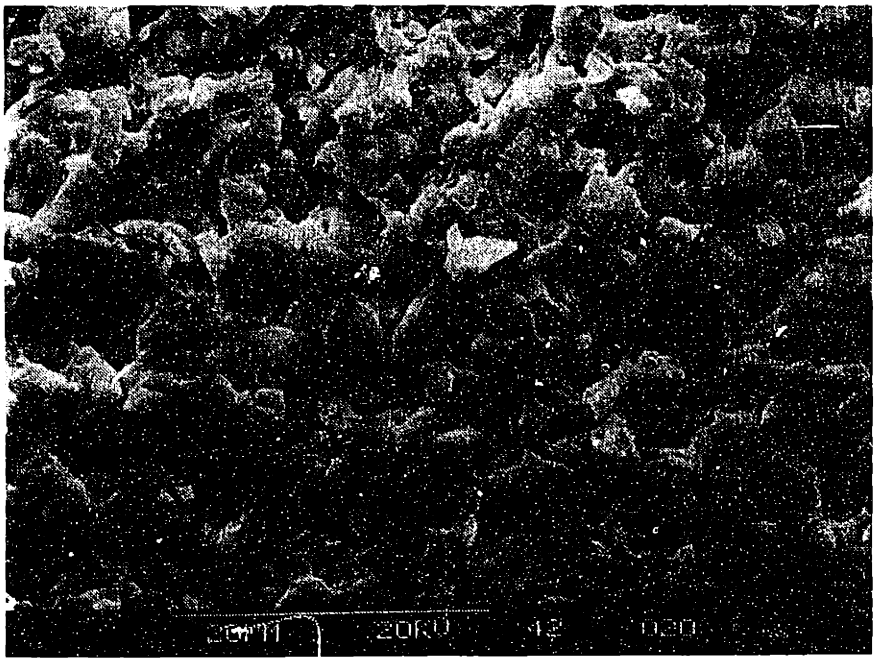

Figure 4.3.8 SEM secondary electron images of undoped FeCrAl after oxidation at 1400°C for (a) 1hr and (b) 50hr.

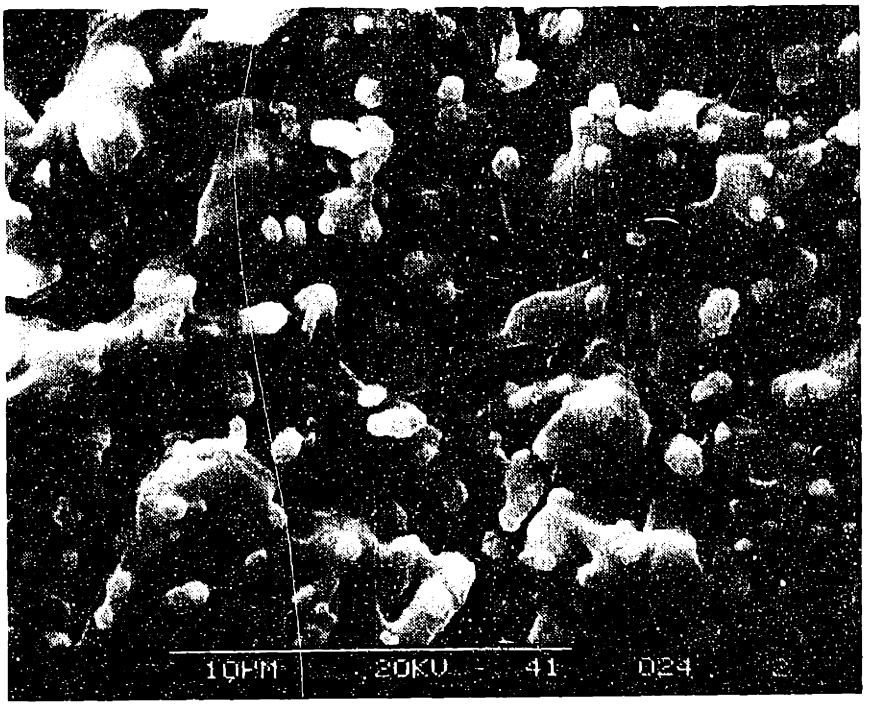

Figure 4.3.9 SEM secondary electron image of APM after oxidation at 1400°C for 25hr. Many of the small bright particles are rich in Zr by EDXA.

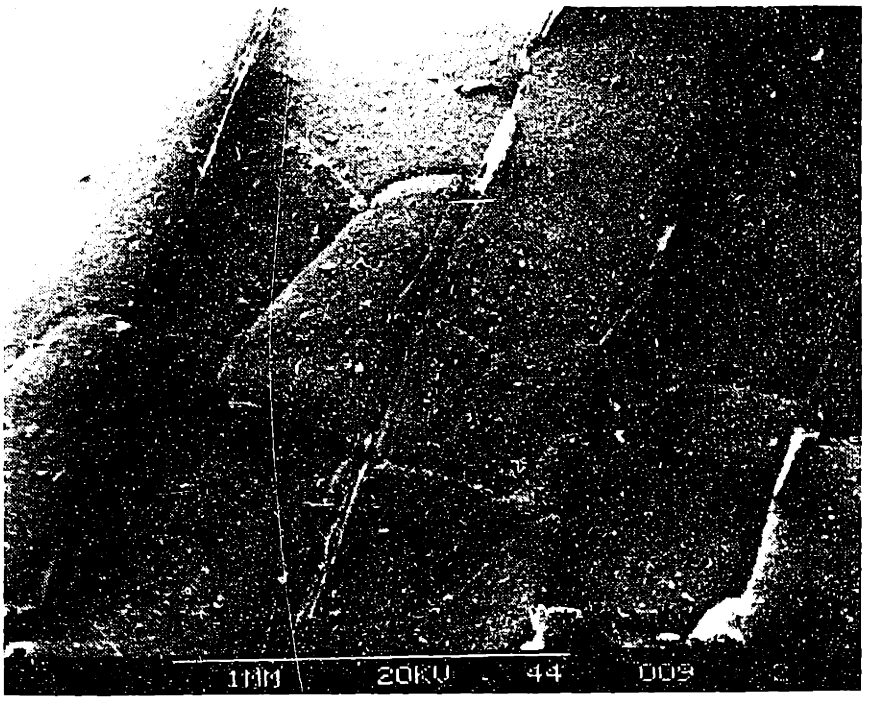

Figure 4.3.10 SEM secondary electron image of APM after oxidation at 1400°C for 20, 1hr cycles. Macro-cracking of the scale occurs, unrelated to the alloy grain structure.

4.3.4 GAXRD Results

Oxide scales on each of the three alloys were analyzed after oxidation at 1400°C for 1hr. Only α-Al_2O_3 could be detected in each case, Figure 4.3.11. The undoped FeCrAl showed stronger peaks from the matrix, most likely because of oxide spallation. Small peaks from oxidized MA956 appeared to best match YAG (which corelates with the observation of Y-rich faceted grains on the scale surface, Figure 4.3.6), while APM had a small peak which best matched ZrO_2, Figure 4.3.12. This also corelates with the particles observed on the scale surface, Figure 4.3.9.

4.3.5 AEM Results

Parallel sections of the oxide scale on MA956 after a 25hr exposure to O_2 were analyzed. An unusual cracking of the scale was observed in a number of areas, Figure 4.3.13a. Every oxide boundary examined showed the segregation of Y; however, Ti was discernible in only very small quantities. This is distinctly different from observations at 1000°C and 1200°C, Table 4.2. Rather than strongly segregating at 1400°C, Ti is observed to form TiN_x particles, 0.3-1.5µm in diameter in a matrix of 1-5µm Al_2O_3 grains, Figures 4.3.13b and 4.3.14a. This STEM image (Figure 4.3.13b) also reveals the apparent decohesion of the particle from the matrix in the lower right hand corner. The particles were identified first by EDXA then reconfirmed by EELS, Figure 4.3.15.

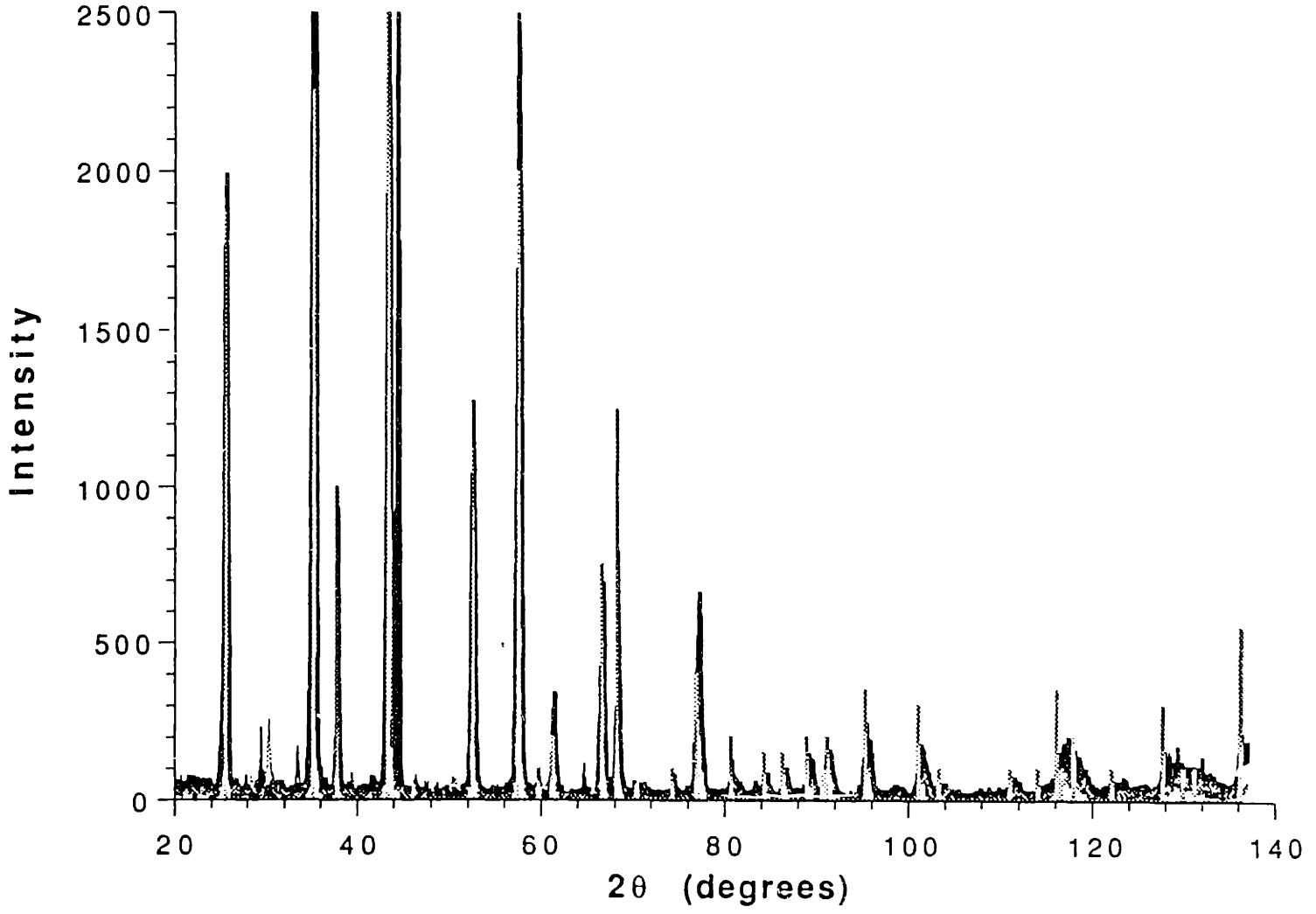

Figure 4.3.11 GAXRD profile of scales formed on MA956 (thin solid), APM (dashed) and undoped FeCrAl (wide solid) after oxidation for 1hr at 1400°C in 1atm O_2. The wide dashed lines denote α-Al_2O_3, which is the major phase detected in each profile.

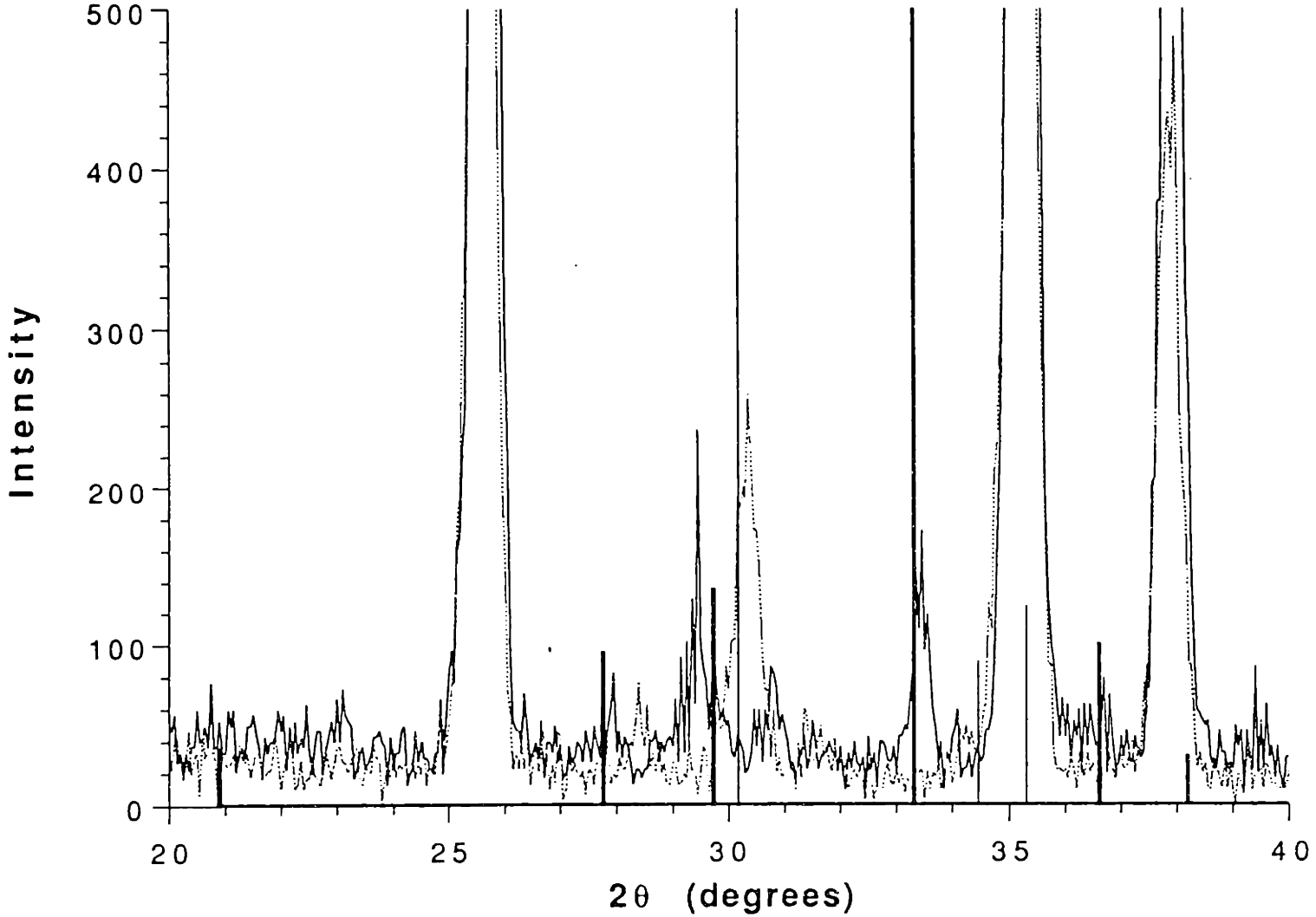

Figure 4.3.12 GAXRD profile of scales formed on MA956 (solid) and APM (dashed) after oxidation for 1hr at 1400°C in 1atm O_2. The wide solid lines denote YAG and the thinner lines ZrO_2. These two JCPDS files represent the best fit for these peaks.

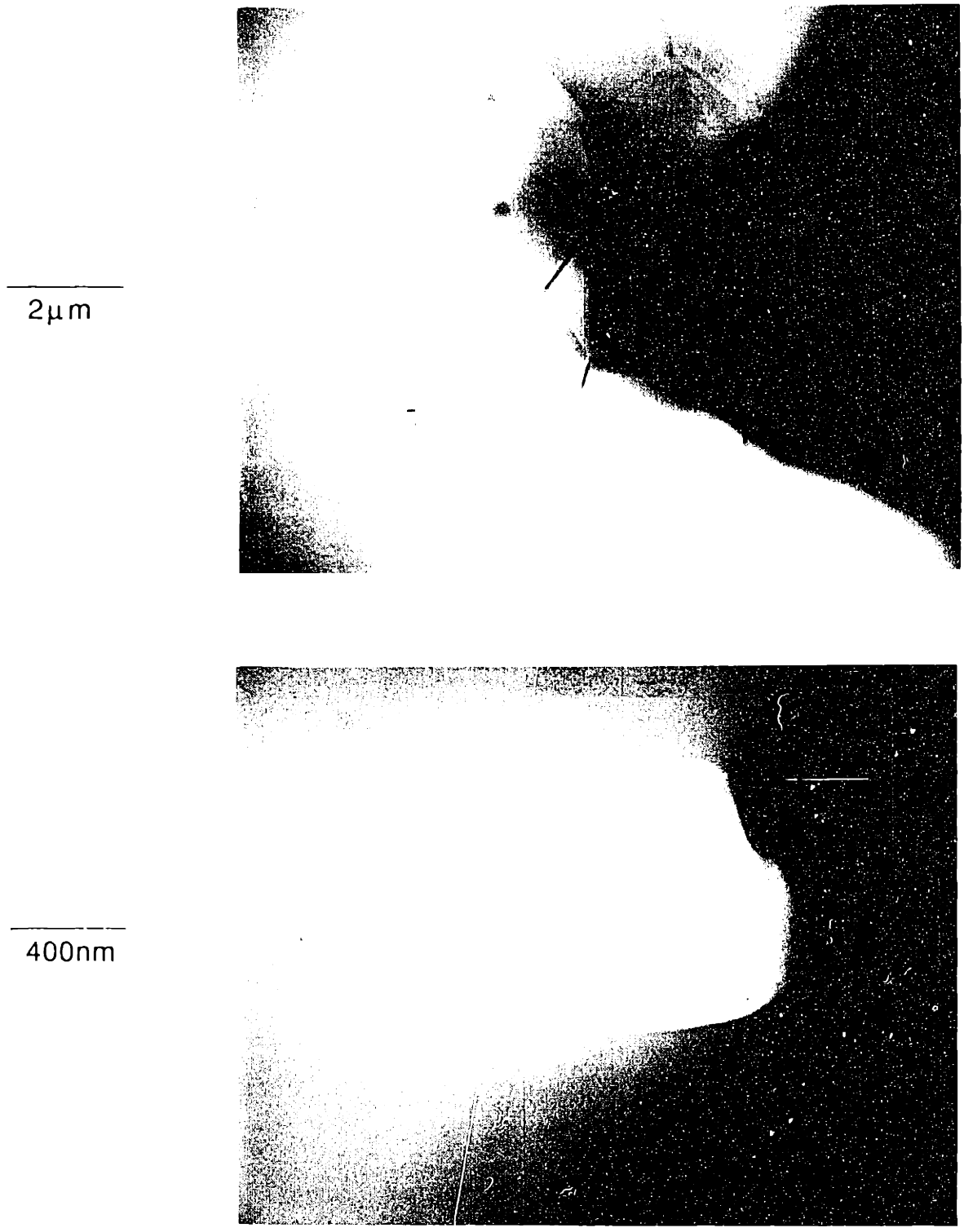

Figure 4.3.13 STEM annular dark field images of the oxide formed on MA956 after oxidation for 25hr at 1400°C - (a) cracks in the oxide and (b) TiN_x particle in the scale, the arrow indicates separation between the particle and the matrix.

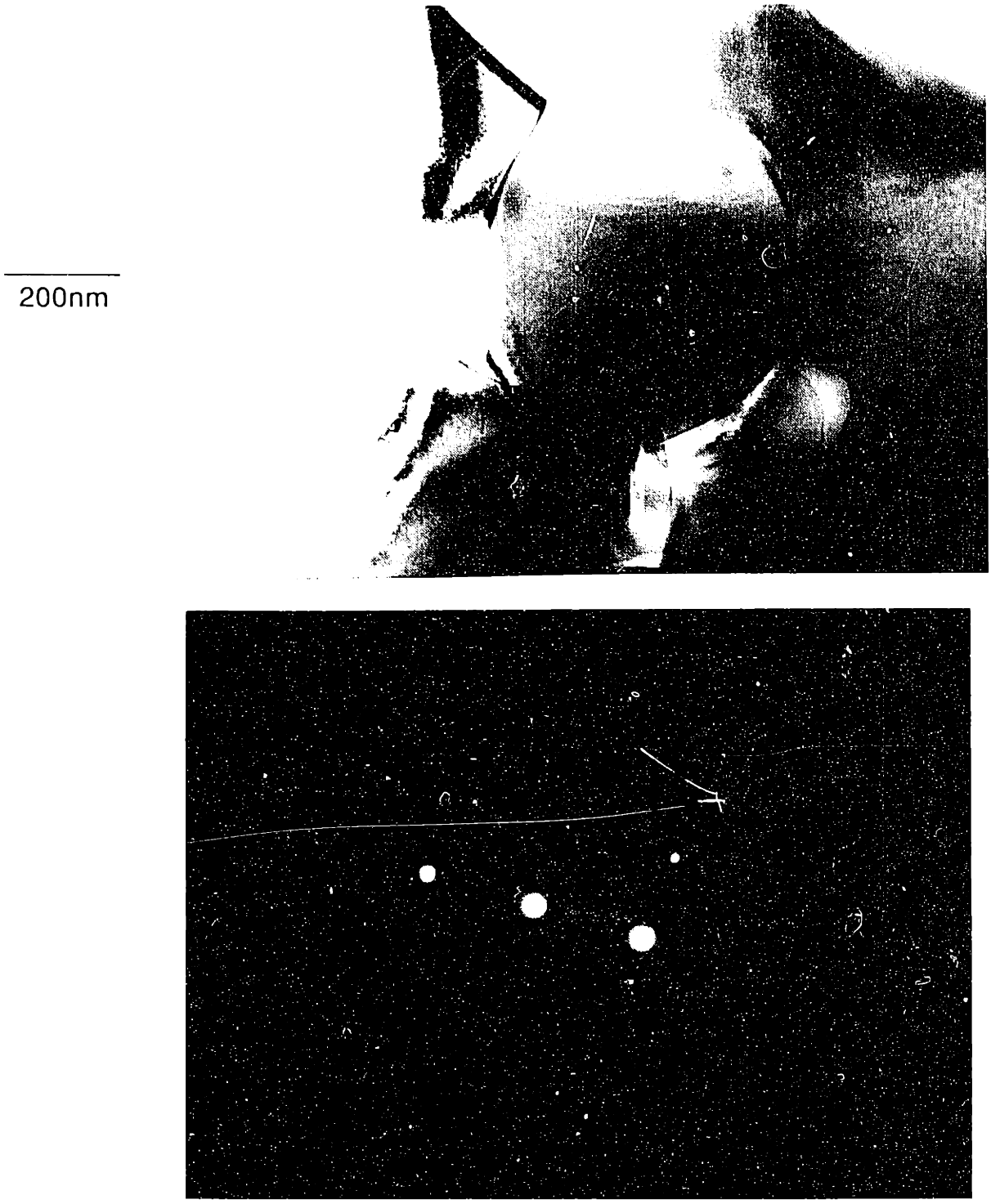

Figure 4.3.14 (a) TEM bright field image of a TiN_x particle in the Al_2O_3 scale formed on MA956 after oxidation for 25hr at 1400°C in 1atm of O_2. (b) selected area diffraction pattern of the same particle.

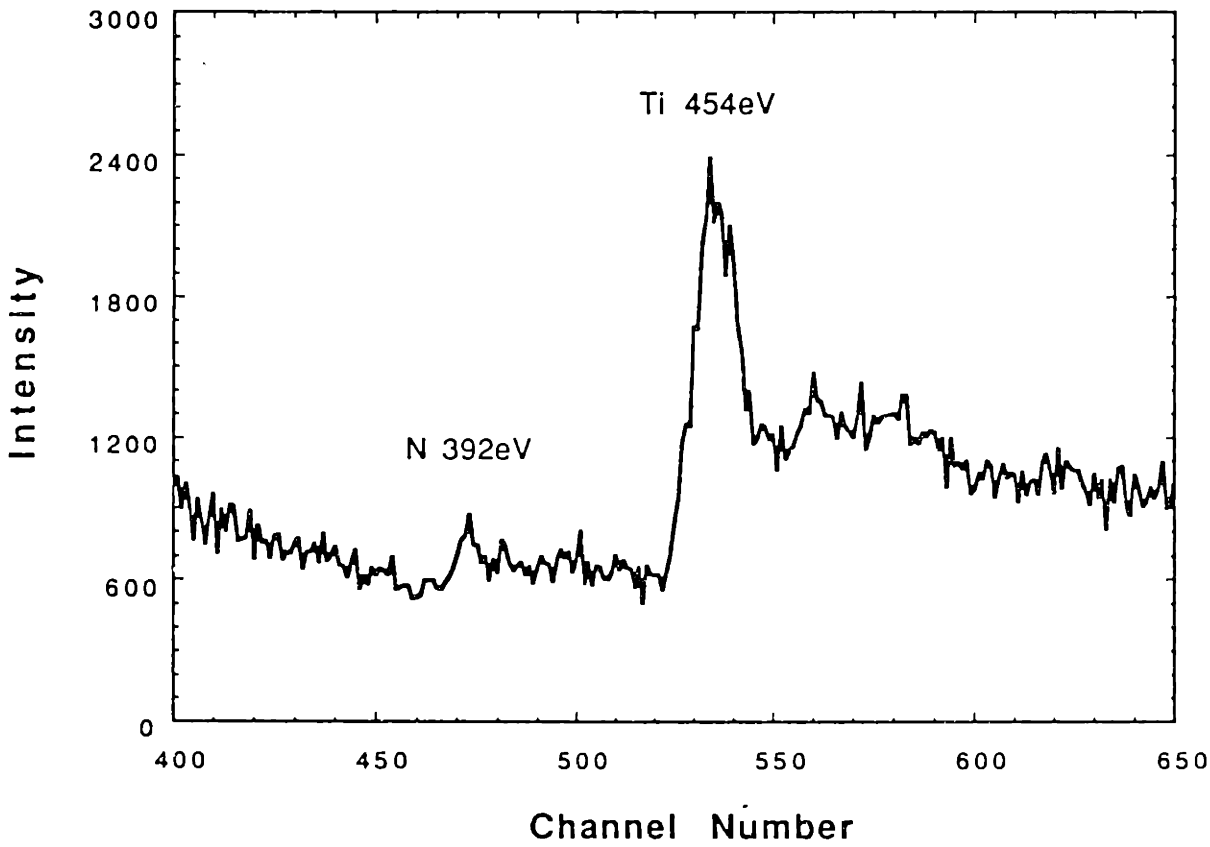

Figure 4.3.15 EELS spectrum from TiN_x particle in the Al_2O_3 scale formed on MA956 after oxidation for 25hr in O_2 at 1400°C. Only peaks for Ti and N are observed.

EDXA and EELS quantifications of the Ti/N ratio were not conclusive. The EDXA spectra also contained some peaks from the surrounding matrix. The EELS quantification of a 2:1 Ti/N atomic ratio could not be confirmed, but the EELS spectra clearly shows that Ti and N are the only significant components. Selected area diffraction of the particle was performed by conventional TEM but a specific structure has not been identified, Figure 4.3.14b. No clear match could be found with compounds such as TiN or Ti_2N.

A second MA956 sample was oxidized in a carefully flushed O_2 atmosphere for 25hr, and TiN_x particles were also observed in this scale. TEM samples of the scale grown on MA956 in air did not have sufficient thin area to observe any particles in the matrix. Analysis of several of the samples ran into resolution problems because FeCrAl is magnetic. This was the case with an APM sample oxidized for 25hr. A large number of ZrO_2 particles were observed near the gas interface, but because of stigmation problems associated with a magnetic sample, no boundaries could be analyzed. Also, because the oxide grain size was so large, it could not be estimated by TEM. An estimation of the grain size was made using SEM images of the scale surface and cross-sections, Table 4.1.

4.4 Summary of FeCrAl Results

The comparison of the doped and undoped FeCrAl samples gives a fairly clear picture of the REE for alumina-formers. The most obvious effect is the improvement in oxide adherence especially at the lower temperatures. There is also a small but discernable

reduction in the oxidation rate. The sequential isotope oxidation experiments conducted at 1200°C indicate a possible change in the oxidation mechanism for α-Al_2O_3, which would explain this change in rate. The doped scale grew solely by a short-circuit inward diffusion mechanism while the undoped scale appeared to grow by a mixed Al and O diffusion mode. At 950°C, θ-Al_2O_3 was found to grow by the outward diffusion of Al.

The oxide microstructure is also changed by the reduction in the grain size at each temperature and the change, especially at 1200°C from an equiaxed-grain, rumpled scale to a columnar-grain, flat scale.

While the REE is observed in these materials, attempting to conclusively explain these effects runs into problems, because of the complexities of the commercial FeCrAl alloys. The Si and Ti additions and the different types of dispersions add more questions to the problem rather than solutions. The work on Y-implanted ß-NiAl was an effort to study the REE in a simpler system.

5.0 ß-NiAl

In order to more fully study the reactive element effect, including the effect of increasing the oxidation temperature, a more idealized system was chosen to eliminate a number of the variables associated with the commercial FeCrAl materials (e.g. Si and Ti alloy additions). A single-phase, high Al material, ß-NiAl, was first characterized and the reactive element (Y) was then added as a surface addition by ion implantation. However, this model-type system, widely used at lower temperatures in the literature, was found to have a number of significant problems. The reactive element effect was not fully observed at any temperature in this part of the study. This section details the results that were observed and their deviation from the typical RE behavior. The effect of Al content was also studied during the first set of experiments at each temperature. The rest of the experiments concentrated on stoichiometric ß-NiAl, viz. 31.5wt% Al (with and without a Y-implant), on RE alloy additions (0.23wt% Zr), and on a Y_2O_3-Al_2O_3 oxide dispersion in Ni_3Al. As a basic nomenclature, the stoichiometric ß-NiAl will often be referred to as NiAl. The Ni- and Al-rich samples will be referred to by their Al weight percentage, e.g. Ni-30Al.

5.1 Results at 1000°C

The initial work on NiAl implanted with Y revealed that not only were the typical RE effects not observed but entirely different

effects were occurring. The main area of interest is the transformation of metastable θ-Al_2O_3 to the stable α-Al_2O_3. In order to further study the effect of implanted species on the phase transformation, Cr and Al were also implanted at the same level as Y ($2x10^{16}/cm^2$). The original selection of 1000°C as the lowest temperature of interest was made in order to avoid the formation of θ, which is predominant (though metastable) at lower temperatures. It was also chosen because much of the literature on alumina-formers was conducted between 1000° and 1200°C.

5.1.1 Kinetic Results

The first set of kinetic results derived from NiAl samples of varying Al content: three from within the ß (NiAl) phase field and one sample of Ni_3Al, Table 3.2. On first examination, the Ni-Al samples appeared to exhibit very non-parabolic behavior, Figure 5.1.1. Taken as a whole, a strong negative deviation from parabolic behavior is observed. The second striking result is that the addition of Y to NiAl has *increased* the oxidation rate rather than resulting in the usual decrease (e.g. see Figure 4.1.1). The ordering of rates based on Al content is also unexpected, with the rate first decreasing, then increasing with Al content.

A more careful examination of these data is necessary. Take for example the case of Ni-30wt%Al without Y, represented by an open triangle in Figure 5.1.1. Rather than considering the data as one set, examine the behavior before and after 2hr ($1.4\sqrt{hr}$). In each of these cases, a parabolic rate law is obeyed. An initial higher rate

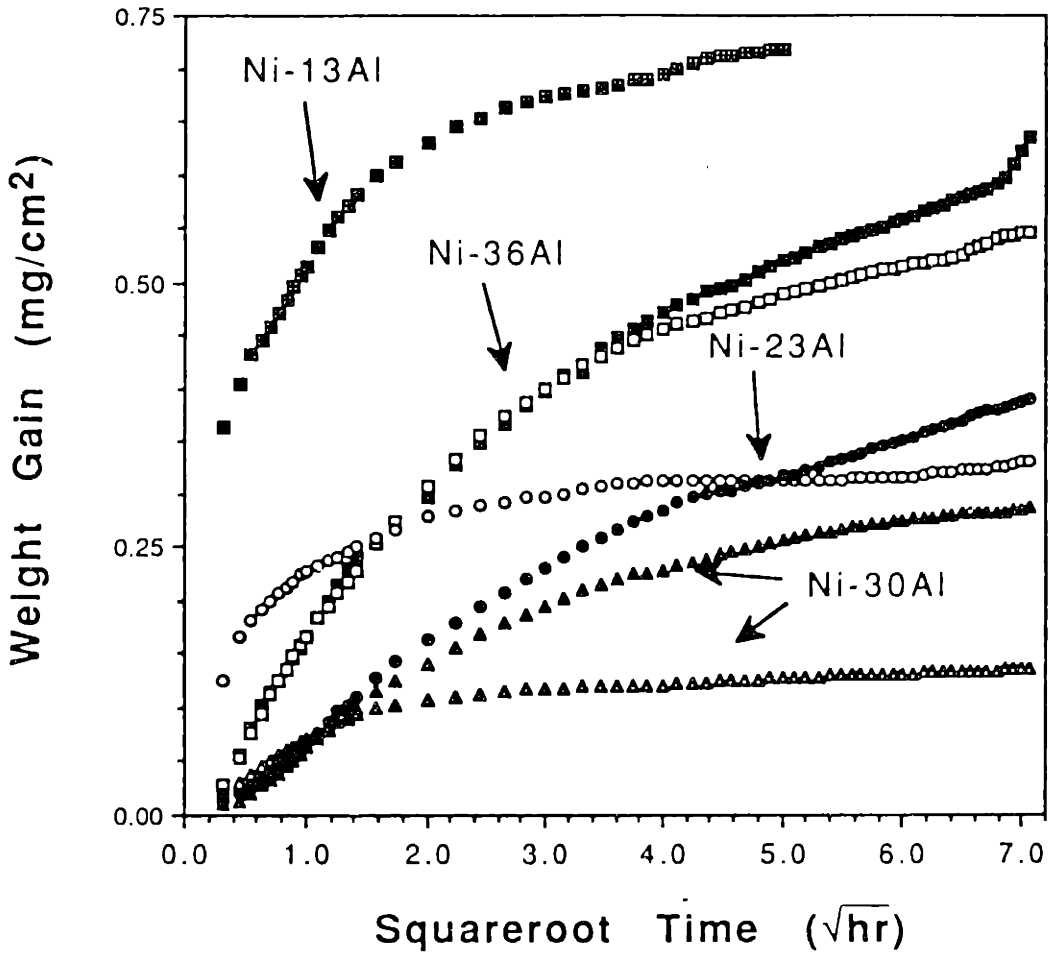

Figure 5.1.1 Parabolic plot of weight gain versus squareroot of time for Ni-Al materials at 1000°C in 1atm O_2. The Al content of each set of materials is marked in weight percent. The closed symbols have been implanted with $2x10^{16}$ Y/cm^2.

followed by a second, extremely low rate. This would suggest two separate, diffusion-controlled, oxidation mechanisms. Now consider the behavior of Ni-30Al with Y implantation. In this case, the initial higher rate lasts for a much longer period and only begins to drop after longer exposure.

With lower Al content, the most important difference is in the initial transient period. Ni_3Al (+ Y_2O_3) experiences more than half of its total weight gain in the first 12min of exposure. With only ≈23at% Al, an initial Ni-rich oxide layer is likely formed. At longer times, a significant rate reduction is observed. Now compare the behavior of unimplanted Ni-23Al to unimplanted Ni-30Al. Remember that the total weight gain is not as important as the rate of oxidation -- the indicator of the steady-state, oxidation mechanism. The major difference between these two materials is the transient period. The slopes after the first 5hr are almost identical, making parallel lines. The exception to this explanation is the implanted Ni-23Al. However, in this case the implant appears to limit the transient period. The result is that the weight gain is very similar to that of implanted Ni-30Al. A note about transient effects and TGA data is in order: The initial stability of the balance is very delicate, and there is no way to denote the initial weight. The initial weight is determined by a combination of extrapolation, experience and total weight gain (e.g., comparison of the measured total change from the Cahn balance and the total weight change after oxidation on the Mettler balance). Thus, an estimation of the weight gain during the transient stage is difficult.

The unusual behavior of Ni-36%Al requires a different explanation. In this case, the numerous cracks and voids in the alloy are likely an important factor. With all of these "nooks and crannies", there is probably a significant miscalculation of surface area. This would mean a higher than normal weight gain calculation (mg/cm^2). It would also mean that as these areas filled in with oxide, the effective surface area would be reduced thus reducing the oxidation rate at longer times. This idea fits the experimental results quite well. As a final note, the implanted Ni-36Al (which presumably has the same surface area problems as the unimplanted material) has a higher weight gain (and slope) than the unimplanted case. This is consistent with an increase in oxidation rate with the addition of Y.

Additional tests were made of the isothermal kinetic behavior at 1000°C, Figure 5.1.2. Ni-31.5%Al (NiAl) was included in this case and exhibited a behavior similar to the other Ni-Al samples. Without Y, two separate stages can be identified; and with Y, a more gradual transition is observed. The Cr- and Al-implanted samples were implanted only on one side so no clear kinetic data could be measured during their oxidation. No cyclic experiments were conducted at 1000°C. However, limited spallation was visible on many samples, both implanted and unimplanted.

5.1.2 Glancing Angle X-ray Diffraction Results

Although the initial research plan called for only a small amount of x-ray diffraction work, the unexplained oxidation behavior

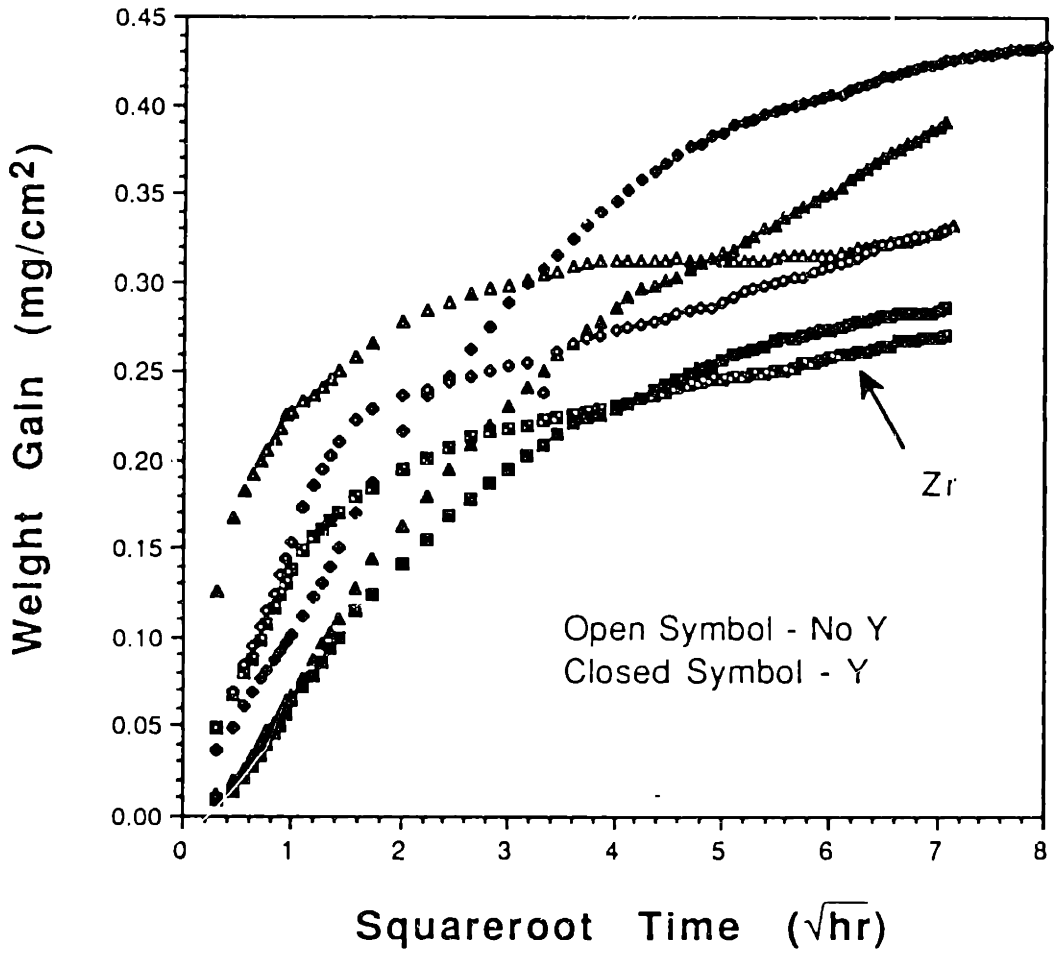

Figure 5.1.2 Parabolic plot of weight gain versus squareroot of time for Ni-Al materials at 1000°C in 1atm O_2.

at 1000°C required more careful study. (The original plan was merely to confirm the phase as α-Al_2O_3 and then move on to more in-depth characterization.) The increase in oxidation rate with the implantation of Y was unusual and previously unreported in the literature. The first step was to identify the phases present in the oxidation product.

By first looking at the scales formed after 50hr in the first set of experiments, it became clear that there was a definite difference in oxide phases between the two samples. Figure 5.1.3 identifies two peaks unique to the implanted sample. These are two of the main peaks for θ-Al_2O_3, the first is larger compared to the JCPDS card (35,121) because it also coincides with a ß-NiAl peak, (JCPDS card No. 20,19, see Table 3.5). After 50hr the unimplanted sample appears to have a scale consisting of mainly α-Al_2O_3. The implanted sample appears to have a significant amount of θ-Al_2O_3 in its scale. Examining the scales after just 1hr of oxidation revealed that the scales on Y-implanted NiAl were exclusively θ with no α peaks detected, Figure 5.1.4. The results for the unimplanted NiAl were less consistent. The unimplanted NiAl profile in Figure 5.1.4 after a 1hr exposure shows very strong θ peaks and weak α peaks, indicating the transformation is just beginning at this time. In comparison, the unimplanted sample in Figure 5.1.5 has a scale which is almost exclusively α after 1hr. NiAl with a Zr alloy addition showed strong θ peaks after 1hr but only α-Al_2O_3 after 50hr, indicating less of an effect on the transformation than an Y implant.

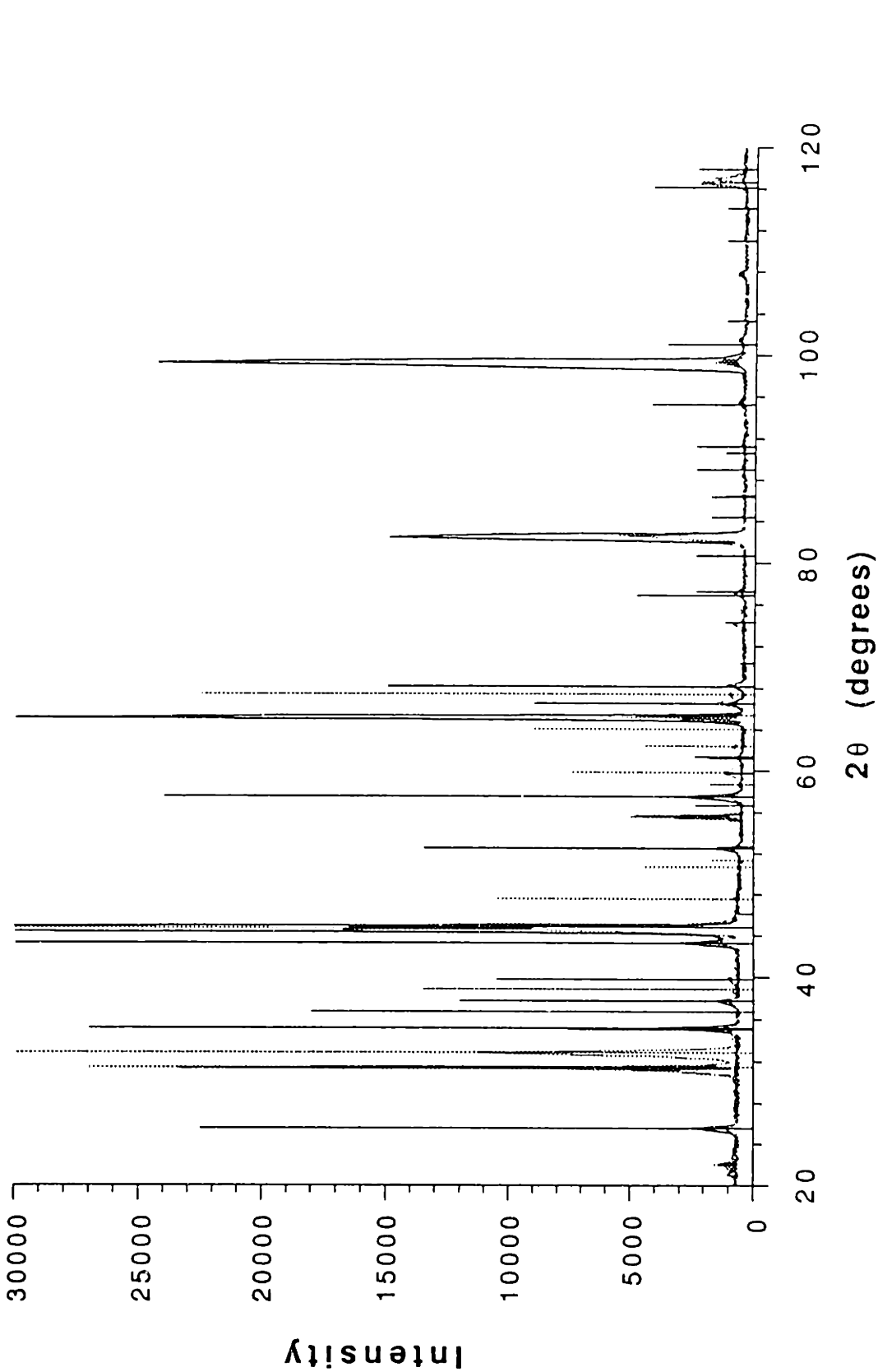

Figure 5.1.3 GAXRD profile of scales formed on unimplanted (solid) and Y-implanted (dashed) Ni-23wt%Al after oxidation for 50hr at 1000°C in 1atm O_2. The solid lines denote α-Al_2O_3 and the broken lines θ-Al_2O_3. Only the scale on Y-implanted NiAl has a significant amount of θ.

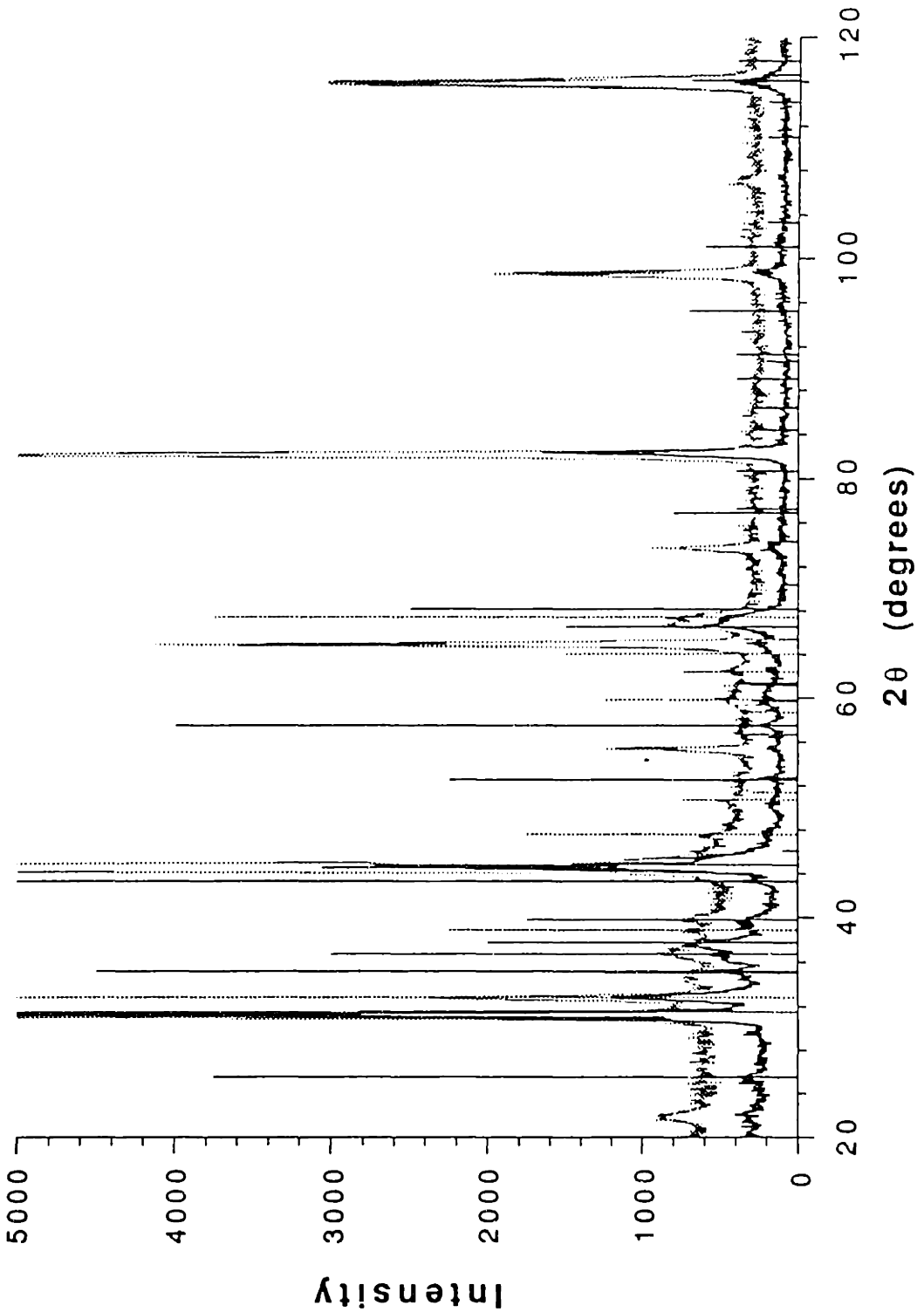

Figure 5.1.4 GAXRD profiles of scales formed on unimplanted (solid) and Y-implanted (dashed) Ni-31.5wt%Al after oxidation for 1hr at 1000°C in 1atm O_2. The solid lines denote α-Al_2O_3 and the broken lines θ-Al_2O_3.

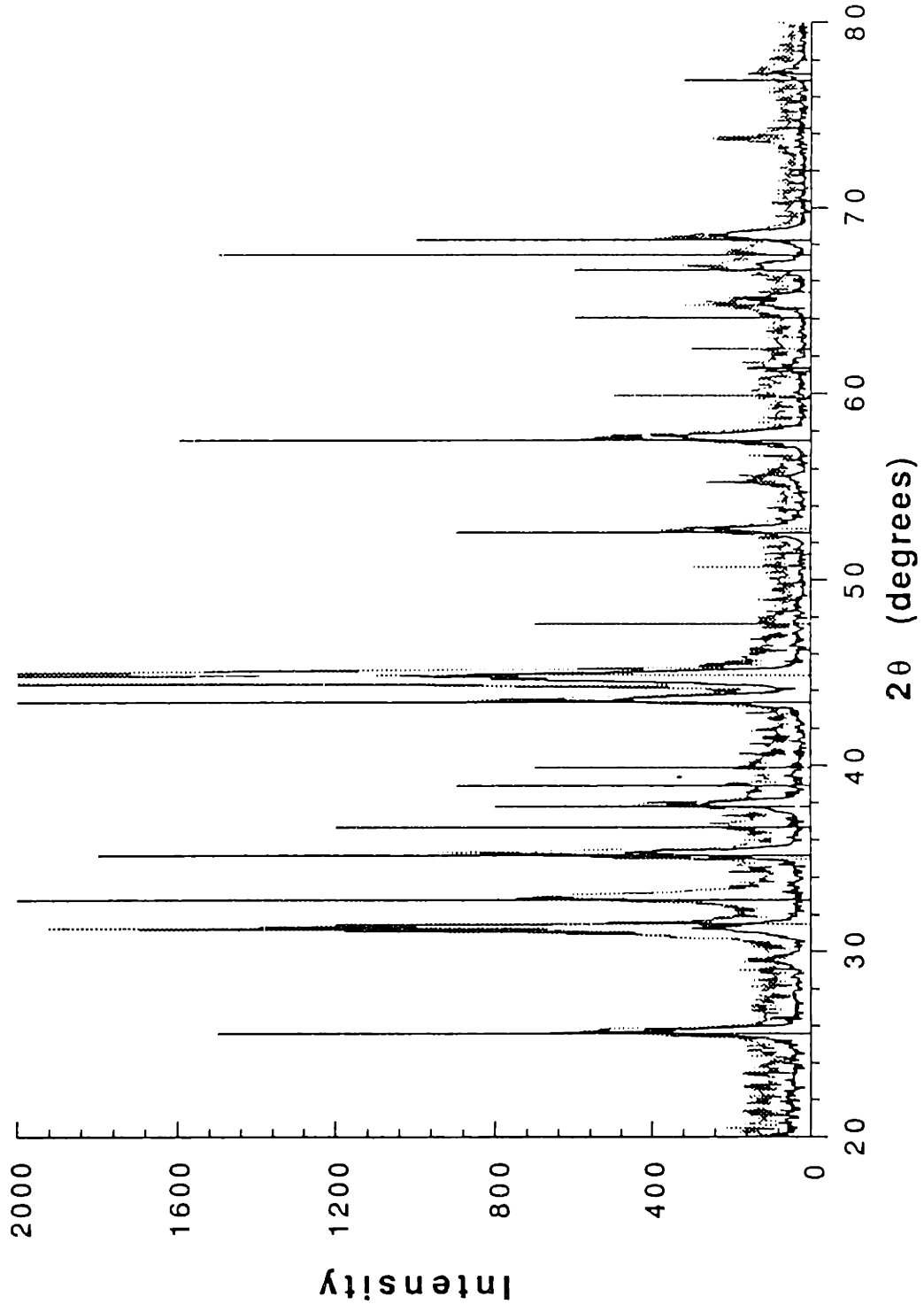

Figure 5.1.5 GAXRD profile of scales formed on unimplanted (solid) and Al-implanted (dashed) Ni-31.5%Al after oxidation for 1hr at 1000°C in 1atm O_2. The solid lines denote α-Al_2O_3 and the broken lines θ-Al_2O_3. Some θ is retained in the scale on the Al-implanted sample.

The means by which the Y implant slows the θ-α transformation was further investigated by implanting NiAl with Cr and Al at the same level as Y ($2x10^{16}/cm^2$ at 70keV). After 50hr, the profiles of Cr- and Al-implanted NiAl contained no θ peaks but appeared to be only α. This indicates that neither Cr nor Al has as strong an effect on the phase transformation as Y, which clearly stabilized some θ-Al_2O_3 up to 100hr.

After a 1hr oxidation, both Cr- and Al-implanted samples showed strong θ peaks. An obvious difference was found in both cases by comparing profiles of the implanted and unimplanted sides of the same sample. Figure 5.1.5 shows strong θ peaks only on the Al-implanted side of this sample after 1hr. This 1hr test was repeated on a second Al-implanted sample and the same result was achieved. While Cr was thought to have an effect on the transformation, Al was implanted to check the effect of the implantation process itself. In order to check the effect of increased Al content on the phase transformation, Ni-30Al and Ni-36Al were compared after oxidation for 1hr. Ni-36Al had a stronger θ-Al_2O_3 peak than Ni-30Al indicating a possible effect of Al content on the phase transformation.

The retention of θ-Al_2O_3 on the Al-implanted sample may also indicate a possible effect of the implantation process on the phase transformation. However, this is only a temporary effect. The implantation process clearly cannot explain the retention of θ-Al_2O_3 on Y-implanted NiAl after 100hr at 1000°C.

To return to the REE for a moment, this stabilization of θ is not one of the conventional REE and is not beneficial because θ

grows at a faster rate than α. Thus at 1000°C, Y-implanted NiAl is not an appropriate model system for studying the REE.

5.1.3 SEM Results

Morphologies at 1000°C also revealed a clear difference between the θ and α phases. The θ–α transformation appears to be the most important factor in determining the morphology of the scale at 1000°C. A variety of "typical" examples are given in this section to illustrate an overall trend. Twenty samples of varying times and compositions were examined to form a data matrix.

Typical morphologies of the unimplanted and Y-implanted samples are shown in Figure 5.1.6. These are the same two Ni-23Al samples profiled in Figure 5.1.3. The blade-like structure in Figure 5.1.6a is the hallmark of θ-Al_2O_3, which grows by an outward diffusion mechanism (Sec. 4.1.4). This type of morphology was found on virtually every Y-implanted sample regardless of time of oxidation. The blade tips in this image are charging. The darker areas apparently without blades are believed to be areas where the oxide has been transformed to α-Al_2O_3. The morphology of the unimplanted Ni-23Al has a variety of Ni-rich oxide grains on the surface but none of the distinctive large blades. In kinetic weight gain experiments, this sample was observed to gain a large amount of weight during the early transient period. This behavior is also observed on Ni_3Al, for which after 1hr large Ni-rich grains are observed, Figure 5.1.7a. However, at longer times when the outer transient scale is undercut by Al_2O_3, the outer scale appears to "fill

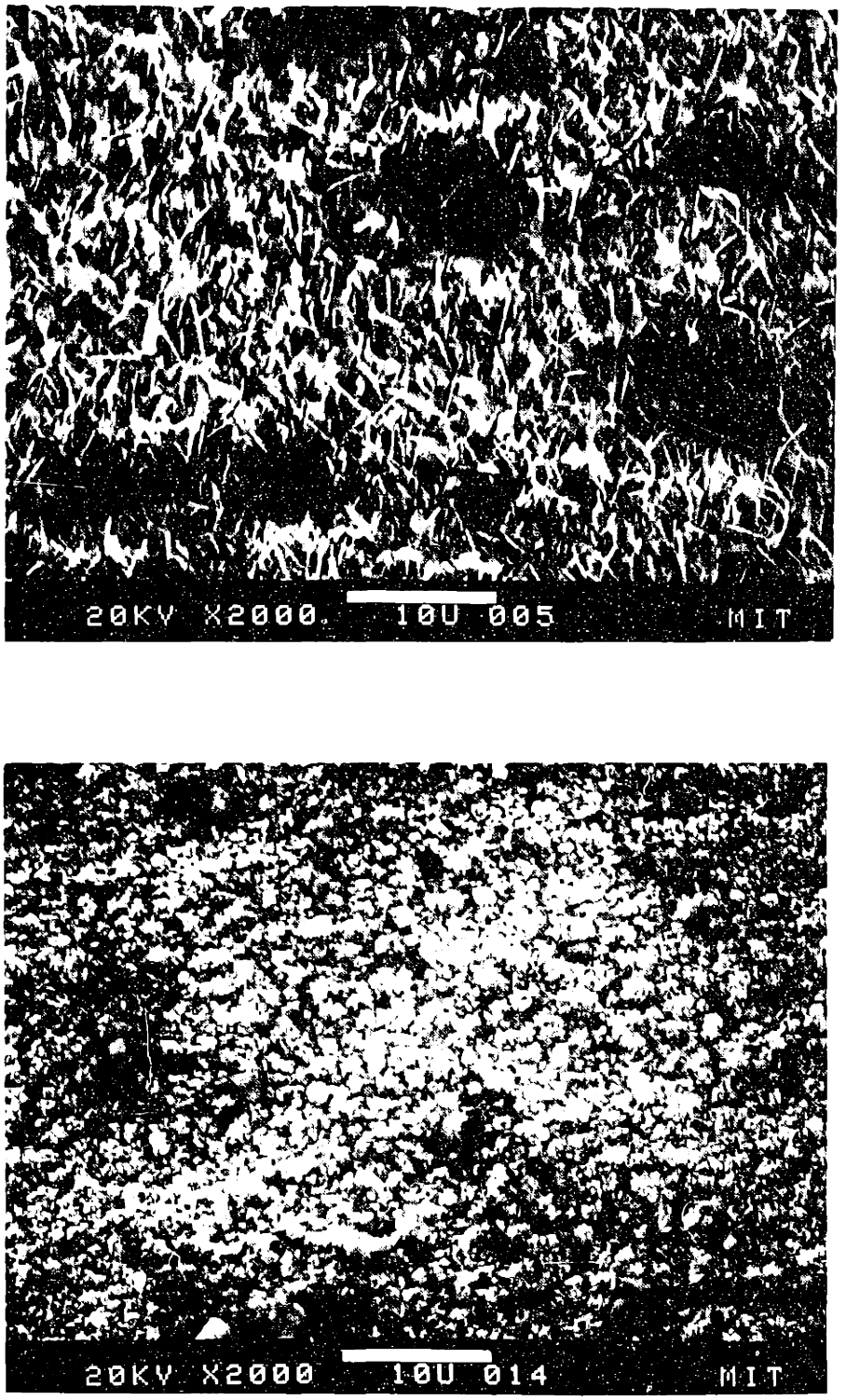

Figure 5.1.6 SEM secondary electron images of Ni-23Al after oxidation at 1000°C for 50hr. (a) Y-implanted and (b) unimplanted.

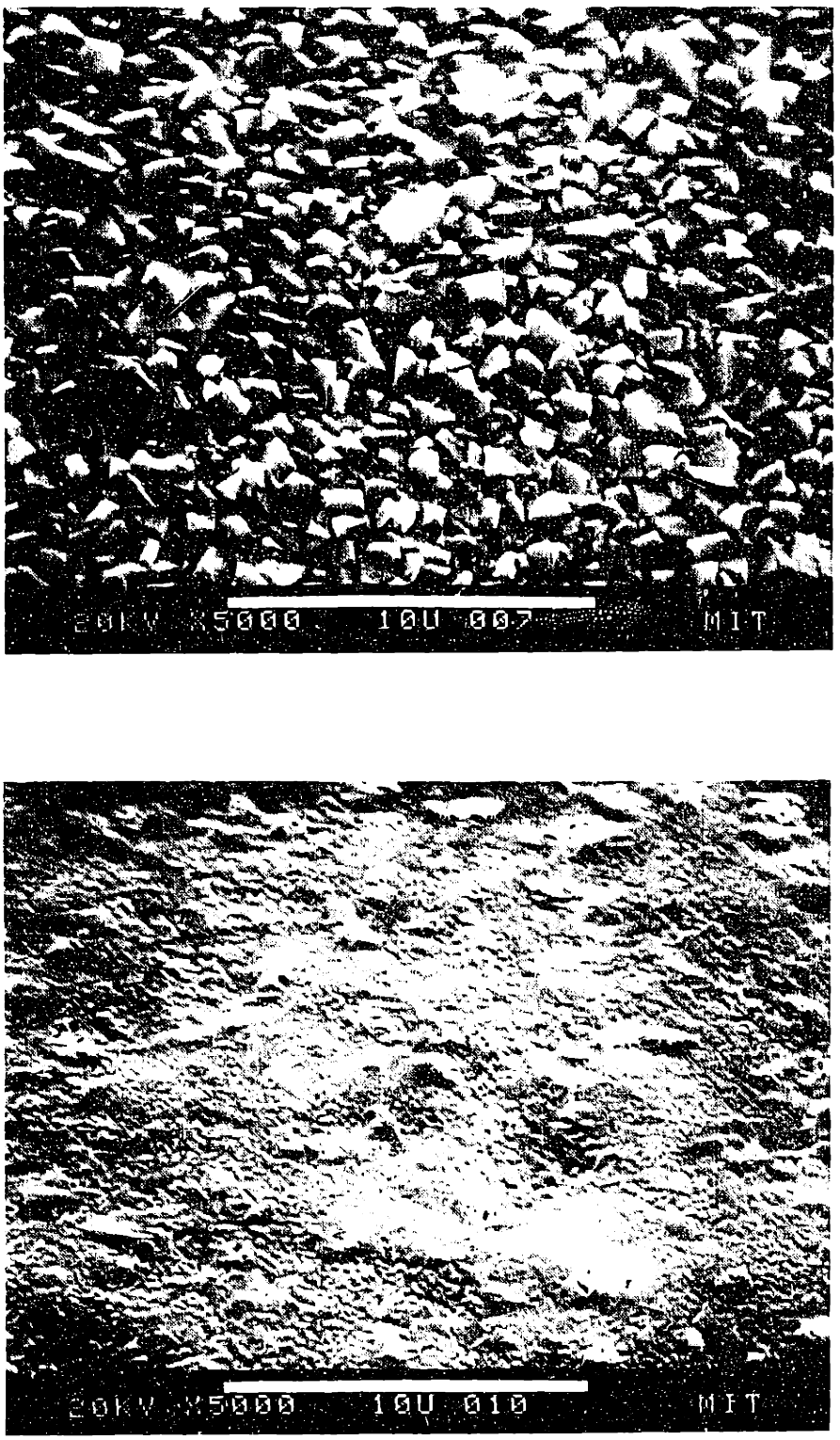

Figure 5.1.7 SEM secondary electron images of Y_2O_3-dispersed Ni_3Al after oxidation at 1000°C for (a) 1hr and (b) 50hr.

in" and smooth out, Figure 5.1.7b. The original, large Ni-rich oxide grains can still be observed among a finer grained scale. Neither case shows any indication of θ-Al_2O_3.

Examination of samples with a higher Al content reveals fewer Ni-rich oxides. Figure 5.1.8a shows the morphology of NiAl after oxidation for 1hr. The morphology in this area of the sample indicates the presence of θ as was found by GAXRD, Figure 5.1.4. After a 50hr exposure, some areas still show signs of θ, but most areas have a ridge morphology, Figure 5.1.8b.

Polycrystalline NiAl reveals a clear variation in oxide morphology with substrate orientation, which was documented by Doychak [1986]. An excellent example is found on an Al-implanted NiAl which happens to have a much finer grain size than most samples, Figure 5.1.9a. In this case where the scale was found to be mainly θ-Al_2O_3, the contrast occurs because of charging on grains with a higher density of blades. However, it is not clear whether the darker grains transform to α more quickly or if the θ-Al_2O_3 just has a smoother morphology. The difference is shown quite strikingly in Figure 5.1.9b, where a grain with a very high density of oxide blades is adjacent to a grain with a much sparser blade content. Returning for a moment to the effect of the implanted species on the phase transformation, Figure 5.1.10 shows adjacent grains on Cr-implanted NiAl. In this case, the θ-Al_2O_3 structure is retained after 50hr on one NiAl grain while the other grain contains a ridge-like morphology typical of α-Al_2O_3 that has transformed from θ. While GAXRD, showed the scale consisted mainly of α, this indicates that there may be some effect of the Cr-implant after 50hr.

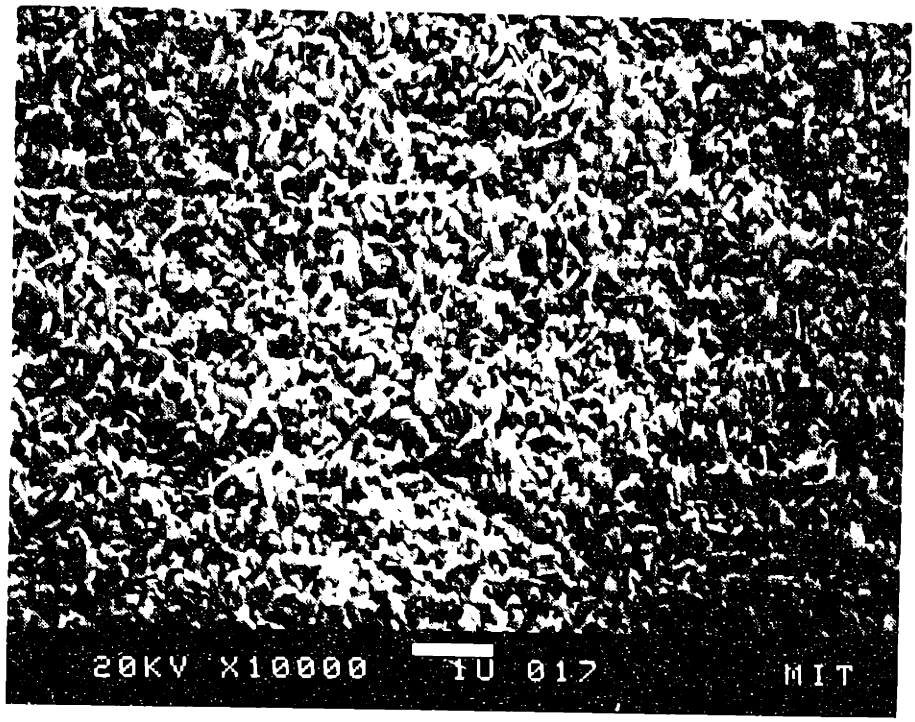

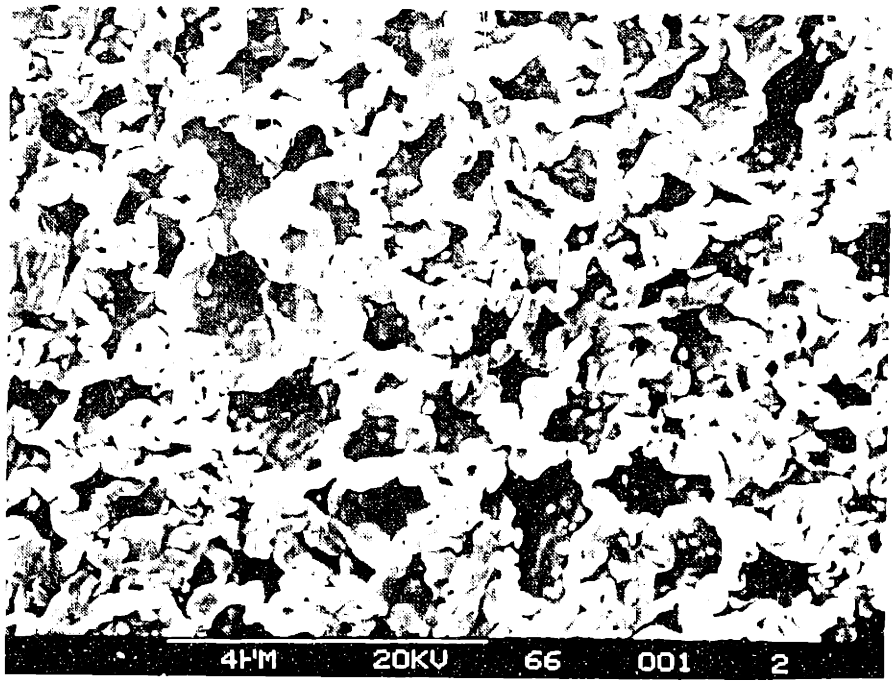

Figure 5.1.8 SEM secondary electron images of NiAl after oxidation at 1000°C for (a) 1hr and (b) 50hr.

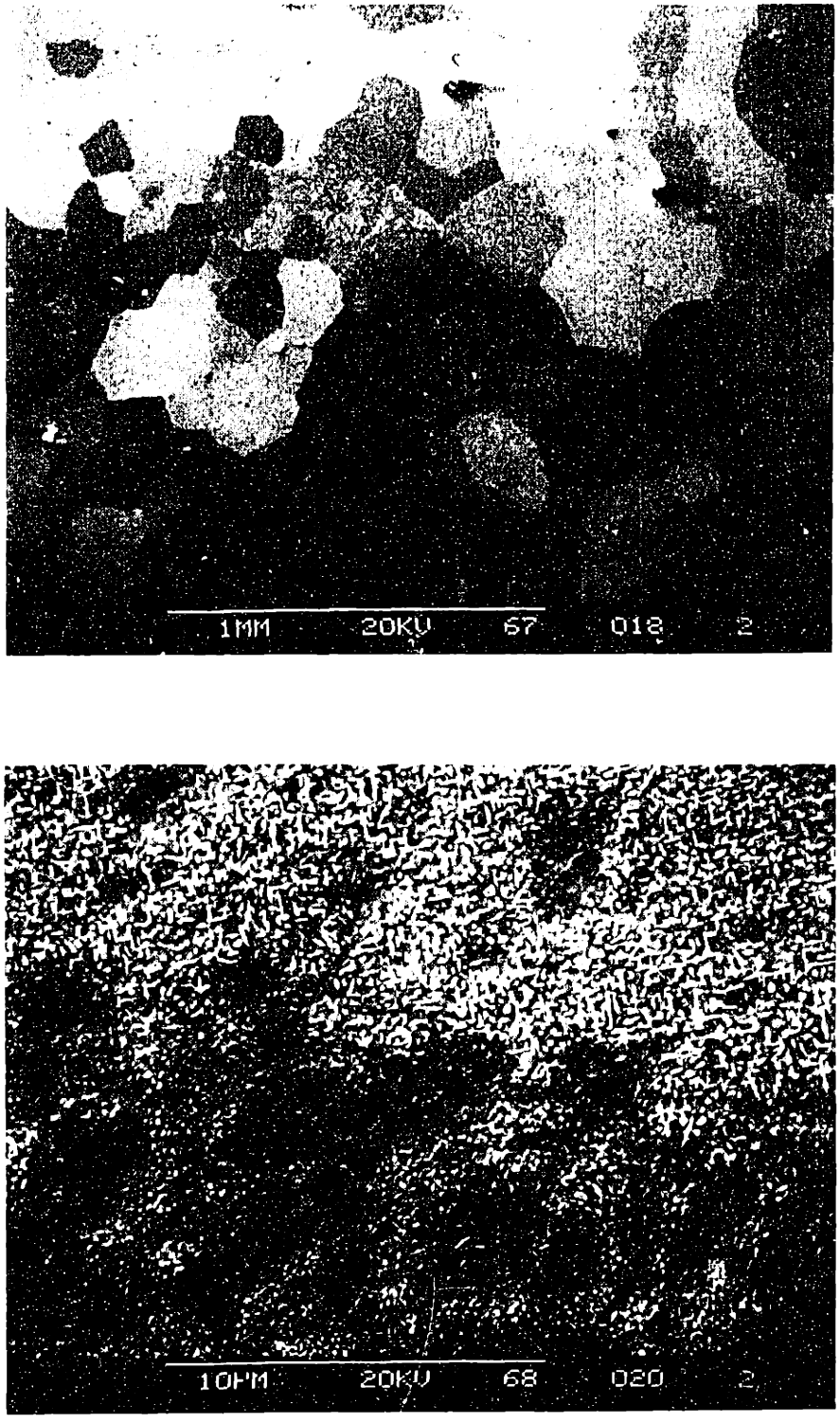

Figure 5.1.9 SEM secondary electron images of Al-implanted NiAl after oxidation at 1000°C for 1hr: (a) the lighter NiAl grains contain a higher density of charging oxide blades, and (b) adjacent high- and low-density NiAl grains.

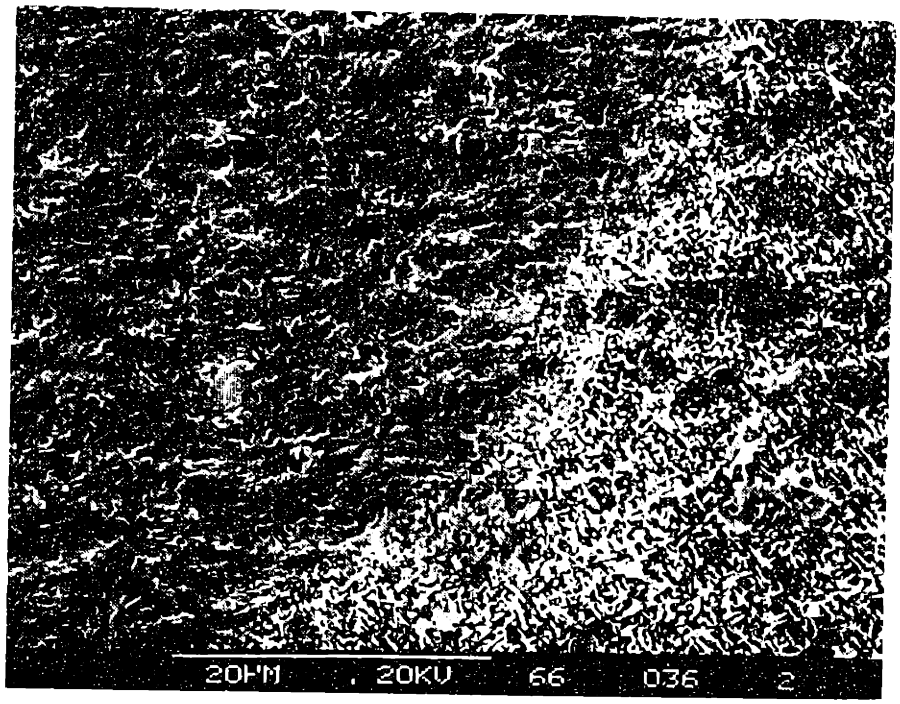

Figure 5.1.10 SEM secondary electron image of Cr-implanted NiAl after oxidation at 1000°C for 50hr. Adjacent substrate grains have oxide ridges typical of α-Al_2O_3 and oxide blades typical of θ.

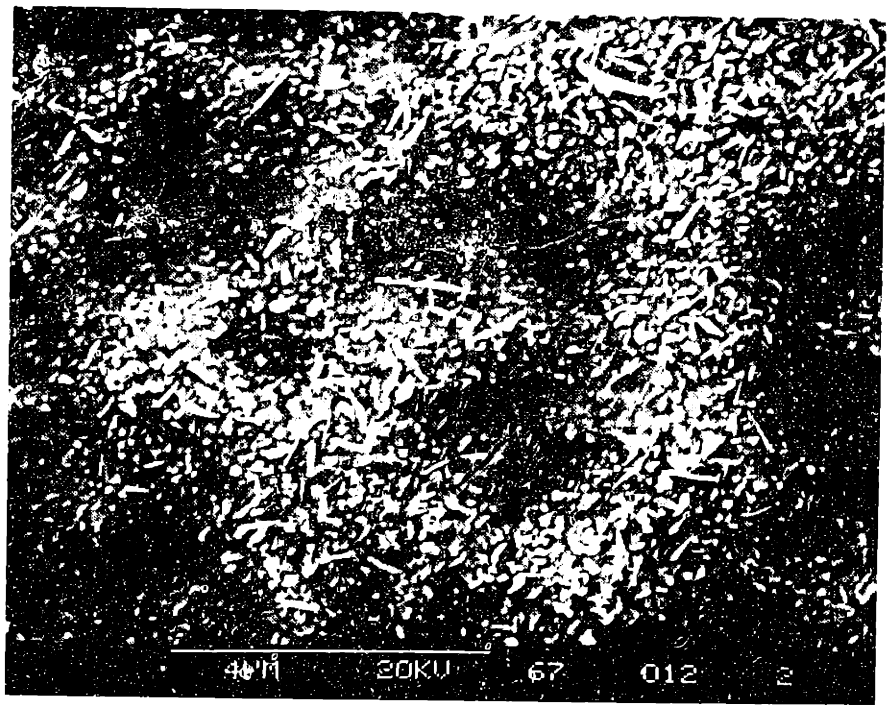

Figure 5.1.11 SEM secondary electron image of NiAl after oxidation at 1000°C for 1hr. Cracking appears to occur due to the θ-α phase transformation.

While having a large effect on the scale morphology, the phase transformation may also affect scale adherence. Figure 5.1.11 shows commonly-occurring cracks in the scale after 1hr. These cracks are associated with the more than 10% volume reduction between the defective θ structure and the denser α-Al_2O_3 [Hagel, 1965a]. The structure in Figure 5.1.11 appears to be the precursor of the ridge structure where the oxide blades after 1hr will transform into interconnecting ridges observed after 50hr, Figure 5.1.10. These cracks, apparently due to the phase transformation, may also lead to spalling. Figure 5.1.12a shows a spalled region where the spallation is to the bare metal. This type of spallation occurred on a very small scale but was found on almost every sample examined. Figure 5.1.12b is a lower magnification image of the same area on NiAl + Zr oxidized for 50hr. The spallation appears to be concentrated on NiAl grains where the blade density is highest. This may indicate that cracking associated with the transformation leads to oxide spallation.

The potential effect of specimen surface preparation was not addressed in this project. Specimens were uniformly prepared with a 0.3μm surface polish. However, a single scratch on the surface provides an interesting revelation about the oxide morphology formation. Figure 5.1.13a shows a large scratch across a number of substrate grains. The scratch stands out clearly because it is a string of charging oxide blades, Figure 5.1.13b. The scratch crosses numerous grains with different morphologies but is still clearly evident. The large ridges in Figure 5.1.12b are also brighter because they are composed of a high concentration of oxide blades. Thus, one

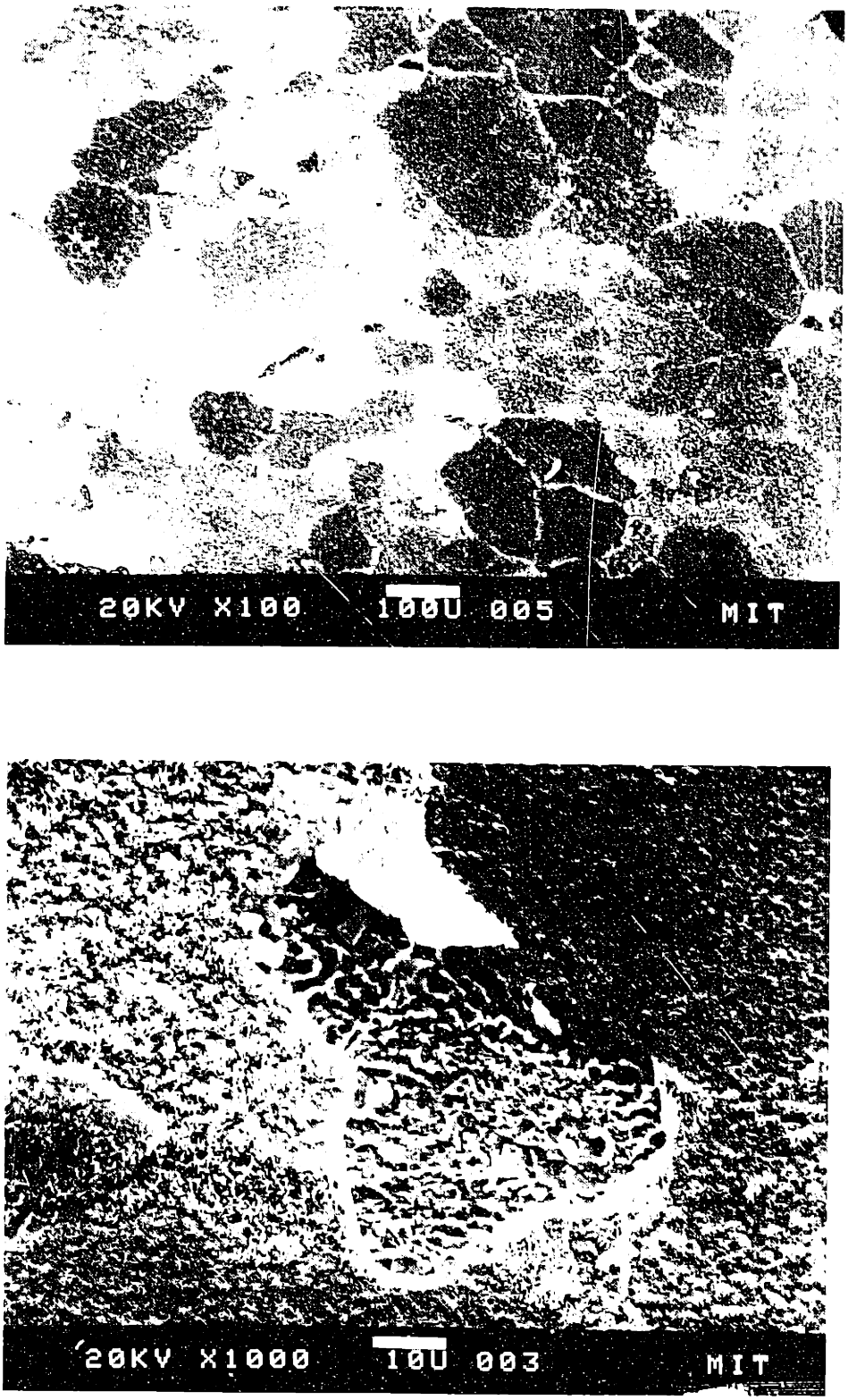

Figure 5.1.12 SEM secondary electron images of oxide spallation on NiAl + Zr after oxidation at 1000°C for 50hr. (b) is a higher magnification of the spalling observed in (a).

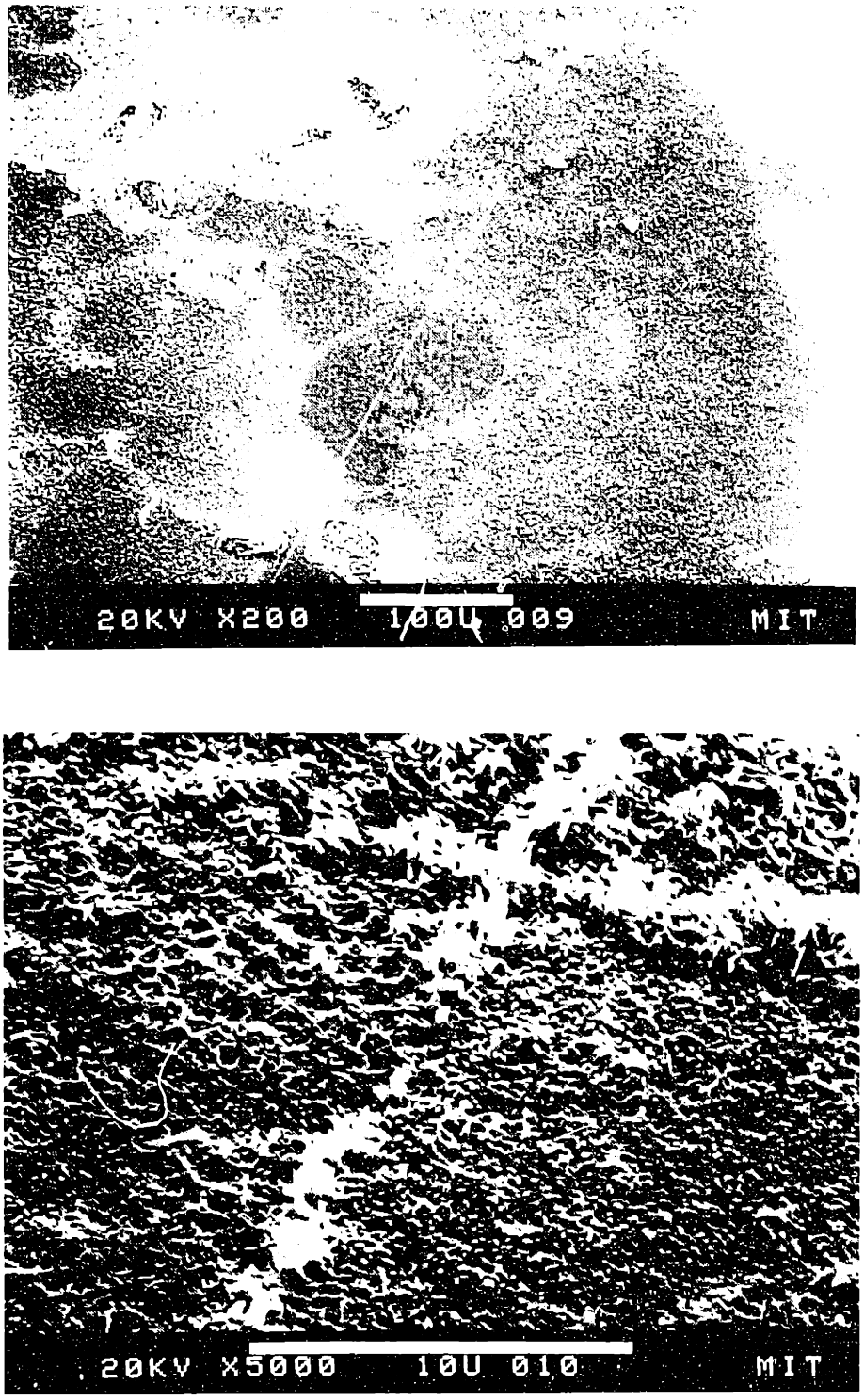

Figure 5.1.13 SEM secondary electron image of a "scratch" on NiAl + Zr after oxidation at 1000°C for 50hr. The line is charging in (a) because it is made up of a row of oxide blades (b).

difference between this work and some of the other results in the literature may be due to specimen preparation. For instance, Doychack, et al. [1989] reported uniform morphologies of oxide ridges after transformation to α-Al_2O_3 but used a 600-grit finish ($\approx$40μm). A coarser finish may produce a different type of ridge structure, with the ridge size and spacing reflecting the pre-oxidation surface preparation.

5.1.4 Tracer Results

The ^{18}O/SIMS experiments were hampered at 1000°C because of the phase transformation. Because the two Al_2O_3 phases are suspected to grow by different mechanisms, it is essential that before the second oxidant (either ^{18}O or ^{16}O) is introduced that the scale be fully α; or, to study θ, that no α form during any part of the oxidation.

Unfortunately at 1000°C, and even 950°C, analysis by GAXRD showed no scale formed on NiAl contained only one phase. As a result, the sputter depth profiles were spurious, varying from location to location, presumably depending on the local phase composition. One example is shown in Fig 5.1.14, where the scale on NiAl implanted with Y was profiled. The majority of the second oxidant ^{16}O was found near the gas interface, indicating strong Al diffusion outward. However, a secondary ^{16}O peak is found slightly further into the scale. With both phases present in the scale, there is no way to make any conclusions about the growth mechanism at this temperature. There may be a mixed diffusion process in θ-

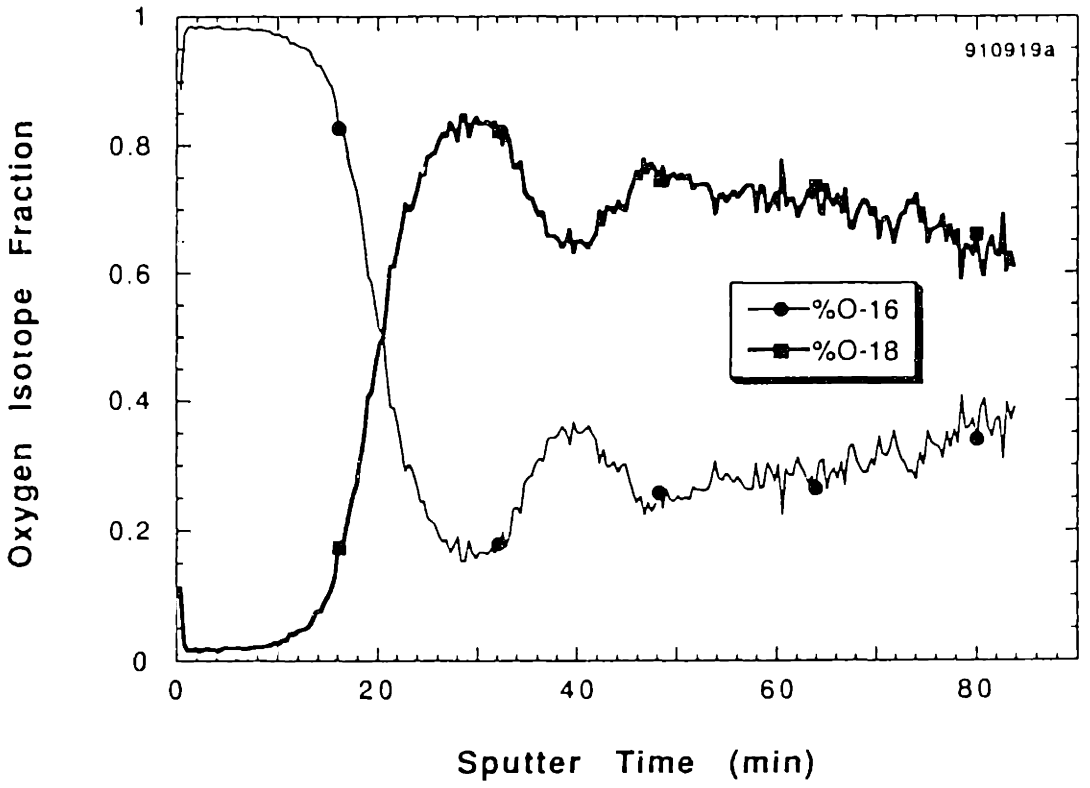

Figure 5.1.14 SIMS sputter depth profiles of the scale formed on Y-implanted NiAl after oxidation for 1hr at 1000°C. The second oxidant ^{16}O is found primarily near the surface but a second peak is found deeper in the scale.

Figure 5.1.15 STEM bright field image of the Al_2O_3 scale on Y_2O_3-dispersed Ni_3Al after oxidation at 1000°C for 50hr. The arrow points to a YAl_xO_y particle identified by EDXA.

The average grain size was approximately 300nm, Figure 5.1.15. A number of YAl_xO_y particles (50-100nm) also were observed in the Al_2O_3 scale (see the arrow in Figure 5.1.15). Since these particles occasionally fall out during TEM sample preparation, it is difficult to determine the exact void content. However, the number of voids is clearly not as high as observed in undoped FeCrAl, Figure 4.1.13.

5.2 Results at 1200°C

The oxidation behavior at 1200°C was much more consistent because of the limited role of the phase transformation at this higher temperature. The scales were predominantly α-Al_2O_3, yet once again the Y-implanted samples did not clearly show the REE.

5.2.1 Isothermal Oxidation Results

A parabolic plot of the kinetic data is shown in Figure 5.2.1 for the various Al contents. Except for Ni-23Al, the data appear to follow a parabolic rate law. None of the major deviations, observed at 1000°C, appear at 1200°C. Also unlike at 1000°C, the Y-implant appears to have reduced the total weight gain in each case. A change in the oxidation rate is not as clear.

The most unusual behavior is that of Y-implanted and unimplanted Ni-23Al. It appears that after ≈4hr both samples experience a large weight gain. This type of behavior may indicate a breakaway condition where an initial Al_2O_3 scale is formed, but the

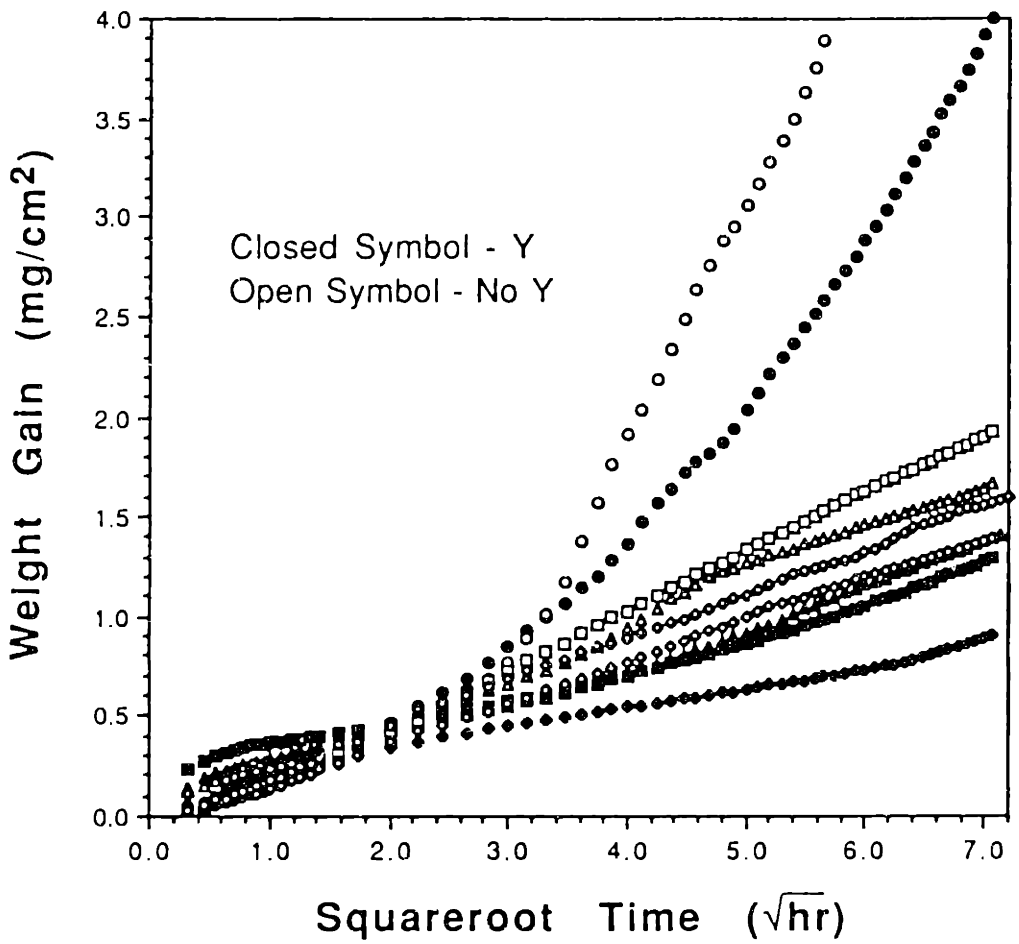

Figure 5.2.1 Parabolic plot of weight gain versus squareroot of time for Y-implanted and unimplanted Ni-Al materials at 1200°C in 1atm O_2. Circles = 23wt%Al, triangles = 30wt%Al, diamonds = 31.5wt%Al and squares = 36wt%Al.

Al content in the near-surface alloy drops to the point where Ni begins to oxidize. This would cause a more rapid weight gain when the protective Al_2O_3 scale is compromised. Since this behavior is not typical for the REE, this behavior was not investigated further.

With Al content higher than 23wt%, variation in Al content did not significantly affect the oxidation rate. All of the unimplanted samples (30, 31.5 and 36wt%) lie within a definable band and the implanted samples lie within a second band slightly lower than for unimplanted NiAl. A parabolic plot of NiAl only with and without a RE addition, is shown in Figure 5.2.2. In this case, a clear reduction in the oxidation rate is evident when either Y or Zr is present. The reduction is by a factor of 3, comparable to the reduction observed in FeCrAl alloys (Sec. 4.2.1).

No significant transient periods were observed at this temperature. Also, there is no kinetic evidence to suggest a significant effect of the phase transformation at 1200°C.

5.2.2 Cyclic Oxidation Adherence Results

The reduction in the isothermal oxidation rate suggests a beneficial effect of the Y-implant. Once this effect was confirmed, the next test was to check to see if the oxide adherence was also improved by the Y-implant. Figure 5.2.3 shows the weight change during twenty 2hr cycles for NiAl and Ni_3Al samples. While the Zr alloy addition appears to improve the oxide adherence, the Y-implant does not appear to have a lasting effect on adherence. The first few cycles show little weight loss, but afterward the adherence is little

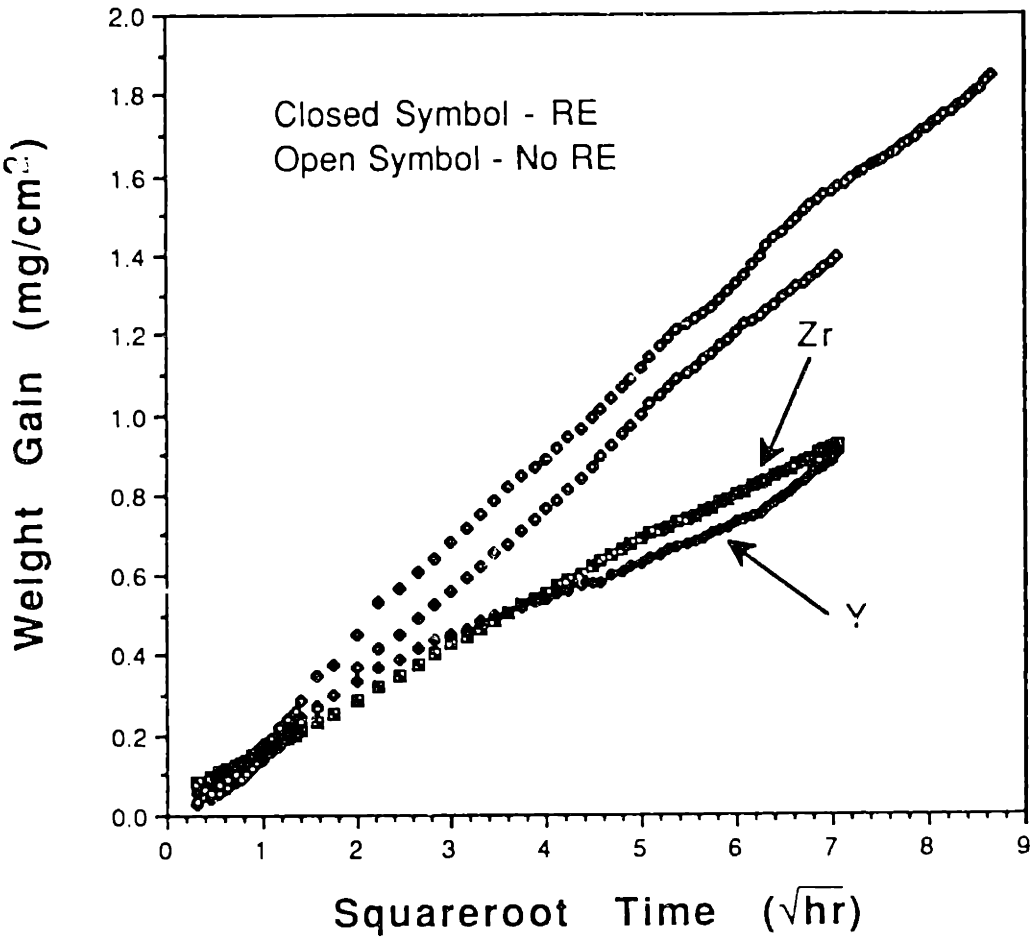

Figure 5.2.2 Parabolic plot of weight gain versus squareroot of time for doped and undoped NiAl at 1200°C in 1atm O_2. A clear reduction in oxidation rate is evident here with the addition of Zr and Y.

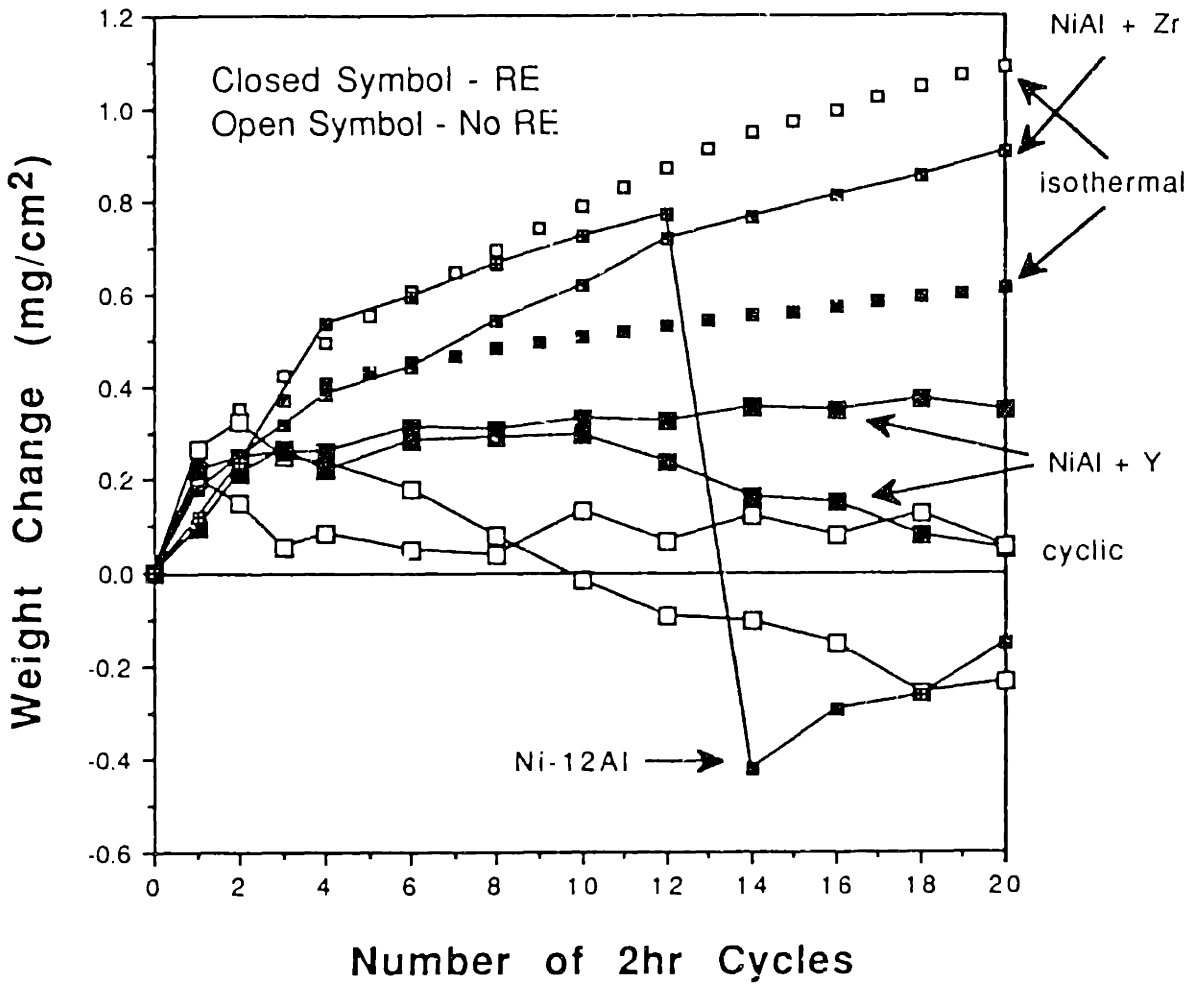

Figure 5.2.3 Isothermal weight gains plotted with the weight change over 20 2-hr cycles at 1200°C in 1atm O_2. A consistent improvement in oxide adherence is not observed when NiAl is implanted with Y. The Zr addition appears to significantly improve the adherence.

better than the unimplanted case. Included in Figure 5.2.3 are two Y implanted samples, one implanted at MIT, the other implanted at the Naval Research Laboratory (NRL) in Washington, D.C. (the slightly higher result). Both samples were implanted with 2 x 10^{16} Y/cm^2 at 70keV. The second implant was made in order to check the implantation work done at MIT. While the second implant shows a slightly higher weight gain, both samples exhibit a significantly lower weight gain than in the isothermal case. This indicates loss of oxide during cycling.

The Y_2O_3-dispersed Ni_3Al was a most unusual case. During the first two cycles, a dark, Ni-rich (by EDXA) oxide formed on the surface of the sample. This is similar to the transient oxide observed at 1000°C. The total weight gain over the next 10 cycles appears to be quite low, indicating protective behavior. Between the 13th and 14th cycle, the sample lost more than 1mg/cm^2 -- massive spallation, but not to the bare metal. The sample was still covered with a light gray film, indicative of Al_2O_3; the outer dark oxide appeared to be completely spalled off. However, over the next six cycles this dark surface layer grew back and no further weight loss was detected. Apparently the outer Ni-rich layer was able to grow back with additional exposures, while the underlying Al_2O_3 remained somewhat protective. This observation raises the question of how Ni was able to get to the surface through an intermediate Al_2O_3 oxide layer. The cyclic tests are also equivocal about improvement in adherence associated with the addition of a Y_2O_3 oxide dispersion to Ni_3Al.

5.2.3 SEM Results

The morphologies at 1200°C observed by SEM shed a little more light on the effect of the Y-implant and allow a more careful study of the oxide after cyclic exposures. Just as at 1000°C, the morphology of the Y-implanted scale after oxidation for 50hr at 1200°C shows remnants in certain areas of initial θ-Al_2O_3 formation, Figure 5.2.4. This includes cracking and some spallation, but also what appear to be remnants of oxide blades or whiskers. The Y-implanted NiAl morphology is significantly different from the morphology on NiAl + Zr and undoped NiAl, Figure 5.2.5. With the addition of Zr, a ridge structure is found. In areas where the scale is still adherent on undoped NiAl, a ridge-type structure is also observed, but the ridges are much finer, nearly covering the entire surface. Unique to the undoped NiAl, whiskers are also observed to occur across the entire surface, though somewhat sparsely compared to undoped FeCrAl, Figure 4.2.3.

After isothermal exposure of undoped NiAl, much of the scale spalls off. After a 50hr exposure, the underlying substrate has two distinctive regions, Figure 5.2.6. One type is imprinted with oxide grains ($\approx$1μm grain size). The other type is much smoother. In Figure 5.2.6a the smoother areas also contain areas with faint imprints. These areas appear to be areas which once were imprinted and subsequently lost contact with the oxide. In Figure 5.2.6b, the smooth areas in this particular image appear to be faceted, probably with respect to the substrate orientation. This is very similar to

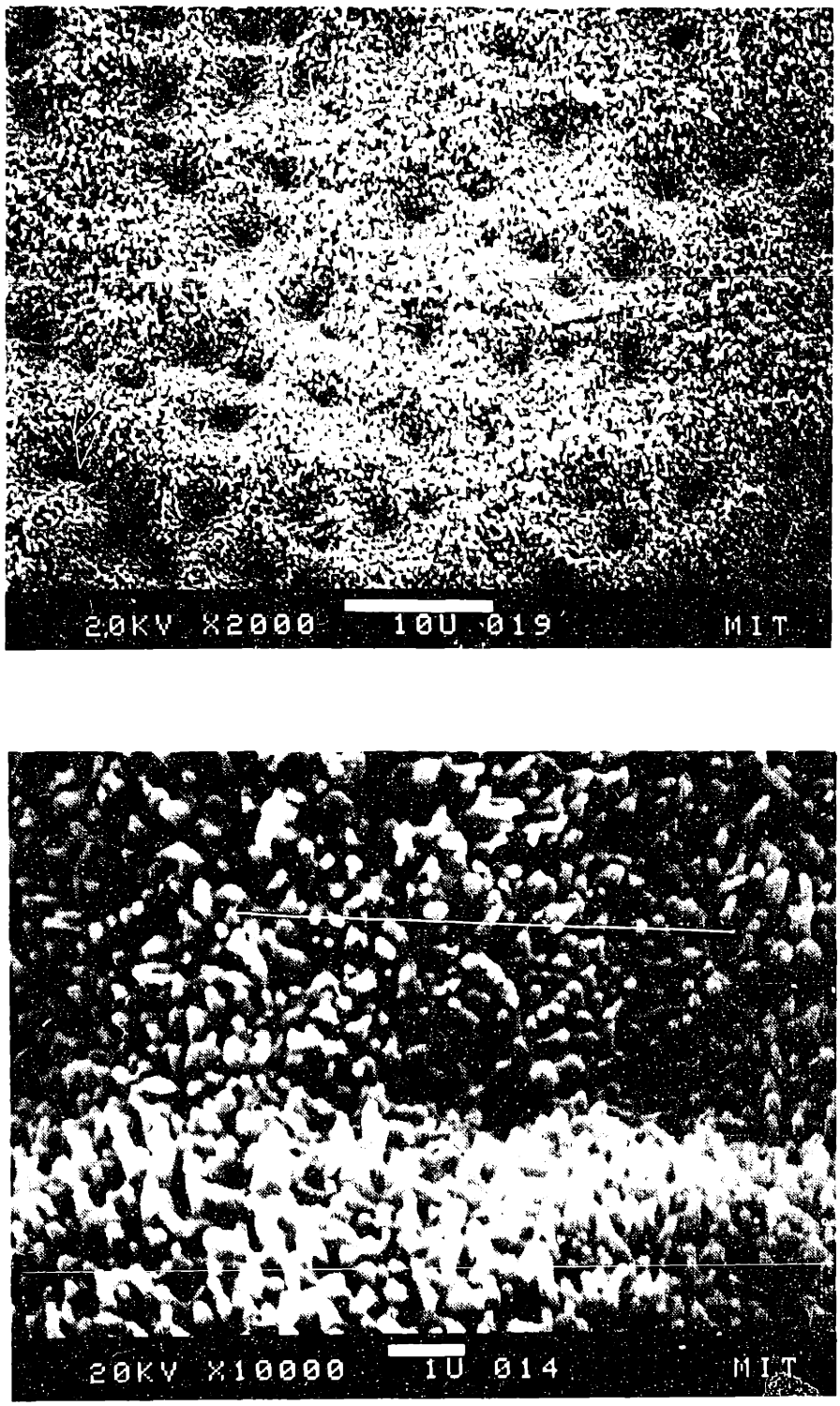

Figure 5.2.4 SEM secondary electron images of Y-implanted NiAl after oxidation at 1200°C for 50hr.

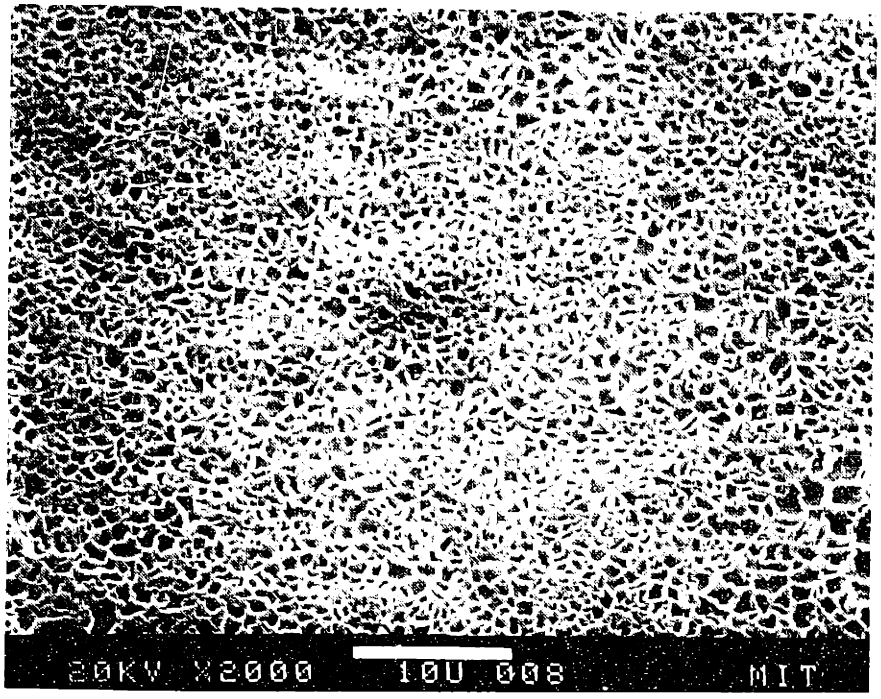

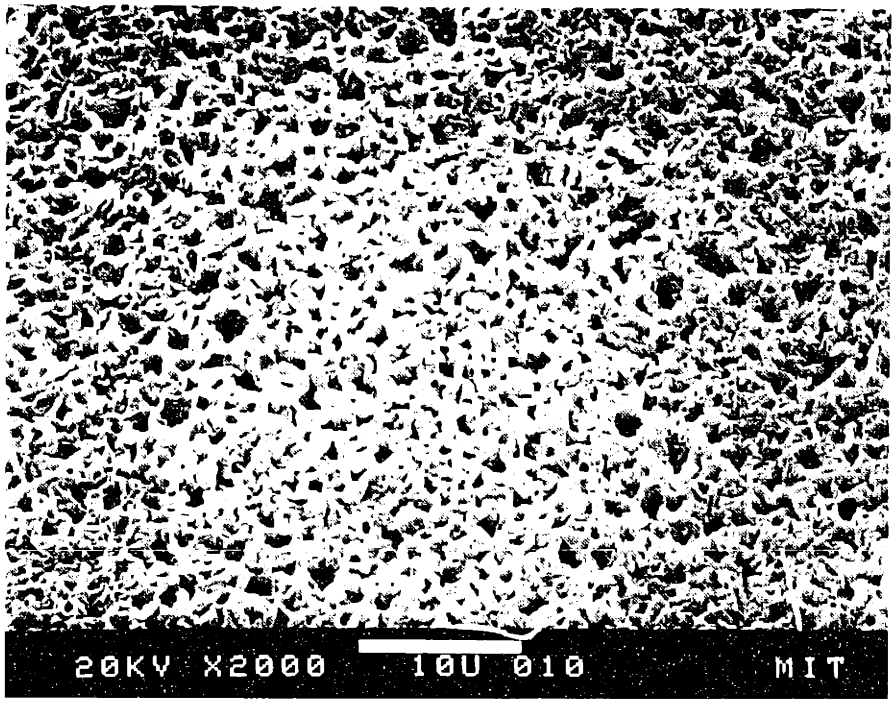

Figure 5.2.5 SEM secondary electron images of oxide scales after oxidation at 1200°C for 50hr on (a) NiAl + Zr and (b) NiAl.

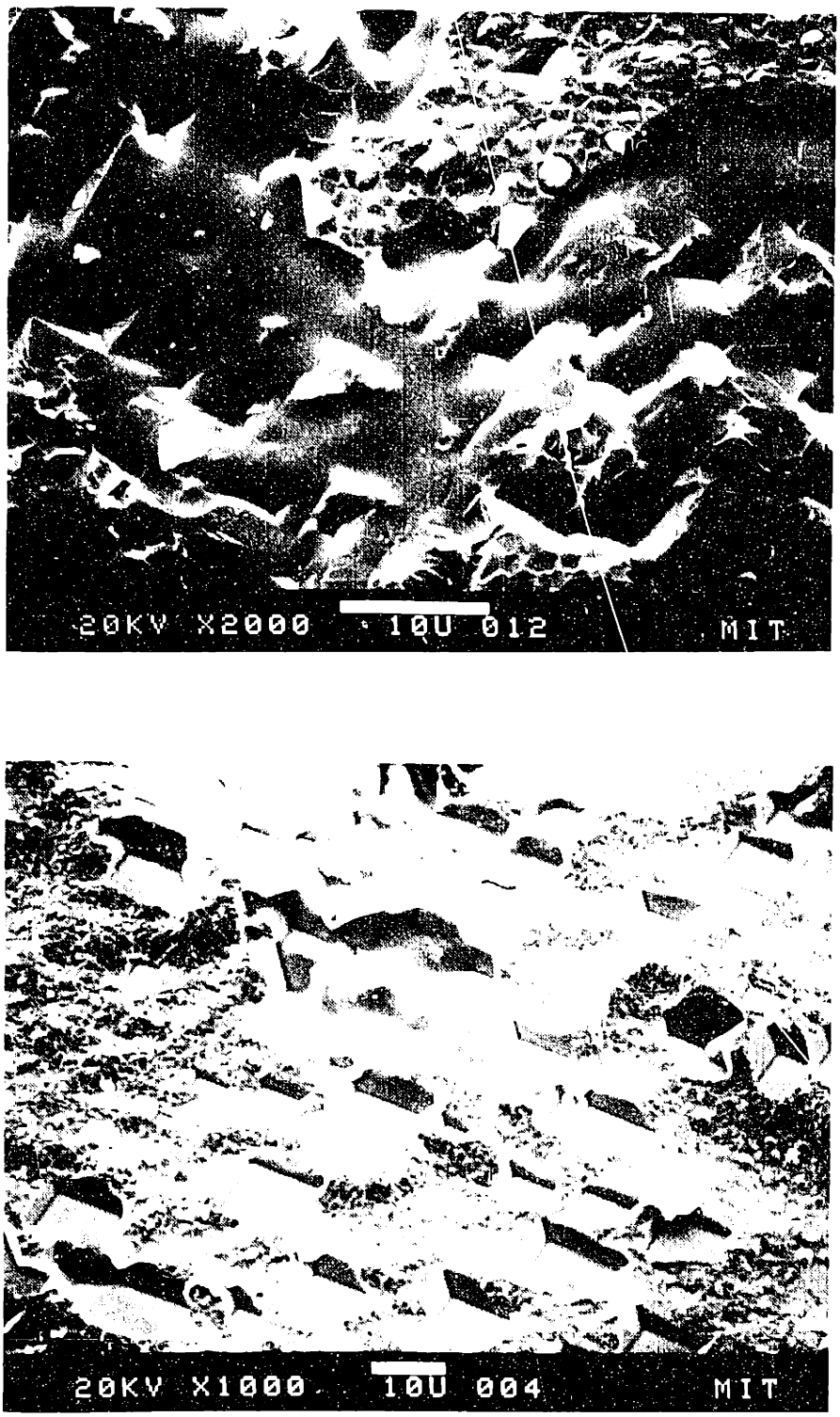

Figure 5.2.6 SEM secondary electron images of the Ni-Al substrate underneath oxide grown at 1200°C for 50hr on (a) Ni-31.5wt%Al and (b) Ni-30wt%Al.

the observations of Smialek [1978] on NiAl. The faceting may be enhanced by evaporation of Al during oxidation.

Another set of samples were examined after a 2hr exposure. Figure 5.2.7 shows the extensive spallation of the scale on undoped NiAl after a 2hr exposure (1 cycle). The morphology of the adherent scale comprises a very fine ridge structure, with no evidence of θ-Al_2O_3. With an Y implant after 2hr, it is a very different case. Figure 5.2.8a shows the scale to be much more adherent than the undoped case. However, the morphology in some areas is reminiscent of the oxide blades of θ-Al_2O_3, Figure 5.2.8b.

While the SEM observations show a difference in oxide adherence after 1 cycle (2hr), the differences disappear after 20 cycles. Figure 5.2.9 shows the surface spallation on Y-implanted and unimplanted NiAl. There is a similar scale morphology and the amount and type of oxide spallation is virtually the same.

The addition of Zr was observed to improve the oxide adherence (Figure 5.2.3), and this was also observed in the SEM. Figure 5.2.10 shows that the scale on NiAl + Zr is very adherent. There is a slight variation in the ridge morphology, possibly due to variations in substrate orientation. The surface on Y_2O_3-dispersed Ni_3Al consisted mainly of Ni-rich oxide which appeared to be somewhat cracked and finely spalled, Figure 5.2.11. There were no areas where the oxide scale had spalled to the bare metal. However, it is difficult to come to any conclusions about the underlying Al_2O_3 scale because of the overlying Ni-rich layer.

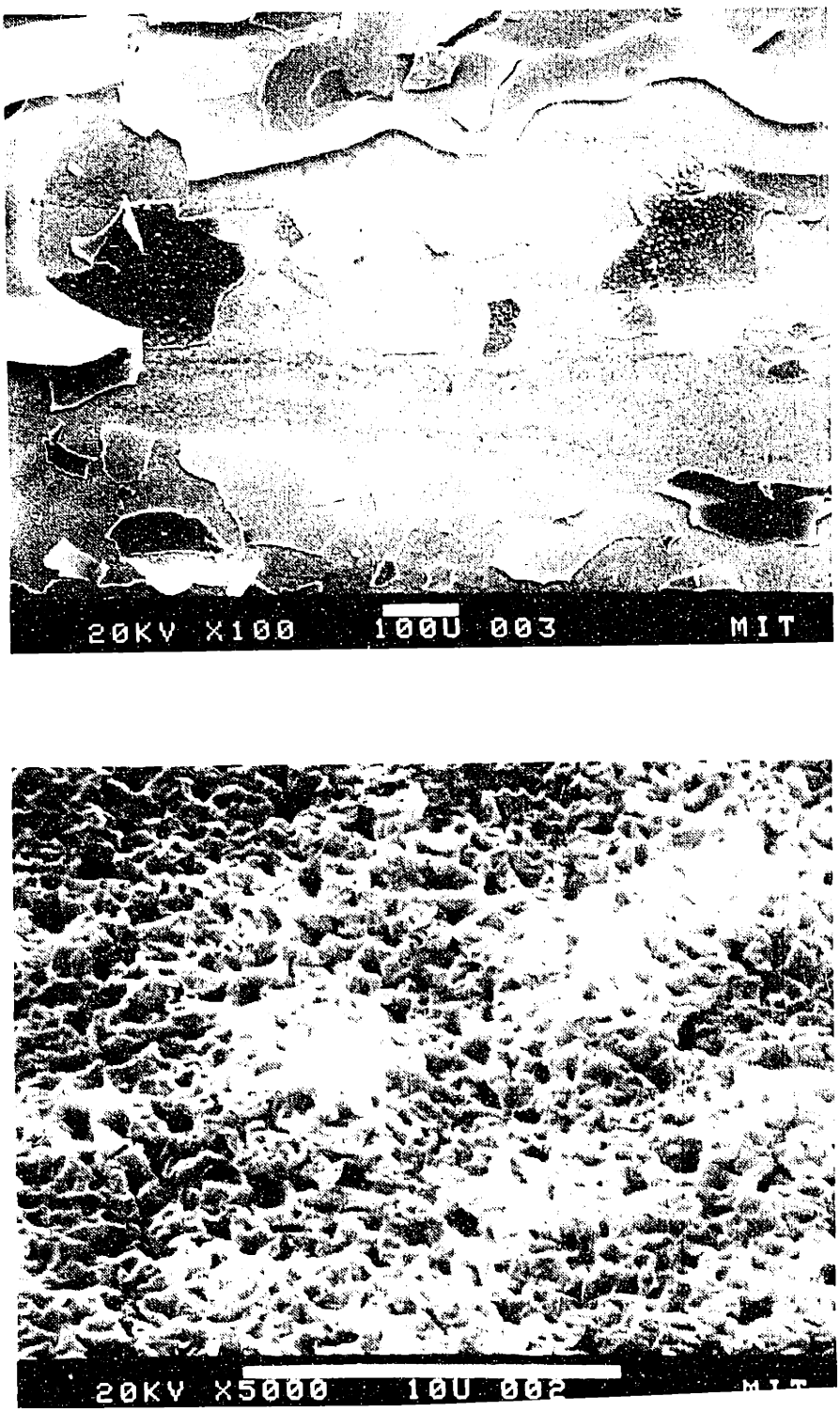

Figure 5.2.7 SEM secondary electron images of undoped NiAl after oxidation at 1200°C for 2hr. A large fraction of the scale is spalled (a); the adherent scale has a fine ridge-type morphology.

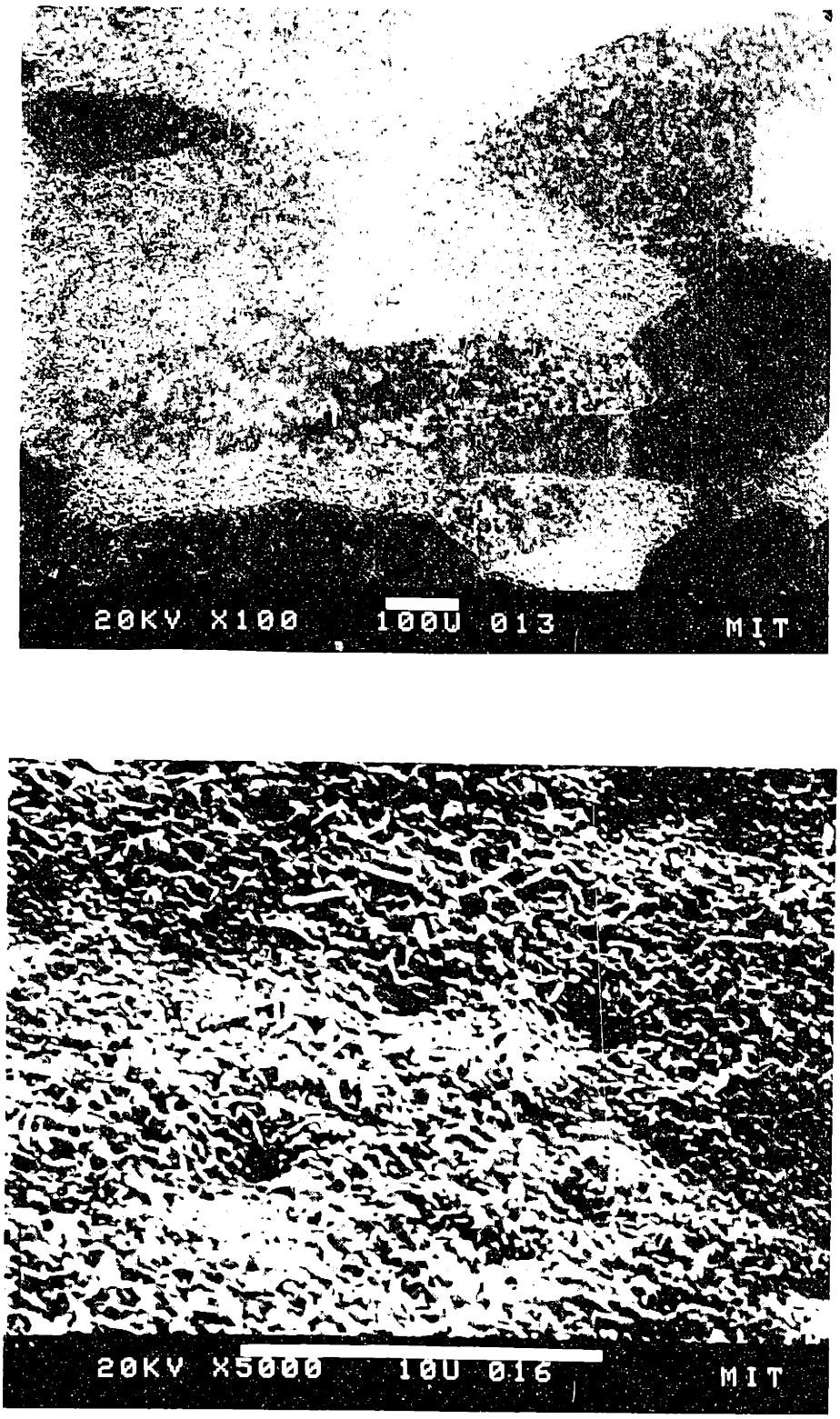

Figure 5.2.8 SEM secondary electron images of Y-implanted NiAl after oxidation at 1200°C for 2hr; (a) the substrate grain orientation effects the density of oxide blades on the scale surface; (b) a higher magnification image of the high-density blade morphology.

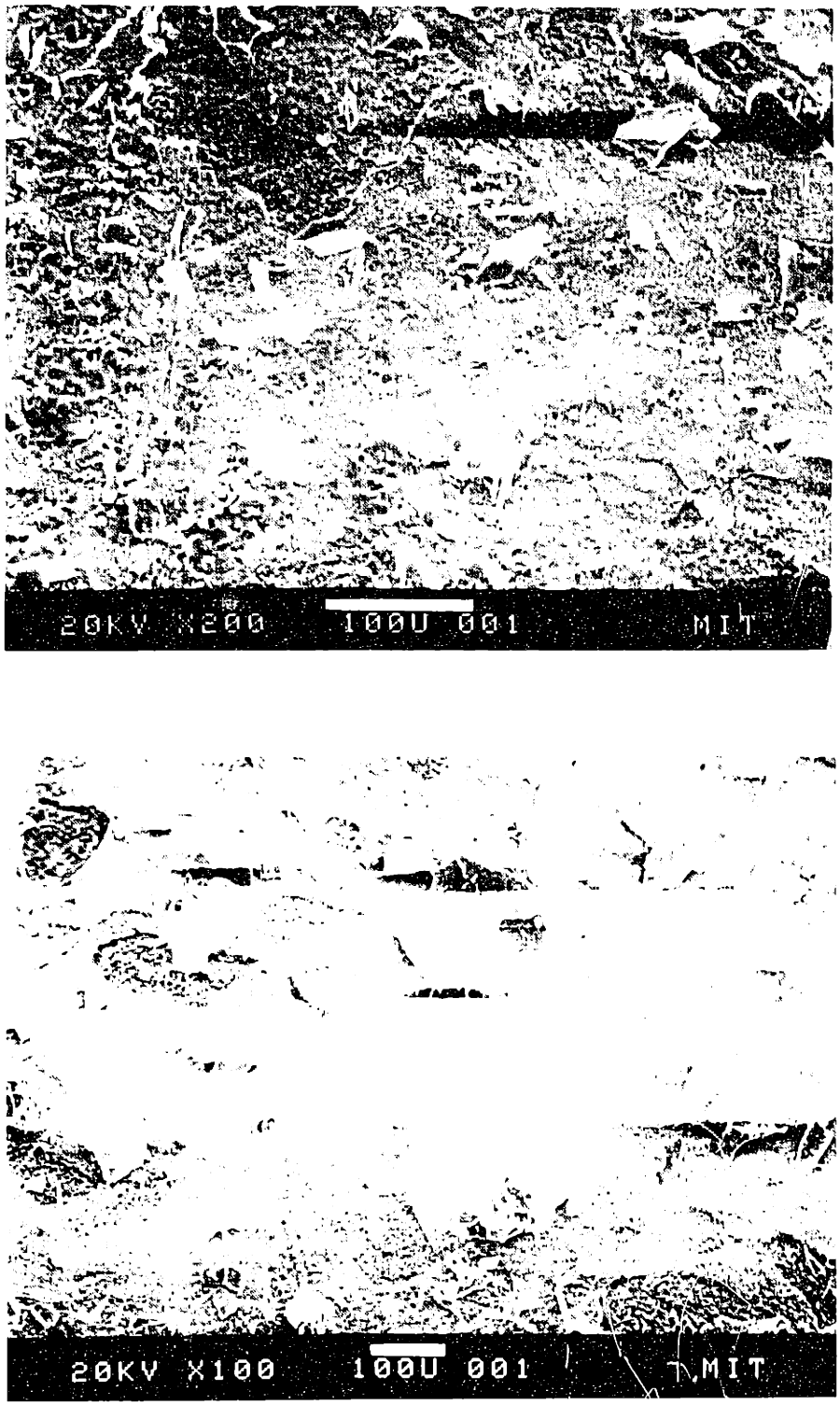

Figure 5.2.9 SEM secondary electron images of surface spallation after 20, 2hr cycles at 1200°C on (a) Y-implanted NiAl and (b) undoped NiAl.

Figure 5.2.10 SEM secondary electron image of NiAl + Zr after 20, 2hr cycles at 1200°C. Only a small amount of spallation is found on this sample.

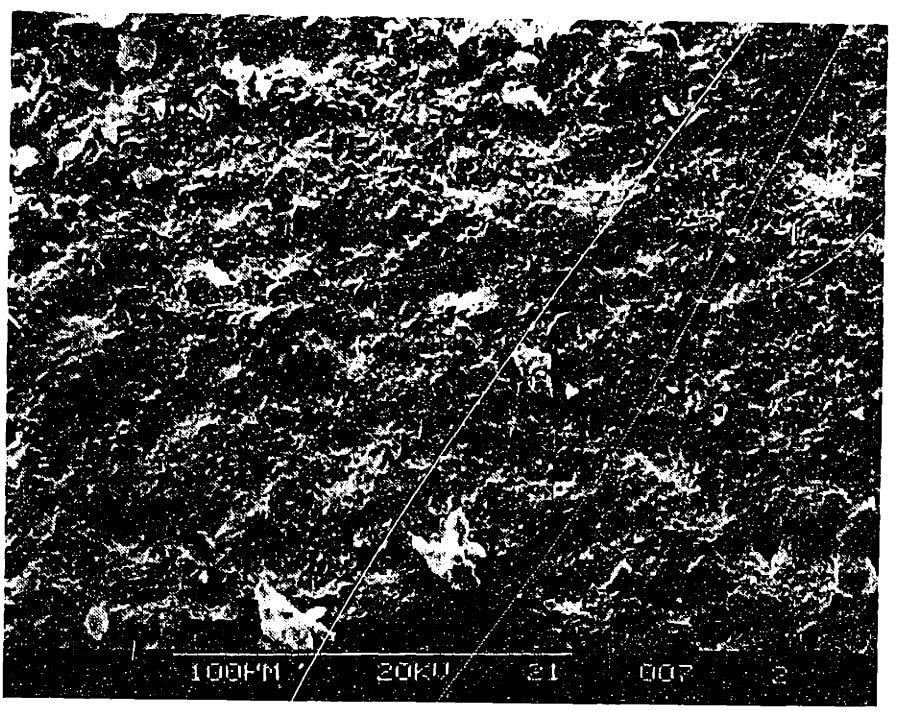

Figure 5.2.11 SEM secondary electron images of Y_2O_3-dispersed Ni_3Al after 20, 2hr cycles at 1200°C.

5.2.4 GAXRD Results

Because of the more-parabolic behavior at this temperature, only a few x-ray diffraction experiments were done. The most important issue was the phase formation for the sequential isotope oxidation experiments. Profiles of the oxide were made after 2hr on the undoped and doped samples. The only significant deviations from the undoped case are shown on an expanded scale in Figure 5.2.12. In the case of Y-implanted NiAl, a significant peak for θ-Al_2O_3 is still detected after a 2hr exposure. This is not found for either the Zr-doped or undoped samples which are primarily α-Al_2O_3. The Zr-doped sample is distinguished by the presence of a small peak for ZrO_2.

Testing of initial sequential isotope oxidation samples revealed that after a 40min total exposure at 1200°C, a small amount of θ-Al_2O_3 was retained on Y-implanted NiAl but that undoped NiAl formed a scale of only α. A second set of samples was tested after exposures of 20min and 1hr. After 20min and 1hr, undoped and Zr-doped NiAl samples were found to form α-Al_2O_3 scales. These were chosen for profiling because of the possibility of finding a mixed phase scale in Y-implanted NiAl.

5.2.5 Tracer Results

Sequential isotope oxidation samples at 1200°C had two conflicting purposes: first, to oxidize for a long enough time to form only α-Al_2O_3, and second, to grow a scale thin enough that it

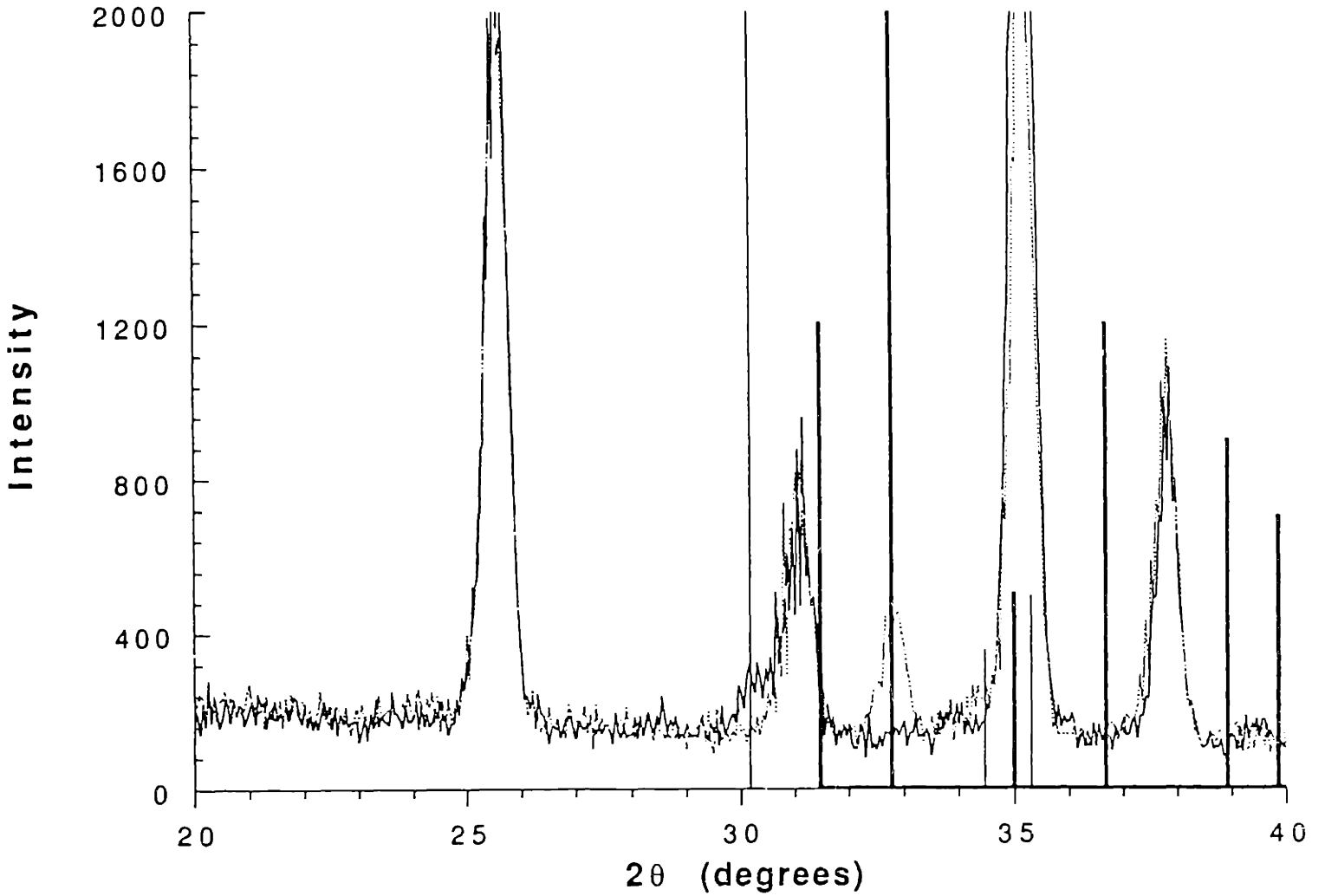

Figure 5.2.12 GAXRD profile of scales formed on Zr- (solid) and Y-doped (dashed) Ni 5at%Al after oxidation for 2hr at 1200°C in 1atm O_2. The thin solid lines denote ZrO_2 and the wider lines θ-Al_2O_3. The larger unmarked peaks match α-Al_2O_3. The scale formed on Y-implanted NiAl has retained some θ while the Zr-doped scale is primarily α with a small peak matching ZrO_2.

could be sputtered through in a reasonable amount of time (less than 1μm thickness). Initial sequential oxidation experiments were performed at 1200°C for a total of 40min (10min ^{18}O, 30min ^{16}O). A comparison of the sputter depth profiles for undoped and Y-doped NiAl is shown in Figure 5.2.13. Both profiles are similar, with some fraction of the new oxide being formed near the surface and the remainder being formed beneath the old oxide. However, the first isotope exposure of 10min is insufficient for the formation of a 100% α-Al_2O_3 scale on Y-implanted NiAl. Thus, while the α-Al_2O_3 scale on undoped NiAl may grow by a mixed diffusion mode, it is impossible in this case to make any more definitive conclusions about the effect of Y.

Increasing the first stage oxidation to 20min still failed to form a fully α-Al_2O_3 scale on Y-implanted NiAl. The emphasis was then switched to the Zr-doped NiAl, on which only α was formed after the first 20min of oxidation. In this case, the Zr-doped α-Al_2O_3 very clearly can be seen to grow by only the inward diffusion of oxygen, Figure 5.2.14a. The same result can also be seen when the oxidant order is reversed in Figure 5.2.14b. In each case, the second oxidant enriches the oxide surface slightly, but the strongest signal is found beneath the first-formed oxide layer. The shape of the profiles indicates predominant short-circuit diffusion with the small surface peak reflecting a small amount of lattice diffusion, Figure 2.6.

Figure 5.2.15 shows the profiles for the α scales on undoped NiAl in the same conditions as Figure 5.2.14. In each case, the undoped NiAl is observed to grow by a mixed diffusion mode, with a

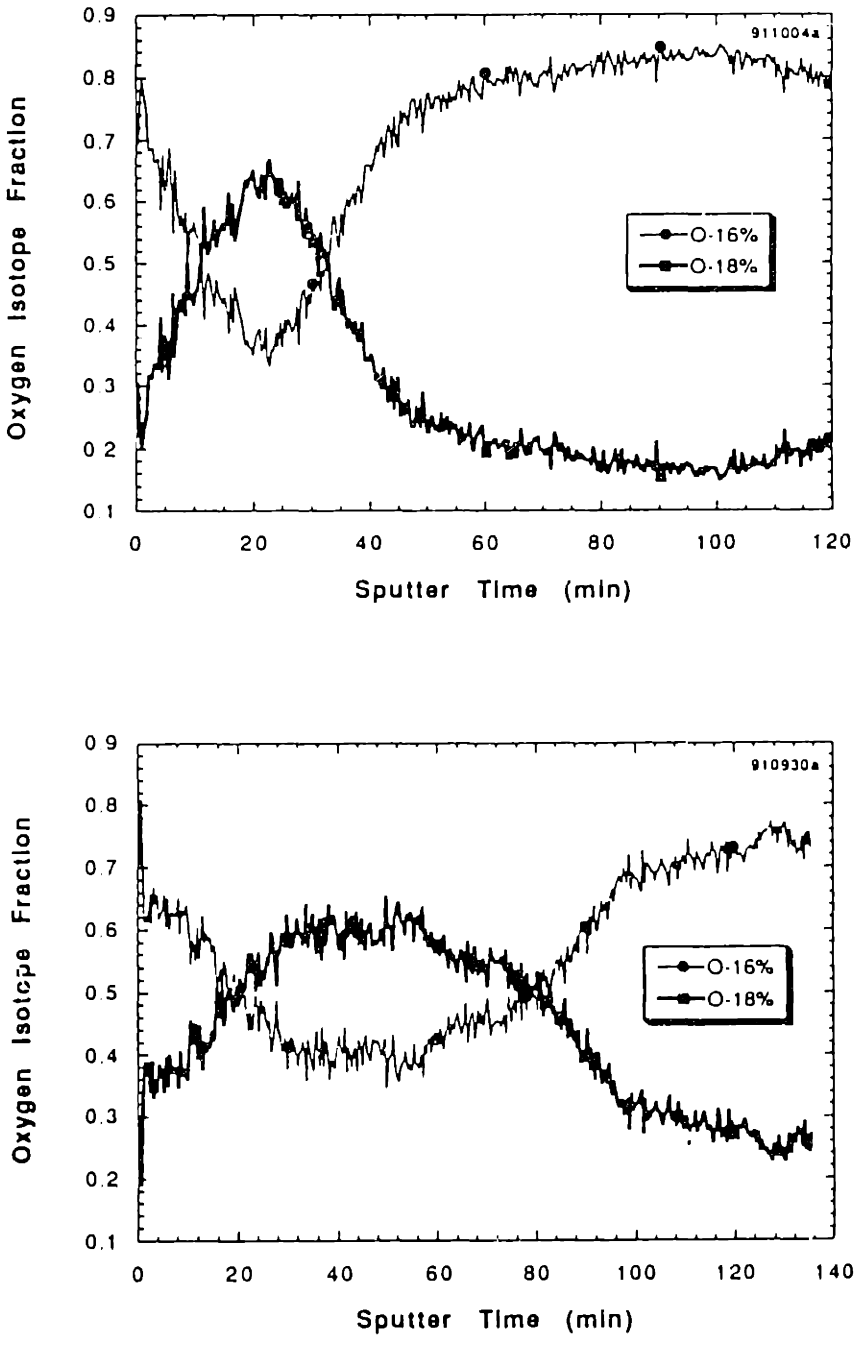

Figure 5.2.13 SIMS sputter depth profile of Al_2O_3 grown for 10min in ^{18}O and 30min in ^{16}O on (a) undoped NiAl and (b) Y-implanted NiAl.

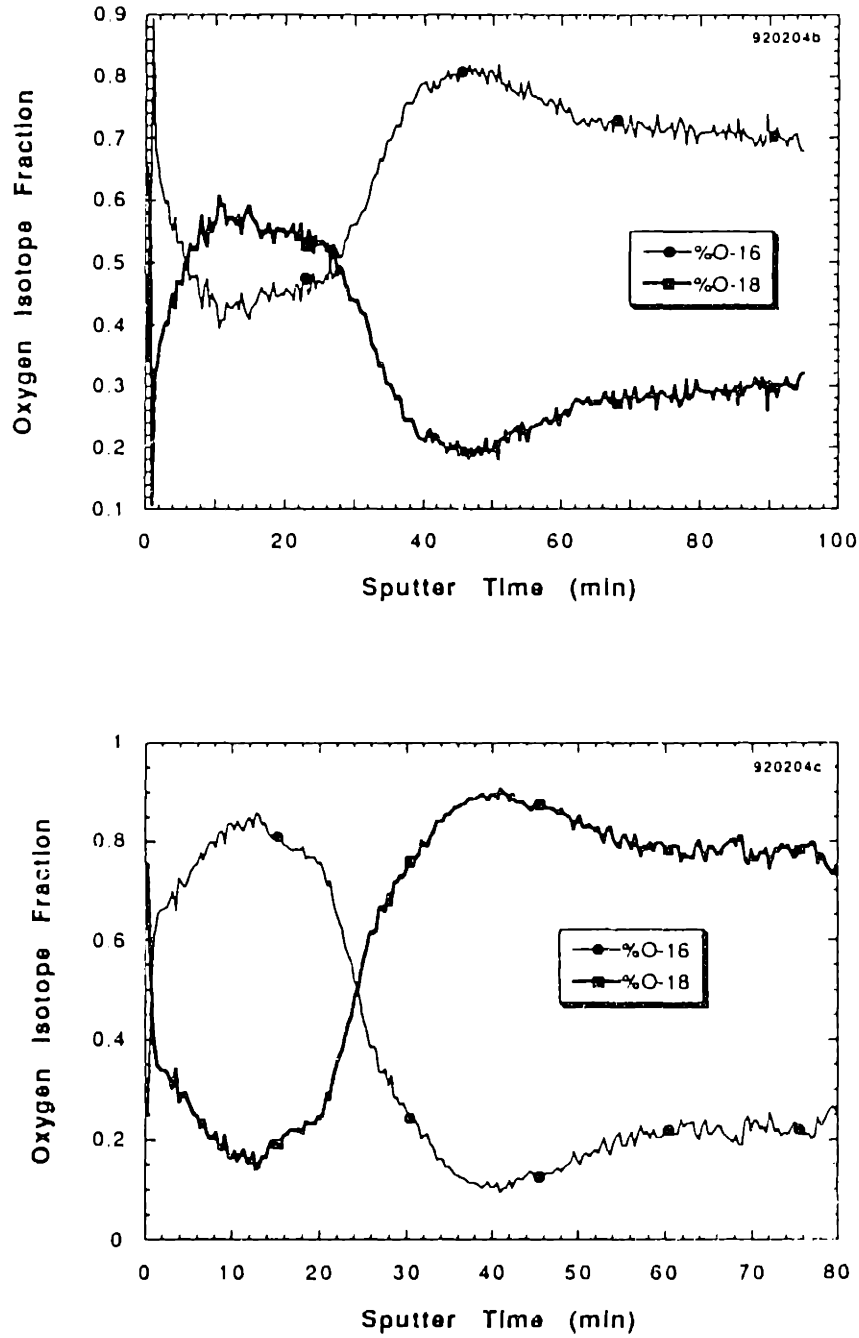

Figure 5.2.14 SIMS sputter depth profile of Al_2O_3 grown on NiAl + Zr at 1200°C for (a) 20min in ^{16}O and 40min in ^{18}O, and (b) 20min in ^{18}O and 40min in ^{16}O.

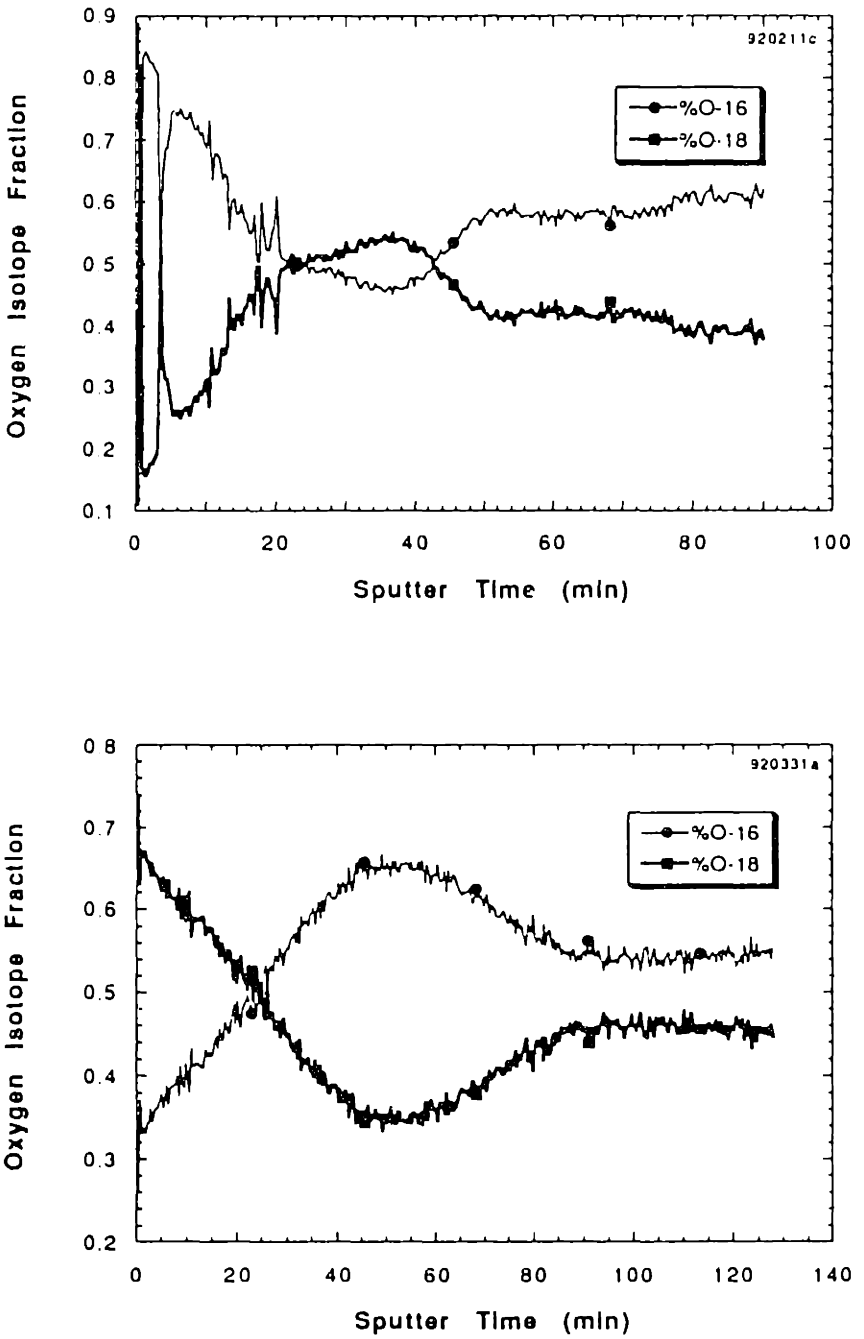

Figure 5.2.15 SIMS sputter depth profile of Al_2O_3 grown on undoped NiAl at 1200°C for (a) 20min in ^{16}O and 40min in ^{18}O, and (b) 20min in ^{18}O and 40min in ^{16}O.

layer of oxide rich in the second isotope at the gas interface. The absolute values of the two profiles are slightly shifted but the shapes are very similar. The shift in value is probably due to the difference in isotope gases. The ^{18}O gas is only ≈95% enriched while the ^{16}O gas is 99.8% pure. Comparing the doped and undoped profiles clearly establishes an effect of the reactive element addition on the oxidation mechanism.

5.2.6 AEM Results

Based on the results for the FeCrAl alloys, the goal in this case was to determine the location of the RE in the doped NiAl samples. Figure 5.2.16 is from a parallel section near the gas interface of oxide grown on Y-implanted NiAl after a 50hr exposure. It is difficult to find grain boundaries (or any structure) in this region of the Al_2O_3 matrix because of the abundance here of YAl_xO_y particles and voids. The composition variations and voids are clearly seen in the x-ray maps of Al and Y in Figure 5.2.16b. Attempts to identify these Y-rich particles using selected area diffraction were inconclusive, although $YAlO_3$ most closely fit the measured lattice plane spacings.

Based on the size and density of the Y rich oxides, most of the implanted Y must be present in this layer. This does not leave much Y to dope the oxide below this layer. This Y-rich layer at the gas interface is also an indicator that the oxide is growing by an inward growth mechanism as this layer was concentrated prior to oxidation at the metal interface.

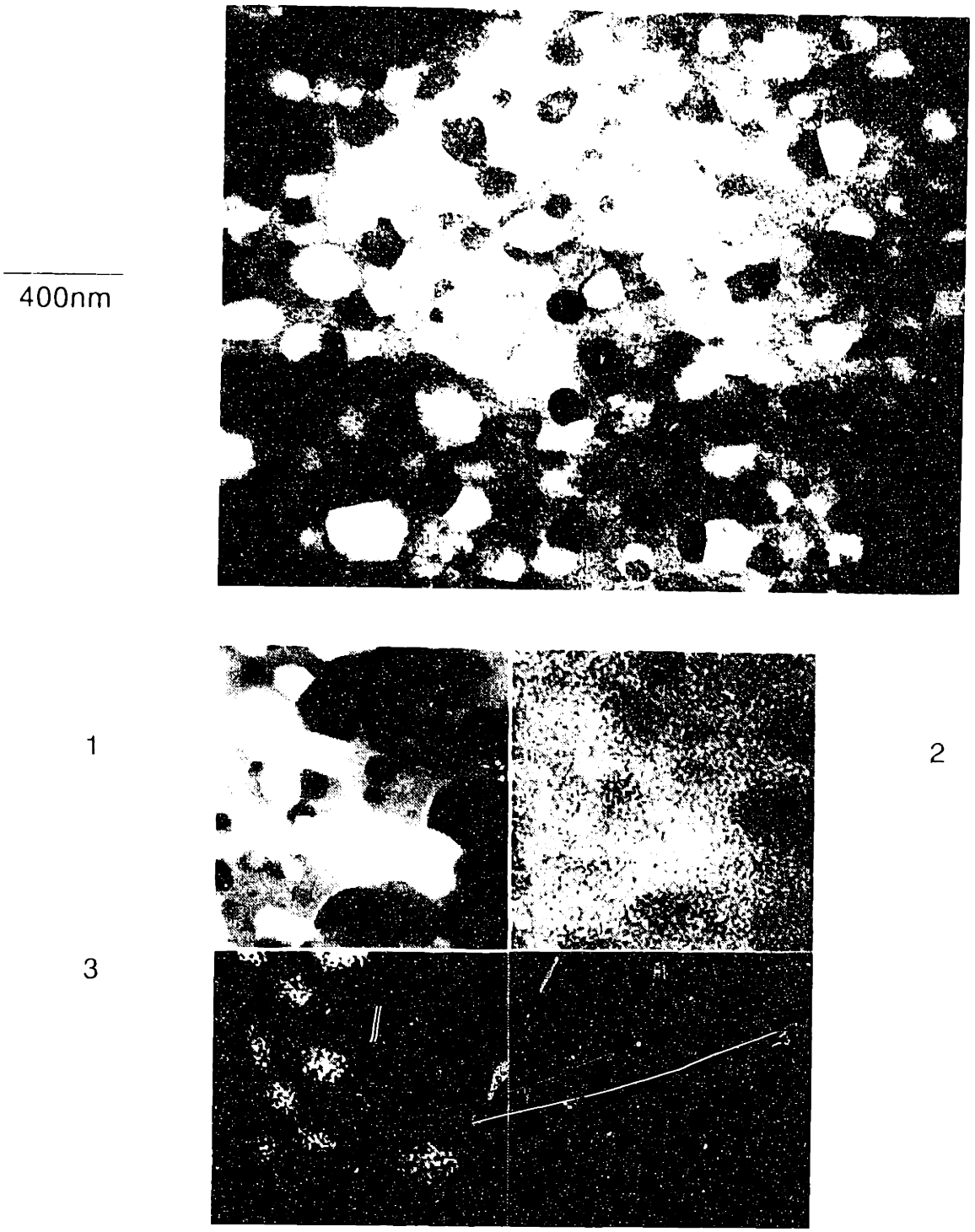

Figure 5.2.16 STEM (a) annular dark field image and (b) high resolution X-ray map of Al_2O_3 formed on Y-impanted NiAl near the oxide-gas interface after 50hr at 1200°C; 1) the binary image, 2) Al x-ray map and 3) Y x-ray map.

Figure 5.2.17 STEM bright field image of the Al_2O_3 scale on Y-implanted NiAl after oxidation at 1200°C for 50hr. Parallel section near the alloy interface.

Figure 5.2.18 STEM bright field image of the Al_2O_3 scale on NiAl + Zr after oxidation at 1200°C for 50hr. Parallel section near the gas interface. The dark particles are rich in Zr by EDXA.

A second section closer to the alloy interface contained only a few Y-rich oxides, but voids could be seen both on and away from grain boundaries, Figure 5.2.17. Y was found to segregate to the grain boundaries in this section. The average apparent Y/Al ratio at the boundaries was 0.089. This is within the range detected in the doped scales on the FeCrAl alloys, Table 4.2.

A parallel section near the gas interface of oxide formed on NiAl + Zr was also made. In this case, there are numerous ZrO_2 particles, Figure 5.2.18. However, unlike the Y-implanted case, the Al_2O_3 grain structure is clearly observed, and there are very few voids. Zr was found to segregate to the oxide grain boundaries in this sample (average Zr/Al ratio = 0.048). Thus, in both doped cases, the RE was found to concentrate near the gas interface and segregate to the oxide grain boundaries.

5.3 Results at 1400°C

A limited number of experiments was performed at 1400°C on ß-NiAl in order to establish the oxidation rate and to compare with the results obtained for FeCrAl materials. At the time this study was begun there were no published data available for the formation of Al_2O_3 scales at this or higher temperatures. As at lower temperatures, the Y-implant did not exhibit the typical REE, but at this temperature oxide formed on NiAl with an alloy addition of Zr was also observed to break down during both isothermal and cyclic behavior.

5.3.1 Isothermal Oxidation Results

The isothermal kinetic data are shown in Figure 5.3.1. Each of the undoped NiAl samples, regardless of Al content, exhibited parabolic behavior. It should be noted at this point that the correction for the evaporation of the Pt-Rh hangdown wire is significant at 1400°C and above. The raw data and the corrected data for three different NiAl samples are shown in Figure 5.3.2. At the end of the experiment, the evaporation weight loss approaches the oxidation weight gain. Ni-36Al again is somewhat higher than the other two Al compositions. This is most likely because of the cracks and voids in the alloy, making a higher effective surface area for oxidation.

While the undoped samples exhibited parabolic behavior, several of the doped (Y, Zr) samples broke down after ≈20hr, Figure 5.3.3. This breakdown is similar to that observed at 1200°C for Ni-23Al, but in this case it occurred only when a RE was present. The other two runs for Y-implanted NiAl did not exhibit breakdown and exhibited essentially parabolic behavior, Figure 5.3.1.

Breakdown of the Al_2O_3 scales with the addition of a RE is unusual in that this type of behavior was not observed in any of the FeCrAl materials. One significant difference in this case is that the Y and Zr in NiAl are added to the alloy in an unoxidized form. In the case of the oxide dispersed FeCrAl alloys, the RE is present in very stable oxides. Unfortunately the Y_2O_3-dispersed Ni_3Al melts at ≈1395°C and could not be studied for comparison.

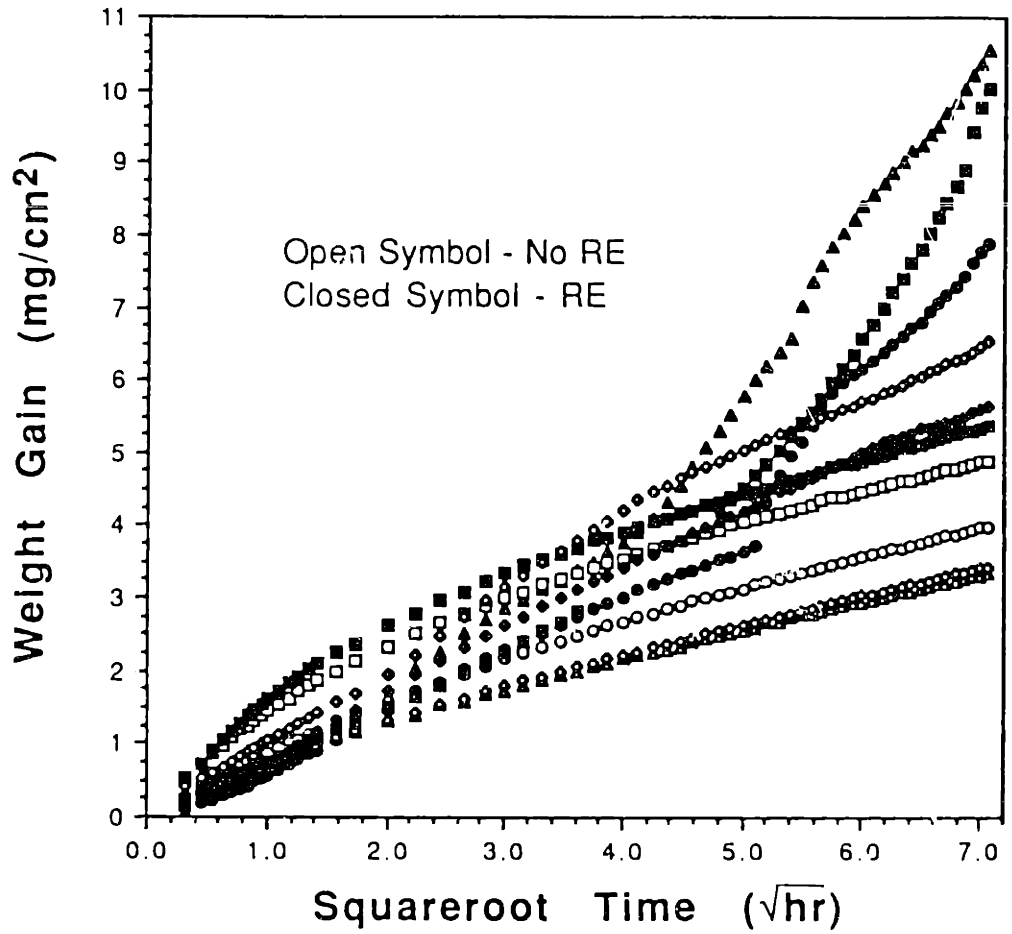

Figure 5.3.1 Parabolic plot of weight gain versus squareroot of time for doped and undoped Ni-Al at 1400°C in 1atm O_2. Circles = 23wt%Al, triangles = 30wt%Al, diamonds = 31.5wt%Al, squares = 36wt%Al, square with X = 31.5wt%Al + 0.23wt%Zr.

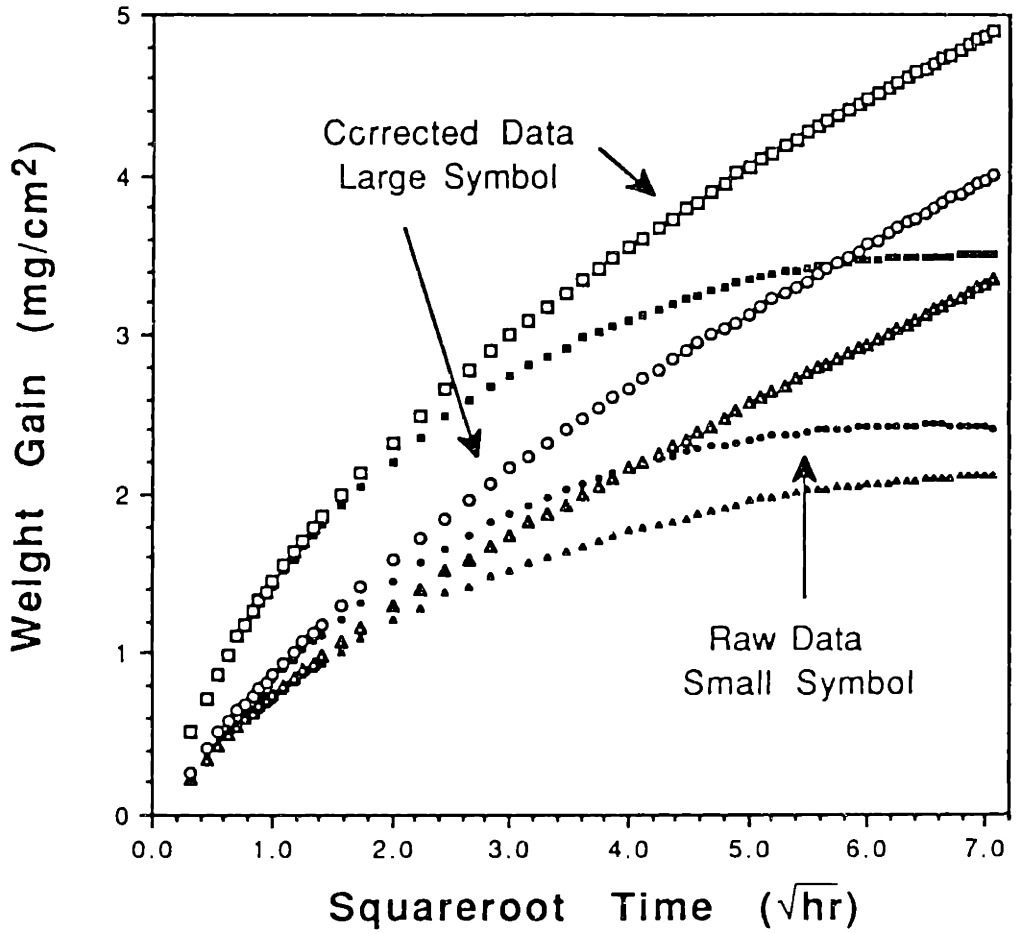

Figure 5.3.2 Parabolic plot of the corrected and uncorrected weight gain versus squareroot of time for undoped NiAl at 1400°C in 1atm O_2. The correction is for the linear evaporation of the Pt-Rh hangdown wire. Circle = 23wt%Al, triangle = 30wt%Al and square = 36wt%Al.

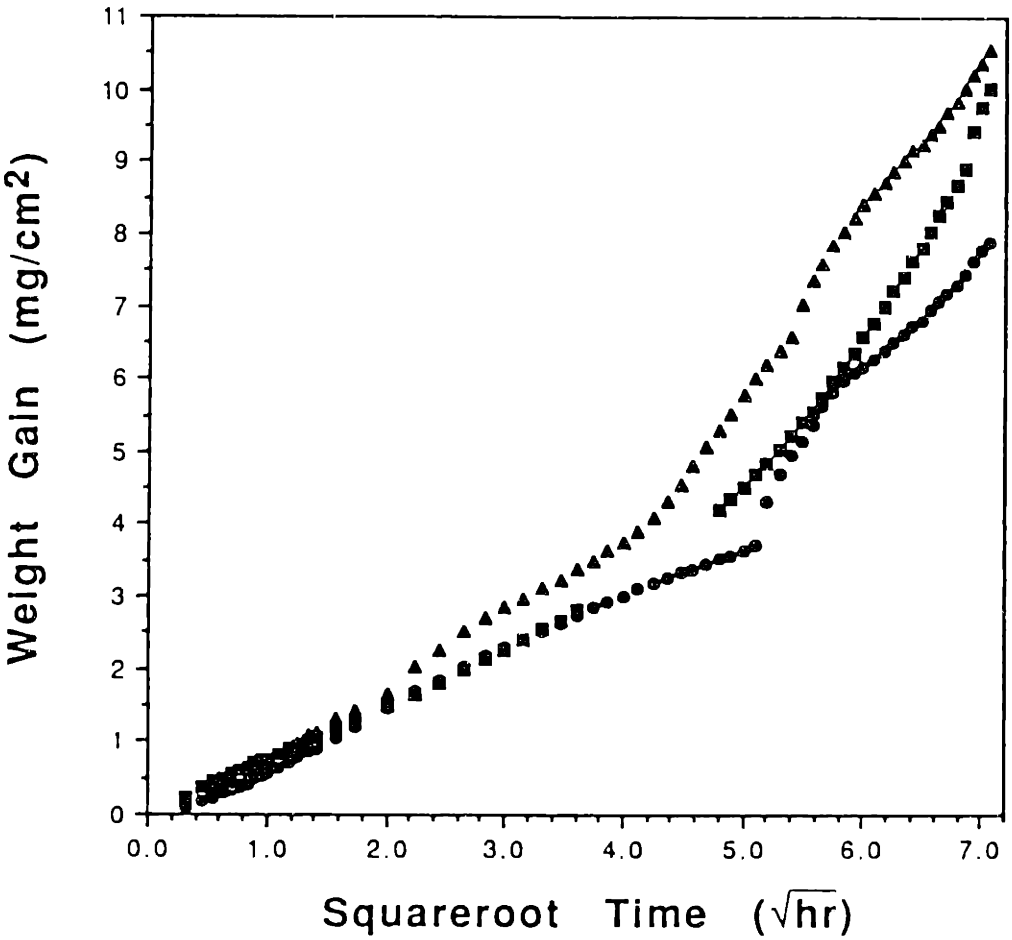

Figure 5.3.3 Parabolic plot of weight gain versus squareroot of time for doped NiAl at 1400°C in 1atm O_2. Circle = 23wt%Al Y-implanted, triangle = 30wt%Al Y-implanted, and square with X = 31.5wt%Al + 0.23wt%Zr.

5.3.2 Cyclic Oxidation Adherence Results

Oxide adherence was evaluated by cycling NiAl samples for twenty 1hr cycles, Figure 5.3.4. Undoped NiAl spalled readily after the first cycle and continued to lose weight after each cycle. In the case of NiAl + Zr, the oxide appeared to be somewhat protective for the first ≈10 cycles. However, during the next 10 cycles, a significant breakdown occurred. This is similar to the breakdown that occurred in the isothermal exposure, Figure 5.3.3. Thus, the REE was not observed in any of the doped NiAl samples at 1400°C.

5.3.3 SEM Results

A few morphologies were examined after oxidation at 1400°C. Figure 5.3.5 shows the oxide ridge structure forming on the undoped NiAl. The ridges (which presumably correspond to the oxide grain boundaries) are observed to coarsen during exposure. These ridges are similar in structure but significantly larger in width and spacing than those observed at 1200°C, Figure 5.2.7b. Another interesting feature of the undoped Ni-Al is buckling of the oxide scale, Figure 5.3.6. While it is not as widespread, this behavior is similar to the scale buckling observed on undoped FeCrAl at 1000°C, Figure 4.1.4.

Because of the eventual breakdown of oxide scales with the addition of a RE at long times, the doped scales were studied only after 1hr exposures. In the case of NiAl + Zr, the most notable morphological feature was the presence of numerous sub-micron particles on the surface, Figure 5.3.7. Some of these particles were

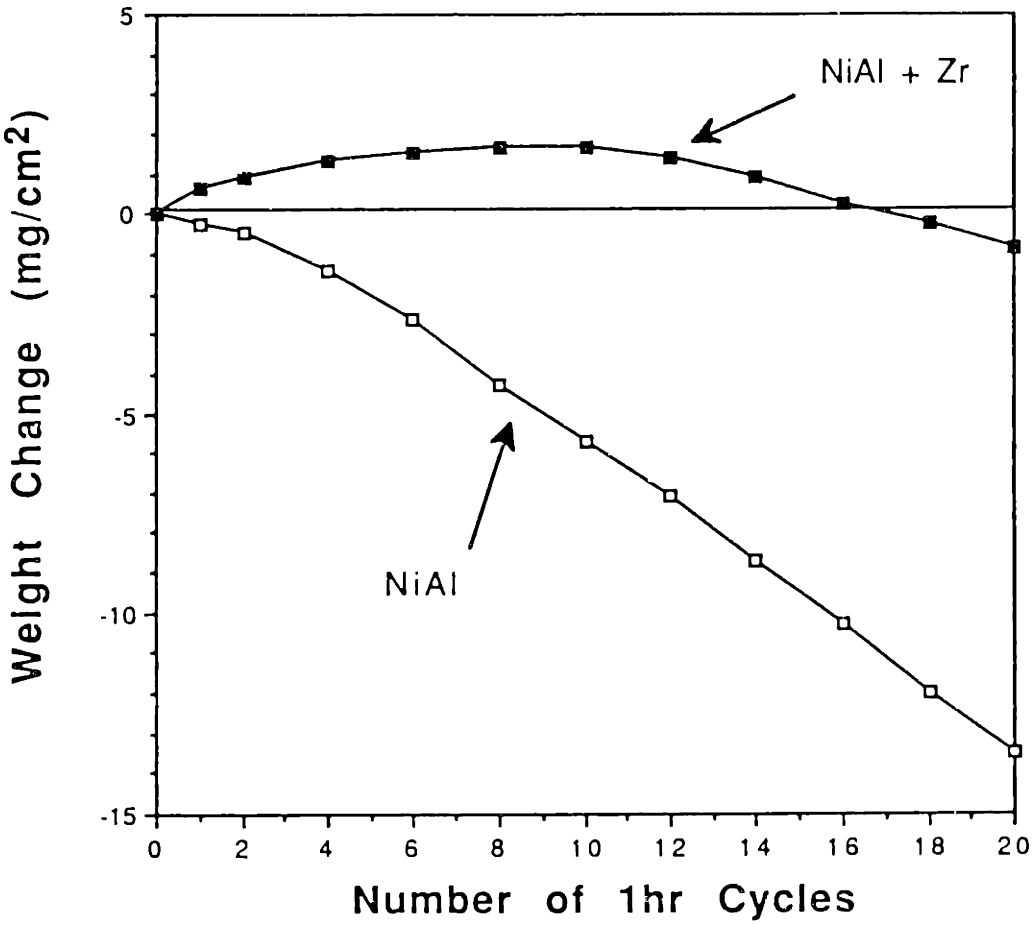

Figure 5.3.4 Weight changes for doped and undoped NiAl over 20 1hr cycles at 1400°C in 1atm O_2. While the Zr alloy addition improves the oxide adherence for the first 10 cycles, thereafter it begins to breakdown.

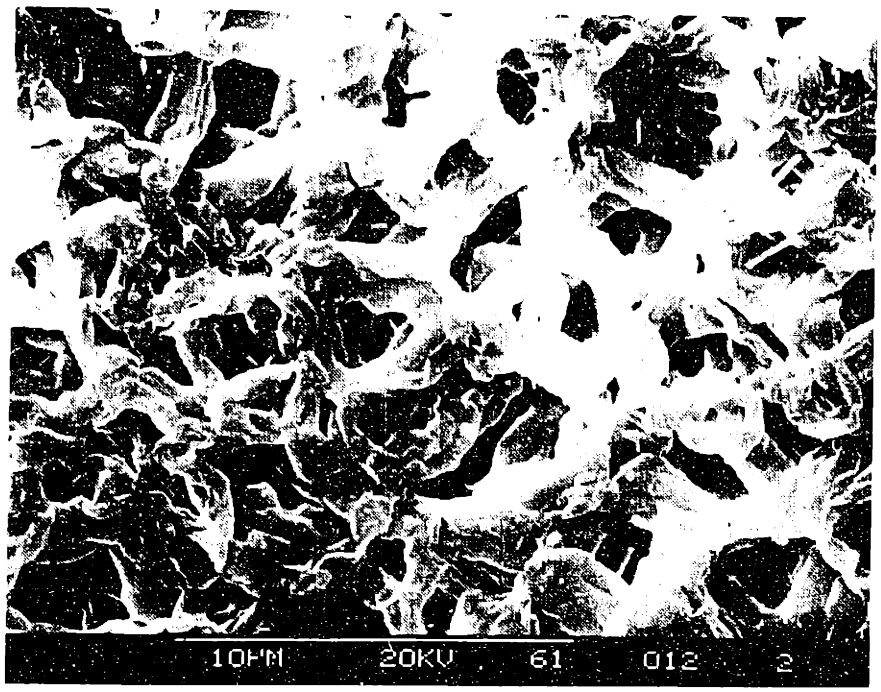

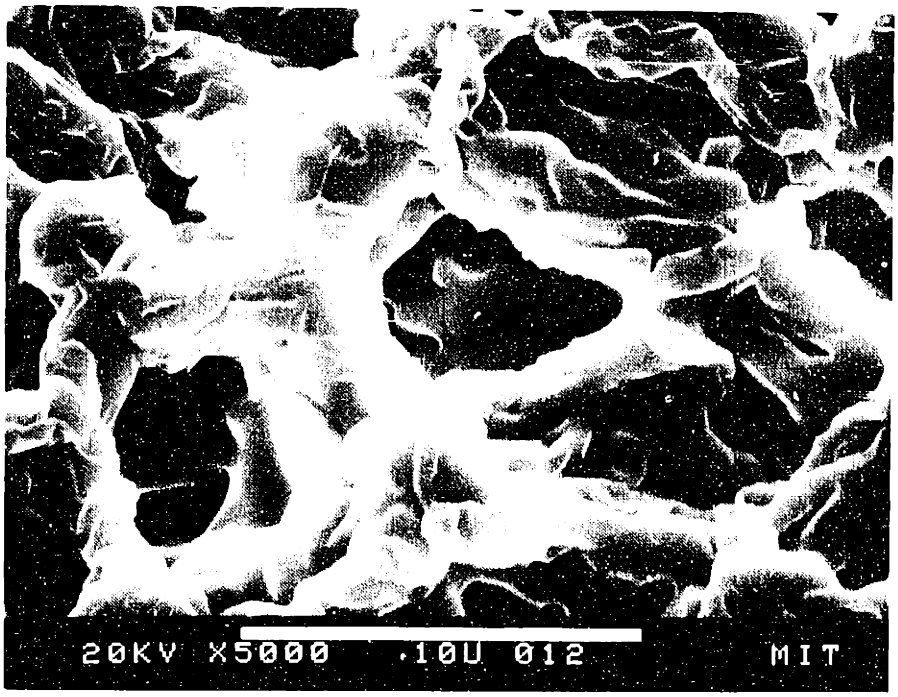

Figure 5.3.5 SEM secondary electron images of undoped NiAl after oxidation at 1400°C for (a) 1hr and (b) 50hr.

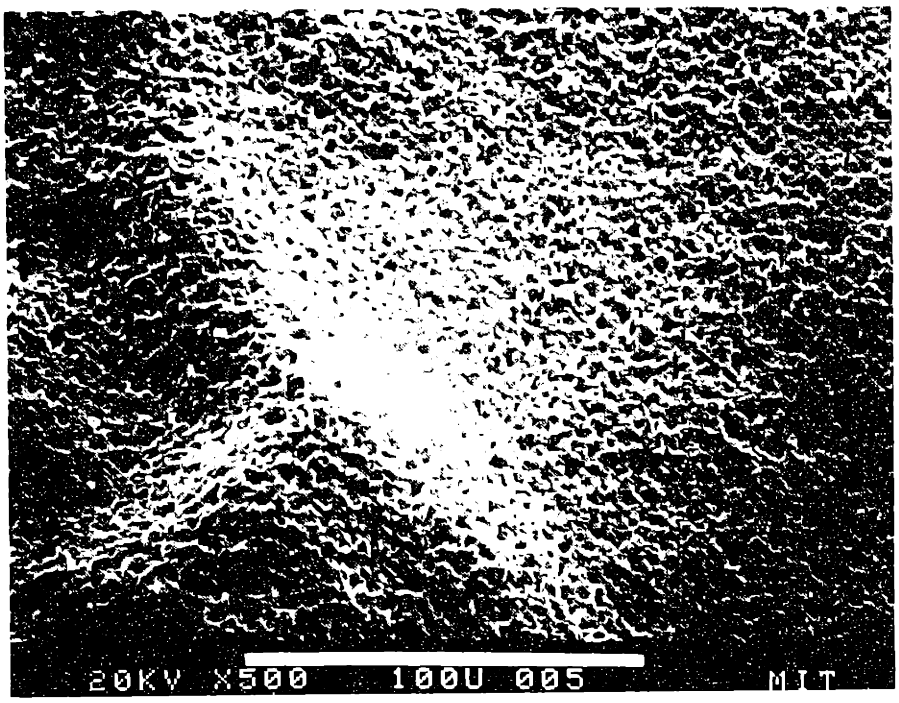

Figure 5.3.6 SEM secondary electron image of undoped Ni-23Al after oxidation at 1400°C for 50hr.

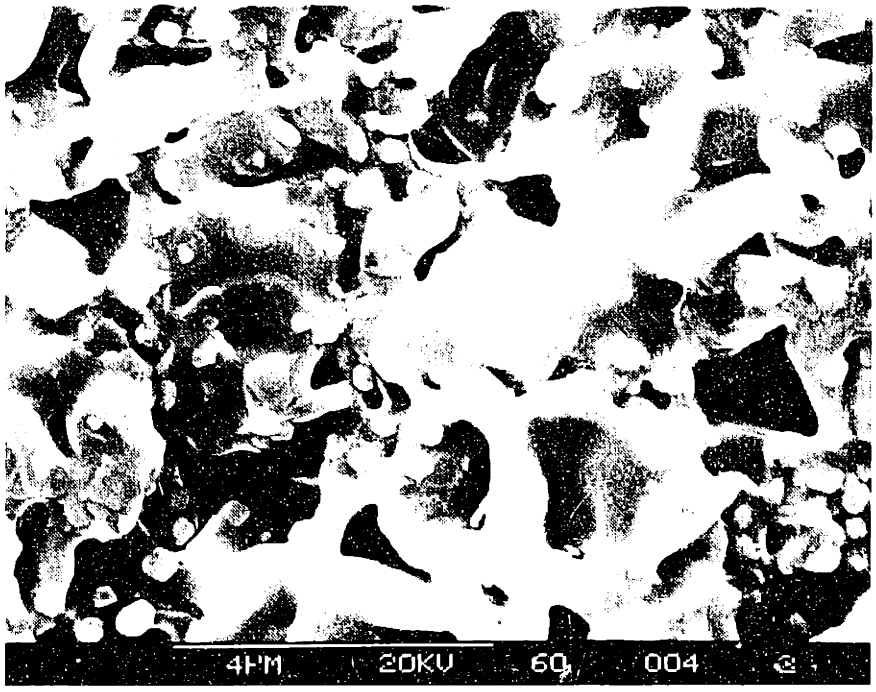

Figure 5.3.7 SEM secondary electron image of NiAl + Zr after oxidation at 1400°C for 1hr. The sub-micron particles on the surface are rich in Zr (by EDXA).

found to be rich in Zr by EDXA. However, detection was sometimes difficult because of their small size relative to the excitation volume of the electron probe. The oxide surface was somewhat rough but did not have the ridged structure like the scale on the undoped NiAl. This morphology was very similar to that observed on APM after oxidation at 1400°C, Figure 4.3.9.

Some oxide spallation was observed on NiAl + Zr, possibly a precursor to later breakdown, Figure 5.3.8. The substrate morphology revealed by the spallation is similar to morphologies at lower temperatures, Figure 5.2.6. Some of the areas appear to be imprinted with oxide grains while other areas appear to be smooth. Prior to spallation, the latter areas were likely to have been unattached to the overlying oxide. Some faceting and terracing can be seen in this case.

Figure 5.3.9 shows the scale surface on Y-implanted NiAl after oxidation for 1hr. The scale morphology in this case is also very different from the undoped NiAl. However, no Y-rich particles are observed in this case. The Y-implanted NiAl had more spallation than NiAl +Zr, but the type of spallation was similar.

5.3.4 GAXRD Results

The Y- and Zr-doped NiAl samples were profiled after a 1hr oxidation period, Figure 5.3.10. Because of the severe spallation, the undoped NiAl was not analyzed. Both doped samples formed predominantly α-Al_2O_3 scales. The substrate peaks are more prominent on the Y-implanted sample because of the increased

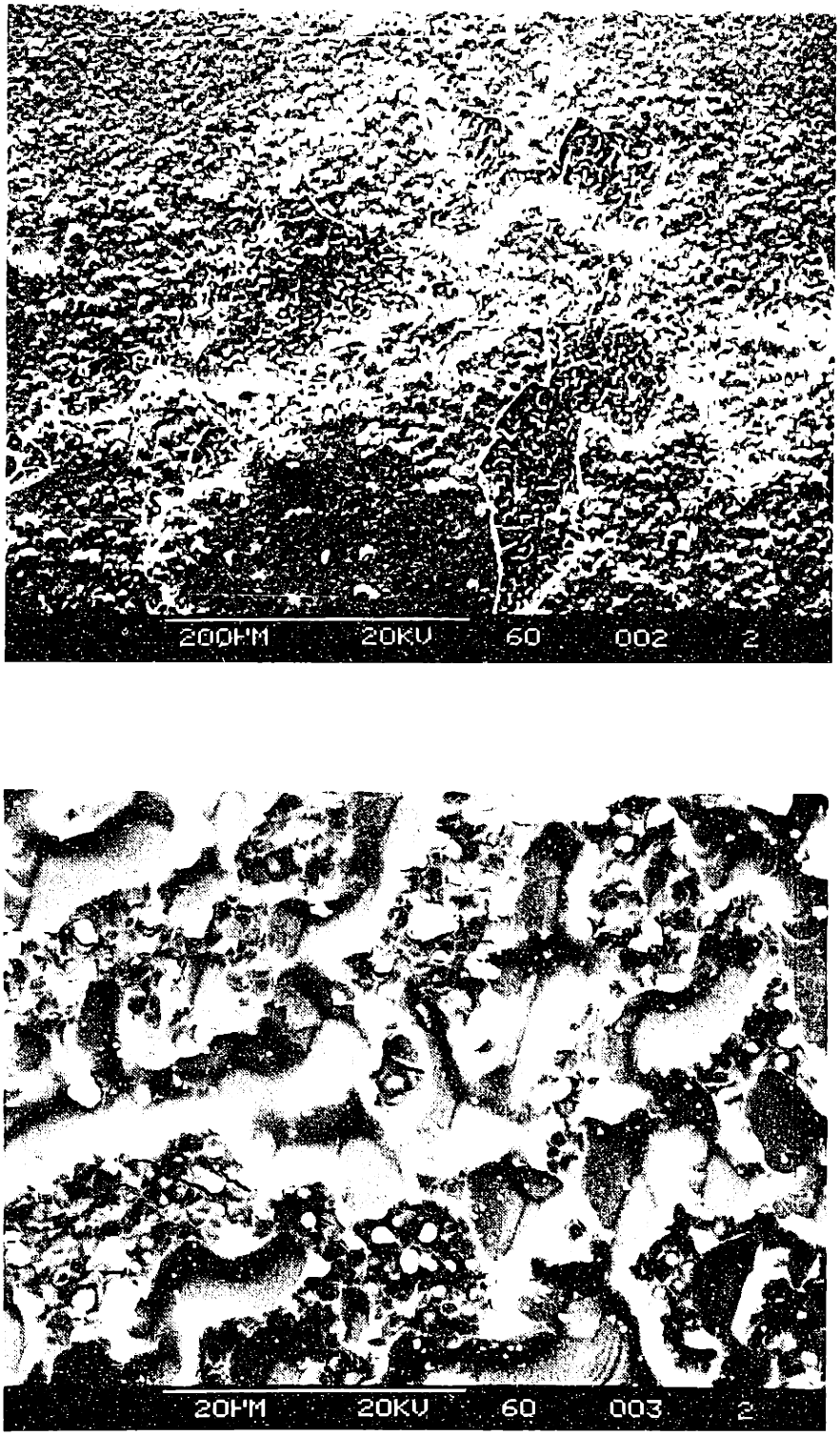

Figure 5.3.8 SEM secondary electron images of NiAl + Zr after oxidation at 1400°C for 1hr (a) region where oxide has spalled and (b) bare metal revealed by oxide spallation.

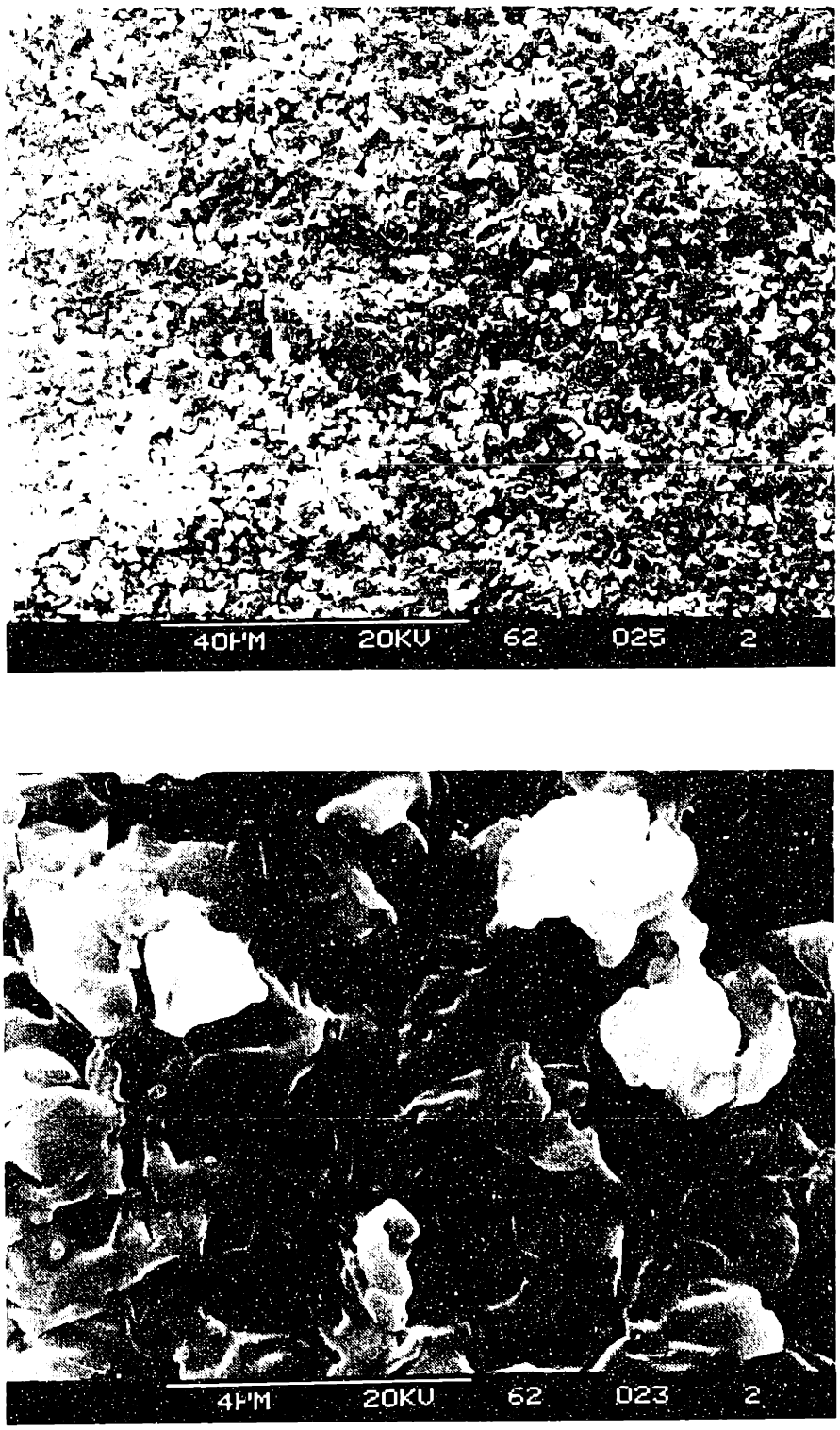

Figure 5.3.9 SEM secondary electron images of Y-implanted NiAl after oxidation at 1400°C for 1hr

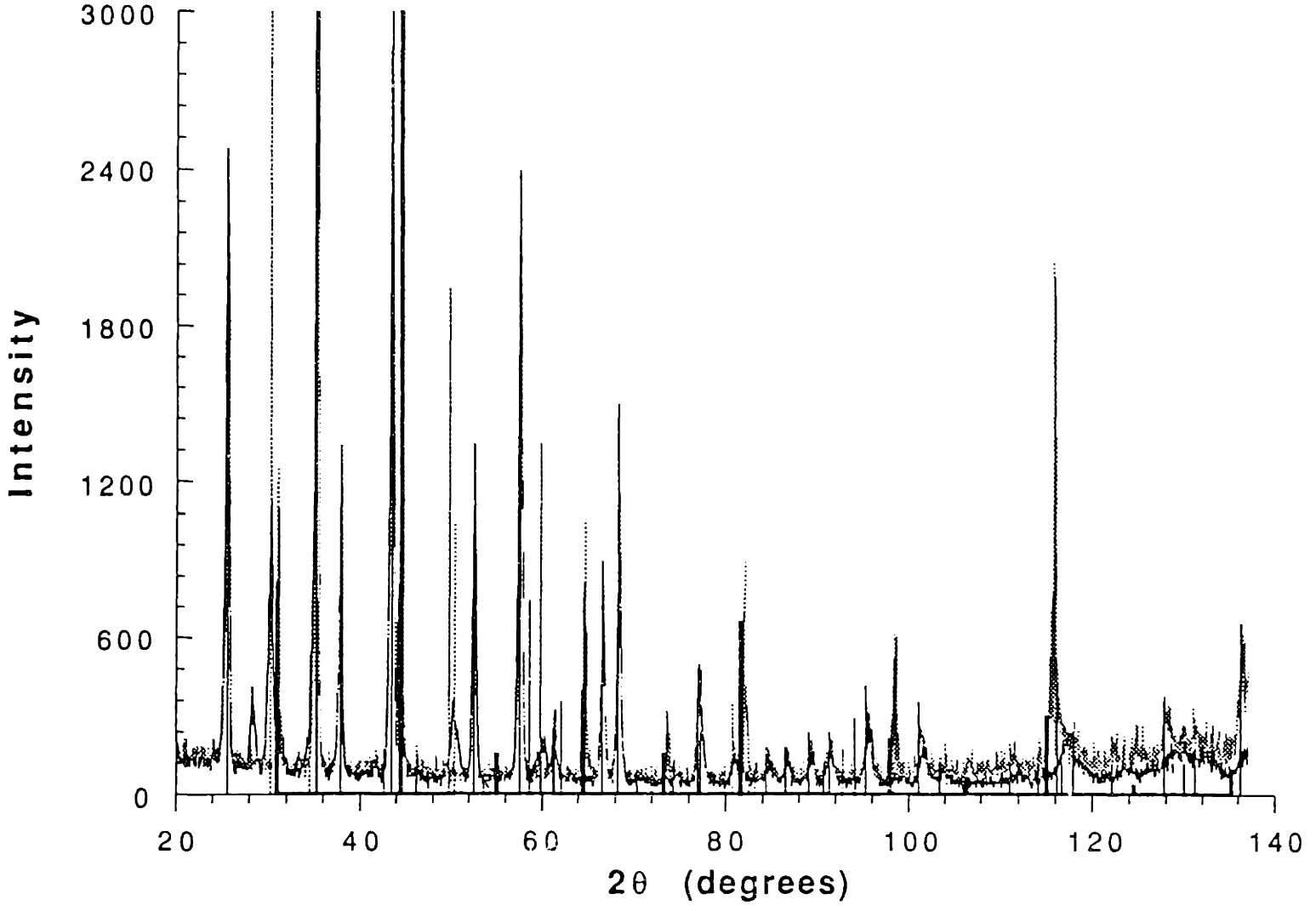

Figure 5.3.10 GAXRD profile of scales formed on Zr- (solid) and Y-doped (dashed) Ni-31.5at%Al after oxidation for 1hr at 1400°C in 1atm O_2. The thin solid lines denote α-Al_2O_3, the broken lines ZrO_2 and the wide solid lines ß-NiAl. Both samples have a primarily α scale. The profile of NiAl + Zr also contains ZrO_2. The substrate peaks are stronger on Y-doped NiAl due to increased scale spallation.

spallation. The most interesting observation is that after a 1hr exposure, very strong ZrO_2 peaks are observed on NiAl + Zr.

5.4 Results at 1500°C

More extensive experiments were conducted at 1500°C on NiAl with and without an Y implant. Just as at 1400°C, there were no published data for Al_2O_3 scales or the REE at this temperature. Therefore numerous kinetic tests, both long- and short-term were conducted as well as a variety of characterization techniques. Unfortunately, these experiments were conducted before the NiAl + Zr was acquired. Thus the only RE addition was by ion implantation -- a surface modification contending with a substantial oxidation rate at this temperature.

5.4.1 Isothermal Oxidation Results

The isothermal kinetic data at 1500°C are shown in Figure 5.4.1. The data have been corrected for the evaporation of the Pt-Rh hangdown wire. A number of points are clearly illustrated here. First, a parabolic rate law is obeyed. The lone exception is a doped sample which experiences breakaway similar to that observed at 1400°C. Secondly, the effect of alloy content is minimal. Once again Ni-36Al has the highest weight gain, presumably because of the higher effective surface area. And finally, the effect of the Y implant is negligible in these long term experiments. Several isothermal experiments were conducted for shorter times, but in

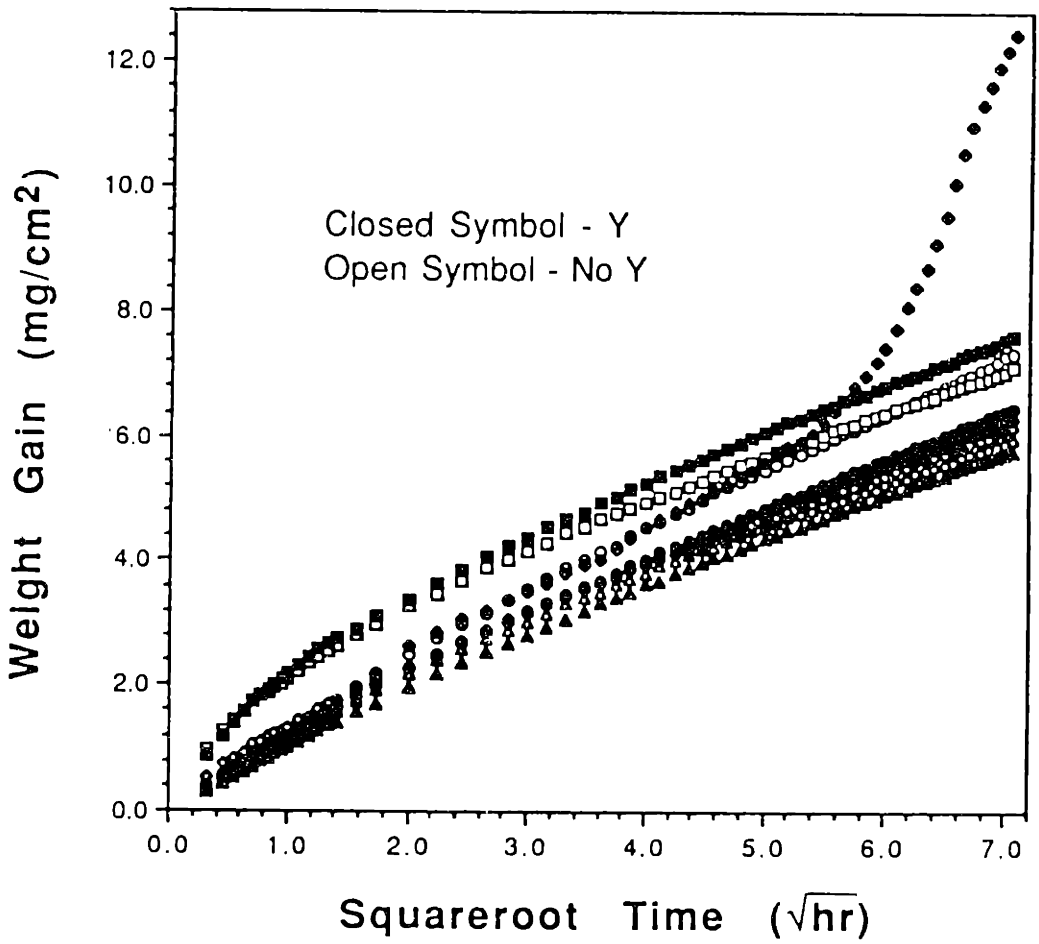

Figure 5.4.1 Parabolic plot of weight gain versus squareroot of time for Y-implanted and unimplanted Ni-Al at 1500°C in 1atm O_2. Circles = 23wt%Al, triangles = 30wt%Al, diamonds = 31.5wt%Al and squares = 36wt%Al.

each case the kinetics matched those of the longer term experiments.

Spallation after the 50hr exposures was massive and usually complete, i.e. pieces almost as large as the coupon (≈1cm x 1cm x 30μm) would be intact but unattached to the substrate. Occasionally these pieces would fall back into the furnace during cooldown. The NiAl would be left essentially free of surface oxide. This type of behavior was also reflected in the cyclic oxidation results.

5.4.2 Cyclic Oxidation Adherence Results

Based on the limited effect of the Y implant after 50hr exposures at 1500°C, the cycle time was reduced to 0.2hr (12min). The adherence was still tested by maintaining the number of cycles at 20. Figure 5.4.2 shows the isothermal weight gain plotted along with the weight change during twenty 0.2hr cycles. The Y-implanted NiAl appears to have a higher weight gain for the first 2 cycles but then begins to spall at the same rate as the unimplanted NiAl. This is a strong indication of an improvement in oxide adherence but is far from conclusive. It is also indicates that, if there is an effect of the implant, it is very short-lived. After the first few cycles, the spallation by both undoped and doped NiAl is massive. Virtually all of the oxide is lost after each cycle.

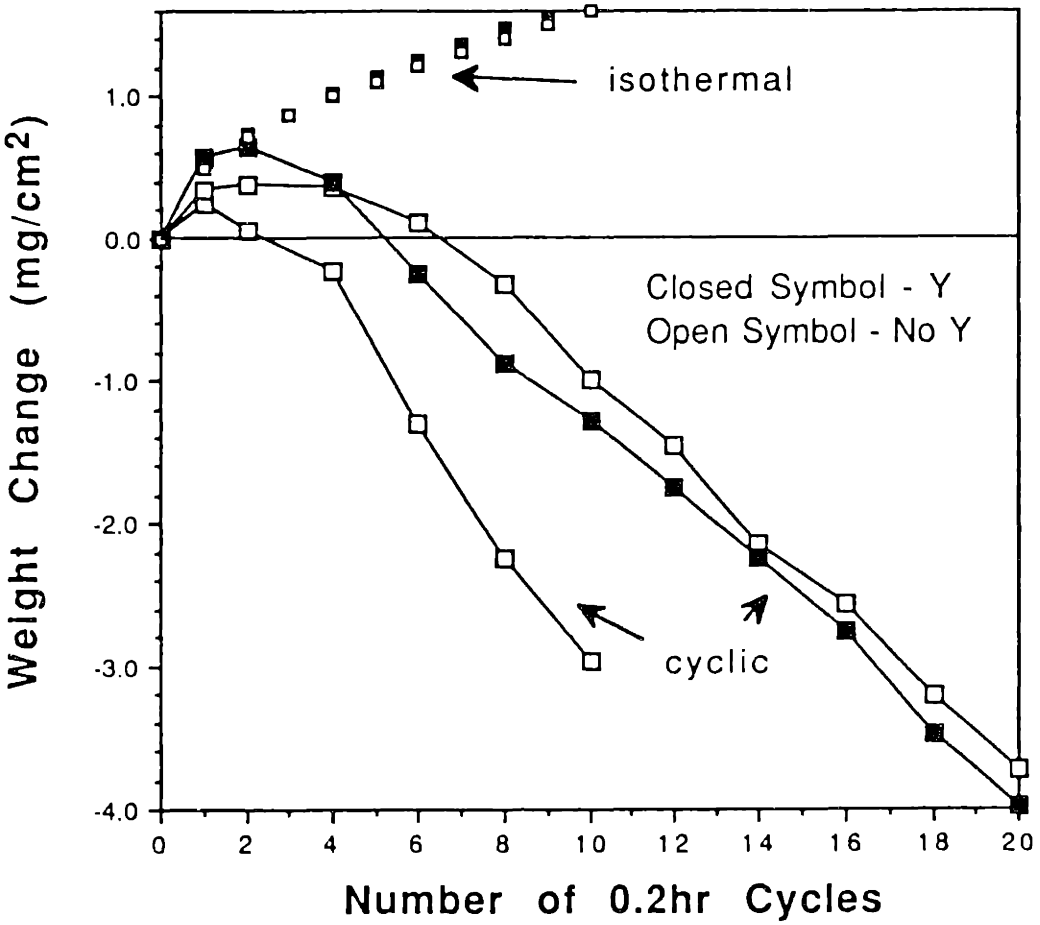

Figure 5.4.2 Isothermal weight gains plotted with the weight change over 20 0.2hr cycles at 1500°C in 1atm O_2. The Y-implant improves the adherence for 2 cycles but then fails.

5.4.3 SEM Results

Morphologies were investigated at several times for both Y-implanted and unimplanted NiAl. After only a 0.2hr exposure (1 cycle), the most significant difference was the improvement in oxide adherence with the Y implant, Figure 5.4.3. A small amount of oxide was observed to spall on the implanted sample. However, this was significantly better than the unimplanted NiAl, where massive spallation occurred. The adherent oxide formed a ridge morphology as seen at lower temperatures, Figure 5.4.4. This morphology was observed on both Y-implanted and unimplanted samples.

In agreement with the weight loss data, the morphology after 20 cycles showed no effect of the Y-implant, Figure 5.4.5. After an isothermal exposure of 4hr, which is equal to the total cyclic exposure, the oxide scale on Y-implanted NiAl spalled almost entirely. A cross-section of the oxide showed large voids in the scale, Figure 5.4.6a. The scale thickness, approximately 10μm, is in good agreement with a calculated estimate based on the corrected isothermal TGA weight gain. The grain size is several micrometers and is not particularly columnar nor is it equiaxed. The substrate beneath the spalled oxide is mostly smooth, with few indications of oxide grain imprints, Figure 5.4.6b. The troughs in the substrate are found throughout but appear to be on a much finer scale than the substrate grain size.

After exposure for 50hr, the scale completely spalled from the substrate upon cooling. Pieces of this scale were mounted for SEM cross-section analysis and were tilted in the SEM to look at the gas

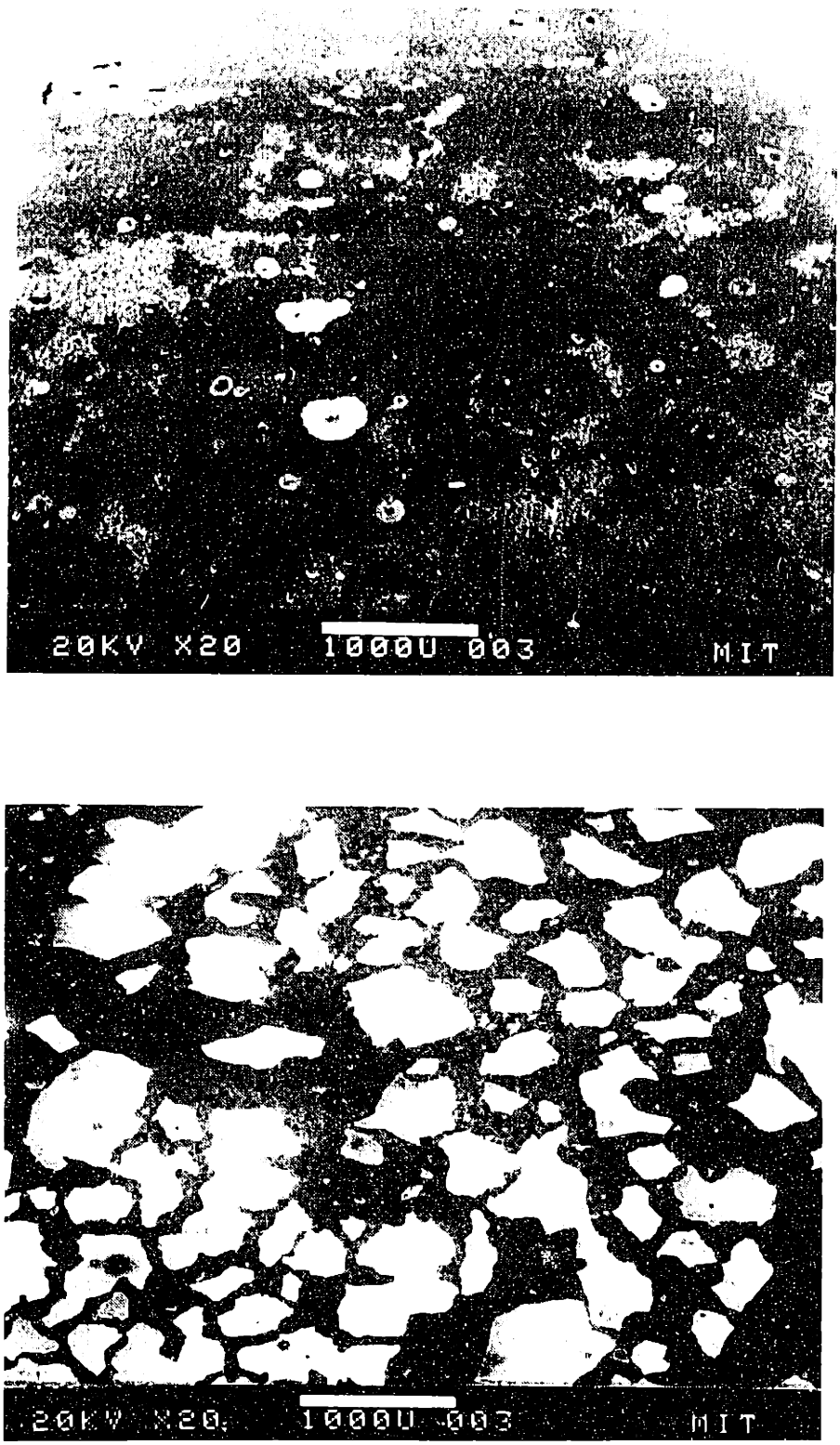

Figure 5.4.3 SEM secondary electron images of the oxide after oxidation at 1500°C for 0.2hr on (a) Y-implanted NiAl and (b) unimplanted NiAl. Both images are at the same magnification.

Figure 5.4.4 SEM secondary electron images of the oxide after oxidation at 1500°C for 0.2hr on (a) Y-implanted NiAl and (b) unimplanted NiAl.

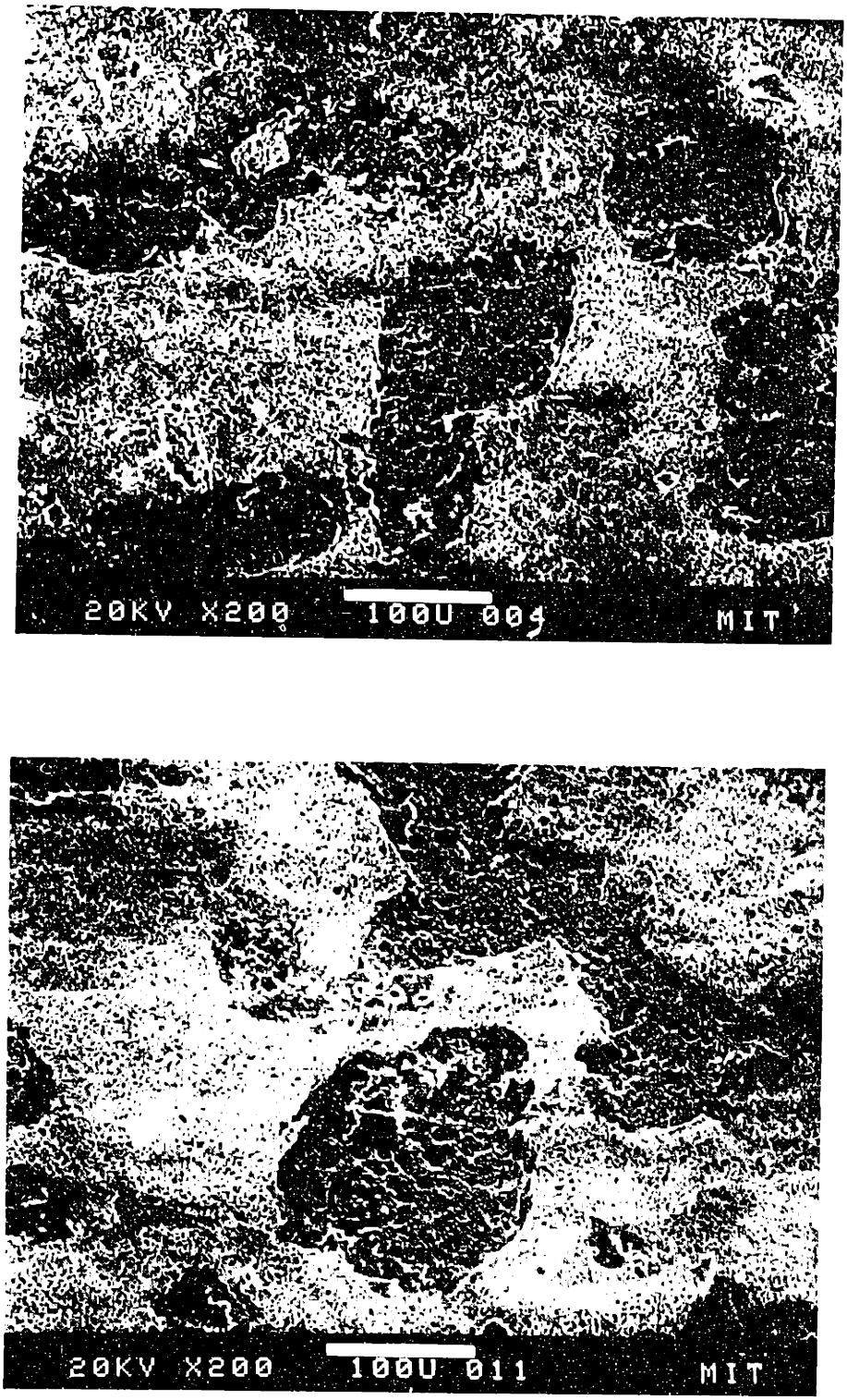

Figure 5.4.5 SEM secondary electron images of the oxide after oxidation at 1500°C for 20, 0.2hr cycles on (a) Y-implanted NiAl and (b) unimplanted NiAl.

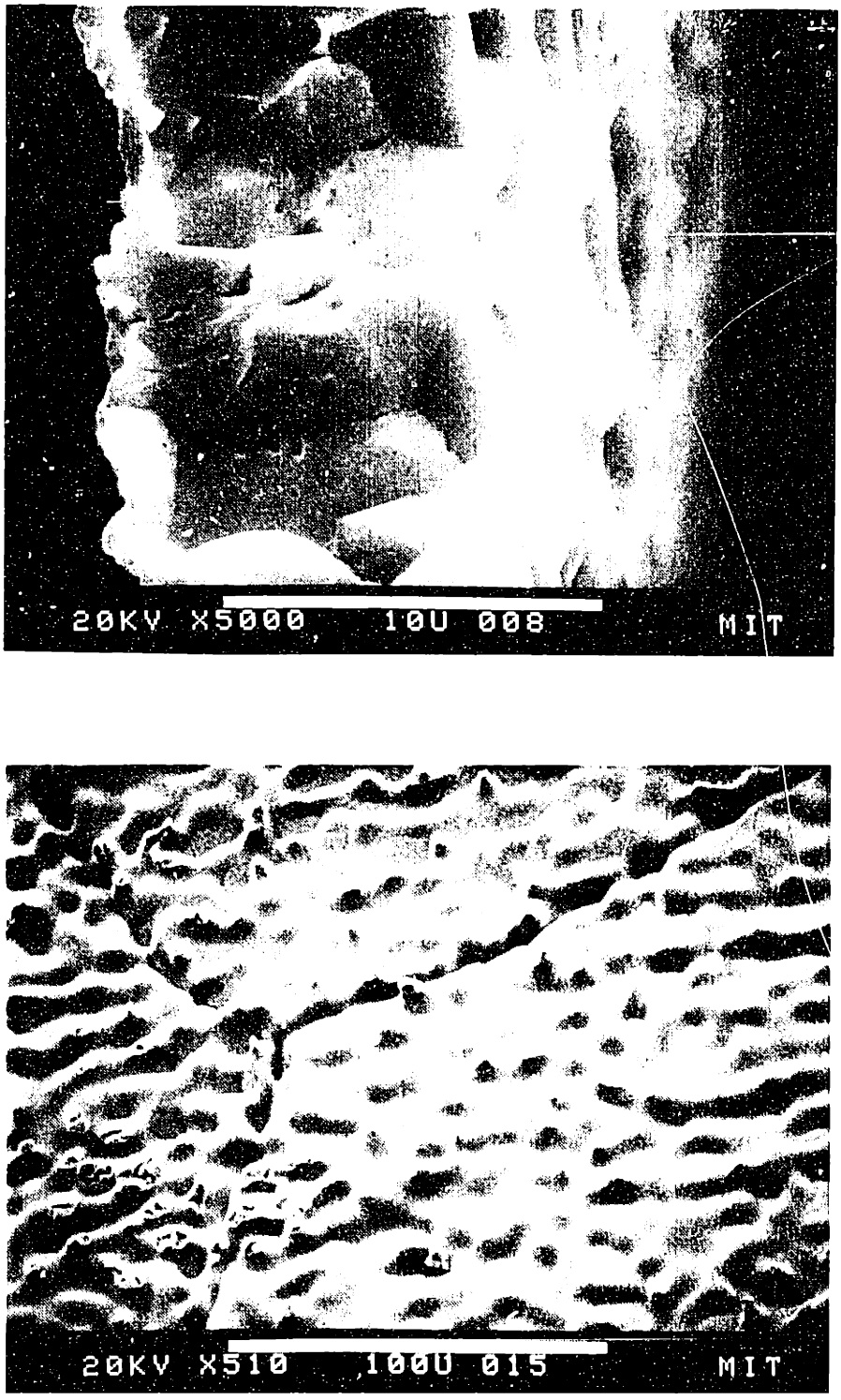

Figure 5.4.6 SEM secondary electron images of Y-implanted NiAl after oxidation at 1500°C for 4hr; (a) cross-section of the oxidation product, and (b) substrate beneath the spalled oxide.

and oxide surfaces. Oxide grown on Y-implanted NiAl showed few differences from that grown on unimplanted NiAl. Figure 5.4.7 is an example typical of the oxide morphology after these long-term exposures. The grains near the gas interface appear to have a smaller grain size than the underlying grains. Both cross-sections show numerous voids along the grain boundaries at the fracture surface. In other locations where the fracture is intragranular, voids are also observed within the grains. The oxide surface adjacent to the substrate has a most unusual morphology, Figure 5.4.7b. Each of the oxide grain boundaries is marked by a ridge. In this particular area, whiskers are also observed to be growing *towards* the substrate -- exactly the opposite behavior of whiskers observed at lower temperatures. While these whiskers are not observed on most of the surface, a denser region is shown in Figure 5.4.8a. The feature on the left is unidentified but may be a contaminant. On the right, the whiskers are observed to grow only from the oxide ridges.

A more typical region of the near-substrate oxide is shown in Figure 5.4.8b. Ridges on the oxide grain boundaries can be seen throughout. At higher magnification, the grain surfaces away from the ridges are either smooth or terraced, Figure 5.4.9 This may be an indication of growth by evaporation.

Figure 5.4.10 shows the oxide cross-section after 50hr. Comparing this to Figure 5.4.8b, it is clear that the oxide on both implanted and unimplanted samples is buckled (Figure 2.7a). Considering both the ridges and the buckling, it is clear that the contact between the oxide and the substrate is minimal. The

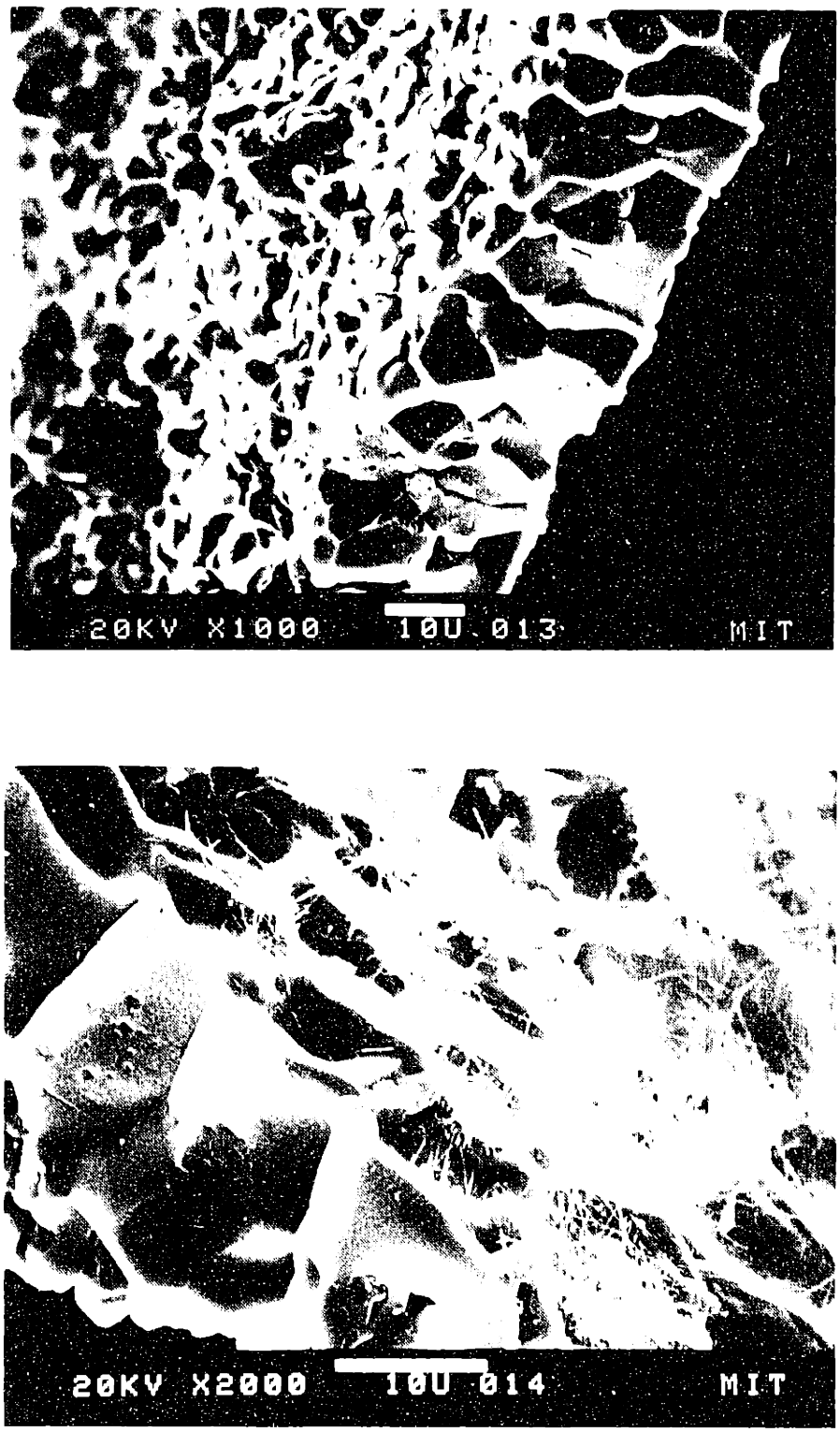

Figure 5.4.7 SEM secondary electron images of Y-implanted Ni-30Al after oxidation at 1500°C for 50hr; (a) cross-section tilted toward the gas interface and (b) the same sample tilted toward the alloy interface.

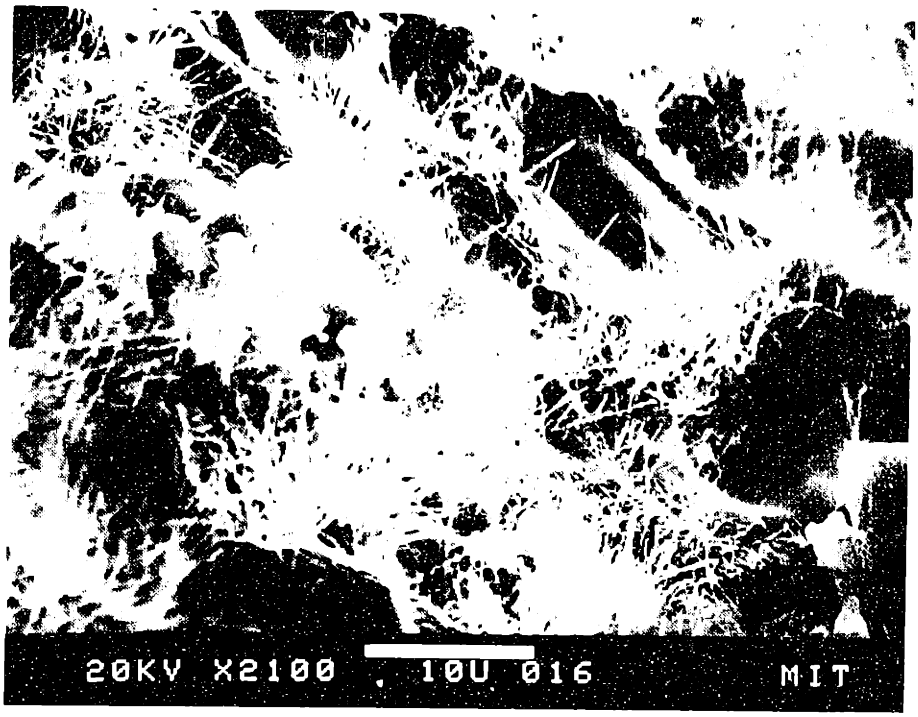

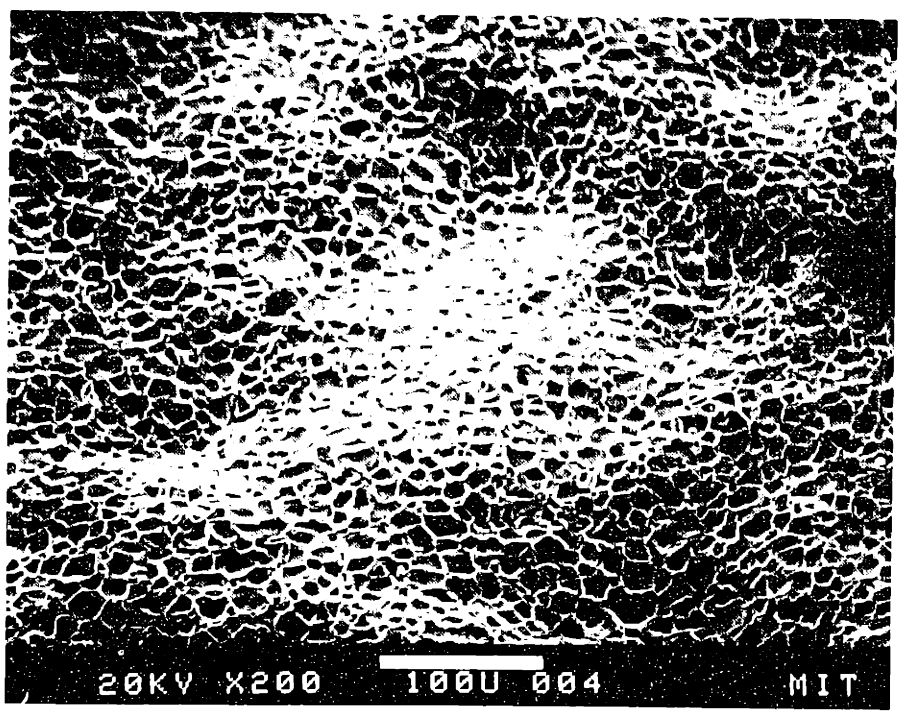

Figure 5.4.8 SEM secondary electron images of the substrate surface of oxide grown on Y-implanted Ni-30Al after oxidation at 1500°C for 50hr.

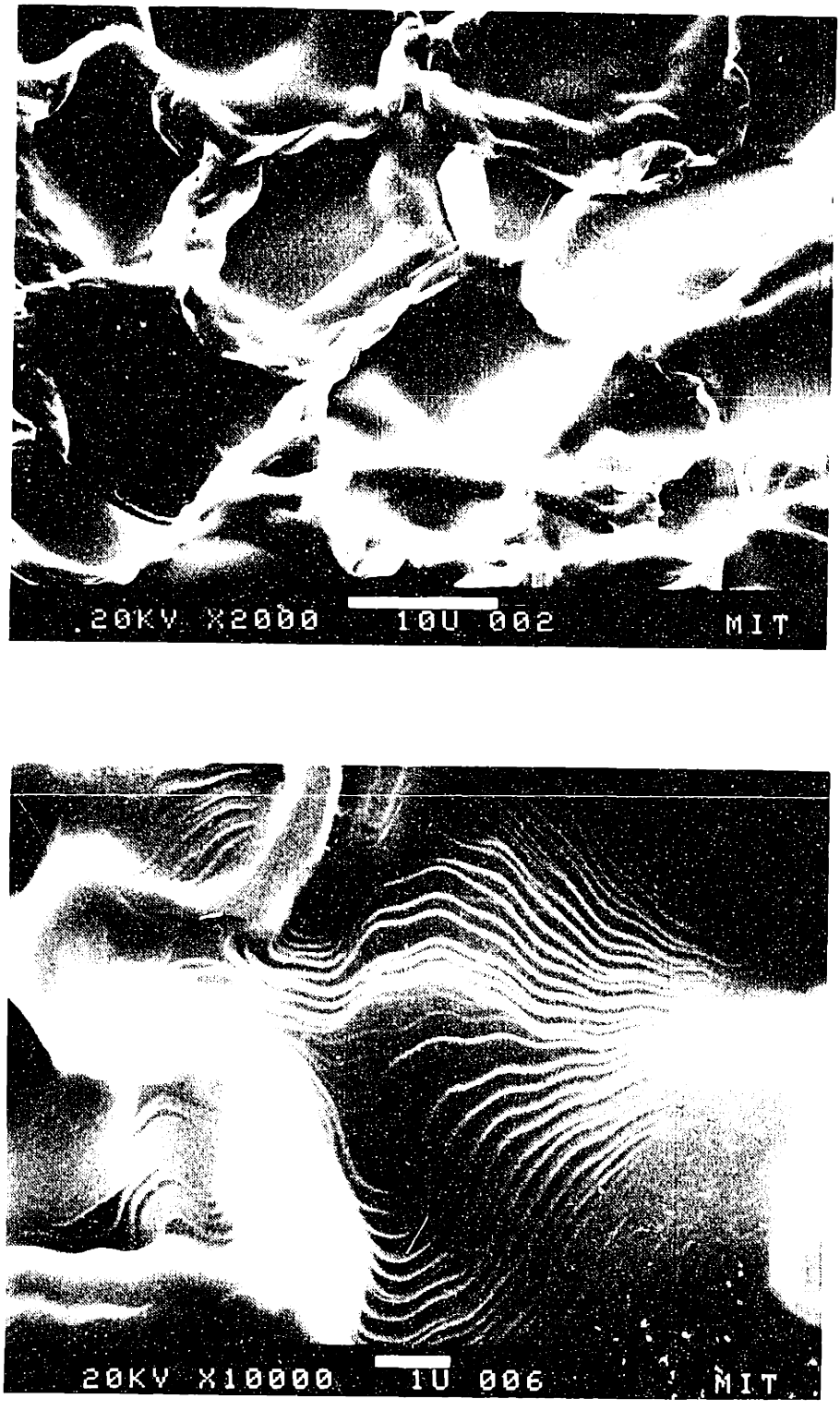

Figure 5.4.9 SEM secondary electron images of the oxide surface adjacent to the substrate after oxidation at 1500°C for 50hr. The oxide was grown on (a) unimplanted Ni-30Al and (b) Y-implanted NiAl.

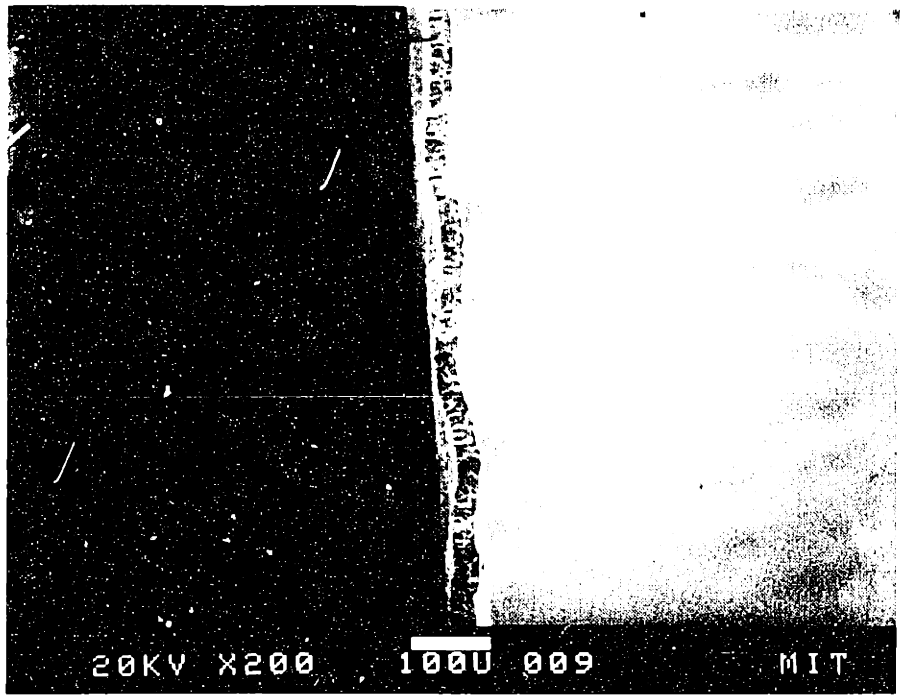

Figure 5.4.10 SEM secondary electron image of the oxide grown on undoped Ni-30Al after oxidation at 1500°C for 50hr.

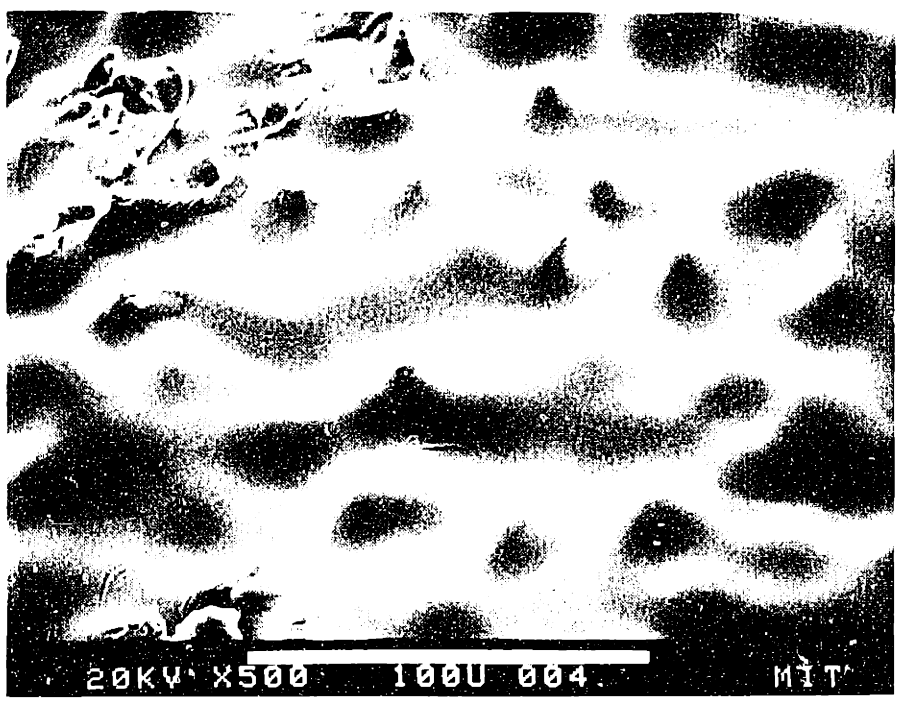

Figure 5.4.11 SEM secondary electron image of the Y-implanted Ni-30Al substrate after oxidation at 1500°C for 50hr.

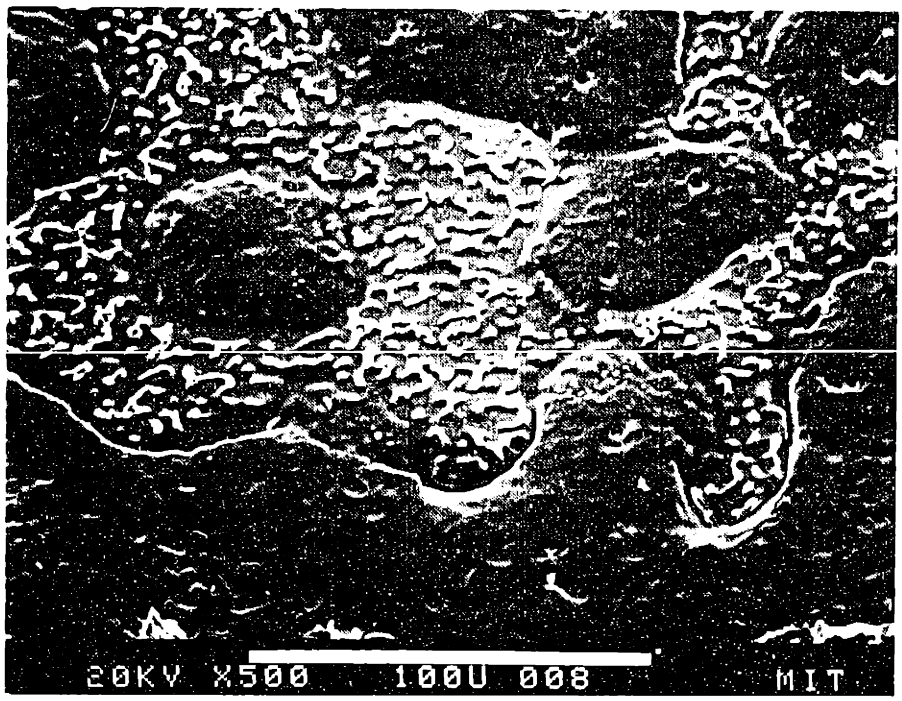

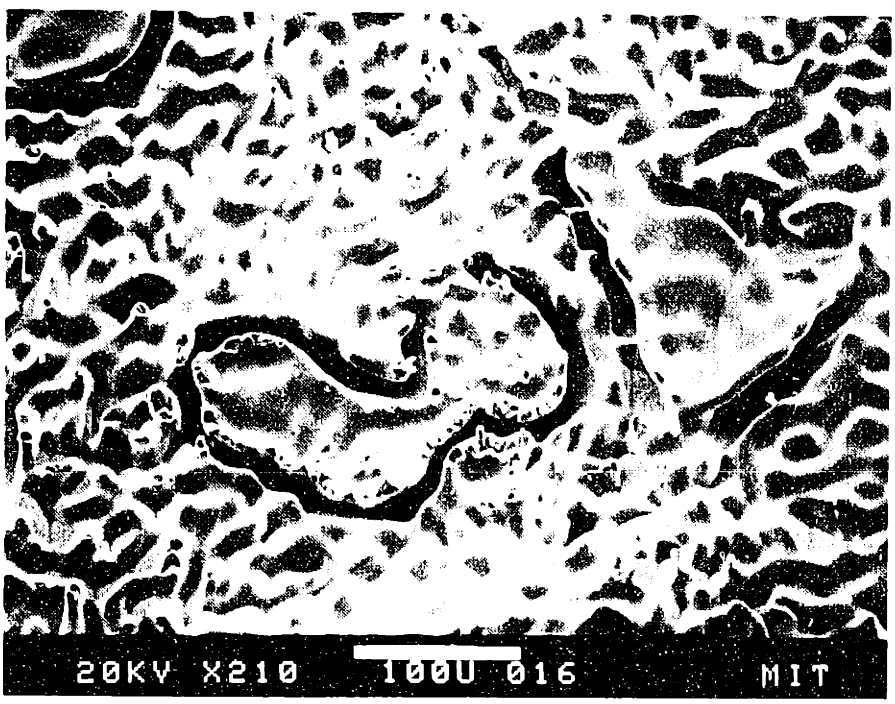

Figure 5.4.12 SEM secondary electron images of the substrate of undoped Ni-31.5Al after oxidation at 1500°C for (a) 0.2hr and (b) 50hr.

relatively-flat substrate morphology reflects this lack of contact, Figure 5.4.11. A few selected areas appear to have been in contact with the oxide but most of the surface appears smooth as if evaporation has been very significant. Further observations of the substrate after 0.2hr and 50hr shows terracing at short times and some faceting at longer times, Figure 5.4.12. The troughs in the substrate (Figures 5.4.12 and 5.4.6b) may be remnants of contact with the oxide.

Overall, the oxide morphology at 1500°C shows rapid grain growth, non-adherent oxides and no effect of an Y implant of 2 x $10^{16}/cm^2$, except for a short-term improvement in oxide adhesion.

5.4.4 GAXRD Results

The only diffraction work carried out after oxidation at 1500°C was to confirm the scale phase for the 160s sequential isotope oxidation experiment. In both the implanted and unimplanted cases, the scale appeared to be predominantly α-Al_2O_3 with no θ-Al_2O_3 peaks observed. As α is the only stable phase at this temperature, scales grown for longer times should also be predominantly α-Al_2O_3.

5.4.5 Tracer Results

Study of the oxidation mechanism at higher temperatures was hampered by the very high oxidation rate. At 1500°C, 1μm of oxide is formed in approximately 160s. This allows little time for

switching oxidants and still leaves a relatively thick oxide that is probably not fully adherent. Sputtering completely through the oxide proved extremely difficult, and only one profile of Y-implanted NiAl gave a consistent profile, Figure 5.4.13a. In this case the first oxidant, ^{18}O, was found mainly near the gas interface, indicating a predominant inward diffusion mechanism.

A similar, but less well-defined, profile was found for the scale on NiAl+Zr. However, a repeatable result was obtained, Figure 5.4.13b. In this case, there is a small peak in ^{18}O near the surface, less prominent than in the case of Y-doped NiAl. It is difficult to draw anything conclusive from this profile, but once again the highest concentration of the first oxidant is near the gas interface. This is an indication of growth by an inward diffusion mechanism.

Attempts to characterize the non-adherent scale on unimplanted NiAl were not entirely conclusive. Again only a single consistent profile was obtained, Figure 5.4.14. This type of profile subtilely reflects a mixed oxidation mode with the peak ^{18}O level being near the middle of the scale. However the fraction of ^{18}O is very low and a clear layer is not defined. The most significant problem with interpreting the results on the unimplanted NiAl is the non-adherent scales. While blatantly spalled regions are avoided during analysis, the areas that are analyzed may be significantly cracked or not in good contact with the substrate. It is not clear what effect if any this has on depth profiling.

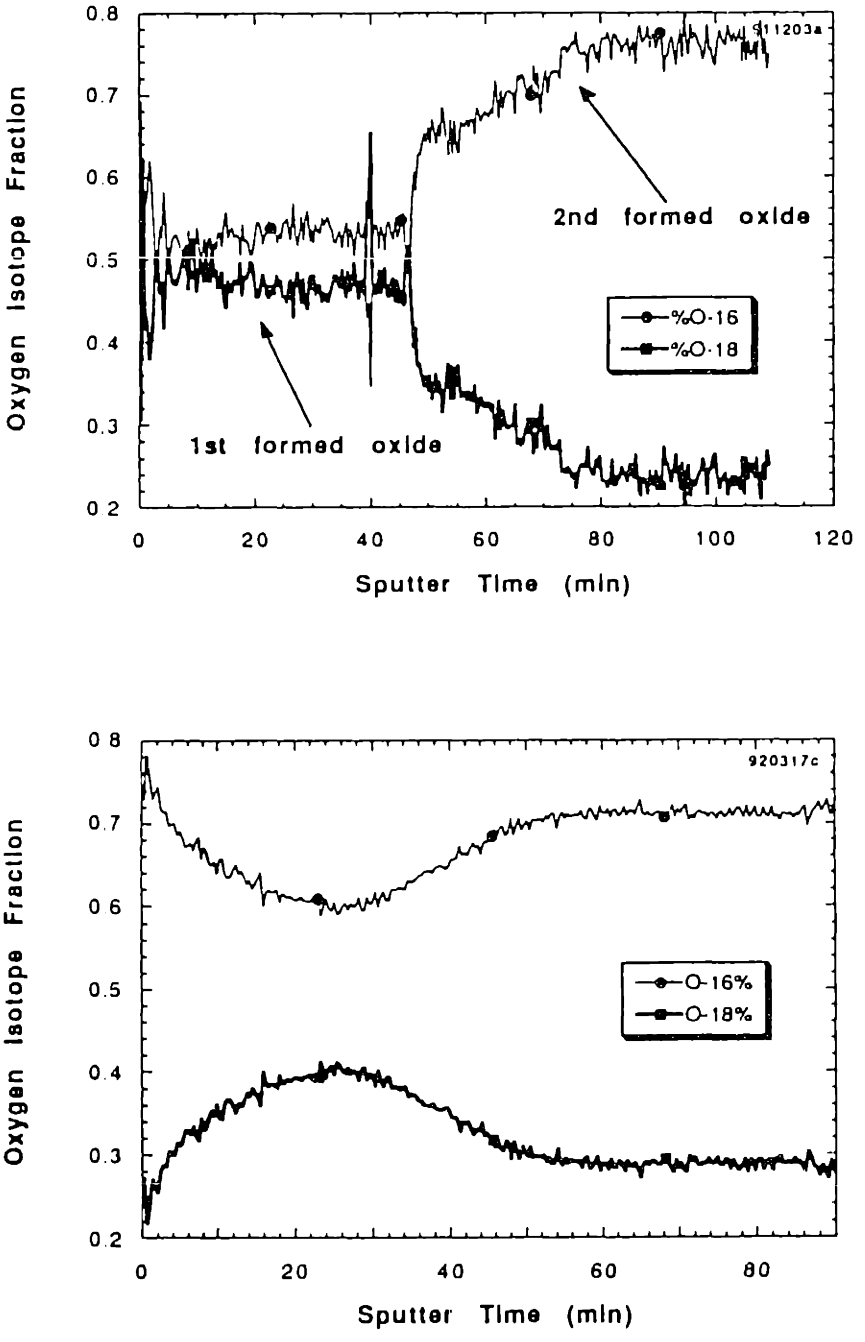

Figure 5.4.13 SIMS sputter depth profile of Al_2O_3 grown at 1500°C on (a) Y-implanted NiAl and (b) NiAl + Zr. Oxidation was for 50s in ^{18}O followed by 110s in ^{16}O.

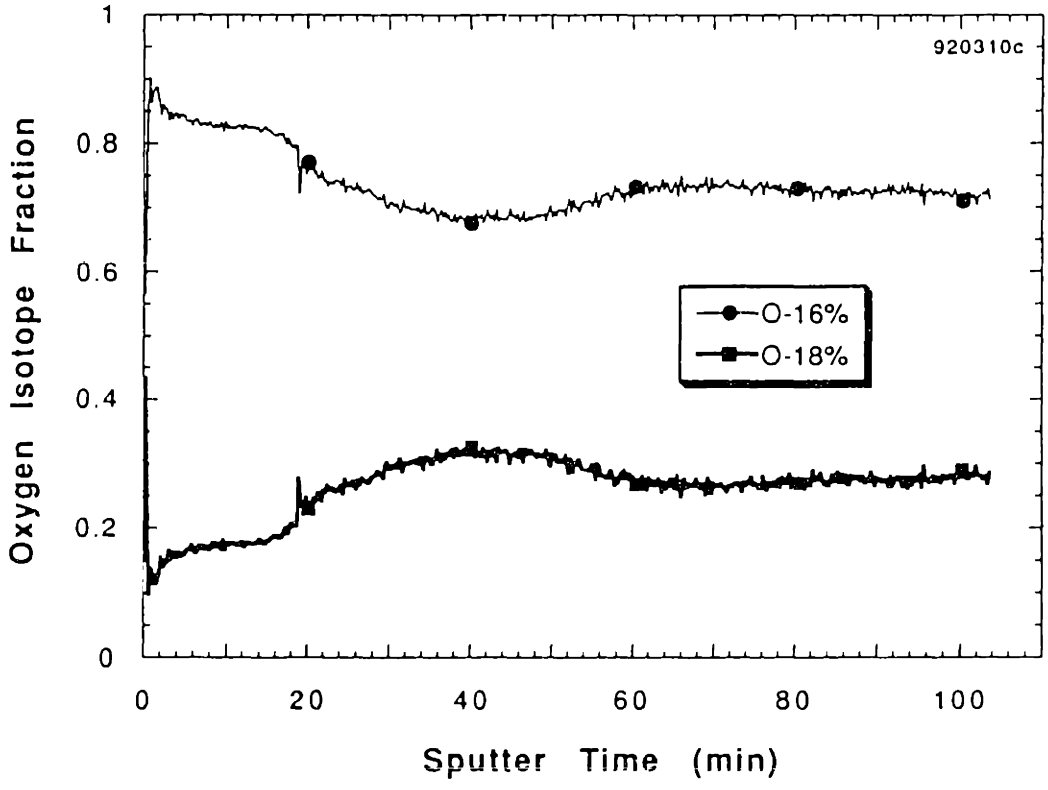

Figure 5.4.14 SIMS sputter depth profile of Al_2O_3 grown on unimplanted NiAl at 1500°C showing the ratios of the two isotopes. Oxidation was for 50s in ^{18}O followed by 110s in ^{16}O.

5.4.6 AEM Results

The results at this temperature involve two sets of samples. The first set comprises the oxide grown isothermally for 50hr. The second consists of a single sample which was Y-implanted and oxidized for 0.2hr. After 50hr, there was very little difference in the oxides formed with and without Y. However, with only a 0.2hr exposure, an improvement in oxide adherence was observed. Thus at short times the segregation of the reactive element to oxide interfaces was expected.

Preparing thin samples after oxidation even for short times was difficult in the case of the implanted NiAl because of the less-than-perfect adherence and the thick scale. Parallel sections were prepared near the gas interface and near the alloy interface. As at 1200°C, the scale near the gas interface was filled with YAl_xO_y particles and voids; although in this case the voids appeared larger and there were fewer particles, Figure 5.4.15a. It was again difficult to see much structure near the gas interface. Rh particles were observed throughout the sample.

Closer to the alloy interface, there were fewer particles and voids, Figure 5.4.15b. In this section, voids could be seen both in grains and on grain boundaries. The grain size was too large (>1μm) relative to the thin area to determine an average. However, the grain boundaries were more easily distinguished and could be analyzed. Y was found to segregate to all of the boundaries examined with an average Y/Al ratio of 0.029.

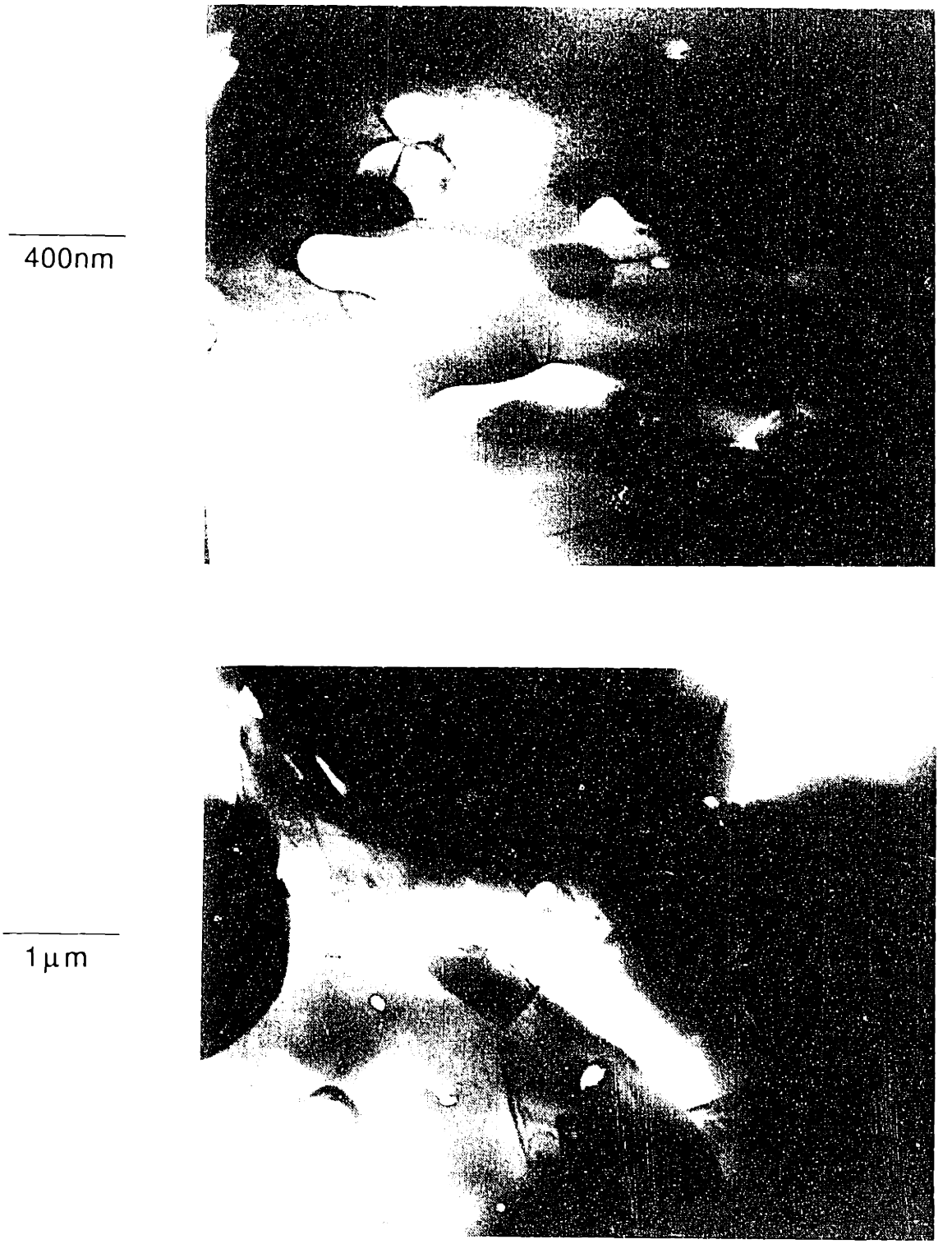

Figure 5.4.15 STEM bright field images of the Al_2O_3 scale on Y-implanted NiAl after oxidation at 1500°C for 0.2hr. Parallel sections made near the (a) gas interface and (b) alloy interface.

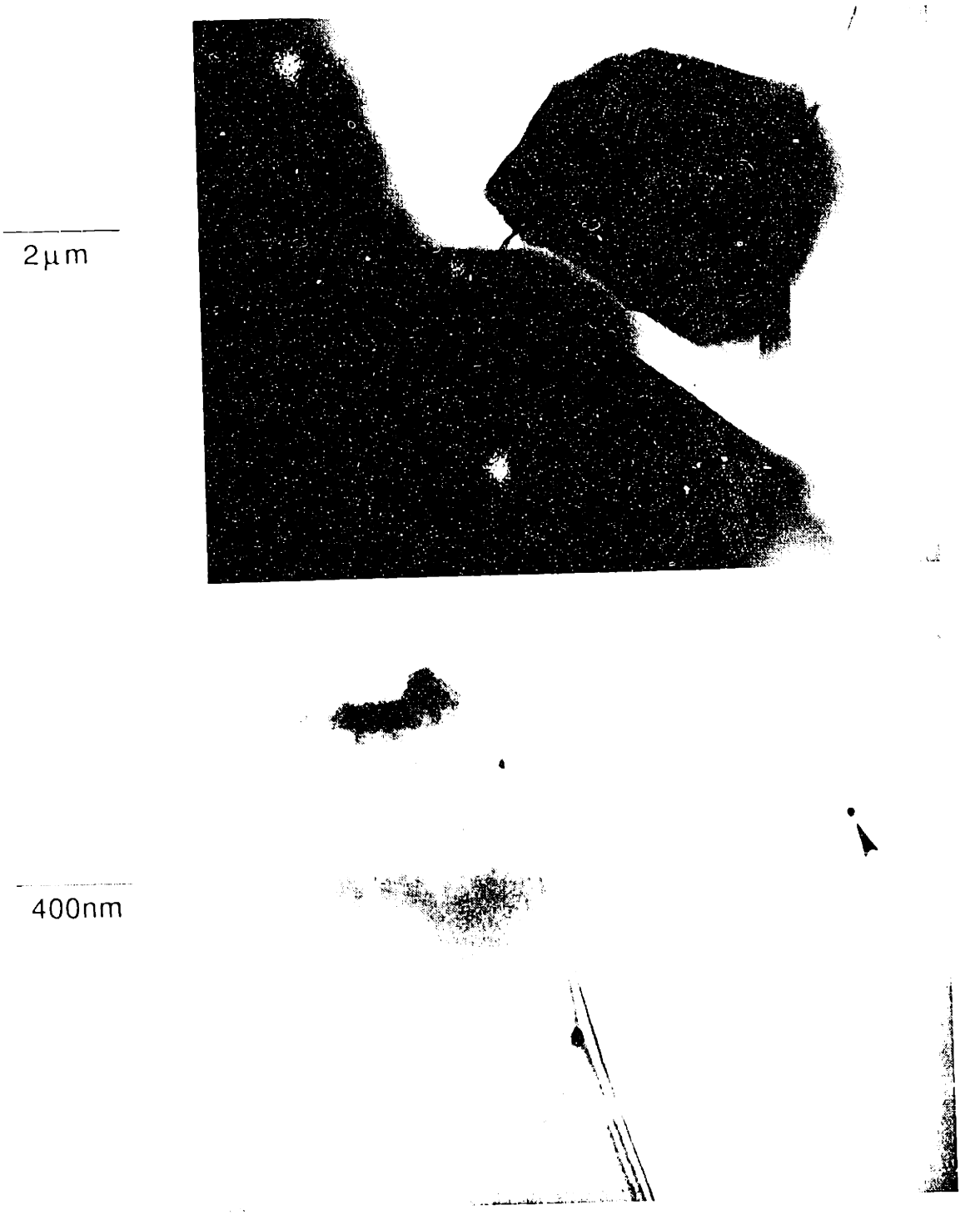

Figure 5.4.16 STEM images of the Al_2O_3 scale on Y-implanted NiAl after oxidation at 1500°C for 50hr: (a) annular dark field image of a parallel section near the alloy interface, and (b) bright field image near the center of the scale -- Rh particles are observed in the grain and pinning the grain boundary.

After a 50hr exposure, spalled pieces of oxide were placed on a Cu-grid and ion thinned. The grain size in these samples was also too large relative to the thin area to estimate the grain size by TEM. It was also difficult to tell the difference between a void and a hole from milling. The voids observed in the SEM cross-sections were very large (up to 1μm in diameter). However a number of observations were made.

In the scale grown on Y-implanted Ni-30Al, YAl_xO_y particles were observed only near the center of the scale. No grain boundary segregation of any elements was detected in either the implanted or unimplanted case. In a parallel section near the substrate, a thinned oxide ridge was found to contain a single grain boundary, but no segregation was detected, Figure 5.4.16a. Because of the rough surface, there was very little thin area -- structures were either too thick or had milled away.

Rh particles were observed in the center of the scale and near the gas interface. Figure 5.4.16b shows Rh particles in an oxide grain and pinning a grain boundary. The detection of these particles (originating from the evaporation of the hangdown wire) within the growing oxide scale is an indication of outward scale growth that would bury these particles

5.5 Summary of NiAl Results

In a nutshell, the study of Y-implanted NiAl revealed that ion implantation is, at best, a flawed technique for the study of the REE. At 1000°C, the Y-implant modified the $\theta-\alpha$ phase transformation,

stabilizing the faster-growing θ phase. This can hardly be considered beneficial to the oxidation behavior. This was also observed at shorter times at 1200°C and may have contributed to the poor scale adherence on the doped NiAl.

At higher temperatures, the implant appeared to be limited in effect because of its concentration at the substrate surface. When several μm thick scales form, the nm-deep implant level was inadequate to modify the oxidation behavior. At 1400°C and 1500°C, the Y-implant did not change the long-term oxidation rate. An improvement in the scale adhesion at 1500°C, lasted less than 0.4hr. At longer times at 1200°C, the limited nature of the implant may have contributed to the poor scale adhesion in cyclic tests of doped NiAl. At both 1200° and 1500°C, a large amount of Y was observed to form Y-rich oxides near the gas interface.

Using NiAl with an alloy addition of Zr, the REE was more easily observable at 1200°C. The oxidation rate was reduced and scale adhesion was improved over 20, 2hr cycles. The reduction in oxidation rate is attributed to the clear difference in the oxidation mechanism using an ^{18}O tracer. Zr doped α-Al_2O_3 was observed to grow solely by the inward diffusion of O while the undoped scale on NiAl grew by a combined diffusion mechanism with new oxide being formed both at the gas and alloy interfaces. This agrees with the mechanisms observed for FeCrAl alloys. The Y-implanted NiAl could not be analyzed at 1200°C because the scale consisted of both θ- and α-Al_2O_3.

At 1500°C, the Y and Zr dopants appeared to change the oxidation mechanism of α-Al_2O_3 in the same way, by reducing the

outward diffusion of Al. However, the evidence was far less convincing then the ^{18}O profiles at 1200°C. The undoped oxide microstructure at 1500°C indicated a mixed mode diffusion mechanism.

6.0 Discussion

This chapter's role is to define the thread that runs throughout the project. The most important issue is trying to explain the reactive element effect based on the observations -- the "how" and the "why", not the "what". The first section deals with the REE. The subsequent sections discuss other aspects of the research relating to this central issue. The goal is to explain the central core of results with a few diversions that were especially noteworthy. Certainly the list of central issues has changed since this project was begun. The following is a list of what is currently felt to be the crux of the work. And of course, many issues are left unresolved. These are topics for future work.

One final note is required. To a certain extent, promoting one's own theory also involves criticizing other theories (some call it negative campaigning). After all, if the other hypotheses were perfectly correct, advocating a new one would be unnecessary. The following arguments represent the most current observations and interpretations. One of the benefits of having begun this project in 1989 is that the analytical techniques available then (and now) far exceeded those of even 10 years before. Some of these new techniques have, so to speak, "thrown dirt" on older theories. Some day all of the following may appear as only a forgotten irrelevant footnote. For now, it is an attempt at an objective assessment of the data.

6.1 Explaining the Reactive Element Effect

Most of the experiments were conceived with the goal of explaining the REE. Some were much more successful than others. Also because of the large number of variables and effects, some issues were neglected. This section attempts to put the results of this study into the context of the REE literature.

Since it's discovery in 1937, no theory has been put forward to explain all of the effects found when a RE is added to an oxidation resistant alloy. Obviously, with 50 years of research preceding this work, the idea that one conclusive theory would come from this work was a bit unrealistic. However, it is necessary in this case to look at all of the available evidence and all of the available theories and decide which one best fits the observations. In my opinion, the segregation theory best fits the majority of experimental evidence. The following sections describe the implications of this theory with respect to these observations both from this study and the literature.

6.1.1 The Choice of the Segregation Theory

The segregation theory is based on one single premise: all of the reactive element effects can be explained by the segregation of the reactive element to the oxide grain boundaries and the metal-oxide interface. This is true for both Al_2O_3 scales and Cr_2O_3 scales.

The explanation is set out over the next few sections, but a brief outline is given here. The growth mechanism is changed by the

segregation of the RE to the oxide grain boundaries where it limits the outward cation diffusion (Al in the case of α-Al_2O_3 scales). This reduction in cation diffusion changes the primary rate-limiting step to the inward diffusion of oxygen. This modification reduces the oxidation rate. This effect is discussed in Section 6.1.2.

The improvement in oxide adherence is discussed in Section 6.1.3. This is one of the more complicated effects and is linked to the role of sulfur on adherence. Other adherence theories have been proposed regarding oxide pegs, vacancy sinks, enhanced chemical bonding and a graded seal. The experimental evidence points to a primary effect of indigenous sulfur on the oxide adherence [e.g. Smialek, 1987a]. Sulfur segregates to the oxide-metal interface and weakens the bond between the metal and oxide. Rather than reacting with sulfur to form YS, as was proposed by Smeggil, et al. [1985], it is suggested that the segregation of the RE to the metal-oxide interface lowers the driving force for S surface segregation and thus eliminates the detrimental effect of S. The role of S in scale adhesion is discussed in Section 6.1.4.

The change in oxide morphology and the reduction in the oxide grain size can be attributed to a simple solute drag effect. The larger RE ions on the oxide grain boundaries reduce the mobility of the boundary, slowing grain growth. This modification is discussed in section 6.1.5. The selective oxidation of Al was not studied specifically, but a few comments are included in Section 6.1.6. The final section discusses the effect of temperature on the REE.

The primary reason for choosing the segregation theory as an explanation is that the other theories either do not satisfactorily

explain all of the REE or else are inconsistent with the available experimental evidence. All of the alternative theories are outlined in Section 2.2.

Some theories are quite easy to discard. For instance, the oxide-dispersed FeCrAl alloys exhibited good adherence without the formation of oxide pegs; thus the peg theory is not a sufficient explanation of any of the observed RE effects. Also, XTEM of the alloy-oxide interface did not detect the formation of a "graded seal" between the metal and scale, thus the graded seal theory can also be discarded.

The vacancy sink theory is difficult to assess because of the difficulty in obtaining experimental evidence on point defects. Voids are observed without a RE and aren't observed with a RE [e.g., Tsuzi, 1980]. One reason for discarding the vacancy sink model is that STEM observation of RE oxide particles near the metal-oxide interface in both MA956 [Katz, et al., 1987] and Ni-20Cr [Pint, et al., 1989] did not identify any voids near these particles. However, the absence of these voids can be explained by a change in the growth mechanism. Voids can be caused by the outward diffusion of metal cations through the scale [Yurek and Schmalzred, 1975], and when this transport is reduced by the RE segregant, the voids are no longer formed.

Other theories such as the altered oxide plasticity and change in growth mechanisms do not account for the role of sulfur in oxide adherence. However, it is my contention that the sulfur theory over-estimates the role of sulfur. This will be discussed further in Section 6.1.4.

The one piece of experimental evidence that remains unexplained by the segregation theory is that regarding the improvement in oxide adherence with the addition of non-RE oxide dispersions such as TiO_2 and Al_2O_3 [Tien and Pettit, 1972; Wright, et al., 1975] This evidence must remain inconclusive because the effect has never been fully characterized. None of these studies compares this improvement "head-to-head" with an RE addition or provides any characterization beyond simple kinetic weight gains. In the case of the paper by Tien and Pettit [1972], no data is given at all. Frankly, the question arises why commercial alloys contain RE oxide dispersions if cheaper Al_2O_3 dispersions would provide the same benefit. The bottom line is that there is not enough experimental data to support this claim. If more data were provided in the future, then the segregation theory may have to be reassessed. In the mean time, this result must remain unexplained.

6.1.2 The Rate-Limiting Step

Based on the kinetic and ^{18}O tracer experiments, there is clearly a change in the diffusion mechanism and thus the oxidation rate with the addition of a RE. The change has been characterized in α-Al_2O_3 as a reduction in Al diffusion outward. This has been observed in both NiAl and FeCrAl and is consistent with the results of Quadakkers, et al. [1989] on FeCrAl. Further discussion of the oxidation mechanism is included in Section 6.3.

While some authors have insisted (in some cases in spite of their data) that an RE addition does not change the oxidation rate

[e.g. Bennett, et al., 1990], the data from this study shows a small but repeatable reduction in the oxidation rate. Figures 6.1.1 and 6.1.2 show a compilation of the isothermal kinetic data for NiAl and FeCrAl alloys at 1200° and 1400°C respectively. At both temperatures, the addition of a RE reduced the oxidation rate. A number of other studies on a variety of alumina-formers also have concluded that there is a clear reduction in the oxidation rate. For example, Allam, et al. [1978] found that the growth rate of Al_2O_3 was reduced when both Y and Hf were added to CoCrAl alloys at temperatures between 1000° and 1200°C.

The insistence that there is no effect of REs on the oxidation rate of alumina-formers occasionally involves a comparison with chromia-formers. For Cr_2O_3, doping with a RE produces a reduction in the parabolic rate constant by 1-2 orders of magnitude. Thus, by simple analogy, a similar reduction is expected when Al_2O_3 is doped. However, the two oxides are not so easily compared. In fact, a very different picture is found when comparing the diffusion data in the literature. Figure 6.1.3 shows the boundary diffusion data for polycrystalline samples. If the REE is interpreted as a reduction in cation transport for both α-Al_2O_3 and α-Cr_2O_3, then the change in oxidation rate for the two oxides will not be the same. For Cr_2O_3, with a large difference between D_{Cr} and D_O, if D_{Cr} is eliminated by RE segregation then growth by D_O will be significantly slower. In fact for pure Cr, the rate reduction is approximately 100 times [Cotell, 1988]. However, in the case of Al_2O_3, a reduction in D_{Al}, leading to rate control by D_O only, does not result in a significant change in the mass transport rate. With the observed growth rate

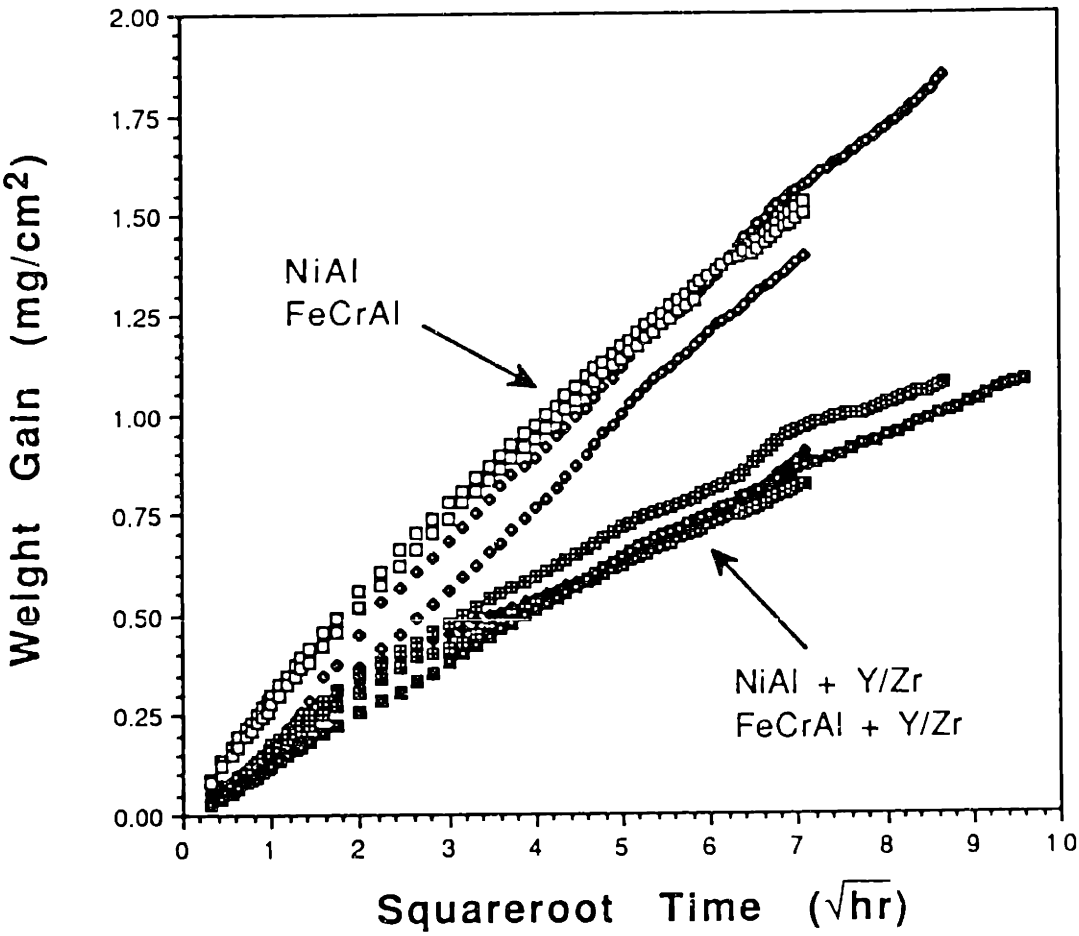

Figure 6.1.1 Parabolic plot of weight gain versus squareroot of time for both NiAl and FeCrAl alloys at 1200°C in 1atm of O_2.

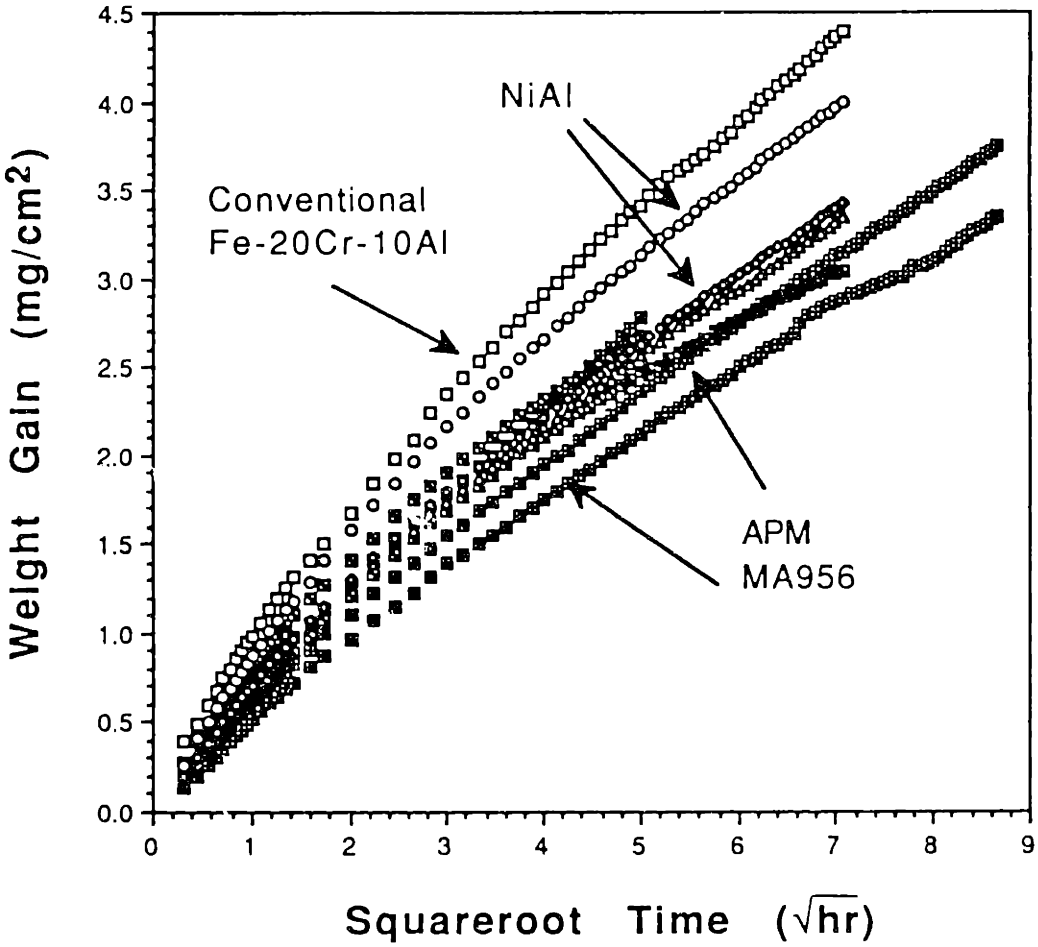

Figure 6.1.2 Parabolic plot of weight gain versus squareroot of time for both NiAl and FeCrAl alloys at 1400°C in 1atm of O_2.

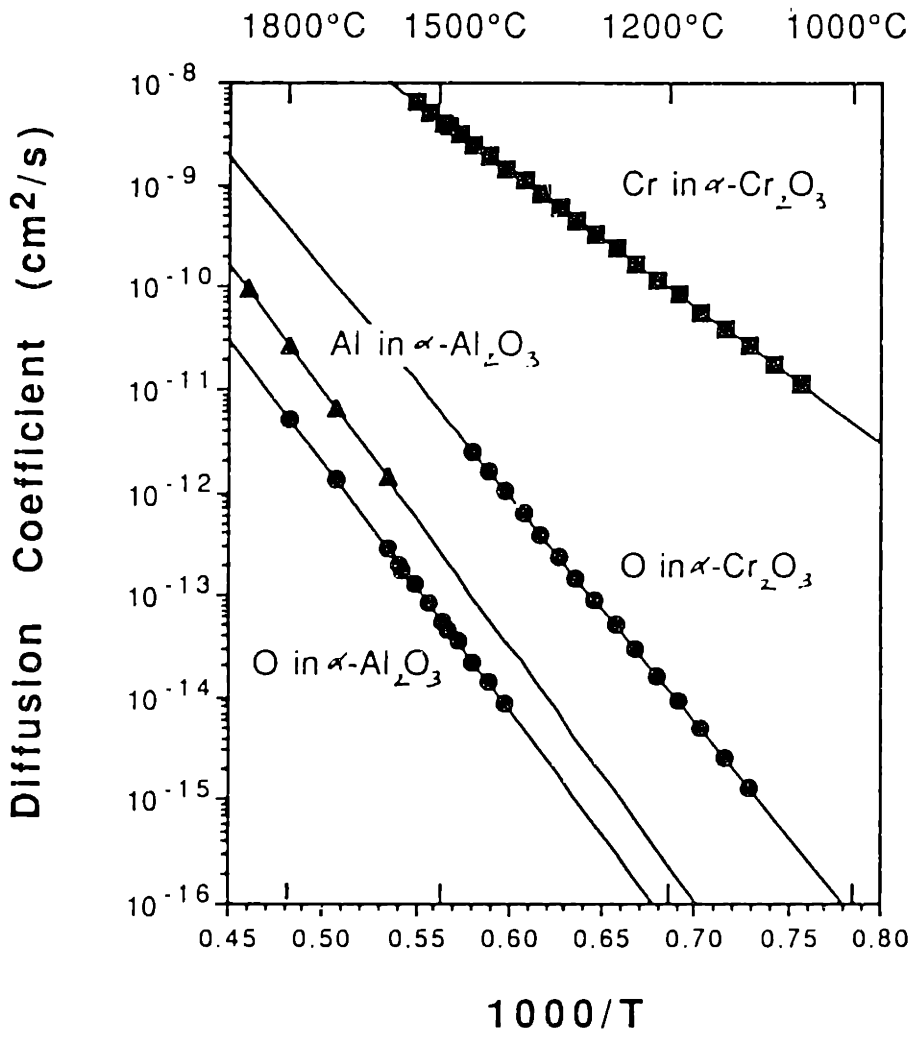

Figure 6.1.3 Boundary diffusion data from the literature for α-Cr_2O_3 and α-Al_2O_3. The points mark the experimentally determined values while the line is an extrapolation of these values. Data for D_{Cr} from Hagel and Seybolt [1961], D_O in Cr_2O_3 from Hagel [1965b], D_{Al} from Paladino and Kingery [1962], and D_O in Al_2O_3 from Oishi and Kingery [1960].

reduction in doped Al_2O_3 being 2-4 times, the correlation with the diffusion data is surprisingly accurate, and the lesser effect found in Al_2O_3 as compared to Cr_2O_3 is consistent with the grain boundary diffusion data. The favoring of boundary transport over lattice transport as the rate-limiting diffusion process is discussed further in Section 6.2.3.

6.1.3 Oxide Adherence

The basic test for oxide adherence is cyclic testing in which, in the present study, the sample goes through the cooldown stage 20 times in order to test the degree of adherence between the metal and the scale. This is mainly an engineering-type test in which the mechanism of scale adherence is not addressed nor any characterization performed beyond a simple analysis of the extent of spallation.

One of the problems in characterizing oxide adherence is not being able to observe the metal-oxide interface of both adherent and non-adherent scales using the same technique. RE segregation to oxide scale grain boundaries has not been detected by any technique other than STEM analysis using a very fine electron probe. Thus, in order to detect the segregation of a RE to the metal-oxide interface this technique was employed in this study also.

XTEM samples were made from APM substrates with adherent scales oxidized at 1000°C and 1200°C. In each case, Zr segregation was detected at the interface. In a previous study, Y was found to segregate to the interface after oxidation of MA956 for 100hr at

1000°C [Katz, et al., 1987]. Y was also found to segregate to the Cr_2O_3/alloy interface for a Y_2O_3-dispersed NiCr alloy oxidized for 20hr at 900°C [Pint, et al., 1989]. With each of these adherent, doped scales, the RE but not S was found to segregate to the interface. Based on the literature, S would be expected to segregate to the metal-oxide interface and promote decohesion of the scale. However, XTEM is limited to nominally adherent scales. In the case of alumina-formers, undoped scales spall readily and the interface does not remain intact to be sectioned for XTEM.

Conclusions about non-adherent scales thus must be based on other observations. The morphologies of scales formed on the undoped NiAl and FeCrAl substrates are the best available examples. In the case of the buckled scale formed on undoped FeCrAl, the substrate beneath the spalled oxide shows clear indications of regions where the oxide has remained in contact with the alloy and other smooth areas where the oxide had lost contact at temperature. However, while the morphology gives an indication of where the failure originated, it does not indicate why failure occurred. For example, the coalescence of vacancies to form voids could be occurring or a chemical effect of S segregation could lead to this loss of cohesion. No S was detected in any location by EDXA in the SEM, but monolayer segregation would be undetectable by this technique. The best suggestion from the literature about observing S segregation at the metal-oxide interface is to use AES and remove loosely adherent scales *in situ*. However, this type of equipment was not readily available at MIT or elsewhere.

Thus, while the RE addition is observed in each case to at least temporarily improve oxide adherence, no experimental evidence suggests a reason for this improvement. Further discussion about the potential role of sulfur is included in the next section.

6.1.4 The Role of Sulfur

The role of sulfur was not explicitly addressed in this work. For instance, no effort was made to minimize the S content in any of the alloys or to study a sulfur-free alloy. Yet, based on the experimental evidence in the literature, there is virtually no question that there is a detrimental role of sulfur on oxide adherence (see Section 2.5). While not studied explicitly, the possible presence of S was examined. S was always looked for during characterization, especially in microchemical analysis of the oxide-metal interface. However, while the analytical techniques used in this study are well suited to analyzing S segregation, XTEM sample preparation is not well suited to study non-adherent scales, where S segregation is most likely to be observed.

Thus, this discussion is based largely on experimental evidence in the literature and simple estimations. The considered result is that the other theories present in the literature do not adequately explain the experimental evidence. A new theory based on RE segregation is presented to explain the interaction between the RE addition and S.

6.1.4.1 The Formation of Sulfides

One explanation regarding the combined effect of a RE addition and S is that a RE sulfide is formed which ties up the indigenous S and prevents the segregation of S to the metal-oxide interface [Smeggil, et al., 1985]. Unfortunately, there is very little experimental evidence to suggest that these sulfides are formed. Simple mass balances and thermodynamics also do not favor this formation.

An STEM/EDXA study of MA956 [Katz, et al. 1987] looked specifically for sulfide formation in the alloy both before and after oxidation at 1000°C for 100hr. Sulfide formation was not detected in either case, despite the large S content in the alloy (110ppm). It could be argued that YS_x particles are preferentially removed during TEM specimen preparation. However, no other study has identified the presence of RE sulfides in the alloy, either.

Another unexplained issue regarding sulfide formation concerns surface ion implantation. Numerous studies have shown that ion implantation at 700°-1000°C improves the oxide adherence of both Cr_2O_3 and Al_2O_3 (see section 2.3.2). Consider for example, the case of an Y implant. If the Y reacts with indigenous S to form YS, then S would be unable to segregate to the metal-oxide interface. YS is deemed to be the stable sulfide formed because the addition of Y_2S_3 to NiCrAl produced catastrophic oxide spallation [Smeggil, et al., 1986]. A simple estimate of the quantity of sulfur reveals that in a coupon 0.1 x 1.0 x 1.0cm there are approximately 10^{17} S atoms for 10ppm S in the bulk. With a typical implant of 2 x

$10^{16}/cm^2$ and 40ppm S content, the ratio of S atoms to Y atoms is 10 to 1. Thus, there is a significant fraction of S in the alloy that would not be tied up as a sulfide.

Furthermore, analysis of scales formed on implanted substrates reveals large quantities of the implanted RE present in the scale as RE-rich oxides [e.g. Bennett, et al., 1985; Cotell, 1988; Przybylski, et al., 1986] This further reduces the quantity of RE available to react with S to form RE sulfides.

Comparisons of ion implantation results from this study are not relevant since the implant did not consistently improve oxide adherence. The ineffectiveness of the implant is most likely a result of too little RE. This could mean too little to tie up all of the sulfur present in the NiAl coupon. It could also be argued that there is not enough RE to segregate sufficiently to the metal-oxide interface. This is discussed further in Section 6.8.1.

Finally, there is a thermodynamic issue regarding the formation of YS when an oxide dispersion of Y_2O_3 is present in the alloy (MA956). At all temperatures, Y_2O_3 has a lower free energy of formation than YS or Y_2S_3, [Sigler, 1989]. Therefore, there is no apparent driving force for the formation of a sulfide when Y is present in the alloy as Y_2O_3 or YAl_xO_z.

The formation of stable RE sulfides may occur on a limited scale but as an explanation for the REE improvement in oxide adherence, it does not appear to be adequate.

6.1.4.2 Inconsistencies with the Sulfur Effect

While the presence of sulfur in alloys is clearly important, the sulfur effect which attempts to explain all of the REE by the presence of sulfur [Lees, 1987] appears to overstate the role of sulfur. This theory, the youngest in a long line, is a sort of "anti-theory". According to Lees, the improvements associated with the addition of an RE act only to tie up S. Without S (and a RE) in the alloy, the oxidation rate would be slower, the oxide adherence would be excellent and the growth mechanism would be primarily inward O transport. S is proposed to enhance the outward diffusion of Cr and Al. There are numerous studies to support the role of S on oxide adherence (see Section 2.5). Unfortunately, there is no experimental evidence to suggest that S changes the rate-limiting step of oxidation, despite the fact that a simple inert marker experiment for Cr_2O_3 is quick, reliable and inexpensive.

The attractive feature of this theory is that it seeks to explain why non-RE oxide dispersions appear to improve oxide adherence. According to Lees, any stable particle in the alloy will provide an interface that will attract sulfur away from the metal-oxide interface. Thus, this effect is independent of particle composition and works for RE and non-RE oxide dispersions.

However, experimental evidence does not support this idea. An STEM/EDXA study of MA956 [Katz, et al. 1987] found no evidence for S segregation to alloy-particle interfaces, despite the high sulfur content in the alloy (110ppm). S segregation has been detected in other AEM studies [Kim, et al., 1986; Pint, et al., 1989; Fox, et al.,

1991], so there is little question that S segregation is detectable. However, for MA956, the Y_2O_3-Al_2O_3 particles in the alloy are not found to be sinks for S. There have been no other studies in the literature regarding the effect of S segregation on oxidation.

The sulfur theory is another example of a single observation (the effect of S on oxide adherence) being extended to explain all of the REE. In this case, however, the explanation is not sufficiently supported by experimental evidence.

6.1.4.3 Sulfur and Reactive Element Segregation

Models involving the formation of sulfides and the oxide dispersion sulfur sinks do not appear to adequately explain the effect of RE on indigenous S. A new theory is thus proposed as part of the segregation theory in which the segregation of the RE to the alloy-oxide interface lowers the interfacial free energy, thereby decreasing the driving force for the segregation of S. This idea recognizes the importance of both S as being detrimental to oxide adherence and the RE as necessary to neutralize the deleterious role of indigenous sulfur.

This is one of the less well established effects of segregation. The segregation of REs to the metal-oxide interface may have no effect on scale adhesion. On the other hand, if the segregant effectively reduces the driving force for S segregation, then it is no longer energetically favorable for S to segregate to the metal-oxide interface. Thus the detrimental role of sulfur is eliminated not by a bulk effect of tying up sulfur but by a localized interface effect.

This localization better explains the improvements associated with an implanted RE.

This theory is supported by the work of Briant and Luthra [1988]. In their study, when pure metal blocks of Fe, Ni, Cr, Al, and Y doped with 100ppm S were heated in vacuum, S was detected by AES on the surface of each block except Y. Although it is certainly not conclusive, their result is an indication that Y reduces the surface-active nature of S.

One thing to keep in mind in this discussion is that the failure of the oxide-metal interface requires some source of stress. This requirement is particularly well illustrated by the work of Lee and Worrell [1989] on Al_2O_3 grown on Ir_2Al_5. With no RE addition and no S reduction, adherent Al_2O_3 scales are grown on Ir_2Al_5. This particular alloy was chosen because the CTE between the alloy and the oxide are nearly equal. Without any cooling stresses generated during cooling, the undoped oxide reportedly remained adherent on a S-containing metal substrate. However, in the case of engineering alloys such as NiCrAl, stresses are inevitably generated, and dopants are crucial to achieving good oxide adherence.

6.1.5 Oxide Morphology and Grain Growth

Alteration of oxide morphology and grain growth behavior is often discarded from the list of REEs; rather, from an engineering standpoint, the oxidation rate and oxide adherence are often emphasized. However, it is quite clear that the addition of a RE has an effect on the oxide morphology and especially oxide grain growth.

This effect is found for both chromia-formers [Przybylski and Yurek, 1989] and alumina-formers in this study, e.g. Table 4.1. The change in oxide microstructure is conveniently ignored in many other REE explanations, because it is difficult to explain this effect without looking at the segregation phenomena. There is no evidence that oxide pegs, interface voids, growth stresses, and the absence or presence of sulfur changes the oxide grain size or morphology. Also, TEM sections did not reveal sufficient particles or pores to account for the reduced grain growth. There is however abundant evidence from the ceramics literature (e.g. Kingery, et al., 1976, p.457) to suggest that segregation of foreign ions to ceramic grain boundaries reduces grain boundary mobility. This is commonly referred to as the solute drag effect.

One of the strengths of the segregation theory is that it explains these observed changes. However, the question remains if this effect is of any practical significance. Perhaps it can be ignored because it is only a minor effect. The issue of whether the oxide scale grain size is of first-order importance to the oxidation behavior has not been fully addressed by any work in the literature. While it has been proposed that a finer scale grain size improves the scale plasticity which in turn improves oxide adherence, there is no experimental evidence to support this contention. Plasticity may indeed be improved at the reaction temperature, but in fact most failures occur during cooldown when the temperature is significantly reduced. However, no conclusive evidence has been observed concerning the effect of oxide morphology on oxidation behavior. This topic is discussed further in Section 6.9.

6.1.6 Selective Oxidation of Al

Pettit's calculations [1967] about the thermodynamics of Ni-Al alloys determined that only 1ppm of Al was necessary to achieve thermodynamically-stable, selective oxidation of Al. His experimental observations indicated that the formation of a continuous alumina scale was a kinetic issue. Selective oxidation was not formally addressed in this study but some comments on selective oxidation can be made. First of all, combined with the other RE effects, the improvement is not unexpected. If the rate at which the metal (in this case, Al) is consumed is reduced, then less Al is required in the alloy to maintain scale growth. Also, if spallation is reduced, then extra Al for regrowing or healing the scale is not necessary.

The usual technique for studying selective oxidation is to add a RE to a substrate that does not have a sufficient Al content to form an Al_2O_3 scale. However, for the most part, the materials studied in this project form continuous Al_2O_3 scales during oxidation with or without a RE addition. Even Ni_3Al is an alumina-former according to the analysis of Pettit [1967]. Thus, this issue was not specifically addressed in any of the experiments.

The effect of Al content was explored initially for several compositions within the ß-NiAl phase field (see Section 6.5). This is not really an issue of selective oxidation since all compositions of ß will form an Al_2O_3 scale. It has more to do with the mechanical properties of NiAl. In this case, increasing the Al

content too much degrades alloy ductility [Russell and Edington, 1972]. For FeCrAl alloys, at least as based on the work of Lambertin and Beranger [1990], Al content is not a significant issue, since only ≈4wt% Al is necessary to form a protective alumina scale.

In this study, varying the Al content in the ß-NiAl phase field produced very little change in the oxidation behavior up to 1500°C, (e.g. Figure 5.4.1). Thus, it appears that reducing the Al-content in NiAl to improve its mechanical properties would not be detrimental to the oxidation behavior. One point of caution is warranted. If the Al content is reduced too far in the ß phase field, long-term oxidation may induce a phase transformation to Ni_5Al_3 or Ni_3Al (see Figure 2.3) which could prove detrimental to the oxidation behavior.

6.1.7 Reactive Element Effects at Higher Temperature

It has been predicted in the literature that there is an upper bound to the applicability of the REE [Whittle and Stringer, 1980]. However, there are very few published studies investigating the REE at high temperature (>1300°C). From the standpoint of the segregation model, there is presumably a relationship between temperature and the extent of segregation. The driving force for segregation in Al_2O_3 is most likely a strain-relief mechanism for larger cations -- in this case Y, Zr and Ti. It is possible that, as the temperature is increased, foreign ions could be more easily accommodated into the lattice, thus limiting the extent of segregation. Based on the segregation theory, there would be a critical temperature above which segregation would be too low to

modify the oxidation behavior. At this point, the REE would no longer be observed.

An upper bound in the REE also could occur in other ways. At some point, if the contribution of lattice diffusion of either Al or O became significant relative to that of boundary diffusion, then even with a boundary segregant the RE would no longer be effective. Furthermore, if RE segregation could no longer slow grain growth sufficiently, then the oxide microstructure would not be modified.

Results from the higher temperatures experiments carried out in this study produced mixed results. Those for RE oxide-dispersed FeCrAl clearly show an improvement at 1400°C with the RE addition, (Figures 4.3.1 and 4.3.2). However the Y and Zr additions to NiAl effected only temporary improvements at 1400°C and 1500°C. While there is not sufficient evidence to claim that RE effects are definitively observed at 1500°C, there is clear evidence to show that the effects are not restricted to lower temperatures and persist well above 1200°C.

For example, Y ions were found to segregate at each temperature investigated (up to 1500°C). Thus (if it exists), a critical upper-limit temperature was not reached for Y. However, a change in segregation behavior with temperature was observed in the case of Ti segregation in the scale formed on MA956 at 1400°C. This result is discussed further in Section 6.7.3.

Other RE effects are also still observed at higher temperatures. For oxidation of doped FeCrAl alloys at 1400°C, the oxidation rate is reduced, oxide adherence is improved, the oxide grain size is reduced, and Y segregation to oxide grain boundaries is

detected. All of these effects are also observed at 1200°C and 1000°C. The observations that were unique to oxidation of MA956 at 1400°C, such as the rumpling of the metal-oxide interface and the minor spallation, did not appear to be overly detrimental to the overall oxidation behavior. Also, at 1500°C with Y-implanted NiAl, the short-term nature of the improvement in oxide adherence appeared to be more related to the limited supply of RE than any general breakdown of the REE. However, more experiments are required to verify the REE at 1500°C. Thus, while it has been proposed that the REE is limited to the range 0.4-0.6T_m (820°-1230°C for α-Al_2O_3, with a melting temperature of 2050°C), a better upper estimate is probably 0.7 or even 0.8T_m.

6.2 General Kinetic Information

Oxidation reaction rate measurements are typically used as an initial characterization to assign oxidation behavior to the appropriate regime. But, such measurements are sometimes relied on as the form of primary characterization, in which case the limitations of measuring only weight changes can lead to incorrect interpretations. There are many examples from the oxidation literature where kinetic data was misleading. However, in the present study of alumina-formers, it is asserted that such has not been the case.

In general, the oxidation rates have been reliable and repeatable. A simple comparison of k_g values measured in this study with some values from the literature reveals that the scatter from

the present data falls well within the scatter of the literature, Figure 6.2.1. There is even a generic difference observable between the doped and undoped cases. The average activation energy is 240kJ/mol with oxidation of undoped material having a slightly lower activation energy and that of doped material slightly higher.

Using the measured oxygen weight gain in mg/cm^2 and the theoretical density of Al_2O_3, a total oxide thickness can be estimated. Comparing these values to SEM observations, the match is reasonable, Table 6.1. These kinetic data have provided an initial starting point for additional characterizations of the oxide phase and scale microstructure and the growth mechanism. The following sections detail the information which is obtainable from the kinetic data. In most cases, these results were also confirmed by further observations.

6.2.1 Parabolic Kinetics

Based on the general parabolic oxidation behavior observed for all times and temperatures, it follows that the rate limiting step is the solid state diffusion of the reactants through the oxide product. This is the fundamental idea behind a parabolic rate law -- as the reaction product grows, the diffusion distance increases, thus slowing the reaction.

The analysis does not specify whether lattice transport or some form of short-circuit transport occurs, but it does eliminate the possibility of significant growth by other means, such as diffusion through cracks or pores. Diffusion through such pathways

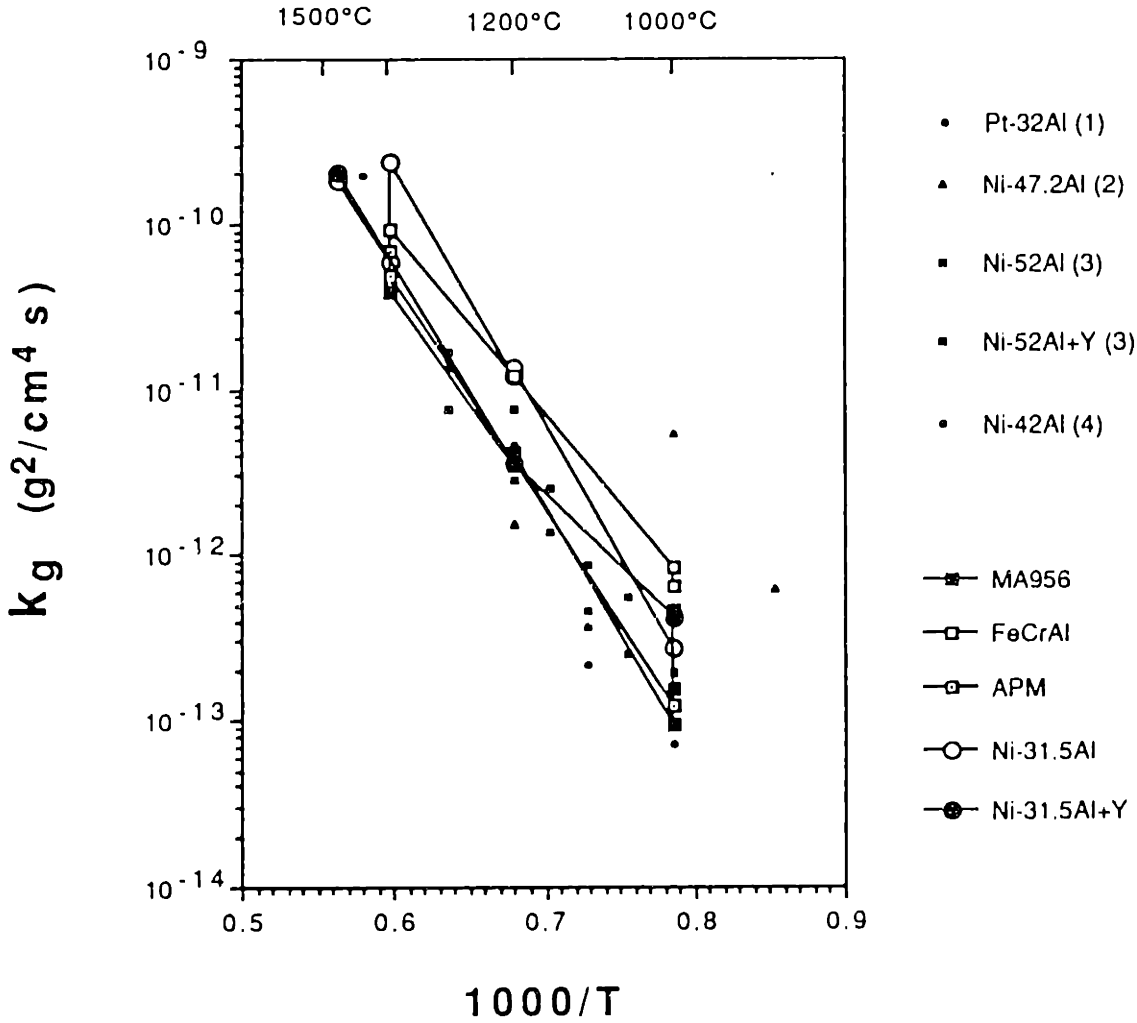

Figure 6.2.1 A comprison of the parabolic rate constants measured in this study with values reported in the literature. The data from this study are connected by lines. The Al contents from the literature are in atomic percent and the references are (1) Felten and Pettit [1976], (2) Rybicki and Smialek [1989] (3) Jedlinski and Mrowec [1987] and (4) Pettit [1967].

Table 6.1 Comparison of the theoretical scale thicknesses calculated from the TGA data and scale thicknesses observed using SEM for various alloys and oxidation conditions.

Substrate/Conditions	Estimation from TGA	SEM Observation Approximation
FeCrAl 1200°C 2hr	1.3μm	1.5μm
FeCrAl 1200°C 50hr	8.3	7.0 + whiskers
APM 1200°C 100hr	5.9	5.0
MA956 1200°C 50hr	4.5	3.5
FeCrAl 1400°C 1hr	5.2	5.0
APM 1400°C 1hr	3.9	3.0
Ni-31.5Al+Y 1500°C 0.2hr	2.1	2.5
Ni-31.5Al+Y 1500°C 4hr	10.7	10
Ni-30Al+Y 1500°C 50hr	31.5	32
Ni-30Al 1500°C 50hr	32.6	31

would be unlikely to result in a single parabolic rate. For cracks, the corresponding reduction in the solid-state diffusion distance should produce a positive deviation from parabolic behavior. The isothermal observation of a unique parabolic rate does not preclude the possibility of cracks forming during cooldown, which may nevertheless affect the oxidation rate in cyclic testing.

6.2.2 Phase Identification

In 1965, Hagel [1965a] determined separate reaction rates for the formation of θ and α-Al_2O_3. 24 years later, Rybicki and Smialek [1989] found a similar result using kinetic data to indicate which phase of Al_2O_3 is formed. In the case of ß-NiAl at 1000°C, this is especially apparent, Figure 5.1.2. The undoped NiAl has a clear

transition between the first-forming, faster-growing θ-Al_2O_3 and the slower-growing α-Al_2O_3.

This analysis, however, is much clearer in hindsight. The kinetic data are not conclusive without further characterization. The repeatability of the transition renders it more than an anomaly, but on first glance it might appear to be the result of a transient oxidation period. Further characterization was required to show that, for ß-NiAl compositions, the volume of Ni-rich oxides was insufficient to explain the initial rapid weight gains. Only an Al_2O_3 phase transformation is consistent with this rate change. In fact, for Ni_3Al, SEM and GAXRD observations after oxidation showed that the initial high weight gain was the result of a large amount of Ni-rich oxide, and there was no indication of any θ-Al_2O_3 formation.

At higher temperatures, where the phase transformation most likely takes place at very short times, the kinetic data is not an especially useful technique for identifying phase transformations. During the first minute or so, the balance is generally erratic and unreliable. Thus the usefulness of kinetic data is also limited at short times and high temperatures.

6.2.3 Diffusion Constants Derived from Rate Constants

Using the derivation of Wagner [1951] and the interpretation of Yurek [1987], the parabolic oxidation rate constant for the formation of Al_2O_3 can be related to the solid state diffusion constant by the following equation for Al_2O_3:

$$k_p = 1/2 \int_{P_{O_2}'}^{P_{O_2}''} [3/2\ D_{Al} + D_O]\ d\ln P_{O_2} \qquad (6.1)$$

where k_p = the parabolic oxidation rate constant, P_{O_2}' = the decomposition pressure of Al_2O_3, P_{O_2}'' = the ambient oxygen pressure, and D_{Al} and D_O are the respective self diffusion coefficients for aluminum and oxygen.

Based on diffusion of both Al and O via either vacancy or interstitial mechanisms, the diffusivities can be written as:

$$D_{Al} = D_{Al}^{i} P_{O_2}^{-3/16} + D_{Al}^{v} P_{O_2}^{3/16} \qquad (6.2)$$

$$D_O = D_O^{i} P_{O_2}^{1/6} + D_O^{v} P_{O_2}^{-1/6} \qquad (6.3)$$

The i and v superscripts refer to diffusion via interstitials or vacancies, respectively. Equations 6.2 and 6.3 both assume that all defects are fully ionized. By substituting these equations into Equation 6.1, a relationship between k_p and P_{O_2} can be determined. Ramanarayanan, et al., [1983] showed that the oxidation of Al_2O_3 is independent of P_{O_2}'' from 1atm to 10^{-14}atm. Only diffusion by oxygen vacancies or Al interstitials can satisfy this requirement. Therefore diffusion will be considered only via these defects, simplifying Equations 6.2 and 6.3.

Overall diffusion of both Al and O is the sum of both lattice and short-circuit or boundary diffusion [Yurek, 1987],

$$D_x = D_l + f_t D_b, \qquad (6.4)$$

$$\text{for } f_t = g\ \delta/\lambda_t \qquad (6.5)$$

where D_l and D_b are the diffusion coefficients for lattice and boundary pathways respectively, f_t is the area fraction at time t of oxide through which boundary diffusion occurs, g is a geometric factor (equal to 2.3 for hexagonal grains), δ is the grain boundary width, and λ_t is the average grain size at time t.

The value for the grain boundary width is an important variable. While Atkinson [1987] uses a value of 1nm universally, other experimental data [Paladino and Coble, 1963] suggests that the "effective" width is as high as 20nm. Using the latter value, experimental data for phenomena such as creep matched better to the theoretical diffusion result. Carter and Sass [1981] measured the boundary width in α-Al_2O_3 using electron diffraction as 6.0-8.5nm. In order to maintain consistency, however, a value of 1nm is used in the following calculations because this value appears more physically significant than larger values. Obviously the choice of the boundary width can significantly alter the contribution ascribed to boundary diffusion.

Other mechanisms of short circuit diffusion are neglected in this simplification. For example, diffusion along dislocations is not considered. The primary reason for their neglect is that Atkinson and Taylor [1985] estimated that the dislocation density required to account for the oxidation of Cr_2O_3 at 1100°C would be $>3x10^{12}/cm^2$. Since virtually no dislocations were observed in TEM sections of Al_2O_3, it seems appropriate to neglect them.

By simplifying Equation 6.1, using Equations 6.2-5 and the fixed value of 1atm for P_{O_2}" used in these experiments, two simpler relationships can be generated:

For boundary diffusion:

$$k_p = f_t [3 D_O^v P_{O_2}'^{-1/6} + 4 D_{Al}^i P_{O_2}'^{-3/16}] \qquad (6.6a)$$

For lattice diffusion:

$$k_p = 3 D_O^v P_{O_2}'^{-1/6} + 4 D_{Al}^i P_{O_2}'^{-3/16} \qquad (6.6b)$$

In order to compare these values to the experimentally-generated parabolic constant k_g, a final relationship is necessary:

$$k_p = 1/2 (V_m/A_x) k_g \qquad (6.7)$$

where V_m = the molar volume of the oxide and A_x = the atomic weight of Al in one mole of Al_2O_3.

The remaining substitutions are relatively straightforward. P_{O_2}' is calculated from the thermodynamic data for the free energy of formation of α-Al_2O_3. The average grain size, λ_t, is established at each temperature from the available microstructural information, e.g. Table 4.1. The values for these variables are included in Table 6.2. For θ-Al_2O_3 at 1000°C, growth is mainly from the diffusion of Al, so the terms for D_O are left out. For doped α-Al_2O_3, growth is mainly from the diffusion of O so the terms for D_{Al} are left out.

However, the first problem with the calculation arises for the case of undoped α-Al_2O_3, because unlike NiO and Cr_2O_3, where one species diffuses faster then the other, undoped α-Al_2O_3 has a mixed diffusion mode. Thus, because there is no information on how much of each species is diffusing, no calculation was made for undoped α-Al_2O_3.

Table 6.2 List of the thermodynamic equilibrium Al/Al_2O_3 oxygen partial pressure and average grain size λ at time t for each reaction temperature [Chase, et al., 1985].

Reaction Temperature	Al/Al_2O_3 equilibrium P_{O_2}'	Average grain size, λ_t, μm
1000°C	$\approx 10^{-35}$ atm	0.25 (100hr)
1200°C	$\approx 10^{-29}$	0.5 (100hr)
1400°C	$\approx 10^{-24}$	1 (1hr)
1500°C	$\approx 10^{-22}$	10 (50hr)

The calculated D values are listed in Table 6.3 and are plotted with some data from the literature in Figure 6.2.2. Between 1000°C and 1400°C, the calculated values for $D_O{}^b$ are within an order of magnitude of the literature data, with a similar activation energy. On the other hand, the calculated $D_O{}^l$ is significantly removed from established values over this same range. The discrepancy indicates that at these lower temperatures the boundary diffusion of O would have to be several orders of magnitude higher in order to account for the observed oxidation rates.

However, there is significantly different behavior at 1500°C, the calculated lattice value being much closer to the literature data than the calculated $D_O{}^b$. This result probably indicates that lattice diffusion is gaining in importance at the higher temperatures. It may also reflect that the k_p value for NiAl at 1500°C was not significantly effected by the Y-implant; thus the rate may reflect a mixed diffusion mode rather than O diffusion alone.

In order to establish the potential realtive contributions of boundary and lattice diffusion, a theoretical parabolic rate constant

Table 6.3 Diffusion constants calculated from the measured parabolic rate constant for substrates at various temperatures. The values for Al are calculated for θ-Al_2O_3 formed by Al diffusion at short times at 1000°C while the other values are for doped α-Al_2O_3 which grows primarily by oxygen diffusion.

Substrate/Reaction Temperature	D_{Al}^b (cm^2/s)	D_{Al}^l (cm^2/s)
NiAl 1000°C (θ)	7.7×10^{-18}	7.1×10^{-20}
Doped NiAl (α)	D_O^b (cm^2/s)	D_O^l (cm^2/s)
1200°C	6.1×10^{-16}	2.8×10^{-18}
1400°C	1.1×10^{-13}	2.6×10^{-16}
1500°C	7.9×10^{-12}	1.8×10^{-15}
Doped FeCrAl (α)		
1000°C	1.0×10^{-18}	2.5×10^{-20}
1200°C	6.1×10^{-16}	2.8×10^{-18}
1400°C	9.0×10^{-14}	2.1×10^{-16}

Table 6.4 Parabolic rate constants at 1200°C calculated from diffusion data from the literature and compared to measured values for doped and undoped FeCrAl.

Predominant Diffusion Pathway and Species	k_g (g^2/cm^4s) 1200°C
Boundary Al	1.5×10^{-11}
Boundary O	1.4×10^{-12}
Lattice O	9.3×10^{-14}
Measured doped FeCrAl	4.0×10^{-12}
Measured undoped FeCrAl	1.2×10^{-11}

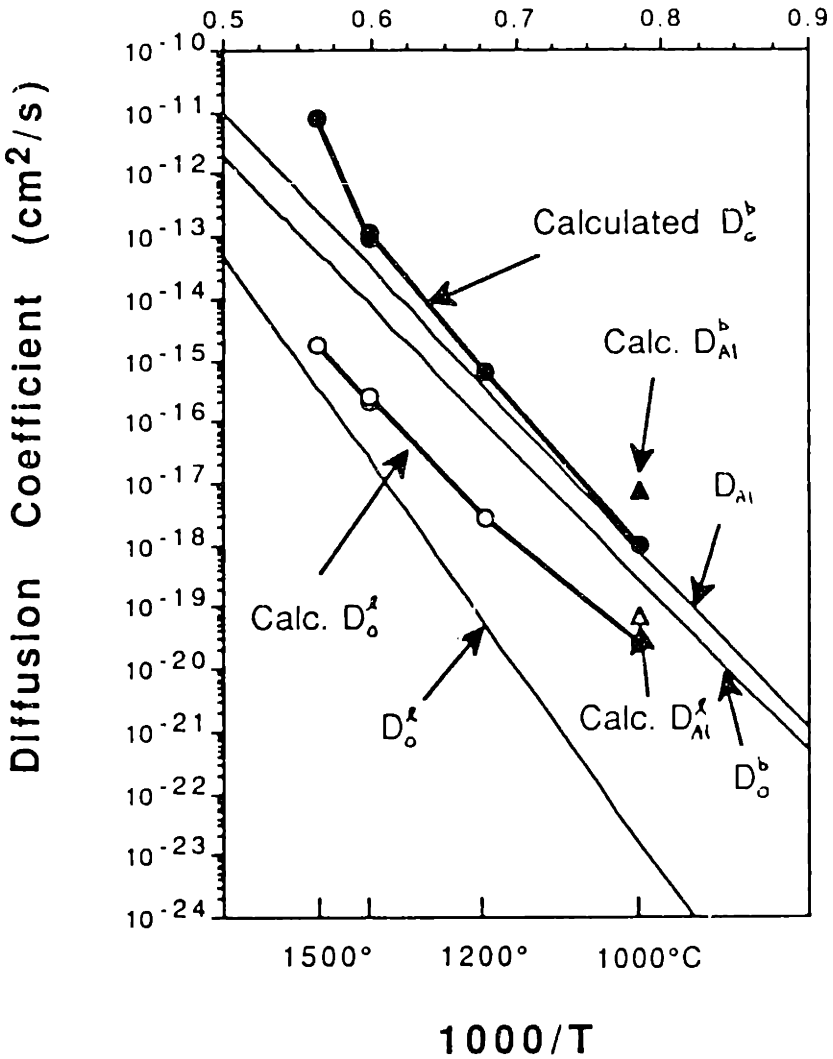

Figure 6.2.2 Diffusion data from the literature plotted with the diffusion values calculated from the parabolic rate constants found in this study. Boundary diffusion data for Al is from Paladino and Kingery [1962] and both lattice and boundary data for O is from Oishi and Kingery [1960].

was calculated using values from the literature at 1200°C. These k_g values are given in Table 6.4. The k_g values calculated using boundary diffusion of both Al (for undoped FeCrAl) and O (for doped FeCrAl) are much closer to the experimental value than the value predicted using lattice diffusion of O. As before, this analysis suggests that boundary diffusion is too slow to account for the observed oxidation rates. It also excludes the possibility of growth by gas diffusion, which would be at least several orders of magnitude higher than solid-state boundary diffusion. The boundary diffusion predictions are at worst within a factor of 3.

A final note on the validity of this analysis: The comparison of the literature diffusion data and oxidation rates is perhaps somewhat simplistic. Tracer diffusion experiments are typically done in relatively static environments with high-purity, high-density constituents. Oxidation experiments involve oxides in a more dynamic state. Grain growth is occurring, a large oxygen potential gradient is present (1 - 10^{-29}atm at 1200°C) and the scale is doped to a certain extent by the substrate, quite apart from any RE segregant. Thus, while it is useful to make an order of magnitude comparison, exact agreement would not be expected.

6.3 Predominant Oxidation Mechanisms of Al_2O_3

While the present research began with the premise that there was a significant issue regarding the growth mechanism of Al_2O_3, this soon became a lessor issue. Based on the literature of the past five years and this research, Young and de Wit [1985] appear to have

neglected one factor -- the metastable phase θ-Al_2O_3 -- in their initial work. Later work from the same group, van Manen, et al., [1987], finally identified the appearance of this phase as a significant issue.

A simple working hypothesis, that θ-Al_2O_3 and α-Al_2O_3 grow by different mechanisms, had a major effect on the design of experiments. The initial experiments on NiAl at 1000° and 1200°C produced mixed phase (θ and α) scales which were unable to be analyzed effectively. Therefore, the second set of samples were oxidized on a time-temperature schedule so as to achieve a uniform single phase of Al_2O_3. A second constraint on the oxidation was that, in order to sputter through the scale in a reasonable amount of time, the total scale thickness was required to be less than 1μm. This restriction and the phase boundary are shown in Figure 6.3.1. The open circles denote the first and second oxidation periods for the first set of experiments. The closed circles are the revised oxidation times.

The following sections discuss the ^{18}O tracer profiles for the various phases and dopants.

6.3.1 θ-Al_2O_3

While NiAl proved an uncooperative material in which to study θ-Al_2O_3 scale formation, the doped FeCrAl materials were more accommodating. The profiles for θ-Al_2O_3 scales on APM and MA956 (Figure 4.1.10) quite clearly indicate a predominant outward diffusion mechanism. Only a minimal amount of the second oxidant

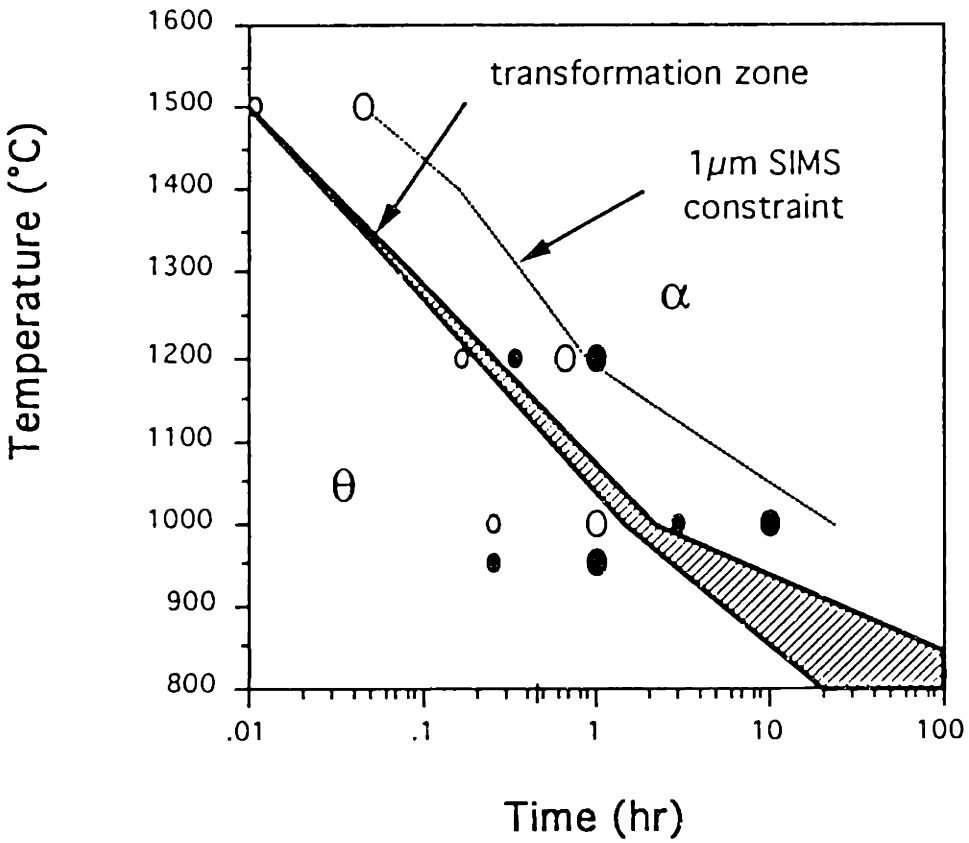

Figure 6.3.1 Approximate time-temperature dependence of the formation of θ- and α-Al_2O_3. The second line denotes the formation of a 1μm scale. The open circles denote the oxidation times for the first set of experiments while the closed circles mark the second set.

was found in the lower portion of scale indicating that most of the new oxide was formed on the surface of the old oxide.

Based on the calculations of D_{Al} from the initial scale growth of NiAl at 1000°C, the lattice diffusion of Al alone was not fast enough to account for the observed oxidation rate (see Section 6.2.3). Therefore, based on this calculation and the relatively low temperature, growth is concluded to be via short-circuit diffusion of Al.

Placed in the context of a predominant θ-Al_2O_3 scale, the results of Young and de Wit [1985] for NiAl at 900°C are similar to those found here. Also, Jedlinski and Mrowec [1987], investigating Y-implanted NiAl oxidized for 24hr at 1075°C, found the same result (≈100% Al outward). This result is expected for a Y-stabilized θ-Al_2O_3 scale (see Section 6.6). However, their study did not determine the phase of the scale.

Since significant θ-Al_2O_3 is formed only at lower temperatures, it is proposed that for all times and temperatures where it is found, θ-Al_2O_3 grows by the outward, short-circuit diffusion of Al.

6.3.2 α-Al_2O_3 with a Reactive Element Addition

In both RE-doped NiAl and RE-doped FeCrAl, there is a strong evidence that α-Al_2O_3 grows by a predominant inward diffusion of O, Figures 4.2.11a, 5.2.13 and 5.4.13. This was found for additions of both Zr and Y and for additions made by alloying, ion implantation and oxide dispersions. In each case, the second oxidant is found in a

The results at lower temperatures are in agreement with those of Quaddakkers, et al., [1989] for scales grown on MA956 at 1000°C. It also matches those of Reddy, et al., [1982] for Zr-doped scales on NiCrAl + Zr. Thus it is concluded that for all temperatures investigated in this study, RE-doped α-Al_2O_3 scales grow primarily by the inward diffusion of oxygen.

6.3.3 α-Al_2O_3 without a Reactive Element Addition

Without the addition of either Zr or Y to the substrate, there is a measurable, repeatable increase in the oxidation rate. Thus it is concluded that some change in the diffusion mechanism is occurring. Tracer results on α-Al_2O_3 grown on both undoped NiAl and undoped FeCrAl show a significant change in the tracer profile, Figures 4.2.11b, 5.2.15, and 5.4.14. Unlike for the RE-doped α-Al_2O_3, in this case a large concentration of the second oxidant is found near the gas interface, while another significant concentration is found beneath a layer rich in the first oxidant. (No θ-Al_2O_3 is detected in these samples by GAXRD, only α-Al_2O_3.) This indicates that at least part of the scale is growing by the outward diffusion of Al. The isotope order was reversed for one experiment at 1200°C and the same result was found for the location of the second oxidant.

At 1500°C, the tracer profile (Figure 5.4.14) is not as distinct as those observed at lower temperatures. However, the mixed diffusion mode is also supported by the scale morphology. For long oxidation exposures, the Y-implant had little effect on the oxidation rate, Figure 5.4.1. Y-rich oxides, which were observed close to the

gas interface after a 12min exposure, are observed after a 50hr exposure only near the center of the ≈30μm thick scale. If the initial Y implant is taken as a marker, this indicates a mixed growth mode. Also the observation of Rh particles, Figure 5.4.16b, at the center of the scale also reflects a mixed growth mode. These particles are the result of the evaporation of the hangdown wire, if the scale were growing only by an inward growth mechanism, these particles would only be observed at the gas interface. A final point regards the observation of oxide whiskers growing towards the substrate, Figures 5.4.7b and 5.4.8a. These whiskers concentrated at the scale grain boundaries most likely grew by the inward transport of oxygen and the evaporation of Al. This morphology is discussed further in Section 6.9.1.

Interpreting these results is somewhat more difficult. Because of the scatter in the SIMS profiles, this must be left as a qualitative characterization. No estimation is made of the relative importance of either diffusing species, although it appears that the inward diffusion of O may account for slightly more of the second-formed oxide than Al. Also because of the mixed mode of oxidation, it is difficult to apply Wagner's analysis to determine diffusion coefficients.

However, the profile results, even if qualitative, are in agreement with other observations. For example, the whiskers on undoped FeCrAl are not observed with a RE addition, Figure 4.2.4. There is a significant volume fraction of these whiskers, and their size and density appear to increase with oxidation time. It is difficult to imagine these whiskers growing except by the outward

diffusion of Al. Also, they appear to form throughout the oxidation process, not just as a transient or other time-dependent stage of oxidation. Fewer whiskers are observed on the scale grown on NiAl. However, for NiAl, the widening of oxide ridges on the gas surface may be an indicator of outward growth.

One issue that is not resolved is that of diffusion paths for concurrent transport. While it has been assumed that O diffusion occurs primarily via grain boundaries, a simultaneous pathway for Al diffusion has not been determined. A theoretical model for mixed mode oxidation (Figure 2.4.1) determined that the tracer profiles should be different, depending on whether the species travel by separate paths or the same path [Jedlinski and Borchardt, 1991]. Clearly, the profiles in this case fit the case of diffusion by separate paths. However, there has been no experimental confirmation of this model.

Golightly, et al. [1976] proposed that Al diffused through the lattice and O along the grain boundaries and reaction occurred at the center of the scale. This internal growth produced growth stresses which caused the scale to buckle. However, while this model is admirable in that it attempts to link the oxide microstructure to the growth mechanism, it does not appear to be supported by the tracer profiles. The formation of new oxide within the scale would have left the second oxidant in the center of scale rather than, as the actual observation shows, at either end.

One possibility is that the oxide that remains attached to the alloy grows by one mechanism (Al out) while the fraction that becomes detached during oxidation grows by another (O in). SIMS

would average over such small-scale spatial differences, and would not detected them. However, if the whiskers are to be used as an indicator of at least partial outward growth, there is no indication of difference in whisker density at the bottom or top of an oxide buckle. It is not clear from the location of the oxide whiskers that their origin can be linked to oxide grain boundaries or any other structure.

Another hypothesis that has not been tested is that certain grain boundary orientations are more conducive to O transport, while others transport Al better. Figure 6.3.2 shows a schematic representation of this model. If after a continuous layer of α-Al_2O_3 is formed, certain boundaries may be more conducive to Al transport. New oxide would then be formed in different areas, depending on the locally favored transport mode. In areas of Al diffusion outward, this would lead to vacancy formation in the alloy. Eventually due to the coalesence of vacancies and the weakening of the metal-oxide interface by S segregation, the oxide and metal would lose contact in these regions. (As an aside, segregation of REs to those boundaries favoring Al transport would eliminate this pathway for diffusion in doped α-Al_2O_3.)

In the other regions where inward growth is favored, new oxide is formed at the metal interface and there is no decohesion. This eventually leads to a rumpled oxide structure. Al is then transported across the void by some type of surface diffusion or evaporation, which leaves the underlying metal smooth, Figure 4.1.6. Other areas in contact with the oxide grow inward into the alloy leaving imprints in the alloy substrate. At very long times as the

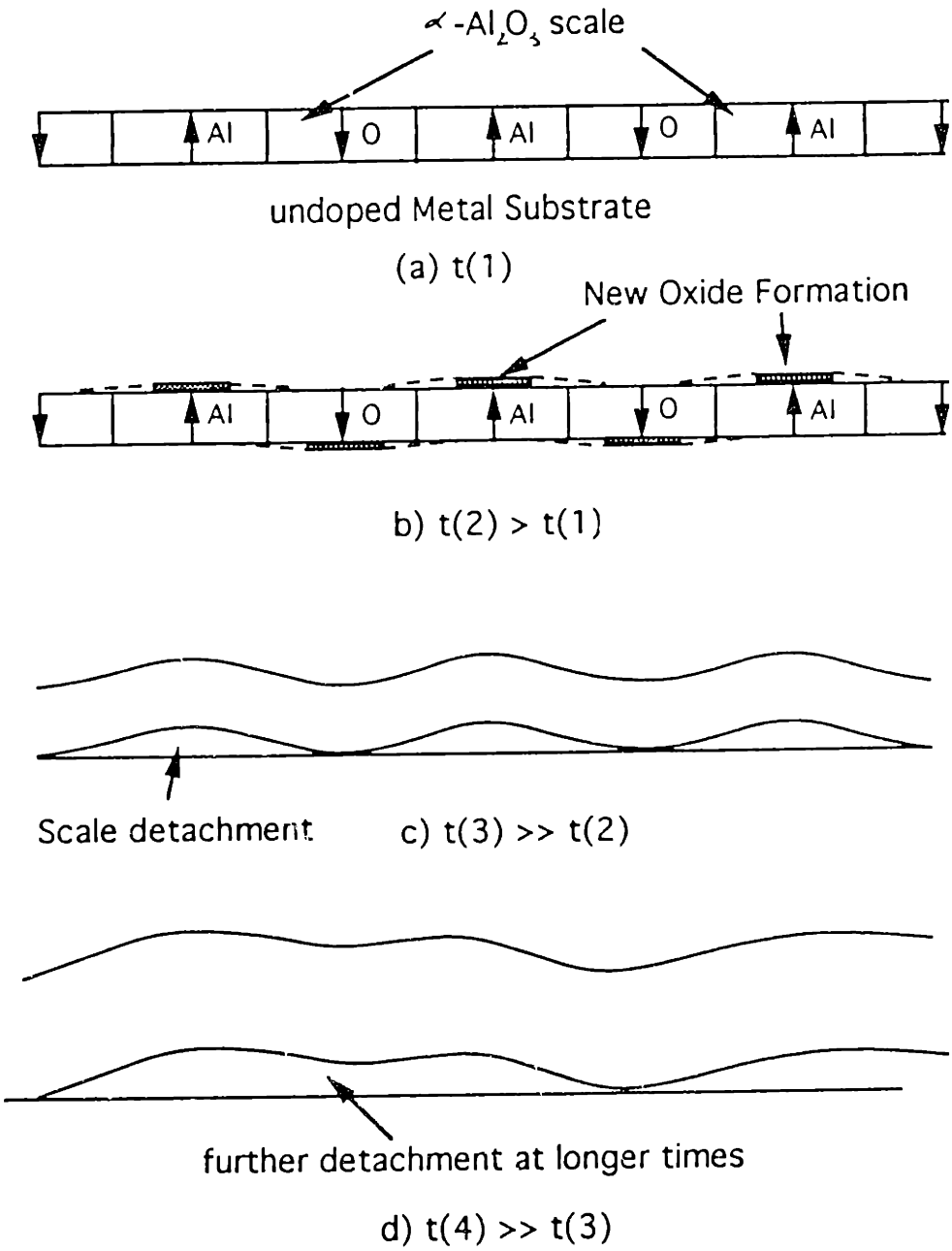

Figure 6.3.2 Model for the formation of undoped α-Al_2O_3.

buckles coarsen (Figure 4.1.4), more areas lose contact with the alloy.

The mixed-mode ^{18}O tracer result is also in agreement with the results of Quaddakkers, et al., [1989]. for scales grown on undoped FeCrAl at 1000°C. However, their study did not discuss the possible pathways for diffusion.

Thus, while it is not clear by what pathways diffusion occurs, undoped α-Al_2O_3 is concluded to grow by the simultaneous diffusion of Al and O.

6.3.4 Sputter Depth Profiles of Thick Films

Based on the numerous SIMS profiles generated in this study, a number of observations can be made in general regarding this technique. Perhaps the clearest advice to the unwary is that the oxide to be analyzed should be kept as thin as possible. Analysis of a thin surface oxide is quicker and eliminates many of the problems associated with sputtering through a thick oxide.

One of the largest problems with sputtering a thick oxide is that, as the crater created by sputtering gets deeper, there is more of a possibility that the bottom and walls of the crater will become distorted. Another problem is that some of the signal may originate from the walls of the crater rather than only the bottom, especially for deep craters. This is minimized by taking data only from the central 5% of the crater and by making a larger crater. However, a thick scale requires a small crater in order to sputter through the oxide in a reasonable amount of time.

Sputtering a non-conductive layer is somewhat problematic by definition. Like an SEM, the charged Cs beam imparts electrons to the sample which must be conducted to the sample holder. A non-conductive sample acquires charge unless coated with a conducting layer (in this case Au). However, unlike an SEM, the sputtering beam then removes this Au layer in the area to be examined. For thick oxides, this can result in charging problems during the extended sputtering period before the conducting alloy substrate is reached.

The presentation of the data is also a relevant issue. Figure 6.3.3 shows the raw data for the profile of the α-Al_2O_3 scale grown on undoped NiAl at 1200°C. The data are plotted on (a) a normal scale, (b) a log scale, and (c) the style of plot used to report the data in this study. The method for preparing plot (c) is described in Section 3.10.1. The data in each form reflect the change in isotope concentration. The technique in (c) was used because it combines the information from both the Al^xO and ^xO signals for each isotope and presents the information in a compact fashion.

A number of other issues are illustrated by these data. First of all, while the Ni signal would be expected to give some indication of the metal-oxide interface, it does not. Monitoring of the Al signal also did not help to identify the interface. One possible explanation is that the Ni and O signals are linked. Because negative ions are being collected (in order to concentrate on the oxygen isotopes), the Ni signal is strongly enhanced by the presence of oxygen. As the O signals fall, because the oxide layer is being sputtered through, the percentage of Ni ions detected also falls. This counters any real increase in Ni revealed by the removal of the oxide layer. Whatever

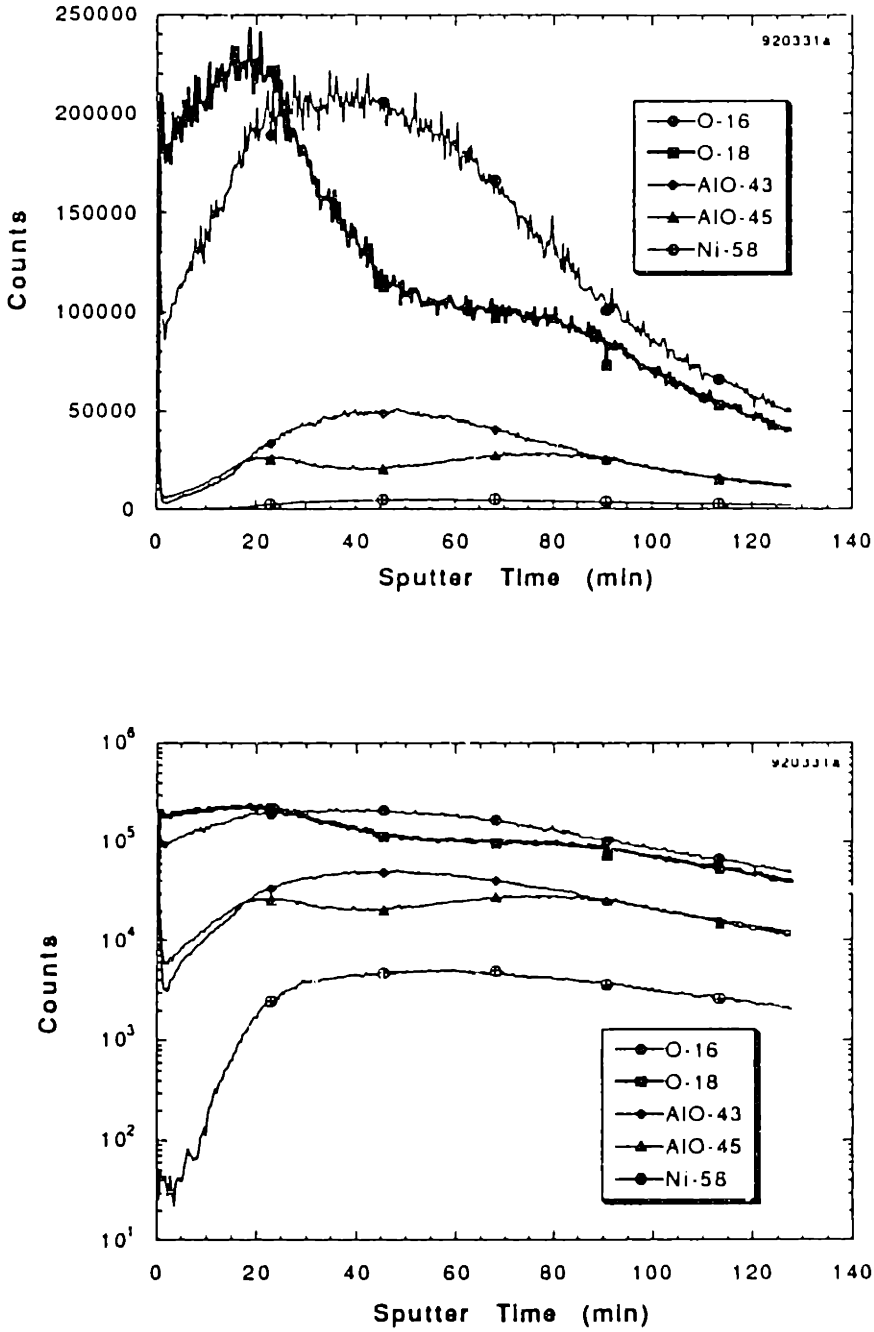

Figure 6.3.3 Data from the SIMS sputter depth profile of the α-Al_2O_3 scale grown on undoped NiAl oxidized at 1200°C for 20min in ^{16}O and 40min in ^{18}O. The same data is plotted in 3 ways; (a) normal plot, (b) log plot, continued on next page

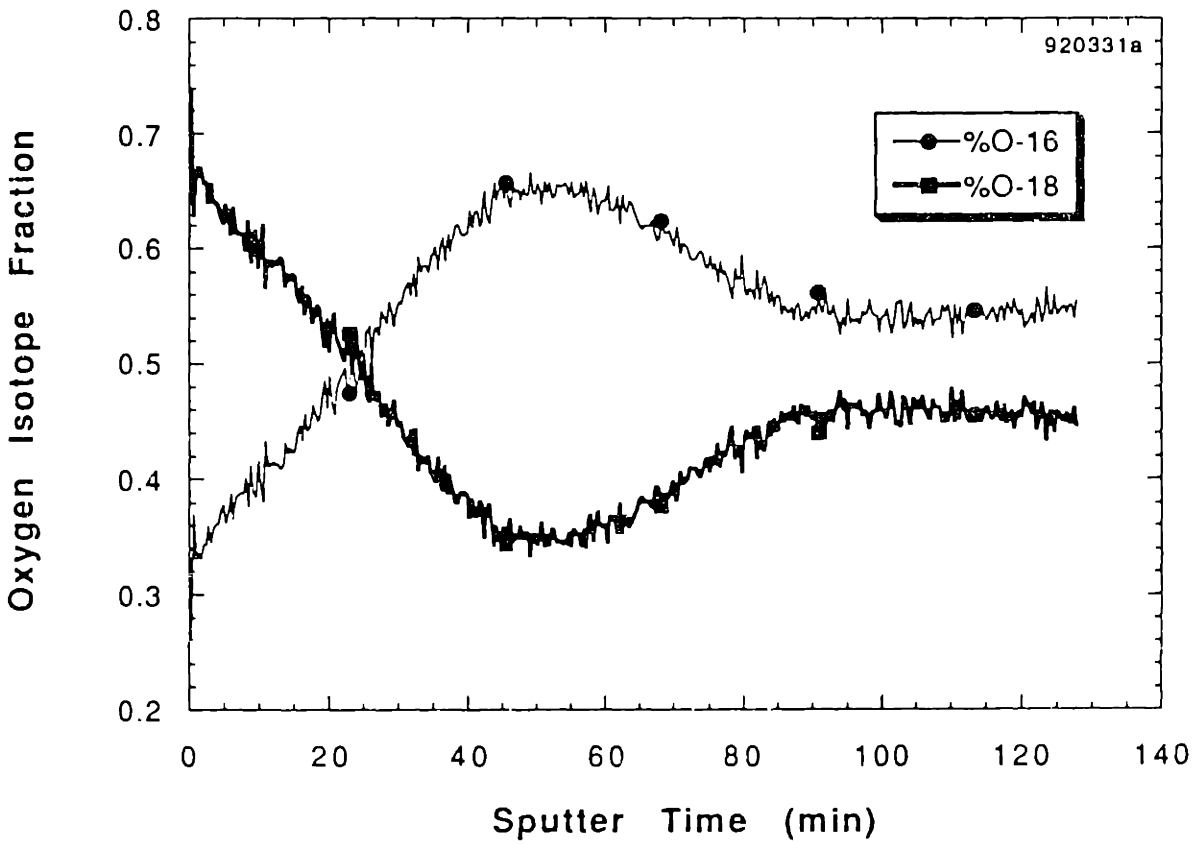

Figure 6.3.3 Continued (c) the standard plot used in this study.

the reason, no accurate indicator of the metal-oxide interface has been identified. The chief indicator used is the gradual loss of the ^{16}O and ^{18}O signals, which does not occur sharply but gradually over a long period of time.

The data are also plotted against sputter time. No attempt was made to convert this information into a depth measurement, primarily because of the uncertainty associated with the crater depth. Figure 6.3.4 shows a typical crater. The walls of the crater are rounded and the bottom is not particularly flat, although it was identified as metal by EDXA. This type of morphology is very difficult to measure by typical surface techniques, because a reference depth is hard to gauge on the rough oxide and an average depth is hard to define on the crater bottom. Thus, the total sputter time reflects the total oxide thickness, but a more precise measurement is not possible.

These problems with defining the metal-oxide interface and the rate of sputtering leave the data best suited to only qualitative conclusions. However, even left at a qualitative level the data are sufficient to indicate overall trends in the transport behavior. Based on the spread of raw data from this study, more quantitative interpretations; such as those arrived at experimentally by Jedlinski and Mrowec [1987] and theoretically by Basu and Halloran [1987], are unwarranted. Overall observed trends were repeatable, but exact profiles were never duplicated. Thus while a theoretical model of inward and outward diffusion is useful [Basu and Halloran, 1987], it is not particularly well suited to the data in this study.

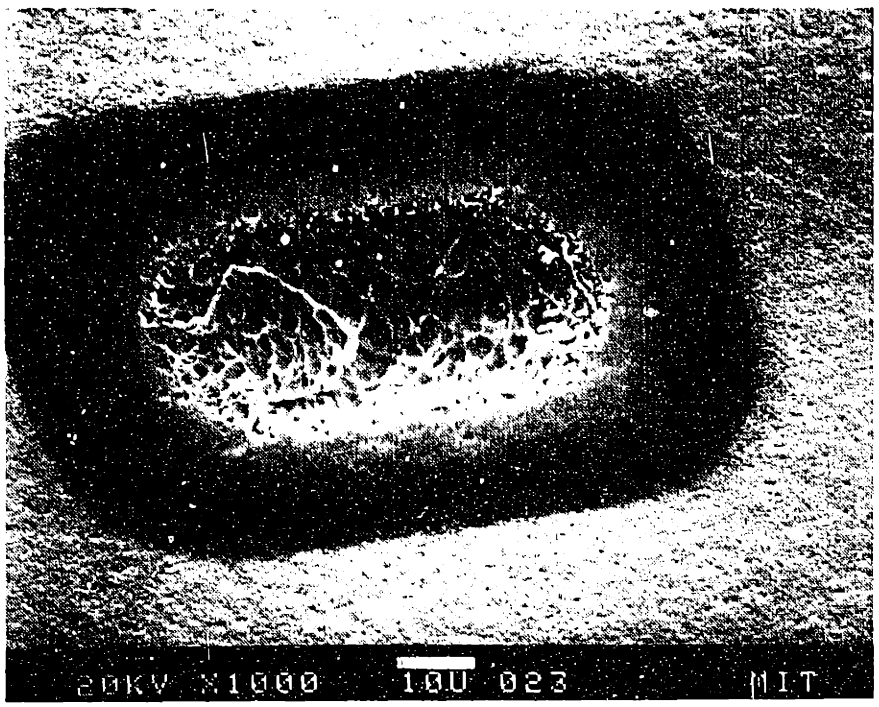

Figure 6.3.4 SEM secondary electron image of a SIMS sputter crater through the scale formed on APM after oxidation at 1200°C for 40min.

Another point concerns the oxide morphology and structure in general. It is often assumed that the scale is a clean flat uniform layer on a substrate. Deposited films on Si wafers fit this model nicely. However, even by starting with a uniformly polished substrate, naturally grown oxide scales usually do not fit this expectation. Spallation is a big problem. Additionally, while tracer experiments work best with a uniform film growing by a single diffusion mechanism, this is also not always the case with oxide scales.

As shown schematically in Figure 6.3.5, a number of situations encountered during this study were far from ideal. In many cases, it was simply impossible to analyze scales because of the mixed ($\theta-\alpha$) phases or the severe spallation (e.g., undoped FeCrAl). Also the possibility of analyzing at special sites such as at small-scale oxide ridges or alloy grain boundaries, was not possible with this SIMS equipment. The sputtering technique inevitably averages over the central window at the bottom of the crater to reflect a general trend. In order to prevent anomalous results, the sputtering is at least done in several locations to check repeatability.

There are also problems associated with the tracer. The principal source of error in the oxidation furnace was gas leakage into the furnace. The oxidation was conducted at ≈50Torr O_2 for each isotope. While the oxidation rate is not affected by the partial pressure of oxygen, leakage would always be primarily ^{16}O, so that during oxidation by 18-enriched (>95%) O_2 the enrichment would be reduced. In order to minimize this leakage, the ^{18}O was usually introduced first, since that was usually the shorter oxidation period.

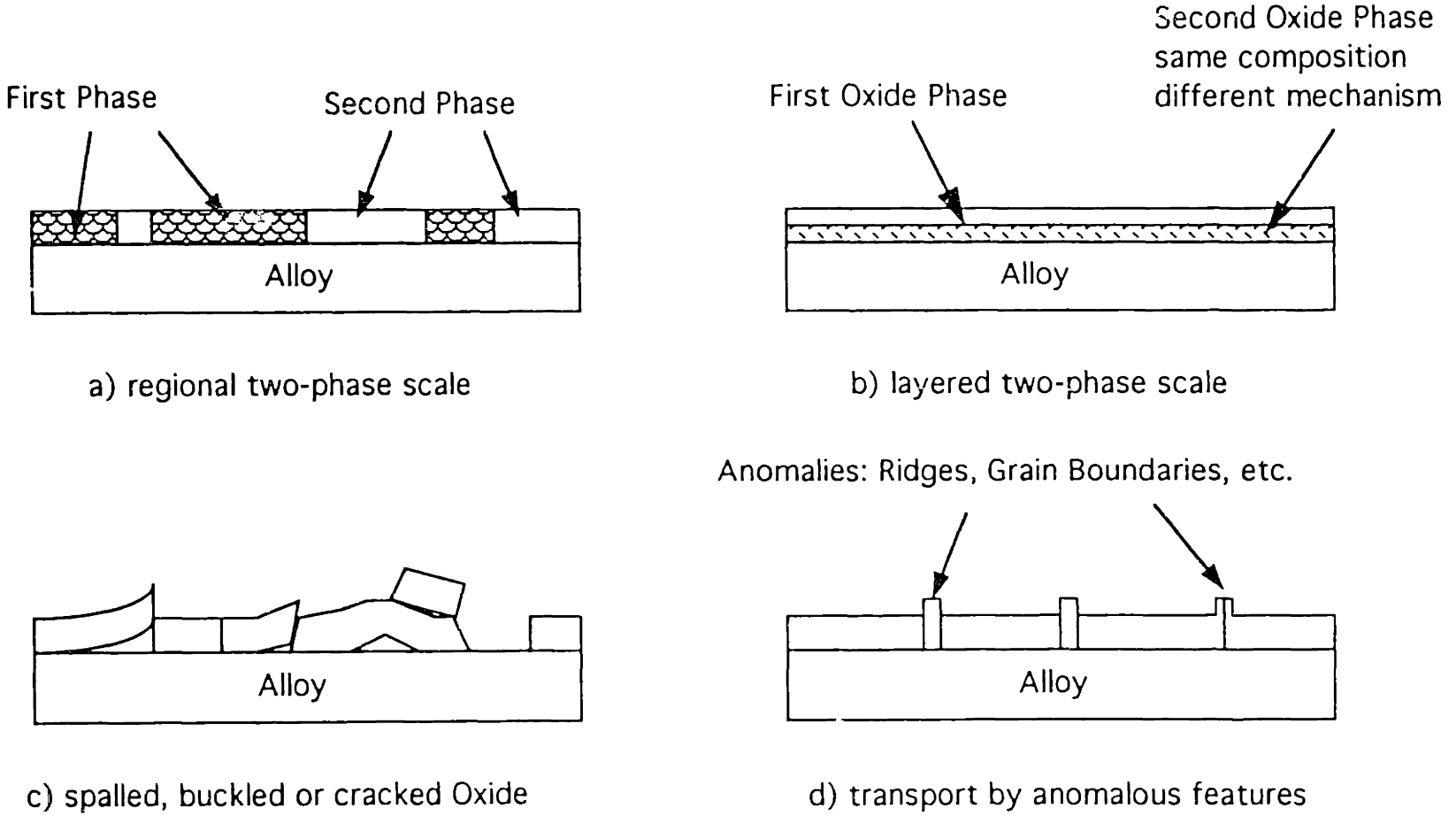

Figure 6.3.5 Schematic examples of oxides which are inappropriate for SIMS study.

As mentioned before, the error of the tracer experiment was checked several times by reversing the isotope order. The differences in the profiles reflect that, while the experiment is repeatable, there is some difference in the detected isotope fractions. The ^{18}O signal is usually lower than the ^{16}O signal, which probably reflects some leakage. It also may reflect the level of purity in the ^{18}O tracer. However, the choice of a nearly pure ^{18}O tracer gas eliminated the need for modifying the raw SIMS data to enhance the ^{18}O signal. (This is done in virtually every published paper in the literature.)

In conclusion, the ^{18}O tracer experiments provided a substantial amount of quality information for this study. While somewhat qualitative in nature, this characterization of the growth mechanism is central to understanding the effect of reactive elements on the growth of Al_2O_3 scales. It is an ironic final note that, despite all of the published work using complex tracer experiments and profiling techniques, a simple analysis of the crystalline phases of the scale has removed much of the basis for the controversy

6.4 FeCrAl vs. Ni-Al Oxidation

A few comments were made at the end of each of the two results chapters regarding overall trends with FeCrAl (Section 4.4) and NiAl (Section 5.5). This section is intended to offer some overall comments about the two materials. Ideally, it would have been better to stay with one substrate; however, based on the

availability of materials, it was necessary to entertain a wider range of alloy substrates.

While the oxidation behaviors of Ni-Al and FeCrAl alloys are not identical, the basic characteristics of the formation of an alumina scale are very similar for the two cases. Figures 6.1.1 and 6.1.2 show that the respective oxidation rates at both 1200°C and 1400°C are remarkably similar. At 1200°C, all of the doped samples (NiAl + Zr, Y-implanted NiAl, APM and MA956) had reaction rates within a factor of two. Likewise, the undoped FeCrAl and NiAl were very similar at 1200°C. Slightly more variation was observed at 1400°C, but even so all of the rates were within a factor of four.

One of the differences between the two materials at 1200°C and 1400°C was the observation of breakdown of the scales on NiAl. Similar breakdown was not observed for the FeCrAl alloys at these temperatures. At 1200°C, the breakdown of Ni-23Al could be ascribed to a depletion of Al, Figure 5.2.1. The FeCrAl alloys have only 4.5-10%Al, but with ≈20%Cr acting as an oxygen getter, there is less of a chance of a breakdown. Nevertheless, this type of depletion breakdown may have occurred on undoped FeCrAl at 1000°C, Figure 4.1.1. In this case, the breakdown was short-lived and appeared to reheal after approximately 1-3hr.

Another type of breakdown was observed for NiAl at 1400°C. In this case, and only with a RE addition, breakaway oxidation took place on both Zr- and Y-doped NiAl. No similar behavior was found on the doped FeCrAl alloys. Rather than Al depletion, this failure appears to be an effect of the RE addition. While the FeCrAl alloys have oxide dispersions, the Zr and Y additions to NiAl are in

unoxidized form. Wholesale diffusion of these elements to the scale surface may lead to isothermal cracking or other detrimental breakdown events. The more stable RE oxide dispersions may restrict this transport. This idea is discussed further in Section 6.8.3.

Probably the most significant difference between Ni-Al and FeCrAl alloys is in the early stages of oxidation at 1000°C. In an attempt to study the $\theta-\alpha$ phase transformation, NiAl, Ni_3Al, FeCrAl, and even NiCrAl were oxidized for 1hr or less at 1000°C. However, only on NiAl (both undoped and doped) was the θ-Al_2O_3 phase detected clearly.

GAXRD of the undoped FeCrAl, NiCrAl and Ni_3Al also found no indication of θ-Al_2O_3. Instead it appeared that the transient formation of less noble oxides precluded the formation of θ-Al_2O_3. Figure 6.4.1 shows a basic schematic of the early stages of oxidation for these alloys. Except for Y-implanted NiAl, all of these materials ended up with predominantly α-Al_2O_3 scales. The paths by which each material gets to this stage are somewhat different. Each of these materials forms some type of transient oxide, although in the case of MA956 there appears to be a minimal transient period. The first-formed transient oxides remain on the surface and determine the surface morphology. However, the transient layer remains essentially constant in thickness during longer exposure. The later-stage reaction rate is controlled by the growth of the underlying α-Al_2O_3 layer.

Transient stage oxidation also appears to be the reason for the morphology differences between the two commercial FeCrAl alloys

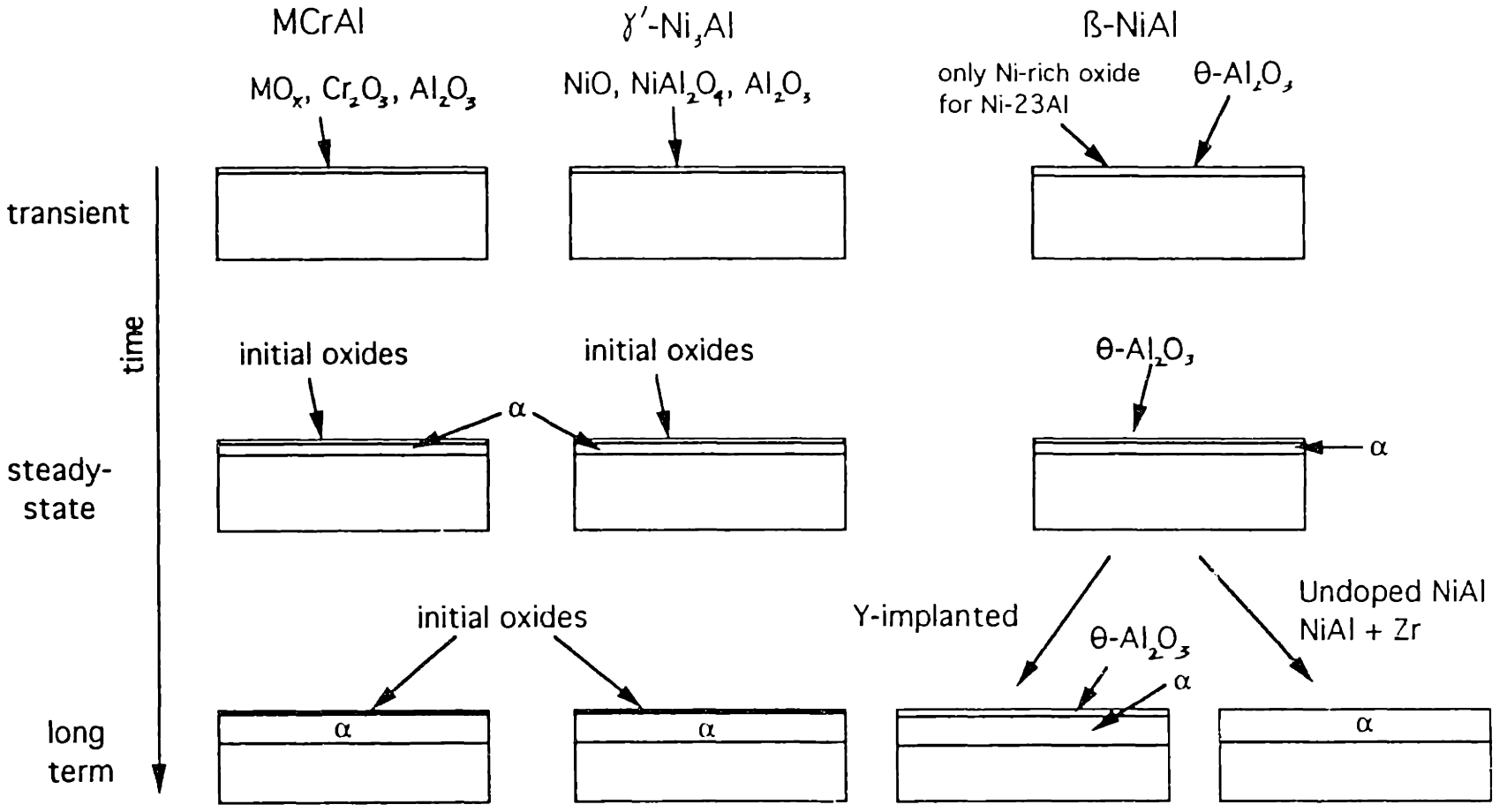

Figure 6.4.1 Schematic model of scale development on various substrates at 1000°C. A significant volume fraction of θ-Al_2O_3 is only formed on NiAl. Without doping, the metastable θ-Al_2O_3 transforms to α after 1-2hr.

at 1000° and 1200°C. At 1000°C, the morphologies of APM (Figure 4.1.8) and FeCrAl (Figure 4.1.4) look remarkably similar except for the buckling. MA956 looks completely different than the other two FeCrAl materials, Figure 4.1.7. The same is true at 1200°C where the structures look similar, just increased in size by grain growth.

GAXRD indicated that there was not a significant difference in the $\theta-\alpha$ phase transformation between the two doped scales at 1000°C. Neither scale contained θ peaks after oxidation for 12min at 1000°C, Figure 4.1.10. The transient period was not investigated at 1200°C, but after oxidation for 12min at 1000°C, XTEM of the scale on APM revealed that the scale contained a large fraction of Fe- and Cr- rich oxides in an Al_2O_3 matrix. A useful diffraction pattern could not be obtained from the complex scale, however GAXRD of the same sample prior to XTEM preparation had indicated a scale of predominantly α-Al_2O_3, not θ.

Thus the GAXRD and XTEM evidence suggest that the difference in the morphology is related to the transient formation of less noble oxides on APM rather than the formation of θ-Al_2O_3. While numerous factors could account for this difference between APM and MA956, the most likely reason is the oxide dispersion in MA956 which appears to be both finer and a higher volume fraction than APM. A simple comparison of the O content of the materials reveals that MA956 has 4 times that of APM, Table 3.1. This denser, finer dispersion may reduce the transient stage formation of Fe- and Cr-rich oxides, thus producing a more uniform scale surface.

Returning to the comparison of Ni-Al and FeCrAl alloys, only in the case of Ni-Al compositions in the ß phase field does the

transient stage involve significant generation of θ-Al_2O_3. At longer times on undoped NiAl and NiAl+ Zr, the θ-Al_2O_3 transforms into α-Al_2O_3, making a uniform layer of α. However, the morphology of the α-Al_2O_3 scale does reflect the transformation from the pre-existent θ, Figure 5.1.8.

Two exceptions of note are undoped Ni-23Al and Y-implanted Ni-Al. In the case of undoped Ni-23Al, the transient stage also includes the formation of a small amount of Ni-rich oxide. This has been attributed to the lower Al content in this material. When Ni-23Al is implanted with Y, these Ni-rich oxides are not detected on the surface.

For Y-implanted Ni-Al in general, the long-term scale is a unique case. Whereas all of the scale on undoped NiAl transforms to α-Al_2O_3 after only a few hours, the scale on Y-implanted NiAl retains between a third and a half the original θ-Al_2O_3 after 100hr. This value is based on a comparison of the principal θ peak to the principle α peak in the GAXRD spectra. The schematic representation of the θ phase on the substrate surface is based on the similarity between the morphologies after 100hr and after 1hr when the scale is almost 100% θ-Al_2O_3. Attempts to provide harder evidence by making an XTEM sample of the scale after oxidation for 50hr at 1000°C were unsuccessful.

Overall, it appears that there are many similarities between the alumina scales formed on NiAl and those formed on FeCrAl alloys. One final point about doped FeCrAl alloys is that, by lowering the oxidation temperature to 950°C, a 100% θ-Al_2O_3 scale (that was also completely adherent) was formed and was very useful

in studying the growth mechanism of θ-Al_2O_3. When the oxidation temperature was raised by only 50°C, only the faintest trace of θ was detected.

6.5 The Effect of Alloy Composition

One of the original ideas of this work was to explore the width of the ß-NiAl phase field in order to see if the quantity of aluminum has an effect on the oxidation behavior. One of the motivations was that Al has a deleterious effect on the mechanical properties of most alloys and intermetallics. Thus a tradeoff could occur between the mechanical and oxidation properties.

The isothermal kinetic data at 1500°C (Figure 5.4.1) probably best characterize the effect of Al content on the oxidation behavior: almost negligible. The most significant effect of Al content at the higher temperatures would be extension of lifetime, based on an eventual depletion or phase transformation of the substrate after long-term exposure.

At lower temperatures (for example, at 1000°C), two features are noteworthy. First, three different ß-NiAl compositions have different weight gains, with Ni-30Al having the lowest and Ni-36Al the highest. The anomolously higher weight gain for Ni-23Al can most likely be explained by a longer transient period during which Ni-rich oxides are formed. After longer times, the Ni-23Al and Ni-30Al curves are almost parallel, indicating similar long-term oxidation mechanisms and weight gains. The difference in the two curves is mainly in the first few minutes of oxidation.

Second, the oxidation behavior of Ni_3Al with a Y_2O_3 dispersion also appears to be dominated by the transient period. After an initial rapid weight gain, the oxidation rate slows significantly at long times. No oxygen isotope experiments were done on this material, but based on similar oxidation rates, doped Ni_3Al appeared to grow by the same mechanism as the other doped alumina-formers.

Ni-36%Al absolutely differently, having a higher weight gain throughout and a different slope. However, it must be kept in mind that this material contained numerous cracks and macrovoids. (The difficulty in producing this material is related to the high Al content, making it a very brittle, porous material.) Thus the effective surface area was likely to be much higher than that calculated simply from the macroscopic dimensions.

The initial results at each temperature give no indication that changes in the Al content have any substantial effect on the oxidation mechanism, oxide microstructure or adherence. The most significant effect is probably on the transient stage rather than the steady-state oxidation. No benefit was found from Al-rich ß-NiAl, although reducing the Al content in ß-NiAl probably affects the very-long term oxidation behavior (orders of magnitude longer than any experiment in this study). At some point Al depletion in the substrate will cause breakaway oxidation, but this eventuality must be weighed against potential improvements in the mechanical behavior.

6.6 The Al_2O_3 Phase Transformation

The $\theta-\alpha$ phase transformation is clearly important to the oxidation behavior. The observation of stabilization of θ-Al_2O_3 by Y-implantation was, however, greeted with mixed emotions. On one hand, it added a level of complexity that was unintended. On the other hand, it served to explain the dispute in the literature regarding the growth mechanism of Al_2O_3 scales. All the early work by the Dutch group (Young, de Wit, et al.) and the Polish group (Jedlinski, Mrowec, et al.) appears to have ignored the importance of this phase transformation.

6.6.1 Transition or Metastable Aluminas

According to the literature, all of the so-called "transition" or metastable alumina allotropes are based on a cubic close-packed anion structure. These include the γ, δ, and θ phases. These structures are generally described as having a defective spinel structure, with δ-Al_2O_3 being the most spinel-like. There are also other less-crystalline structures, such as the η and κ phases, which incorporate water structurally. For the case of the dry O_2 used in this study, the latter structures are less relevant.

The transformation among metastable aluminas can be thought of generally, though with some dispute, as a change in the ratio of occupied octahedral to tetrahedral sites. This ratio decreases from 2.0 in the spinel structure to 1.0 (or lower) in the θ structure.

The ordering of the cations and vacancies on their sublattice leads to the following irreversible transformation [Doychak, et al., 1989a]:

$$\gamma \rightarrow \delta \rightarrow \theta$$

This transformation order appears to be widely accepted. The irreversible nature of the transformation suggests that each step leads to a lower-energy metastable state.

The transformation of θ-Al_2O_3 to the stable α-Al_2O_3 is also irreversible, but in contrast this transformation involves a change in the anion lattice from cubic close-packed (CCP) to hexagonal close-packed (HCP). Wynnyckyj and Morris [1985] have proposed a diffusionless martensitic-type transformation to explain the rapid kinetics of transformation. The transformation data empirically fit an Avrami-like equation, but the actual transformation is not a typical nucleation and growth type. The θ crystallites appear to coarsen before transforming into α after which further coarsening is negligible [Wynnyckyj and Morris, 1985]. Other studies have looked for an aperiodic or other intermediary phase but none has been detected [Carturan, et al., 1990].

The θ-Al_2O_3 phase is often identified in the literature by the distinctive (222) x-ray diffraction peak (32.7° with Cu Kα) [Wynnyckyj and Morris, 1985]. This is the distinctive primary peak that was used in this study to identify the presence of θ-Al_2O_3 in the scales on NiAl.

6.6.2 The Catalyst Literature

The phase transformation of metastable aluminas has been studied extensively in the ceramics community, but is most extensively reported in the catalyst literature. Because of their high surface area, the metastable aluminas are prized as catalyst supports. For example, they have been used in automobile catalytic converters to support various precious metal catalysts. However, when exposed to high temperature exhaust gases, the metastable aluminas can transform to the more stable α-Al_2O_3. Upon transformation, the surface area of the support is reduced and the catalyst is less effective. Additions of various elements (e.g. Ca, Zr, La, Ce etc.) have been found to inhibit this transformation, thus increasing the useful lifetime of these supports.

The first report of the effects of dopants on stabilization of transition aluminas was by Schaper et al.[1983]. La additions were found to inhibit the transformation of γ to α (intermediate phases δ and θ were also identified). Using differential thermal analysis and a constant heating rate, the transformation temperature of doped Al_2O_3 was observed to occur 100°C higher than for the undoped powder. Surface diffusion inhibition by $LaAlO_3$ was deemed to be the most important factor in impeding the transformation.

A more extensive study by Burtin et al. [1987a] found that certain elements (Zr, Ca, La and Th) had a major inhibiting effect on the θ–α phase transformation. Other additions (In, Ga, and Mg) were instead found to accelerate the formation of α-Al_2O_3. In this case the dopants were added as nitrates to the alumina powder and then

calcined. An interpretation of this effect proposed that vacancy annihilation was the rate-limiting step in the reduction of surface area and in the transformation to α [Burtin, et al., 1987b]. Therefore, the valence and ionic radii of the dopants were significant to the sintering rate and the transformation to α.

Further characterization has been attempted to determine exactly how certain elements stabilize these structures. For example, Ozawa et al. [1990], using electron spin resonance (ESR) showed that La enters the defective θ-Al_2O_3 lattice substitutionally and occupies a cation site. (This result contradicts the ESR work of Schaper et al. [1983] which indicated $LaAlO_3$ on the surface of the alumina powder.) Ozawa et al. determined that Ce, however, remains on the surface of the transition alumina. Both elements inhibit the θ–α transformation, but La is proposed to be more effective because it inhibits lattice diffusion. On the surface, Ce limits only surface diffusion and thus sintering. Burtin et al. [1987a] also found that La was a better inhibitor.

While Y has not been explicitly considered in any of these studies, its effect appears to fit with a similar explanation. In the case of Y, it has been observed that Y is insoluble in the closed packed α-Al_2O_3 corundum structure [Cawley and Halloran, 1986]. However, it might be possible to situate the larger Y ion in the more defective θ lattice, as is suggested by the results by Ozawa, et al. [1990] with La. In this location, distorting the surrounding structure, it could stall a diffusionless transformation from θ to α by requiring more energy to overcome the distortion. This explanation would be especially plausible if a rapid martensitic

transformation occurs in the undoped case. The observed inhibiting effect of Y on the phase transformation found in the present study is thus entirely expected.

6.6.3 Cr-implanted NiAl

Hagel [1965a] observed that Cr additions enhanced α-Al_2O_3 formation on FeAl, which initially grows θ-Al_2O_3 at 1000°C much like NiAl. In order to compare this potential Cr effect with that of Y, Cr was implanted in NiAl ($2 \times 10^{16}/cm^2$ at 70kV) on one side of a coupon. GAXRD profiles showed that θ-Al_2O_3 was retained only on the Cr-implanted side of the coupon after oxidation for 1hr at 1000°C. After a 50hr exposure, though, both the implanted and unimplanted sides had exclusively α-Al_2O_3 scales. Clearly, the Cr-implant did not have as large an effect on the phase transformation as an equivalent Y implant. With the Y implantation, strong θ diffraction peaks were present even after a 100hr exposure at 1000°C.

SEM examination revealed that the Cr-implant did have some effect on the oxide morphology even if it did not effect the bulk scale phase content, Figure 5.1.10. Some of the blade-like morphology of θ-Al_2O_3 is retained on the Cr-implanted side but not on the unimplanted side.

Hagel's findings with Cr alloy additions to Fe-4wt%Al were quite different from those with Cr implanted into an Al-rich substrate. A comparison of FeCrAl and NiAl oxidation behavior without Cr-implants, indicates that the transient formation of Fe-

and Cr- rich oxides likely precludes the formation of the metastable θ phase. When Al_2O_3 undercuts these transient oxides, it is exclusively α However, Hagel's characterization of Fe-4.4wt%Al indicates that θ-Al_2O_3 was formed along with a large amount of FeO_x. His observation may indicate that the transient formation (on FeCrAl) of Cr_2O_3, which has the α-corundum structure, may help nucleate α-Al_2O_3. This is an effect opposite to that of an Y implant.

6.6.4 Al-implanted NiAl

NiAl was implanted with Al (2 x $10^{16}/cm^2$ at 70kV) in order to investigate the effect of the implantation process itself on the θ−α phase transformation. In retrospect, this choice was not particularly prudent, because it left open the question whether increasing the Al content affects the phase transformation. The result was that after 1hr at 1000°C, θ was retained on the Al-implanted side of the coupon, while the unimplanted side formed primarily α, Figure 5.1.5. After a 50hr exposure, both sides had scales of exclusively α-Al_2O_3. SEM observations of the morphology confirmed the GAXRD result, Figure 5.1.9. Comparing the 1hr and 50hr exposures, however, it is clear that neither increased Al at the surface nor the implantation process itself can match the effect of Y implantation.

Comparing Ni-30Al and Ni-36Al after 1hr exposures showed that a larger θ peak was found on Ni-36Al. Thus, there is some indication that an increased Al content affects the phase

transformation and the early stages of oxidation. Both of these materials form exclusively α scales after 50hr.

This set of experiments still leaves a potential effect of the implantation process on the phase transformation. Pre-oxidation characterization of the Y implant revealed a ≈100Å oxide layer on the surface after implantation (Section 3.2.3). Its presence could potentially affect the phase transformation, but as judged by the Al implantation, it is not a significant effect.

6.6.5 Reactive Element Doping of Metastable Aluminas

While it has been established that a RE addition, changes the oxidation mechanism of α-Al_2O_3, it does not appear to have any effect on the growth mechanism of θ-Al_2O_3 (Section 6.3). Taking the case of MA956, at 950°C the predominantly θ-Al_2O_3 scale grows by an outward diffusion mechanism, Figure 4.1.12a. However, at higher temperatures, the RE dopant retards the Al diffusion in α-Al_2O_3 thus reducing the oxidation rate, Figure 4.2.11a. For metastable aluminas, especially for the case of Y implantation, the RE appears to mainly effect the phase transformation. A number of factors may explain this behavior.

The defective spinel-type structure of θ-Al_2O_3 is probably a major factor. Comparing the crystal structures of α and θ-Al_2O_3 (Section 2.8.2), the θ phase has a 13% larger volume than α [Rybicki and Smialek, 1989]. While Y and Zr are found to segregate to α-Al_2O_3 grain boundaries (Table 4.2), there are inidications that these larger ions are more easily incorporated into the θ lattice [Ozawa, et

al., 1990]. If the RE does not segregate and the reaction is limited by Al boundary transport, the RE would not be expected to effect the growth rate. RE segregation is discussed further in Section 6.7.

Another possibility is that the θ structure allows a different type of Al transport process. At 1000°C, the rate of growth of θ is approximately two orders of magnitude faster than the growth of α [Rybicki and Smialek, 1989]. With boundary transport for Al and O being the same magnitude (Figure 6.1.3), a switch from Al transport to O transport would not appear to account for this large change in oxidation rate. Compared to the close-packed corundum (α) structure, the spinel-type θ structure with a cubic anion sublattice may permit more rapid lattice transport. With the more open structure, both vacancy and interstital volume diffusion would likely be faster in the θ structure than in α-Al_2O_3. If Al RE boundary segregation would not effect Al lattice transport.

Unfortunately, there is very little diffusion or microstructural information available about θ-Al_2O_3 scales. Attempts in this study to make TEM sections of these scales were unsuccessful and the catalysis literature is mainly concerned with the $\theta-\alpha$ phase transformation. Doychak and Ruhle [1989] made a cross-section of a θ-Al_2O_3 scale on ß-NiAl and observed a dense scale. No grain boundary segregation was detected in the scale. The dense scale indicates that growth by voids or other large defects is unlikely. However, the TEM used in this study did not have the high spatial resolution of the FEG-STEM used in this study. Thus, a low level of segregation may not have been detected.

Thus while the RE dopant has been found to effect boundary transport in α-Al_2O_3 by segregating to the oxide grain boundaries, in θ-Al_2O_3, it is possible that Al is transported by pathways other than grain boundaries and that RE segregtion does not occur. Both possiblities eliminate the effect of the RE on the θ-Al_2O_3 growth mechanism.

6.7 Segregation Phenomenon

The segregation theory is based on the observation of RE ions on Al_2O_3 grain boundaries and the metal-oxide interface. The reasons for this enrichment on the boundaries are discussed in the following section, along with its possible effect on Al diffusion. A few considerations concerning detection and quantification of segregation are also discussed. Additionally the apparent effect of temperature on Ti segregation is outlined.

6.7.1 Segregation Driving Forces

The segregation of elements such as Y to Al_2O_3 grain boundaries is not completely unexpected. Cawley and Halloran [1986] used EDXA, AES, and SIMS to examine a single crystal of α-Al_2O_3 grown from a melt containing 100ppm Y. While Y-rich oxides were found on the surface of the boule, none of their techniques found Y within the crystal. From their analysis, it was concluded that the solubility of Y in α-Al_2O_3 is less than 10ppm.

The precise reason for the segregation is not conclusively established. However, the most likely reason is that the size of the RE ion relative to Al creates a driving force to relieve the associated lattice strain. Yan et al. (1977) determined that the elastic energy was proportional to the square of the size misfit of the solute atom. Thus for Y(0.87Å) which is ≈68% larger than Al(0.53Å) and Zr (0.72Å, ≈36% larger) there would be a substantial energy associated with accommodating a larger ion into the lattice [Kingery, et al., 1976, p.58].

Other arguments for segregation include electrostatic forces and dipole forces from the formation of solute-defect pairs [Cotell, 1988]. However, it is difficult to draw any conclusions about these other forces. While Zr^{4+} may engender some charge effects, it is more difficult to argue for Y^{3+} which is isovalent with Al. The size misfit alone appears to be sufficient to explain RE segregation.

6.7.2 Detection and Quantification

The first identification of Y segregation to Al_2O_3 grain boundaries was by Nanni [1976] using AES. However, this sintered alumina sample appears to have had an anomolously high degree of segregation. Normally, because of the low detectability of Y, AES has not been successful in detecting Y segregation in oxide scales.

In general, without the use of FEG-STEM, there have been problems detecting the segregation of RE dopants to scale boundaries. For instance, Ramanarayanan and Petkovic-Luton [1985], while detecting the segregation of Y in Al_2O_3 in an earlier study

[Ramanarayanan, et al., 1984], did not detect the segregation of Y in Cr_2O_3. In their study, a TEM-STEM was used with a very large (20nm) probe size. Numerous other studies using FEG-STEM (<2nm probe size) have detected Y segregation in Cr_2O_3 [Cotell, et al., 1988; Przybylski, et al., 1987; Yurek, et al., 1987].

Quantification techniques generally rely on the thin-film method of Cliff and Lorimer [1975]. Theirs is a rather simplistic interpretation in which the characteristic x-rays are assumed to not interact with the sample. Intensities are related by a simple constant to the concentration. This method appears to work quite well and, for lack of a better one, is usually judged sufficient.

Determining the actual quantity of segregant on the boundary has proved to be a difficult issue. Existing theories of beam broadening in thicker samples rendered quantification procedures very combersome and difficult to verify [Garratt-Reed, 1986]. By taking into account beam broadening, a weak RE signal on a boundary could actually represent a substantial segregant level in a thick sample.

More recent work by Furdanowicz, et al. [1991] has established that a much smaller level of beam broadening than expected occurs in crystalline thin films due to electron channelling. While this finding simplifies the quantification process, it also changes the estimate of the segregant on the boundary. With no beam broadening, the amount of segregant detected in this study and others appears to be quite small. For example, after oxidation at 1000°C, the detected Zr/Al ratio on the Al_2O_3 grain boundaries is only 0.012, Table 4.2. This indicates at most only 2-3% Zr on the boundary. If this is an

accurate reflection of the level of segregation, then it is no wonder that larger STEM probes and other analytical techniques are unable to detect the presence of a segregant.

6.7.3 The Effect on Al Diffusion

Once the RE segregates to the oxide grain boundaries, it is expected that it will have some effect on the properties of the scale. In this case, it has been demonstrated that Zr and Y on Al_2O_3 boundaries limit the boundary diffusion of Al (Section 6.3). However, it is not entirely clear how this inhibition occurs. A number of hypotheses have been proposed to explain this effect [Cotell, 1988].

One possibility is that there is a charge effect of the segregant which produces an effective charge on the boundary. For Zr^{4+} this is a plausible explanation, but Y^{3+} normally could not be considered to have the same effect. However, El-Aiat and Kroger [1982] have concluded that Y acts as an isoelectric donor because of its large ionic radius. Al diffusion in α-Al_2O_3 is assumed to occur predominantly by motion of positively-charged Al interstitials. Thus, if the boundary becomes positively doped, then Al diffusion would be inhibited. However, the concept of isoelectric donors is still largely unverified.

Another hypothesis is that RE dopants physically block the diffusion path or limit it by replacing Al on the boundary. However, the low level of segregant detected makes this seem improbable. Furthermore, since it appears the larger O ions must continue to

diffuse along the same boundaries, a physical blocking of the boundary seems unlikely.

Other explanations involve the formation of solute-defect pairs, a change in the boundary structure eliminating dislocations or point defects, and a generic increase in the Al migration enthalpy by the presence of the RE, based on Borisov, et al. [1964]. All of these explanations are possible, but no particular evidence points to any of them. One of the difficult issues is that Y and Zr appear to affect diffusion in the same way. While they are similar in size, they differ in other ways, especially valence. Thus arguments regarding charge and defect pair formation do not appear to apply equally to both elements.

One feature that is not usually considered is that the high oxygen affinity of both of these elements may play a role in a dynamic oxidation environment. After all, at the reaction temperature, it is difficult to imagine that these segregants are static. In the high potential gradient in the oxide, there is a driving force for the diffusion of the RE to the gas interface. In the case of the scale grown on NiAl + Zr, large ZrO_2 particles are detected by GAXRD and observed by STEM near the gas interface. The Y-rich grains in the scale of MA956 are also observed to coarsen well beyond their initial size in the alloy [Ramanarayanan, et al., 1984]. These particles are evidence of this outward RE diffusion.

Now, if one assumes, that their large size slows their flux and that the cation sublattice boundary structure contains only a limited number of actual migration pathways, the outward diffusion of the RE would cause an effective "traffic jam" on the boundaries. Even if

a diffusing Al ion could successfully get around a single RE ion, it would still get stuck behind the next RE ion. Al diffusion would no longer be limited by the energy required to move Al cations from site to site; instead it would be limited by the energy required to "pass" an RE ion on the boundary, or by the enthalpy of RE boundary diffusion. Unlike other proposed mechanisms, this is not a replacement of the Al ions on the boundary, this is a dynamic blocking on the cation sublattice which requires only a few percent RE ions to slow the Al diffusion.

This hypothesis explains how a low level of segregation can have an anomolously large effect on the Al diffusion. It also explains why RE implantation has a time-limited efficacy. As the RE diffuses outward, there is not enough dopant left to cover the metal-oxide interface or the oxide-grain boundaries. At high temperature (or long time exposures) the oxide adherence would be lost as well as any change in the oxidation mechanism. This is the behavior observed for Y-implanted NiAl at 1400° and 1500°C.

6.7.4 The Formation of TiN_x

One of the more interesting side excursions of this project was the observation of TiN_x particles in the α-Al_2O_3 scale of MA956 at 1400°C [Pint, et al., 1992]. At lower temperatures, both Ti and Y segregate to the oxide grain boundaries. However, at 1400°C, Ti segregates at much lower levels than Y, Table 4.2. Instead of segregating, Ti is observed to form TiN_x particles. This indicates that, while at lower temperatures segregation is stable or at least

metastable, at higher temperatures particles form rather than segregation being favored. (Since Y and not Ti improves the oxidation behavior [Ramanarayanan and Petkovic-Luton, 1985; Nagai, et al., 1982; Lagrange, et al., 1984], the REE is still observed at 1400°C). The particles appear to cause spallation within the scale during cooling, but no oxide spallation from the alloy.

One possible reason for the change from segregation to TiN_x formation at 1400°C is that the driving force for segregation is reduced at this higher temperature. Since Ti(0.61Å) is only ≈15% larger than Al, the elastic misfit energy is considerably less than that for Y which is ≈68% larger than Al. As the temperature is increased, the smaller Ti ions may be more easily accommodated within the lattice. This accomodation would limit the extent of segregation. Arguments based on the increased stability of TiN at higher temperatures do not appear to be valid, in view of the reported free energies of TiN formation [Chase, et al., 1985, p.1542].

The source of the nitrogen is of considerable interest, as is the stability of a nitride within an oxide film. In order to investigate the gas phase as a potential source, MA956 was oxidized in flowing air and in a carefully-flushed oxygen environment. These changes had no appreciable effect on the oxidation rate nor on the surface morphology (including the observed spallation). A more likely source of nitrogen is Inco's use of air as a mechanical alloying environment [Mason, 1992]. This may promote the formation of TiN_x in the alloy which is a more stable nitride than Fe, Cr or Al nitrides. Nitrides present in the alloy may be incorporated and ripen in the growing scale to become effective crack initiators, leading to

eventual spallation. A study of MA956 before and after oxidation at 1000°C did not detect these particles in the alloy [Katz, et al., 1987]. However, they were not specifically looked for and therefore may have been ignored.

At 1400°C, TiN is stable with a nitrogen dissociation pressure of $\approx 10^{-11}$atm; however both TiO and TiO_2 have a lower free energy of formation than TiN [Chase, et al., 1985]. While kinetic factors may limit the transformation to the more stable oxide, oxygen activity in the scale could present a thermodynamic issue. Figure 6.7.1 illustrates a conventionally-envisaged oxygen gradient across the scale and a second, hypothetical one. If the oxygen activity were to drop precipitously near the gas interface, a TiN_x particle in an Al_2O_3 matrix would be below the dissociation pressure of TiO and TiO_2. Al and Y, forming more stable oxides, would prevent TiO_x formation.

This change in the behavior of Ti with temperature may be a sign of a similar effect with the larger Zr or Y ions at higher temperatures. For example, presumably if at some temperature segregated Y is no longer stable and begins to form YAl_xO_y, then at this temperature and above the REE should no longer be observed. Segregation was observed at 1500°C in Y-implanted NiAl; thus apparently such a critical point was not reached in this study. If boundary diffusion were still predominant, identification of a critical temperature would be another indicator of the importance of segregation for the REE. However, if lattice diffusion began to dominate, the REE would also be modified without any change in segregation behavior.

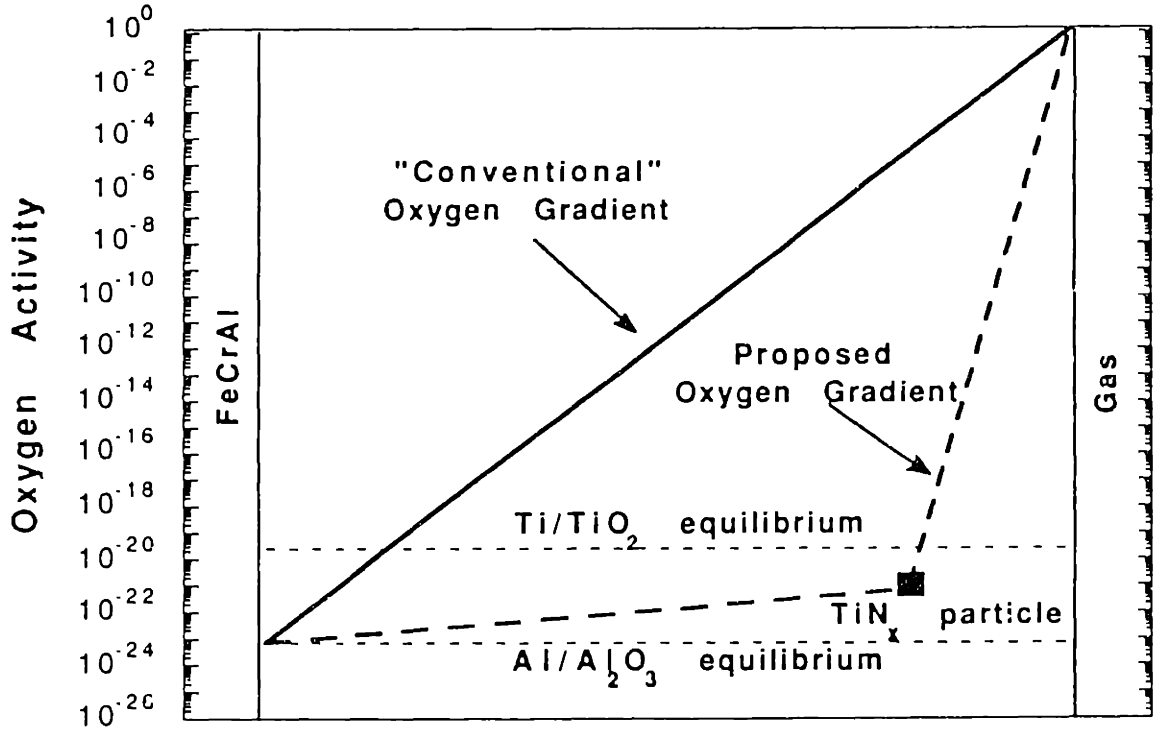

Figure 6.7.1 Schematic diagram of the oxygen activity across the scale thickness indicating the dissociation pressure of TiO_2 and Al_2O_3 at 1400°C and the general location of the TiN_x particles in the scale.

6.8 The Method of Reactive Element Addition

The original research plan proposed to study the REE by ion-implanting Y into ß-NiAl. An additional goal was to implant other REs such as Zr and La, to see if these elements would react differently as a function of their atomic radii or valence. The problem with the plan was that Y-implanted NiAl did not exhibit the REE; thus ion-implanting other elements became a moot point. This revelation added a third layer of complexity to the project that was not anticipated.

Of course, study of the REE could have been abandoned in favor of more successful pursuits (like superconductors). However, personal preferences dictated that the REE should remain the central goal. Thus, the study was broadened to include oxide-dispersed FeCrAl and Ni_3Al and an alloy addition of Zr to NiAl. This approach was also an attempt to solve both problems at once. The REE was studied and at the same time compared to Y-implanted NiAl.

A comparison of the methods for RE addition inevitably addresses the differences in alumina formation on NiAl and FeCrAl. The FeCrAl materials contain the oxide dispersions, while NiAl was alloyed and implanted. One of the problems with making such a comparison is that there are so many differences between the materials beyond just the bulk composition and the type of RE addition that the possible explanations for any particular observed difference are difficult to pin down. However, in many cases it fortunately appears that the RE addition was a dominating factor in determining the oxidation behavior.

6.8.1 Ion Implantation

The overwhelming question here is simply why an Y implant of $2x10^{16}cm^{-2}$ did not produce the REE. Jedlinski and Mrowec [1987] found "perfect" adherence after more than 100hr cycles at 1200°C on NiAl implanted with Y using the same dose and energy. NiAl implanted under the same conditions at MIT and NRL appeared to have significant spallation after just a few cycles, Figure 5.2.2. There appears to be an irreconcilable difference between the two results at 1200°C. The oxidation rate (and mechanism) appear to be modified by the Y implant at 1200°C but not the oxide adherence.

At 1500°C, the effect of the implant on adherence disappears after only a 0.4hr exposure and there is no effect of the implant on the long term oxidation rate or oxide microstructure. At 1000°C, the oxidation behavior appears to be controlled by the $\theta-\alpha$ phase transformation and is a unique case.

The most likely explanation for the breakdown of Y-implanted scales is that there is not enough RE to dope the rapidly-growing scale. Also, because of the oxygen potential gradient, Y near the surface cannot diffuse back to the metal-oxide interface.

The idea is best illustrated by comparing it to a case where Y implantation was successful in improving the oxidation behavior. Using the same implantation of Y as used in this case ($2x10^{16}cm^{-2}$ at 70kV), Cotell [1988] studied the REE for pure Cr. In her case, with a relatively slow oxidation rate at 900°C, Y was observed to diffuse further into the metal where it could be continuously incorporated into the inwardly growing α-Cr_2O_3 scale, Figure 6.8.1. All of the RE

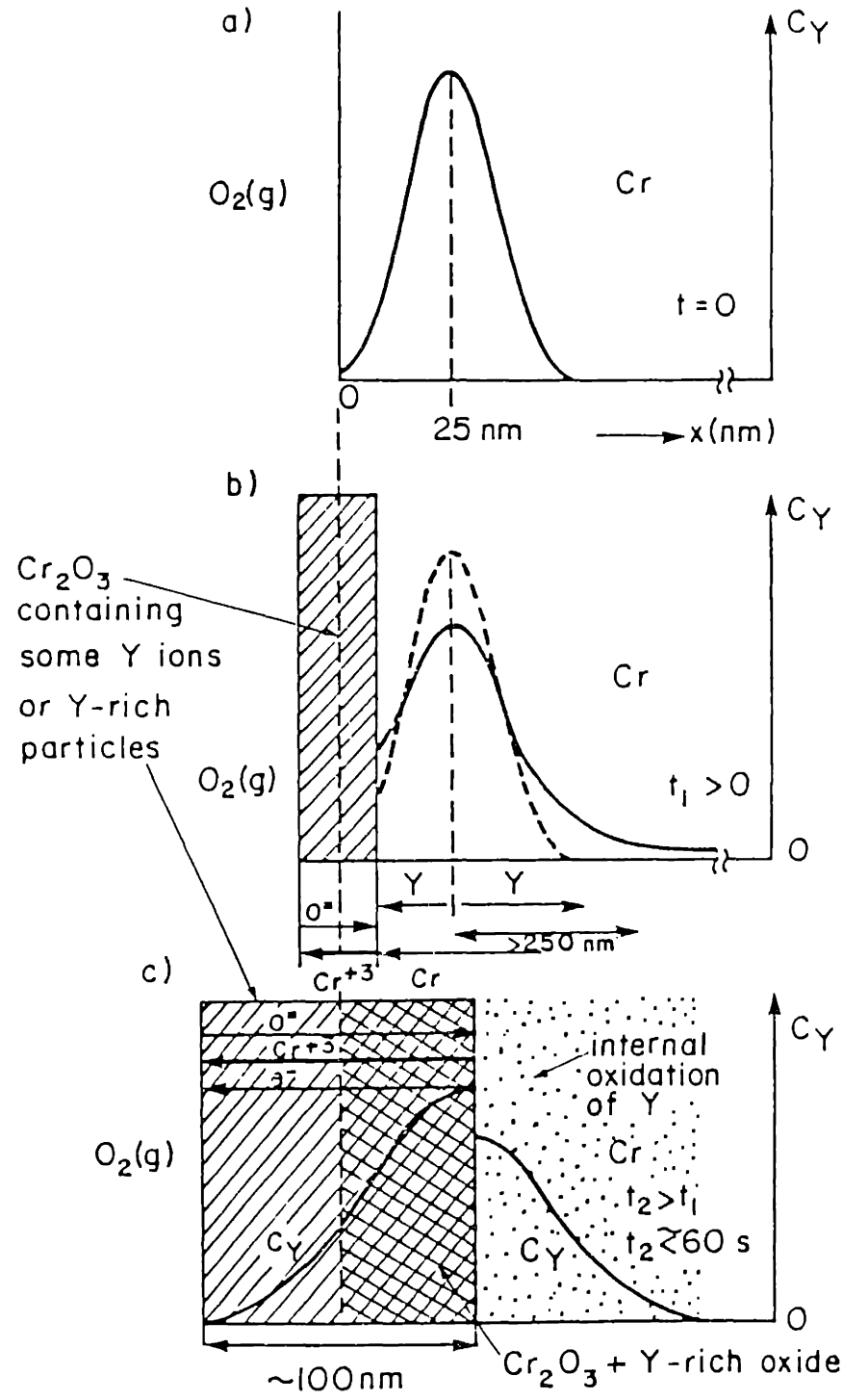

Figure 6.8.1 Model for the early stages of oxidation of pure Cr implanted with $2 \times 10^{16}/cm^2$ in 1atm of O_2 at 900°C [Cotell, 1988].

effects, including an improvement in oxide adherence, were observed in this case.

The important point here is that Y was available in the metal and especially at the metal-oxide interface. According to the Gibbs-Duhem equation, the chemical potentials of the constituents Y, O and YO (either Y_2O_3 or YAl_xO_y) are related by the equation:

$$d\mu_Y = d\mu_{YO} - d\mu_O$$

In the scale, where the oxygen pressure decreases from 1atm at the gas surface to an equilibrium Al/Al_2O_3 pressure (e.g. 10^{-28}atm at 1200°C) at the metal interface, both the O and YO potentials should be falling. Unless $d\mu_O$ is lower than $d\mu_{YO}$, this leaves $d\mu_Y \geq O$. The two extreme cases are illustrated in Figure 6.8.2. In one case, there is no driving force for diffusion. In the other, there is a barrier to diffusion with a positive potential [Cotell, 1988].

Given that Y will not diffuse in the oxide back to the metal, if all of the implanted Y becomes incorporated into the oxide then at long times with an inward growth mechanism the metal-oxide interface will be essentially undoped, Figure 6.8.3. At this point, any improvement associated with RE segregation to the metal-oxide interface would be lost.

Based on the experimental observations at 1200°C and 1500°C, this situation occurred when the scale reached a thickness of several micrometers. The initial peak Y concentration prior to oxidation is at 23nm below the metal surface. With at least a partial inward growth direction, the reaction front would quickly move deeper into the metal leaving the enriched layer behind.

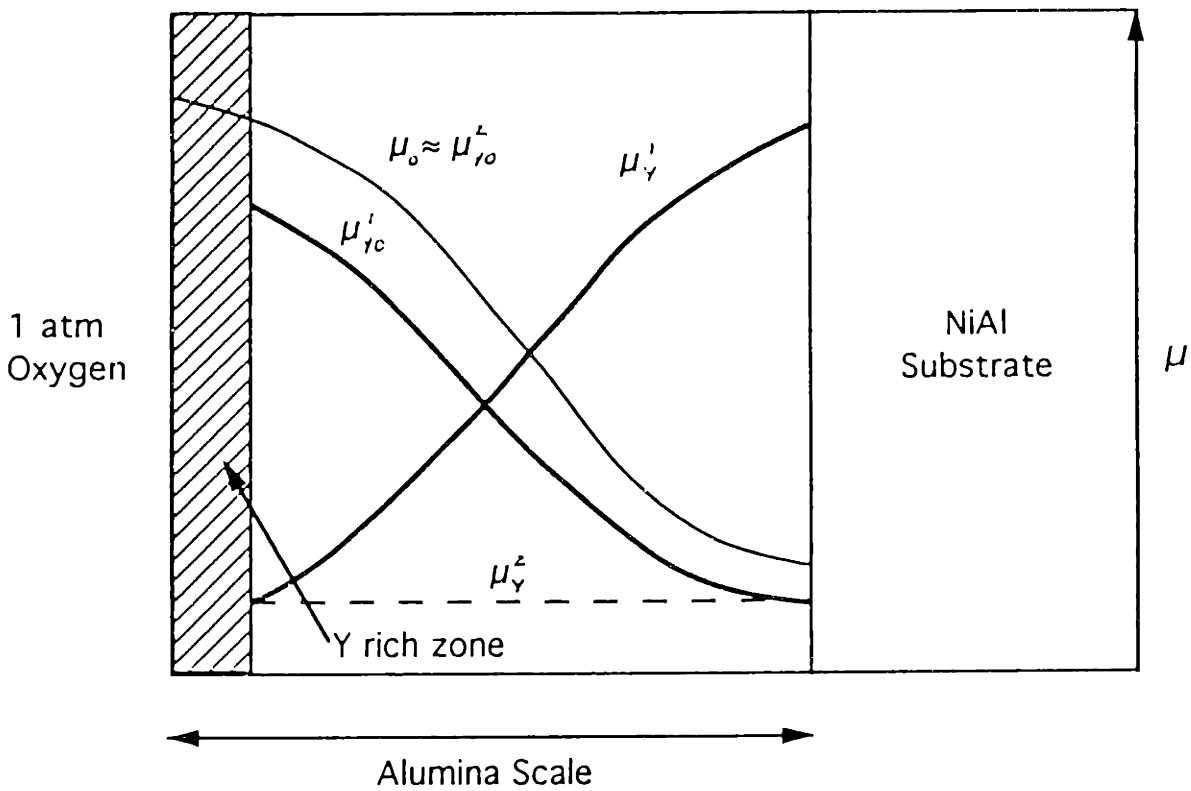

Figure 6.8.2 Schematic diagram of chemical potential gradients for oxygen, yttrium and yttrium oxides in the oxide scale formed on NiAl implanted with Y. Two cases are presented: (1) $\mu_O > \mu_{YO}$ (double line), based on Cotell [1988]; and (2) $\mu_O \approx \mu_{YO}$ (dashed line).

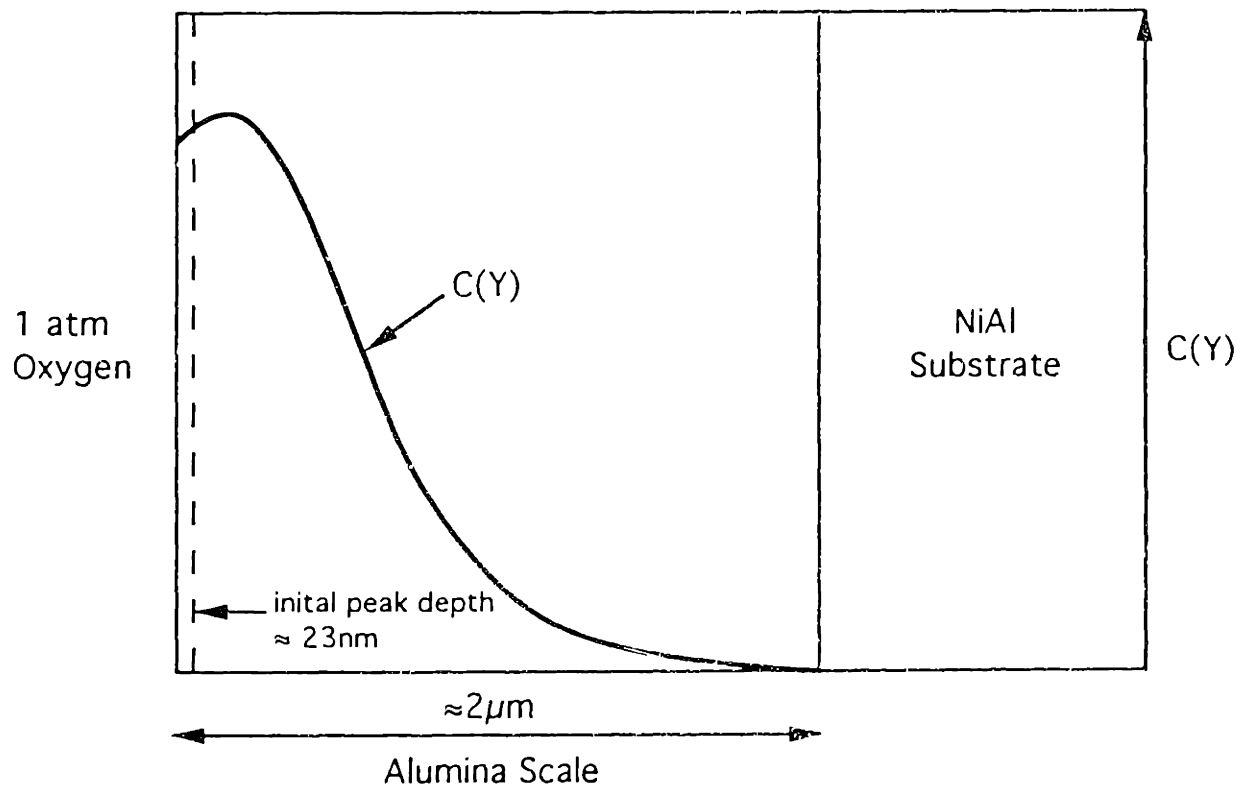

Figure 6.8.3 Model for the distribution of Y in a thick Al_2O_3 scale grown on NiAl. The Y is trapped at the gas interface due to the high oxygen potential across the scale, thus the metal-oxide interface is essentially undoped.

A similar behavior was recently reported for FeCrAl surface coated with RE oxides [Hou, et al., 1992]. The surface coating was not effective in improving the oxidation behavior. A rumpled scale was formed on both the coated and uncoated alloys during oxidation at 1100° and 1200°C and oxide adhesion was not improved by the coating. This again appears to be a case where there is no driving force for the inward diffusion of the RE. Since the RE is added as a surface addition, new scale formed by at least a partial inward growth mechanism would be essentially undoped. This is analogous to ion implantation.

Unfortunately, there is little microstructural evidence to confirm this hypothesis. In the case of adherent scales on doped FeCrAl, the RE is always detected at the metal-oxide interface using XTEM (e.g. Figure 4.2.15). However, in the case of non-adherent scales, XTEM samples are not available. Also, attempts to produce XTEM samples of adherent scales on NiAl were unsuccessful.

6.8.2 Alloy Addition

The improvement in oxide adherence at 1200°C with the addition of 0.23wt%Zr to NiAl is proof that, given a proper RE addition, improvements are possible for NiAl, Figure 5.2.3. Clearly there is a difference between the alloy addition of Zr and the ion implantation of Y. Based on the similarity between oxide dispersions of Y_2O_3 and ZrO_2, it is suspected that the success with Zr has to do with the method of addition and not with any chemical difference between the two elements.

Unlike implantation, where the RE remains only in the near-surface region, the alloy addition is found throughout the coupon. Thus, as the scale consumes the substrate during oxidation, there is more RE available in the metal to segregate to newly formed grain boundaries and the metal-oxide interface. This maintains the REE to longer exposures than an implantation.

This behavior was observed at 1200°C. After twenty 2hr cycles, oxide adherence was excellent (comparable to the oxide-dispersed FeCrAl alloys) with little evidence of breakdown. The Y-implanted sample began to spall after just a few cycles, and after 20 cycles it was virtually indistinguishable from the unimplanted NiAl.

The Zr addition to NiAl did show unusual behavior at 1400°C. After approximately ten 1hr cycles, the scale began to spall significantly, Figure 5.3.4. A large increase in oxidation rate was also observed after ≈20hr in isothermal exposure, Figure 5.3.5. This type of breakdown was also observed in several Y-implanted NiAl samples at approximately the same time. The breakdown could be attributed to excessive stresses of a thick scale or some type of Al depletion, except that none of the undoped NiAl samples exhibited similar behavior. Thus, it is most likely an effect of the RE addition in both samples.

Although no specific observations were made at 1400°C, there are indications at 1200°C for both Zr and Y that a large quantity of Zr- and Y-rich oxide forms in the scale during exposure. This was also observed for Y at 1500°C. In the case of a Zr alloy addition, after oxidation at 1200°C a substantial number of ZrO_2 particles

were observed near the gas interface, Figure 5.2.18. This enrichment likely occurs during oxidation as Zr diffuses out of the alloy into the scale. This diffusion would be driven by the oxygen gradient in the scale and would be analogous to the μ_{YO} gradient shown in Figure 6.8.2. The point to be made is that RE segregation on the oxide boundaries is not a static situation. The RE is moving outward (towards higher P_{O_2}) during oxidation and is not just "sitting" on the boundary. This diffusion would be expected to be much slower than Al or O in Al_2O_3 because of the larger ion size of Zr and Y. Once the RE ions diffuse through the scale to the surface of the oxide, they form RE-rich oxides or coarsen already existing particles.

If this diffusion-induced enrichment of the RE is significant at 1200°C, it should be even greater at 1400°C with a typical temperature-dependent diffusion rate. If the volume of Zr-rich particles (identified by GAXRD as tetragonal ZrO_2) were to grow too large during this process, it could lead to isothermal breakdown of the scale. ZrO_2 particles could cause cracking, acting as stress-concentrators in the scale. This type of breakdown could occur isothermally but would be aggravated by cyclic conditions, with their increased stresses related to a difference in CTE between Al_2O_3 and ZrO_2.

In the case of the oxide dispersions in FeCrAl, this type of RE outward diffusion may be restricted. The RE is not "free" in the alloy like Zr in NiAl. Instead, it is bound in very stable oxides, possibly limiting the diffusion from the alloy into the oxide. This could explain why no major breakdowns analogous to those observed for NiAl + Zr are observed during the oxidation of doped FeCrAl at

1400°C. However, there is also significantly less Zr in FeCrAl (0.1wt%) than in NiAl (0.23wt%), which could also reduce the amount of Zr diffusing to the gas interface

6.8.3 Oxide Dispersion

A more fruitful course would have been to make NiAl with an oxide dispersion of Y_2O_3 (or ZrO_2 or La_2O_3). Without getting into the alloy processing field, the next best alternative was to study the more readily-available commercial ODS FeCrAl alloys. Unlike ion implantation, these alloys did show "perfect" adherence at 1200°C. Overall, the REE was best represented by the RE oxide dispersion over the temperature range investigated. The spalling and cracking observed on MA956 and APM at 1400°C were minimal compared to the major breakdown of scales on the other RE-doped NiAl materials.

At each temperature in the study, a reduction in oxidation rate and an improvement in oxide adherence was clearly observed for these alloys. At 1000°C and 1200°C, numerous observations were made of oxide grain boundaries, and in each case the RE was found to segregate to every boundary analyzed. Also, observations of the metal-oxide interface at various times and temperatures also detected RE segregation in each case.

Establishing exactly what is preferable about an oxide dispersion is difficult. In comparison with the other methods of addition, the RE is evenly distributed both parallel and normal to the metal-oxide interface.

Few attempts have been made to study the different methods of addition. Sorting out the large number of variables has proven very difficult. Hou and Stringer [1988] concluded that oxide dispersions were superior among the three types of additions to Co-25Cr. Ion implanted Y and an oxide dispersion were compared by internally oxidizing an Y implant in Co-25Cr. However, the Y-alloyed material had a much finer grain size than the implanted or internally-oxidized alloy. Also, the internal oxidation process introduced Si contamination which might have affected the comparison.

Thus, while an RE oxide dispersion is the most costly and difficult type of addition, it appears to produce the best oxidation behavior, at least in the limited comparison made in this study.

6.9 Scale Microstructures

From a materials science perspective, the microstructure is always deemed to be influential to the overall properties and performance of the material. Oxidation is a somewhat aberrant case in that the oxide microstructure is often ignored. The principal reason is that there has been no conclusive indication that parameters like the oxide grain size or morphology are a "first-order" indication of good oxidation behavior. The RE effect of modifying the oxide microstructure (*viz* reducing the oxide grain size) is the youngest sibling of the four effects -- it is the least studied and most ignored effect. Even in this discussion it comes last; but it shall not be ignored.

6.9.1 Oxide Grain Size

While it has been proposed that a fine oxide grain size improves the scale plasticity which in turn improves the oxide adherence, there has been no experimental measurement or observation to confirm this idea. There is much stronger evidence to suggest that tramp elements such as sulfur have a much larger effect on scale adherence than oxide grain size.

However, one point about the effect of a RE on oxide grain size requires further discussion. At the temperatures studied here, boundary diffusion is more significant than lattice diffusion (Section 6.2.3). Also, with a RE addition there is a significant reduction in the scale grain size (Table 4.1). It stands to reason that this reduction is counterproductive to a reduction in oxidation rate. With a smaller grain size, there is an increased number of diffusion pathways, which presumably produces a faster oxidation rate, which is reflected in the factor f_t for the calculated rate, Equation 6.7. (The actual reduction in oxidation rate is observed because the RE addition reduces the scale growth by cation diffusion.) In order to minimize the number of diffusion pathways and thus reduce the oxidation rate, a larger grain size would be desirable.

However, while a larger grain size may lower the oxidation rate, it also can be detrimental to the oxidation behavior in other ways. As observed at 1500°C, large grains can result in limited contact between the alloy and the oxide, Figure 5.4.8. This morphology is drawn schematically in Figure 6.9.1. It may be argued that the illustrated gaps occur because of metal-oxide decohesion

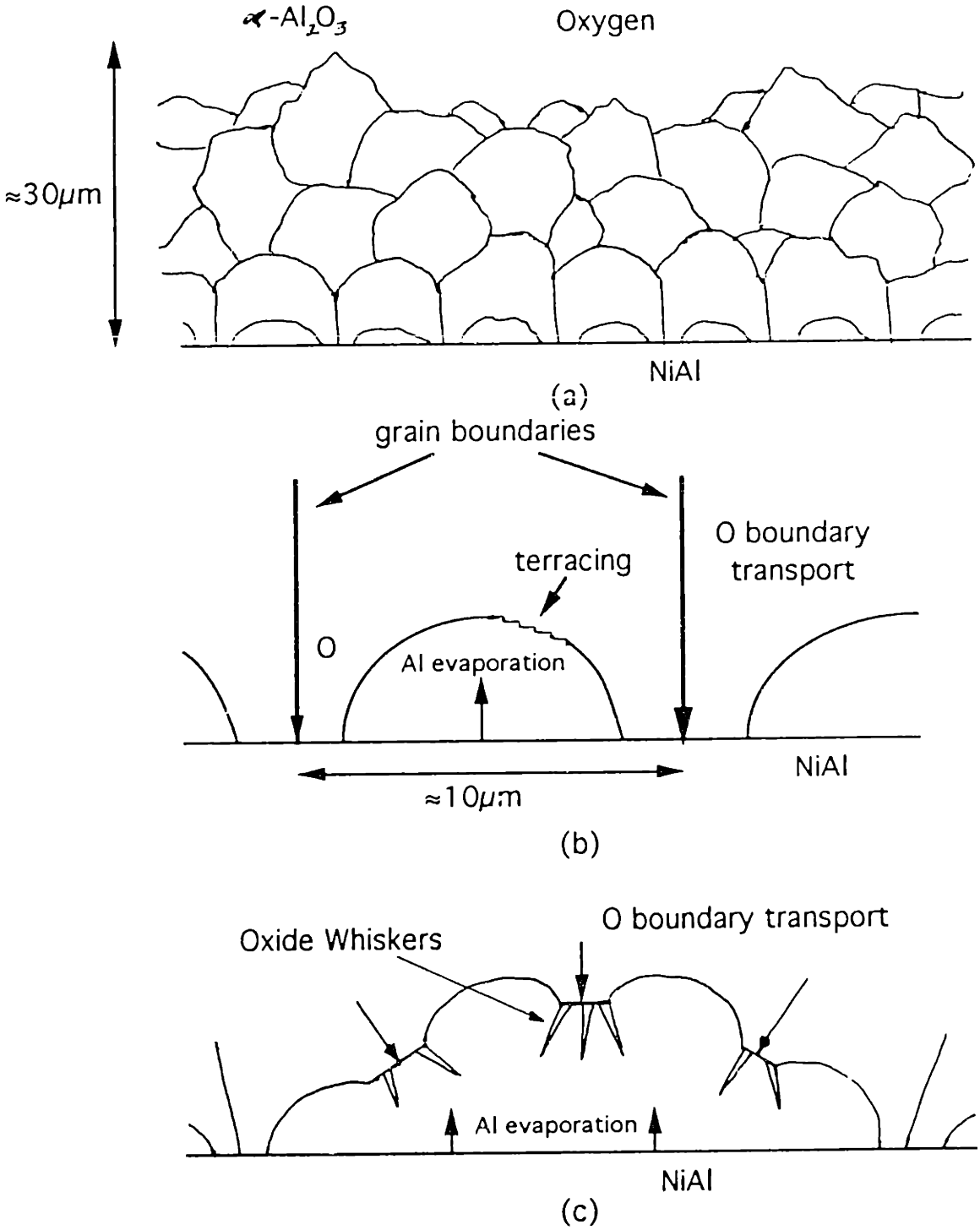

Figure 6.9.1 Schematic model of the scale microstructure on NiAl after oxidation for 50hr at 1500°C. (a) total scale thickness, (b) metal-oxide interface where the oxide is in contact with the NiAl substrate, and (c) metal-oxide interface when the oxide loses contact with the substrate at temperature.

due to sulfur segregation or vacancy coalescence. However, based on the present observations, it appears that the size of the grains also aggravates this decohesion. With new oxide formed primarily at the grain boundaries, the large ≈10μm gaps between the boundaries are not able to fill in. This situation most likely occurs because surface diffusion along the metal-oxide interface which serves to smooth out the oxidation front, cannot keep up with the boundary transport of O. Instead of a smooth interface, an inverted ridge structure is produced in which only the ridges are in contact with the substrate. In this case, a smaller grain size would at least provide more ridges and thus increase contact between the oxide and metal. There is thus a possible tradeoff: smaller grains with RE additions may improve adherence but at the same time increase the number of pathways for oxidation. A suitable comparison was not possible in this study because the Y-implant affected the oxidation behavior only for a very short time and thus had little effect on the long-term microstructure development.

6.9.2 Oxide Whiskers and Blades

The oxide morphology often reflects the growth mechanism, even if the connections are somewhat ambiguous. For example, the observation of whiskers on the oxide surface, especially on undoped FeCrAl, is a clear indicator of an outward growth mechanism, Figure 4.2.4. The oxide blade morphology of θ-Al_2O_3 is also an indicator of an outward growth mechanism. Simply put, it is difficult to imagine a whisker or blade pointing outward growing by an inward growth

mechanism. This would mean that new oxide is formed at the base of the protrusion rather than at the tip or sides. The observation of these structures always coincided with the ^{18}O tracer profiles indicating at least a partial outward diffusion mechanism. Voss, et al. [1982] observed a hollow pipe at the center of an α-Fe_2O_3 whisker. This pipe was believed to allow the rapid transport of Fe to the tip of the whisker.

A more difficult morphology to understand is that of oxide whiskers growing towards the substrate after oxidation at 1500°C. An important point is that these whiskers were not observed across the entire oxide surface but only in patches. This heterogeneity may indicate that whiskers were only found in areas where some special event occurred. The most likely possibility is that the whiskers grew in areas where the oxide buckled, and lost contact with the substrate. Figure 6.9.1c schematically illustrates this scenario. The whiskers are located near the oxide ridges where O is being transported inwards and Al evaporates through the gap to grow the whiskers. The oxide buckling is shown in Figure 5.4.8b, and the concentration of whiskers on ridges can be seen in Figure 5.4.8a. In this case, the whiskers are again indicative of the growth mechanism. However, in this case, it is an inward growth mechanism.

6.9.3 Oxide Dislocations

While several different pathways are possible for short-circuit diffusion, grain boundary diffusion has been emphasized. The

primary reason for this emphasis is that dislocations are decidedly absent from the microstructures in this study. Both for doped and undoped α-Al_2O_3, there were not enough dislocations observed to consider them a viable alternative to grain boundaries for material transport.

6.9.4 Voids

The formation of voids within grains in the growing scale is a significant issue. Besides the large grain size, the large number of macrovoids in the undoped scale is the most distinctive feature in TEM parallel sections, Figure 4.2.12. Despite their prominence at 1000° and 1200°C, there is only one paper in the literature that addresses their presence [Smialek and Gibala, 1983]. Clearly they are linked to the absence of RE-doping, because voids are almost nonexistent in doped scales at lower temperatures. Their appearance is also a function of temperature, because the observation of voids is more frequent at higher temperature. At higher temperatures, the voids also become more prominent on doped scales, Figure 4.3.7.

Smialek and Gibala [1983] concluded that void size increased with distance from the metal-oxide interface and was inversely proportional to the grain size. They also observed the coalescence of smaller voids, which suggested an Ostwald ripening process. The voids were thought to form from the outward diffusion of O vacancies. At the low P_{O_2} near the metal-oxide interface, vacancies are created and are at equilibrium. However, as they diffuse

outward and the P_{O_2} increases the oxide becomes saturated, and they condense out as voids. The Smialek and Gibala study also concluded that there were insufficient dislocations observed to represent a significant diffusion pathway.

Another important factor may be the interplay between grain boundary diffusion (cations, anions and vacancies) and grain growth. Voids within grains are often found in oxide microstructures after rapid grain growth. The faster grain growth in undoped scales and higher temperatures may increase the void content.

The issue of the importance of voids on the oxidation behavior has not been investigated sufficiently in this study. Nor has the effect of RE-doping on void formation (or annihilation) been investigated. The relationship may very well be an important issue for understanding the REE, but this among dozens of other unexplained RE effects is left for another study (see Section 8.0).

7.0 Conclusions

1. θ-Al_2O_3 grows by a predominant outward cation diffusion process at 950°C.

2. Without a reactive element addition, α-Al_2O_3 grows by a mixed diffusion mode of simultaneous Al and O transport. With the addition of a reactive element, Al diffusion is reduced and growth is mainly by the inward transport of oxygen via grain boundaries. This is observed at both 1200°C and 1500°C.

3. The reduction in the transport of Al, which reduces the macroscopic rate of oxidation, is caused by the segregation of the reactive element to the scale grain boundaries.

4. All of the reactive element effects can be explained by the segregation of the reactive element to the oxide grain boundaries and the metal-oxide interface in Al_2O_3. This is analogous to observations for Cr_2O_3.

5. Ion Implantation is not a viable technique for the study of the Reactive Element Effect in Al_2O_3-forming materials.

   a) Yttrium implantation stabilizes the first-forming θ-Al_2O_3 phase, which otherwise transforms into α. At 1000°C without an implant, the transformation to α is complete after ≈2hr. With a Y-implant, θ is still present after 100hr.

   b) Above ≈1300°C, there is little evidence of any effect of the yttrium due to the shallow implant.

c) At 1200°C, while an yttrium implant lowers the oxidation rate, there is no significant improvement in oxide adherence.

6. Al content does not have a significant effect on the oxidation behavior within the ß-NiAl phase field.

8.0 Future Work

1. The obvious continuation of this work is to make NiAl with an oxide dispersion of Y_2O_3. Testing this material in cyclic and isothermal exposures from 1000° to 1600°C, will provide much additional information, *viz*:

a) The effect of the oxide dispersion of Y on the phase transformation at 1000°C. Unoxidized implanted Y in the alloy might be more easily incorporated into the θ structure. Y_2O_3 (and possibly α-Al_2O_3) in the alloy might not be so readily incorporated into θ. It also could have the same effect as the implant.

b) Comparison of the effect of the oxide dispersion in NiAl to that in FeCrAl. Similar effects should be found in the oxidation rate, adherence and reduction in cation transport.

c) Study of the REE at 1500°C and 1600°C. If the RE does segregate, will it reduce the oxide grain growth and improve the contact between the alloy and the oxide as well as produce the other reactive element effects.

2. A second extension is to study the segregation phenomena, varying the cation of the dispersed oxide. It appears that cations of different charge (Y^{3+} and Zr^{4+}) will both segregate. By adding a La_2O_3 dispersion, the behavior of an isovalent ion with a larger ionic radius can be studied. Possibly this ion will behave differently (e.g. forming a second phase rather than segregating) and thus have a different effect on the oxidation mechanism.

3. Another concern is the breakdown of the Al_2O_3 scales. For instance, Y_2O_3-dispersed Ni_3Al forms an outer Ni-rich scale. During

cyclic testing, this scale is observed to spall and then reform. By what mechanism does it break down? And more interestingly, if the underlying Al_2O_3 scale is believed to be protective and dense, how does it grow back? A first guess would be that the Al_2O_3 scale is not dense but rather is cracked during cooldown and allows an initial transient Ni-rich oxide to form. The cracked or otherwise permeable scale should be studied in order to confirm or disprove this idea.

4. Further microstructural characterization of the effect of the RE is also warranted. The large volume fraction of voids in the undoped α-Al_2O_3 was not investigated nor was the scale transformation from θ-Al_2O_3 to α.

5. While the diffusing species were investigated in this study, the conclusions of the diffusion pathways were largely inferred. Thus the mechanism by which diffusion occurs needs to studied further in order to achieve a more fundamental understanding of the growth mechanism. Of special interest is the mechanism by which undoped α-Al_2O_3 can apparently transport Al and O simultaneously.

9.0 Biography

Mr Pint was born October 21, 1966 in Akron, Ohio. He was raised more than a little successfully by his parents, James and Betty, with a little help from his three older sisters, Rebecca, Ellen and Sheila. He attended public schools in Akron, graduating as salutatorian from Garfield Senior High in June 1984. Throughout high school, Mr. Pint was active in the Marching and Concert Bands, Student Council and Boy Scouts. He earned the rank of Eagle Scout in February 1984 and won the Firestone Award of Merit medallion. He was elected president of the Garfield chapter of the National Honor Society.

Mr. Pint entered M.I.T. in September 1984 as a freshman. While initially telling friends and family of an interest in electrical engineering, he quickly became interested in the department of Materials Science and Engineering. As an undergraduate, Mr. Pint worked at the MIT Museum and had a UROP job in Civil Engineering before starting work for Prof. Greg Yurek in September 1986 along with Eric Katz. Mssrs. Pint and Katz worked for the next year together investigating the high temperature oxidation behavior of MA956 and MA754 along with Kaz Przybylski and Tony Garratt-Reed.

Mr. Pint spent the summers of 1986 and 1987 working at The Timken Co. in Canton, OH, under the Engineering Internship Program and living at home. The first summer was spent working with Dennis Hetzner and studying quantitative image analysis of Ca-treated steel and the second summer with Peter Lee studying Fe-matrix metal composites and the reaction of various ceramic whiskers with Fe powders. Mr. Pint also worked at Timken for one month in January 1988.

As an undergraduate, Mr. Pint participated in numerous intramural sports with the inhabitants of the 2nd east floor (The Beast from the East) at the East Campus dorimtory. Mr. Pint worked on the Lecture Series Committee as an undergraduate and continued to do so until 1992. He was also inducted into Tau Beta Pi in 1987.

Graduating in February 1988, Mr. Pint immediately started working for Prof. Yurek as a research assistant studying the simultaneous oxidation-sulfidation of MA754. In April, just two months after Mr. Pint started, Prof. Yurek announced that he was taking a one year leave of absence to become president and CEO of American Superconductor Company. Yurek would never return to MIT, resigning his full professorship effective July 1989.

In April 1989, effective September 1989, Mr. Pint switched advisors to Prof. Linn W. Hobbs. No funding was available at that time but Prof. Hobbs agreed to continue the project that had been outlined with Prof. Yurek. Mr. Pint passed the written portion of the general exam in February 1989 and the oral/thesis proposal phase in June 1989 with both Profs. Hobbs and Yurek acting as co-advisors and Profs. Chiang and Vander Sande on the committee.

Without direct funding for the next year, Mr. Pint obtained a teaching assistantship for the next three semesters. The summer salary was payed by the DOE to help with the ion implantation work with Dr. Amitabh Jain, a visiting scientist from IIT in New Delhi, India. After promised funding from EPRI was delayed in June 1990, Mr. Pint solicited funds from NASA, NRL and The Timken Co.. The Timken Co. supplied funds for Mr. Pint's work in September 1990, which enabled the project to fully proceed for the first time. Funding from EPRI began in April 1991 and continued to the end of the thesis.

As a graduate student, Mr. Pint acted as a freshman advisor for three years including one year helping to teach a seminar on the history of MIT at the MIT Museum. Mr. Pint was also twice elected as the student representative to the department committee on graduate students. His minor was in history.

Dr. Pint's hobbies include travel, history, hiking, intramural sports, reading, music, visiting museums, baking and politics. He is a life-long Roman Catholic and Democrat.

Due to the recession which continues to grip the U.S., Mr. Pint was unable to find employment and has accepted a post-doctoral position with Prof. Hobbs for the next year.

10.0 List of Abbreviations

Å	Angstrom, unit of length; 1Å = 10^{-10}m
Al	Aluminum
AEM	Analytical electron microscopy
AES	Auger electron spectroscopy
Al_2O_3	Aluminum oxide, alumina
APM	Advance powder metallurgy FeCrAl alloy manufactured by Kanthal Inc., contains an oxide dispersion of Al_2O_3-ZrO_2.
Ar	Argon
ASC	American Superconductor Corporation
atm	atmosphere, unit of pressure; 1atm = 760Torr = 760mmHg
Au	Gold
BAP	Bruce Andrew Pint; author
Ce	Cerium
cm	centimeter, unit of length 100cm = 1m
Co	Cobalt
Cr	Chromium
Cr_2O_3	chromium(III)oxide; chromia
Cs	Cesium
CTE	Coefficient of thermal expansion
δ	Grain boundary width
D	Diffusion coefficient, typical units of cm^2/s
DOE	Department of energy, U.S. government agency

D_X^b	Diffusion coefficient of species X along grain boundaries in the matrix
D_X^i	Diffusion coefficient of species X via interstitials
D_X^l	Diffusion coefficient of species X through the lattice of the matrix
D_X^v	Diffusion coefficient of species X by a vacancy exchange mechanism
EDXA	Energy dispersive x-ray analysis
EELS	Electron energy loss spectroscopy
EPMA	Electron probe microanalysis; connotation of x-ray analysis using WDXA
EPRI	Electric Power Research Institute
ESR	Electron spin resonance
EXAFS	Extended x-ray absorption fine-structure technique
f_t	area fraction of matrix at time t, through which grain boundary diffusion occurs
Fe	Iron
FEG	Field-emission gun; produces electron beam for microscopy
FOAD	Typical reply in Bruce's attempts to get a job
g	gram, unit of mass; geometrical factor
GAXRD	Glancing angle x-ray diffraction
HAG	Huge asian girl
hr	hour, unit of time
i	interstitial; an ion which occupies a normally unoccupied lattice site

ICPS	Inductively coupled plasma analysis
ID	Inner diameter; measurement used for a tube
J	Joule, unit of energy; 1J = 0.239cal
J_x	flux through medium x; units of mass per unit area per unit time, e.g. g/cm^2s
JCPDS	Joint committee for powder diffraction stuff
k_g	Parabolic rate constant measured from weight gain data.
kJ	kilojoule, unit of energy; 1kJ = 1000J
k_p	Parabolic rate constant used to calculate diffusion coefficients
kV	Kilovolt unit of electrical potential; 1kV = 1000V
La	Lanthanum
$LaCl_3$	Lanthanum chloride
λ_t	grain size of the oxide at time t
ln	natural logarithm
log	base 10 lagarithm
m	meter, unit of length
M	generic base metal of unspecified identity
mA	milliampere, unit of electric current; 1000mA = 1A
MA956	FeCrAl alloy manufactured by the International Nickel Co., contains an oxide dispersion of Al_2O_3-Y_2O_3.
mg	milligram, unit of weight; 1000mg = 1g
min	Minute, unit of time;
μm	micrometer, unit of length; micron; 1μm = 10^{-6}m

NASA	National air and space administration, U.S. government agency
Ni	Nickel
nm	nanometer, unit of length; 1nm = 10^{-9}m
NRA	Nuclear reaction analysis; not to be confused with the National Rifle Association
NRL	Naval Research Laboratory, Washington, D.C.
O	Oxygen
^{16}O	Oxygen isotope atomic weight of 16
^{18}O	Oxygen isotope atomic weight of 18
OD	Outer diameter
ODS	Oxide dispersion strengthened
Pd	Palladium
P_{O_2}	oxygen partial pressure
P_{O_2}'	Decomposition pressure of Al_2O_3
P_{O_2}''	ambient oxygen partial pressure in the gas phase
psi	Pounds per square inch, unit of pressure; 14.5 psi = 1atm
Pt	Platinum
RBS	Rutherford backscattered spectroscopy
RE	Reactive element
REE	Reactive element effect
Rh	Rhodium
s	second, unit of time
SAD	Selected area diffraction

SEM	Scanning electron microscope
SIMS	Secondary ion mass spectroscopy
Sr	Stereradian; Strontium
STEM	Scanning transmission electron microscopy
t	Time
T	Temperature
TEM	Transmission electron microscopy
TGA	Thermogravimetric analysis
Ti	Titanium
Torr	unit of pressure; 1Torr = 1mmHg = 0.00132atm
T_m	Melting temperature
UK	United Kingdom
v	Vacancy; an unoccupied lattice site
WDXA	Wavelength dispersive x-ray analysis
XPS	X-ray Photoelectron Spectroscopy
XRD	X-ray diffraction
XTEM	Cross-sectional transmission electron microscopy
Y	Yttrium
YAG	Yttrium aluminum garnet
YCl_3	Yttrium chloride
Y_2O_3	yttrium oxide; yttria
Zr	Zirconium
ZrO_2	Zirconium oxide; zirconia

11.0 References

G.B. Abderrazik, G. Moulin, A.M. Huntz, E.W.A. Young and J.H.W. de Wit, (1987) "Growth Mechanism of Al_2O_3 Scales Developed on FeCrAl Alloys", Solid State Ionics, v.22 p.285-94.

I.M. Allam, D.P. Whittle and J. Stringer, (1978) "The Oxidation Behavior of CoCrAl Systems Containing Active Element Additions", Ox. Met., v.12 p.35-66.

J.E. Antill, M.J. Bennett, R.F.A. Carney, G. Dearnaley, F.H. Fern, P.D. Goode, B.L. Myatt, J.F. Turner and J.B. Warburton, (1976) "The Effect of Surface Implantation of Y and Ce Upon the Oxidation Behaviour of Stainless Steels and Aluminized Coatings at High Temperatures", Corr. Sci., v.16 p.729-45.

J.E. Antill and Peakall, (1967) "Influence of an Alloy Addition of Y on the Oxidation Behaviour of an Austenitic and a Ferritic Stainless Steel in Carbon Dioxide", J. Iron Steel Inst., v.205 p.1136-42.

A. Atkinson, (1987) "Grain Boundary Diffusion in Oxides and Its Contribution to Oxidation Processes", Harwell Report No. AERE-R17845, Harwell Laboratory, UK.

A. Atkinson and R.I. Taylor, (1985) "Diffusion of ^{51}Cr Tracer in Cr_2O_3 and the Growth of Cr_2O_3 Films", in Transport in Non-Stoichiometric Compounds, G. Simkovich and V.S. Stubican eds., NATO ASI Series B, v.129, Plenum Press, New York, NY, p.285-95.

A. Atkinson, R.I. Taylor and A.E. Hughes, (1981) "A Quantitative Demonstration of the Grain Boundary Diffusion Mechanism for the Oxidation of Metals", Harwell Report No. AERE-R10000, Harwell, U.K..

C.S. Barrett, (1988) "The Effect of 0.1at% Zirconium on the Cyclic Oxidation Resistance of ß-NiAl", Ox. Met., v.30 p.361-90.

S.N. Basu and J.W. Halloran, (1987) "Tracer Isotope Distribution in Growing Oxide Scales", Ox. Met., v.27 p.143-55.

B. Bender, D.B. Williams and M.R. Notis, (1980) "Investigation of Grain-Boundary Segregation in Ceramic Oxides by Analytical

Scanning Transmission Electron Microscopy", J. Am. Cer. Soc., v.63 p.542-46.

J.S. Benjamin, (1970) "Dispersion Strengthened Superalloys by Mechanical Alloying", Met. Trans., v.1 p.2943-51.

M.J. Bennett, A.T. Tuson, D.P. Moon, J.M. Titchmarsh, P. Gould and H.M. Flower, (1992) submitted to Surf. Coat. and Tech..

M.J. Bennett, H. Romary and J.B. Price, (1991) "The Oxidation Behavior of Alumina Forming Oxide Dispersion Strengthened Ferritic Alloys at 1200-1400°C", in Heat Resistant Materials, K. Natesan and D.J. Tillack eds., ASM International, Materials Park, OH, p.95-103.

M.J. Bennett and M.R. Houlton, (1990) "Comparison Between the Oxidation Behavior of FeCrAlloy Stainless Steel and the MA956 Oxide Dispersion Strengthened Alloy", in High Temperature Materials for Power Engineering, E. Bachelet, et al. eds., Kluwer Academic Publishers, p.227-38.

M.J. Bennett, (1989) "Improved High Temperature Oxidation Protection of Alloys by Ion Implantation", in Environmental Degradation of Ion and Laser Treated Surfaces, G.S. Was and K.S. Grabowski eds., TMS, Warrendale, PA, p.261-76.

M.J. Bennett, J.A. Desport, M.R. Houlton, P.A. Labun and J.M. Titchmarsh, (1988) Mater. Sci. Tech.,v.4 p.1107.

M.J. Bennett, J.A. Desport and P.A. Labun, (1985) "Yttrium Location and Chemical State in the Scale Formed on Y-Implanted 20%Cr/25%Ni/Nb Stabilised Stainless Steel in Carbon Dioxide at 825°C", Proc. 43rd Annual Meeting Elec. Micro. Soc. of Amer., G. W. Bailey ed., San Francisco Press, San Francisco, CA, p.270-1.

M.J. Bennett, M.R. Houlton and G. Dearnaley, (1980) "The Influence of the Surface Ion Implantation of Aluminum and Yttrium upon the Oxidation Behavior of a Fe-15%Cr-4%Al FeCrAlloy Stainless Steel, in Air, at 1100°C", Corr. Sci., v.20 p.69-72.

Binary Alloy Phase Diagrams, 1st edition, (1986) T.B. Massalski et al. eds., ASM International, Metals Park, OH.

V.T. Borisov, V.M. Golikov and G.V. Scherbedinskiy, (1964) "Relation Between Diffusion Coefficients and Grain Boundary Energy" Fiz. Metal. Metalloved., v.17 p.881-5.

D.N. Braski, P.D. Goodell, J.V. Cathcart and R.H. Kane, (1986) "The Effect of Y_2O_3 Dispersoids in 80Ni-20Cr Alloy on the Early Stages of Oxidation at Low Oxygen Potential", Ox. Met., v.25 p.29-50.

C.L. Briant and K. Luthra, (1988) "Surface Segregation in MCrAlY Alloys", Met. Trans., v.19A p.2099-108.

C.L. Briant and A.I. Taub, (1988) "Grain Boundary Segregation of Boron and Sulfur and Its Effect on Ductility in Rapidly Solidified Ni-Base L1(2) Compounds", Acta Met., v.36 p.2761-70.

C.L. Briant and K. Luthra, (1986) "An Auger Electron Spectroscopy Study of Surface Segregation in MCrAlY Alloys", in Fundamental Aspects of High Temp. Corr., v.2, D. Shores and G.J. Yurek eds., Electrochem. Soc., Pennington, NJ, v.86-9 p.187-99.

P. Burtin, J.P. Brunelle, M. Pijolat and M. Soustelle, (1987a) "Influence of Surface Area and Additives on the Thermal Stability of Transition Alumina Catalyst Supports. I: Kinetic Data", App. Catalysis, v.34 p.225-38.

P. Burtin, J.P. Brunelle, M. Pijolat and M. Soustelle, (1987b) "Influence of Surface Area and Additives on the Thermal Stability of Transition Alumina Catalyst Supports. II: Kinetic Model and Interpretation", App. Catalysis, v.34 p.239-54.

C.B. Carter and S.L. Sass, (1981) "Electron Diffraction and Microscopy Techniques for Studying Grain-Boundary Structure", J. Am. Cer. Soc., v.64 p.335-45.

G. Carturan, R. Di Maggio, M. Montagna, O. Pilla and P. Scardi, (1990) "Kinetics of Phase Separation and Thermal Behavior of Gel-Derived Al_2O_3 Doped by Cr_2O_3: an X-Ray Diffraction and Flourescence Spectroscopy Study", J. Mat. Sci., v.25 p.2705-10.

J. Cathcart, (1976) "The Mechanical Properties of Scales and Their Influence on High Temperature Gas-Metal Reactions", in Proc. Symp. on the Properties of High-Temp. Alloys, Electrochem. Soc., Pennington, NJ, p.63-83.

J.D. Cawley and J.W. Halloran, (1986) "Dopant Distribution in Nominally Yttrium-Doped Sapphire", J. Am. Cer. Soc., v.69 p.C195-6.

J.D. Cawley, J.W. Halloran and A.R. Cooper, (1986) "Oxygen Diffusion in α-Al_2O_3", NASA Technical Memorandum Nc. 83622, Cleveland, OH.

M.W. Chase, C.A. Davies, J.R. Downey, D.J. Frurip, R.A. McDonanld and A.N. Syverud, (1985) JANAF Thermochemical Tables, 3rd edition, Amer. Inst. Physics, New York, NY.

H. Chaung, J.B. Lumsden and R.W. Staehle, (1979) "Effect of Segregated Sulfur on the Stress Corrosion Susceptibility of Nickel", Met. Trans., v.10A p.1853-7.

Y.M. Chiang, A.F. Henriksen, W.D. Kingery and D. Finello, (1981) "Characteriza-tion of Grain-Boundary Segregation in MgO", J. Am. Cer. Soc., v.64 p.385-89.

G. Cliff and G.W. Lorimer, (1975) "The Quantitative Analysis of Thin Specimens", J. Microscopy, v.103 p.203-7.

R.A. Collins, S. Muhl and G. Dearnaley, (1979) "The Effects of Rare Earth Impurities on the Oxidation of Chromium", J. Phys. F: Metal Phys., v.9 p.1245-59.

R.F. Cook and A.G. Schrott, (1988) "Calcium Segregation to Grain Boundaries in Alumina", J. Am. Cer. Soc., v.71 p.50-8.

C.M. Cotell, G.J. Yurek, R. Hussey, D. Mitchell and M.J. Graham, (1990a) "The Influence of Grain Boundary Segregation of Y in Cr_2O_3 on the Oxidation of Cr Metal", Ox. Met., v.34 p.173-200.

C.M. Cotell, G.J. Yurek, R. Hussey, D. Mitchell and M.J. Graham, (1990b) "The Influence of Grain Boundary Segregation of Y in Cr_2O_3 on the Oxidation of Cr Metal. II. Effects of Temperature and Dopant Concentration", Ox. Met., v.34 p.201-16.

C.M. Cotell, (1988) "Effects of Yttrium on the Oxidation Mechanisms of Pure Chromium", Ph.D. Thesis, MIT, Cambridge, MA.

C.M. Cotell, G.J. Yurek, R. Hussey, D. Mitchell and M.J. Graham, (1987) "The Influence of Implanted Yttrium on the Mechanism of Growth of Cr_2O_3 on Cr", J. Electrochem. Soc., v.134 p.1871.

D. Delaunay, A.M. Huntz and P. Lacombe, (1980) "Mechanical Stresses Developed in High Temperature Resistant Alloys During Isothermal and Cyclic Oxidation Treatments: The Influence. of Yttrium Additions on Oxide Scale Adherence." Corr. Sci., v.20 p.1109-17.

J. Doychak and M. Ruhle, (1989) "TEM Studies of Oxidized NiAl and Ni_3Al Cross Sections", Ox. Met., v.31 p.431-52.

J. Doychak, J.L. Smialek and T.E. Mitchell, (1989a) "Transient Oxidation of Single-Crystal ß-NiAl", Met. Trans., v.20A p.499-518.

J. Doychak, C.A. Barrett and J.L. Smialek, (1989b) "Oxidation Between 1000°C and 1600°C and Limiting Criteria for the Use of Zr-doped ß-NiAl and ß/γ' alloys", in Corrosion & Particle Erosion at High Temperatures, V. Srinivasan and K. Vedula eds., Proc. TMS-AIME, Metals Park, OH, p.487-514.

J. Doychak, J.L. Smialek and C.A. Barrett, (1988) "The Oxidation of Ni-Rich Ni-Al Intermetallics", in Oxidation of High-Temperature Intermetallics, T. Grobstein and J. Doychak eds., TMS, Warrendale, PA, p.41-56.

J. Doychak, (1986) "The Evolution and Growth of Al_2O_3 Scales on ß-NiAl", NASA Contractor Report No. 175097, Cleveland, OH.

J. Doychak, T.E. Mitchell and J.L. Smialek, (1985) "High Temperature Oxidation of ß-NiAl", MRS Symp. Proc., v.39 p.475-84.

M.M. El-Aiat and F.A. Kroger, (1982) "Yttrium, an Isoelectric Donor in α-Al_2O_3", J. Am. Cer. Soc., v.65 p.280-3.

E.J. Felten and F.S. Pettit, (1976) "Development, Growth, and Adhesion of Al_2O_3 on Platinum-Aluminum Alloys", Ox. Met., v.10 p.189-223.

E.J. Felten, (1961) "High-Temperature Oxidation of Fe-Cr Base Alloys with Particular Reference to Fe-Cr-Y Alloys", J. Electrochem. Soc., v.108 p.490-5.

S.K. Filatov and V.A. Frank-Kamenetskii, (1974) Soviet Phys.Cryst., v.14 p.696.

P. Fox, D.G. Lees and G.W. Lorimer, (1991) "Sulfur Segregation During the HIgh-Temperature Oxidation of Chromium", Ox. Met., v.36 p.491-503.

J.M. Francis and J.A. Jutson, (1968) "High Temperature Oxidation of an Fe-Cr-Al-Y Alloy in CO_2", Corr. Sci., v.8 p.445-9.

K. Fueki and J.B. Wagner, (1965) "Studies of the Oxidation of Nickel in the Temperature Range of 900°C to 1400°C", J. Electrochem. Soc., v.112 p.384-8.

A.W. Funkenbush, J.G. Smeggil and N.S. Bornstein, (1985) "Reactive Element-Sulfur Interaction and Oxide Scale Adherence", Met. Trans., v.16A p.1164.

W. Furdanowicz, A.J. Garratt-Reed and J.B. Vander Sande, (1991) "Measurements of Beam-Broadening in Samples Observed with a FEG-STEM", Inst. Phys. Conf. Ser. No. 119: Sec. 10 (1991) p.437-441.

A.J. Garratt-Reed, (1987) "Analysis of Boundaries", in Proc. 45th Annual Meeting Elec. Micro. Soc. of Amer., G. W. Bailey ed., San Francisco Press, San Francisco, CA, p.300-3.

A.J. Garratt-Reed, (1986) "High Resolution Microanalysis of Interfaces", MRS Symp. Proc., v.62 p.115-22.

D.R. Gaskell, (1981) Introduction to Metallurgical Thermodynamics, McGraw-Hill Book Co., New York, NY.

C.S. Giggins, B.H. Kear, F.S. Pettit and J.K. Tien, (1974) "Factors Affecting Adhesion of Oxide Scales on Alloys", Met. Trans., v.5A p.1685.

C.S. Giggins and F.S. Pettit, (1971) "The Oxidation of TD NiC (Ni-20Cr-2 vol pct ThO_2) Between 900° and 1200°C", Met. Trans., v.2A p.1071-8.

F.A. Golightly, F.H. Stott and G.C. Wood, (1976) "The Influence of Yttrium Additions on the Oxide-Scale Adhesion to an Iron-Chromium-Aluminum Alloy", Oxid. Met., v.10 p.163-87.

W.C. Hagel, (1965a) "The Oxidation of Iron, Nickel and Cobalt-Base Alloys Containing Aluminum", Corrosion, v.21 p.316-26.

W.C. Hagel, (1965b) "Anion Diffusion in α-Cr_2O_3", J. Am. Cer. Soc., v.48 p.70-5.

W.C. Hagel and A.U. Seybolt, (1961) "Cation Diffusion in Cr_2O_3", J. Electrochem. Soc., v.108 p.1146-52.

R. Hales and A.C. Hill, (1972) "The Role of Metal Lattice Vacancies in the High Temperature Oxidation of Nickel", Corr. Sci., v.12 p.843-53.

H.M. Hindam and W.W. Smeltzer, (1980a) "Application of Auger Electron Spectroscopy and Inert Metal Marker Techniques to Determine Metal and Oxygen Transport in Oxide Films on Metals", Oxid. Met., v.14 p.337-349.

H.M. Hindam and W.W. Smeltzer, (1980b) "Growth and Microstructure of α-Al_2O_3 on ß-NiAl", J. Electrochem. Soc., v.127 p.1630-35.

L.W. Hobbs and T.E. Mitchell, (1983) "Studies of Metal Oxidation by Transmission Electron Microscopy", in High Temperature Corrosion, R. Rapp ed., NACE, Houston, TX, p.76-83.

P.Y. Hou, Z.R. Shui, G.Y. Chuang and J. Stringer, (1992) "Effect of Reactive Element Oxide Coatings on the High Temperature Oxidation Behavior of a FeCrAl Alloy", J. Electrochem. Soc., v.139 p.1119-26.

P.Y. Hou and J. Stringer, (1988) "The Influence of Ion-Implanted Yttrium on the Selective Oxidation of Chromium in Co-25wt%Cr", Oxid. Met., v.29 p.45-73.

V.R. Howes, (1969) "Metal Transport in Voids at Metal-Oxide Interfaces", J. Electrochem. Soc., v.116 p.1286-7.

T.T. Huang, R. Richter, Y.L. Chang and E. Pfender, (1985) "Formation of Aluminum Oxide Scales in Sulfur-Containing High Temperature Environments", Met. Trans., v.16A p.2051-2059.

T.T. Huang, Y.C. Lin, D.A. Shores and E. Pfender, (1984) "Corrosion of FeCrAl, FeCrAlY, and FeCrAlHf Alloys in High Temperature H_2-H_2O-H_2S Environments", J. Electrochem. Soc., v.131 p.2191-6.

J. Ikeda, Y. Chiang and C. Madras, (1991) "Grain Boundary Electrostatic Potential as a Function of Acceptor and Donor Doping in TiO_2", in Point Defects & Related Properties of Ceramics, T.O. Mason & J.L. Routbort eds., p.341-8.

Y. Ikeda, K. Nii and K. Yoshihara, (1983) "High Temperature Oxidation and Surface Segregation of Sulfur", in Proc. JIMIS-3, High Temperature Corrosion Transactions Supplement, Japan Inst. Met., Tokyo, Japan, v. 24 p.207-14.

J. Jedlinski and G. Borchardt, (1991) "On the Oxidation Mechanism of Alumina Formers", Ox. Met., v.36 p 317-337.

J. Jedlinski, (1990) "The Influence of Reactive Elements on the Oxidation Behavior of Alumina Formers - Review Paper", in Proc. 11th International Corrosion Congress, v.4, Plenum Press, New York, NY, p.21-27.

J. Jedlinski and S. Mrowec, (1987) "The Influence of Implanted Yttrium on the Oxidation Behaviour of ß-NiAl", Mat. Sci. and Eng., v.87 p281-87.

W.C. Johnson, (1977) "Grain Boundary Segregation in Ceramics", Met. Trans., v.8A p.1413-22.

E.P. Katz, B.A. Pint and G.J. Yurek, (1987) "The Effect of Y_2O_3 Dispersions on the Oxidation Behavior of ODS Alloys", unpublished research.

B.H. Kear, F.S. Pettit, D.E. Fornwalt and L.P. Lemaire, (1971) "On the Transient Oxidation of a Ni-25Cr-6Al Alloy", Ox. Met., v.3 p.557-69.

Y.K. Kim, K. Przybylski and G.J. Yurek, (1986) "Segregation of Sulfur to Grain Boundaries in Chromia and Alumina Scales", in Fundamental Aspects of High Temp. Corr., v.2, D. Shores and G.J. Yurek eds., Electrochem. Soc., Pennington, NJ, v.86-9 p.123.

W.E. King, N.L. Peterson J.F. Reddy, (1984) "Application of Transverse-Section Analytical Electron Microscopy to the Study

of Oxidation of Metal Alloys", in Proc. 9th International Congress on Metallic Corr., Toronto, v.4 National Research Council, Ottawa, Canada, p.28-35.

W.D. Kingery, (1984) "Segregation Phenomena at Surfaces and at Grain Boundaries in Oxide and Carbides", Solid State Ionics, v.12 p.299-307.

W.D. Kingery, T. Mitamura, J.B. Vander Sande and E.L. Hall, (1979) "Boundary Segregation of Ca, Fe, La and Si in Magnesium Oxide", J. Mat. Sci., v.14 p.1766-7.

W.D. Kingery, H.K. Bowen and D.L. Uhlmann, (1976) Introduction to Ceramics, John Wiley & Sons, New York, NY.

J.D. Kuenzly and D.L. Douglass, (1974) "The Oxidation Mechanism of Ni_3Al Containing Yttrium", Oxid. Met., v.8 p.139-78.

A. Kumar, M. Nasrallah and D.L. Douglass, (1974) "The Effect of Yttrium and Thorium on the Oxidation Behavior of Ni-Cr-Al Alloys", Ox. Met., v.8 p.227-63.

M.H. LaBranche, (1985) "The Oxidation of Chromium at Low and High Oxygen Partial Pressures", Ph.D. Thesis, MIT, Cambridge, MA.

M.H. Lagrange, A.M. Huntz and J.H. Davidson, (1984) "The Influence of Y, Zr, or Ti Additions on the High Temperature Oxidation Resistance of Fe-Ni-Cr-Al Alloys of Variable Purity", Corr. Sci., v.24 p.613-27.

M. Lambertin and G. Beranger, (1990) "High-Temperature Oxidation of Fe-Cr-Al Alloys: Influence of Al Content", in High Temperature Oxidation & Sulfidation Processes, W. Embury ed., Can. Inst. Met., Ottawa, p.93-100.

K.N. Lee and W.L. Worrell, (1989) "The Oxidation of Iridium-Aluminum and Iridium-Hafnium Intermetallics at Temperatures Above 1550°C", Ox. Met., v.32 p.357-69.

D.G. Lees, (1987) "On the Reasons for the Effects of Dispersions of Stable Oxides and Additions of Reactive Elements on the Adhesion and Growth-Mechanisms of Chromia and Alumina Scales - The "Sulfur Effect", Ox. Met., v.27 p.75-81.

C.W. Li and W.D. Kingery, (1984) "Solute Segregation at Grain Boundaries in Polycrystalline Al_2O_3", in Structure and Properties of MgO and Al_2O_3 Ceramics, Advances in Ceramics, v.10, W.D. Kingery ed., Amer. Cer. Soc. Inc., Columbus, OH., p.368-78.

C.T. Liu, W. Jemian, H. Inouye, J.V. Cathcart, S.A. David, J.A. Horton and M.L. Santella, (1984) "Initial Development of Nickel and Nickel-Iron Aluminides for Structural Uses" Oak Ridge National Laboratory Report No. ORNL-6067, Oak Ridge, TN, p.25.

M.K. Loudjani, J. Roy and A.M. Huntz, (1985) "Study by Extended X-ray Absorption Fine-Structure Technique and Microscopy of the Chemical State of Yttrium in α-Polycrystalline Alumina", J. Am. Cer. Soc., v.68 p.559-62.

K.L. Luthra and C.L. Briant, (1986) "Mechanism of Adhesion of Alumina on MCrAlY Alloys", Ox. Met., v.26 p.397-416.

R. Mason, (1992) private communication.

T. Mitamura, E.L. Hall, W.D. Kingery and J.B. Vander Sande, (1979) "Grain Boundary Segregation of Iron in Polycrystalline Magnesium Oxide Observed by STEM", Ceramurgia, v.5 p.131-6.

D.P. Moon, (1988) "Mechanisms of the Reactive Element Effect on the High Temperature Oxidation of Metals and Alloys", Harwell Report No. AERE-R12930, Harwell, U.K..

S. Mrowec, A. Gil and A. Jedlinski, (1987) "The Effect of Certain Reactive Elements on the Oxidation Behaviour of Chromia- and Alumina-forming Alloys", Werk. Korr., v.38 p.563-74.

H. Nagai, M. Okabayashi and T. Murakami, (1982) "High Temperature Oxidation of Ni-20Cr-xTiO_2 Alloys", Trans. Japan Inst. Metals, v.23 p.473-9.

P. Nanni, C.T.H. Stoddart and E.D. Hondros, (1976) "Grain Boundary Segrega-tion and Sintering in Alumina", Mater. Chem., v.1 p.297-320.

W.D. Nix, (1990) "High Temperature Strengthening of Metals and Alloys", ASM News, April, p.6-7.

T. Noguchi and T. Kozuka, (1966) Solar Energy, v.10 p.203.

Y. Oishi and W.D. Kingery, (1960) "Self-Diffusion of Oxygen in Single Crystal and Polycrystalline Aluminum Oxide", J. Chem. Phys., v.33 p.480-6.

M. Ozawa, M. Kimura and A. Isogai, (1990) "Thermal Stability and Characterization of γ-Al_2O_3 Modified with Lanthanum or Cerium", J. Mat. Sci. Let., v.9 p.709-11.

A.E. Paladino and R.L. Coble, (1963) "Effect of Grain Boundaries on Diffusion-Controlled Processes in Aluminum Oxide", J. Am. Cer. Soc., v.46 p.133-6.

A.E. Paladino and W.D. Kingery, (1962) "Aluminum Ion Diffusion in Aluminum Oxide", J. Am. Cer. Soc., v.37 p.957-62.

R. Pendse and J. Stringer, (1985) "The Influence of Alloy Microstructure on the Oxide Peg Morphologies in a Co-10%Cr-11%Al Alloy With and Without Reactive Element Additions", Ox. Met., v.23 p.1-16.

F.S. Pettit, (1967) "Oxidation Mechanisms for Nickel-Aluminum Alloys at Temperatures Between 900° and 1300°C", Trans. Met. Soc. AIME, v.239 p.1296-1305.

L.B. Pfeil, (1937) "Improvements in Heat Resistant Alloys", U.K. Patent no. 459848; (1945) U.K. Patent No. 574088.

B.A. Pint, A.J. Garratt-Reed and L.W. Hobbs, (1992) "The Effect of Y and Ti on FeCrAl Oxidation at 1400°C," in Proc. 3rd International Symp. on High Temp. Corrosion and Protection of Materials, in press.

B.A. Pint, K.C. Wills, A.J. Garratt-Reed and L.W. Hobbs, (1991) "The Reactive Element Effect in Commercial FeCrAl Alloys," Electrochemical Society Extended Abstracts, v.91-2, p.913-4.

B.A. Pint and L.W. Hobbs, (1991) "The Effects of Ion Implanted Yttrium on the Oxidation Mechanism of ß-NiAl," Electrochemical Society Extended Abstracts, v.91-2, p.915-6.

B.A. Pint, A. Jain and L.W. Hobbs, (1991) "The Effect of Yttrium Ion Implantation on the High Temperature Oxidation Properties of NiAl," Mat. Res. Soc. Symp. Proc., v.213, p.981-6.

B.A. Pint, A.J. Garratt-Reed and G.J. Yurek, (1989) "The Effect of Yttrium and Sulfur on the Oxidation of Ni-Cr Alloys", unpublished research.

J.C. Pivin, C. Roques-Carmes, J. Chaumont and H. Bernas, (1980) "The Influence of Yttrium Implantation on the Oxidation Behaviour of 67Ni-33Cr, Fe-43Ni-27Cr and Fe-41Ni-25Cr-10Al Refractory Alloys", Corr. Sci., v.20 p.947-62.

K. Przybylski and G.J. Yurek, (1989) "The Influence of Implanted Yttrium on the Mechanisms of Growth of Chromia Scales", in W. King, ed., The Reactive Element Effect, Materials Science Forum, Trans Tech Publ. Ltd., Aedermannsdorf, Switzerland, p.1-45.

K. Przybylski, A.J. Garratt-Reed and G.J. Yurek, (1988) "Grain Boundary Segregation of Yttrium in Chromia Scales", J. Electrochem. Soc., v.135 p.509-17.

K. Przybylski and G.J. Yurek, (1988) "The Influence of Implanted Yttrium on the Microstructures of Chromia Scales Formed on a Co-45wt%Cr Alloy", J. Electrochem. Soc., v.135 p.517-23.

K. Przybylski, A.J. Garratt-Reed, B.A. Pint, E.P. Katz and G.J. Yurek, (1987) "Segregation of Y to Grain Boundaries in the Al_2O_3 Scale Formed on an ODS Alloy", J. Electrochem. Soc., v.134 p.3207.

K. Przybylski, A.J. Garratt-Reed and G.J. Yurek, (1986) "Observation of Coherent Perovskite Particles in Growing Chromia Films", J. Am. Cer. Soc., v.69 p.C264-66.

K. Przybylski and S. Mrowec, (1984) "The Influence of Implanted Y on Protective Properties of Cr_2O_3 and α-Al_2O_3 Scales Formed on Cobalt Base Alloys and ß-NiAl", in Proc. 9th International Congress on Metallic Corr., Toronto, v.1 National Research Council, Ottawa, Canada, p.47-52.

W.J. Quaddakkers, H. Holzbrecher, K.G. Briefs and H. Beske, (1989) "Differences in Growth Mechanisms of Oxide Scales Formed on ODS and Conventional Wrought Alloys", Ox. Met., v.32 p.67-88.

T.A. Ramanarayanan, R. Ayer, R. Petkovic-Luton and D.P. Leta, (1988) "The Influence of Yttrium on Oxide Scale Growth and Adherence", Ox. Met., v.29 p.445-72.

T.A. Ramanarayanan and R. Petkovic-Luton, (1985) "Investigations on the Growth Mechanisms of α-Cr_2O_3 on Ni-Base Alloys with and without Y_2O_3 Dispersions", Ber. Bunsenges. Phys. Chem., v.89 p.402-9.

T.A. Ramanarayanan, M. Raghavan and R. Petkovic-Luton, (1984) "The Characteristics of Alumina Scales Formed on Fe-Based Yttria-Dispersed Alloys", J. Electrochem. Soc., v.131 p.923-31.

T.A. Ramanarayanan, M. Raghavan and R. Petkovic-Luton, (1983) "Al_2O_3 Scales on ODS Alloys", in Proc. JIMIS-3, High Temperature Corrosion Transactions Supplement, Japan Inst. Met., Tokyo, Japan, v. 24 p.199-206.

K.P.R. Reddy and A.R. Cooper, (1982) "Oxygen Diffusion in Sapphire", J. Am. Cer. Soc., v.65 p.634-8.

K.P.R. Reddy, J.L. Smialek and A.R. Cooper, "^{18}O Tracer Studies of Al_2O_3 Scale Formation on NiCrAl Alloys", Oxid. Met., v.17 (1982) p.429-49.

D.J. Reed and B.J. Wuensch, (1980) "Ion-Probe Measurement of Oxygen Self-Diffusion in Singel-Crystal Al_2O_3", J. Am. Cer. Soc., v.63 p.88-92.

K.C. Russell and J.W. Edington, (1972) "Precipitation Behavior and Mechanical Properties of a Nickel-36at% Aluminum Alloy", Metal Science Journal v.6 p.20-4.

G.C. Rybicki and J.L. Smialek, (1989) "Effect of the θ-α-Al_2O_3 Transfor-mation on the Oxidation Behavior of ß-NiAl+Zr", Oxid. Met., v.31 p.275-304.

H. Schaper, E.B.M. Doesburg and L.L. Van Reijen, (1983) "The Influence of Lanthanum Oxide on the Thermal Stability of Gamma Alumina Catalyst Supports", App. Catalysis, v.7 p.211-220.

M.S. Seltzer and B.A. Wilcox, (1972) "Diffusion of Chromium and Aluminum in Ni-20Cr and TDNiCr (Ni-20Cr-2ThO_2)", Met. Trans., v.3 p.2357-62.

D.R. Sigler, (1989) "Aluminum Oxide Adherence on Fe-Cr-Al Alloys Modified with Group IIIB, IVB, VB, and VIB Elements", Ox. Met., v.32 p.337-55.

J.G. Smeggil and G.G. Peterson, (1988) "Nature of Indigenous Sulfur Segregated to the Free Metal Surface and to the Scale-Metal Interface", Ox. Met., v.29 p.103-19.

J.G. Smeggil, (1987) "Some Comments on the Role of Yttrium in Protective Oxide Scale Adherence", Mat. Sci. and Eng., v.87 p.261-65.

J.G. Smeggil, A.W. Funkenbusch and N.S. Bornstein, (1986) "A Relationship Between Indigenous Impurity Elements and Protective Oxide Scale Adherence Characteristics", Met. Trans., v.17A p.923-32.

J.G. Smeggil, E.L. Paradis, A.J. Shuskus and N.S. Bornstein, (1985) "The Use of Ion Implantation Techniques to Study Protective Oxide Scale Adherence Effects", J. Vac. Sci. Tech. A, v.3 p.2569-73.

J.L. Smialek, (1989) "The Effect of Sulfur Removal on Al_2O_3 Scale Adhesion", in Corrosion & Particle Erosion at High Temperatures, V. Srinivasan and K. Vedula eds., Proc. TMS-AIME, Metals Park, OH, p.425-57.

J.L. Smialek, J. Doychak and D.J. Gaydosh, (1988) "Oxidation Behavior of FeAl + Hf,Zr,B", NASA Report No. TM-101402, Cleveland, OH.

J. Smialek, (1987a) "Adherent Al_2O_3 Scales Formed on Undoped NiCrAl Alloys", Met. Trans., v.18A p.164-66.

J.L. Smialek, (1987b) "The Effect of Sulfur and Zirconium Co-doping on the Oxidation of NiCrAl", NASA Report No. TM-100209, Cleveland, OH.

J.L. Smialek and R. Gibala, (1983) "Diffusion Processes in Al_2O_3 Scales: Void Growth, Grain Growth, and Scale Growth", in High Temperature Corrosion, R. Rapp ed., NACE, Houston, TX, p.274-83.

J.L. Smialek, (1979) "Comment on Golightly, Stott and Wood Paper", J. Electrochem. Soc., v.126 p.2275-6.

J. Smialek, (1978) "Oxide Morphology and Spalling Model for NiAl", Met. Trans., v.9A p.309-20.

J.A. Sprague and G.R. Johnston, (1983) "Microstructures and Compositions of Oxide Films Formed on CoCrAlY and Y-Ion-Implanted CoCrAl Alloys", in Proc. 41st Annual Meeting of Elec. Microscopy Soc. of Amer., G.W. Bailey ed., San Francisco Press, San Francisco, CA, p.216-7.

J. Stringer, (1966) Met. Rev., v.11 p.113.

J. Stringer, B.A. Wilcox, and R.I. Jaffe, (1972) "The High-Temperature Oxidation of Nickel-20wt% Chromium Alloys Containing Dispersed Oxide Phases", Ox. Met., v.5 p.11-47.

J.K. Tien and F.S. Pettit, (1972) "Mechanism of Oxide Adherence on Fe-25Cr-4Al (Y or Sc) Alloys", Met. Trans., v.3 p.1587-99.

M.T. Tinker and P.A. Labun, (1982) "Transverse Sections for Electron Microscopy of Oxide Scales on Metals", Oxid. Met., v.18 p.27-36.

P.F. Tortorelli and J.R. Kaiser, (1991) "The Measurement of the Mechanical Properties of Oxide Scales by Submicron Indentation Testing", Electrochemical Society Extended Abstracts, v.91-2, p.924-5.

E. Tsuzi, (1980) "The Role of Yttrium on the Oxide Adherence of Fe-24Cr Base Alloys", Met. Trans., v.11A p.1965-72.

P.A. van Manen, E.W.A. Young, D. Schalkoord, C.J. van der Wekken and J.H.W. de Wit, (1987) "The Influence of Y on the Structure and Growth Mechanism of Alumina Scales", Surf. Inter. Anal., v.12 p.391-6.

D.A. Voss, E.P. Butler and T.E. Mitchell, (1982) "The Growth of Hematite Blades during the High Temperature Oxidation of Iron", Met. Trans., v.13A p.929-35.

C. Wagner, (1933) "Beitrag zur Theorie des Anlaufvorgangs", Z. Phys. Chem., v.B21 p.25.

C. Wagner, (1951) "Diffusion and High Temperature Oxidation of Metals", in Atom Movements, Amer. Soc. Metals, Cleveland, OH, p.153-73.

I. Warshaw and R. Roy, (1959) "Stable and Metastable Equilibria in the Systems Y_2O_3-Al_2O_3 and Gd_2O_3-Fe_2O_3", J. Am. Cer. Soc., v.42 p.434-38.

D.P. Whittle and J. Stringer, (1980) "Improvement in Properties: Additives in Oxidation Resistance', Phil. Trans. R. Soc. Lond. A, v.295 p.309-29.

D.P. Whittle, M.E. El-Dahshan and J. Stringer, (1977) "The Oxidation Behaviour of Cobalt-Base Alloys Containing Dispersed Oxides Formed by Internal Oxidation", Corr. Sci., v.17 p.879-91.

R.G. Wilson, F.A. Stevie and C.W. Magee, (1989) Secondary Ion Mass Spectroscopy: A Practical Handbook for Depth Profiling and Bulk Impurity Analysis, John Wiley & Sons, New York, NY.

G.C. Wood and J. Boustead, (1968) "The Influence of Group IIIA Metals on the Oxidation of Fe-Cr Alloys", Corr. Sci., v.8 p.719-23.

I.G. Wright, B.A. Wilcox and R.I. Jaffee, (1975) "The High-Temperature Oxidation of Ni-20%Cr Alloys Containing Various Oxide Dispersions", Ox. Met., v.9 p.275-305.

C.S. Wukusick and J.F. Collins, (1964) Mater. Res. Std., v.4 p.637-46.

J.R. Wynnyckyj and C.G. Morris, (1985) "A Shear-Type Allotropic Transfor-mation in Alumina", Met. Trans., v.16B p.345-53.

M.F. Yan, R.M. Cannon and H.K. Bowen, (1977) "Solute Segregation at Ceramic Interfaces", in Interfacial Segregation, ASM, Metals Park, OH, p.255.

E.W.A. Young, H.E. Bishop and J.H.W. de Wit, (1986) "On the Use of Markers and Tracers to Establish the Growth Mechanism of Alumina Scales During High Temperature Oxidation", Surf. Interface Anal., v.9 p.163-8.

E.W.A. Young and J.H.W. de Wit, (1986) "An ^{18}O Tracer Study on the Growth Mechanism of Alumina Scales on NiAl and NiAlY Alloys", Oxid. Met., v.26 p.351-61.

E.W.A. Young and J.H.W. De Wit, (1985) "The Use of a ^{18}O Tracer and Rutherford Backscattering Spectrometry to Study the Oxidation Mechanism of NiAl", in High Temperature Oxydation of Alloys, E. Young ed., p.30-37.

E.W.A. Young and J.H.W. de Wit, (1984) "The application of RBS on the study of high temperature corrosion processes with special emphasis on the oxidation of ß-NiAl", in Proc. 9th International Congress on Metallic Corr., Toronto, v.4, National Research Council, Ottawa, Canada, p.50-3.

E.W.A. Young and J.H.W. de Wit, (1983) "Rutherford Backscattering Spectro-metry as an Experimental Method to Study the Oxidation Mechanism of $NiAl_3$ Alloy", Surf. Interface Anal., v.5 p.177-80.

G.J. Yurek, (1987) "Mechanisms of Diffusion-Controlled High-Temperature Oxidation of Metals", in Corrosion Mechanisms, F. Mansfield ed., Marcel Dekker Inc., New York, NY, p.397-446.

G.J. Yurek, K. Przybylski, C.M. Cotell and Y.K. Kim, (1987a) "Segregation of Foreign Ions to Grain Boundaries in Cr_2O_3 and Al_2O_3 Scales", in Proc. Symp. High Temp. Mat. Chem. IV, Electrochem Soc., Pennington, NJ, p.107.

G.J. Yurek, K. Przybylski and A.J. Garratt-Reed, (1987b) "Segregation of Y to Grain Boundaries in Cr_2O_3 and NiO Scales Formed on an ODS Alloy", J. Electrochem. Soc., v.134 p.2643.

G.J. Yurek and H. Schmalzred, (1975) "Deviations from Local Thermodynamic Equilibrium During Interdiffusion of CoO-MgO and CoO-NiO", Ber. Bunsenges. Phys. Chem., v.79 p.255.

bruCE and HOBBS